

# Pulse Energy Scaling of Thulium-Doped Fiber Lasers for Nonlinear Conversion into the Mid-Infrared





Julian Schneider

**Pulse Energy Scaling of Thulium-Doped Fiber Lasers  
for Nonlinear Conversion into the Mid-Infrared**

Lasers and Optronics:  
Materials, Technologies and Applications  
**Volume 6.2026**

Editor: Prof. Dr. rer. nat. habil. Marc Eichhorn

Professur für Optronik am  
Karlsruher Institut für Technologie (KIT)

Fraunhofer-Institut für Optronik, Systemtechnik  
und Bildauswertung (IOSB)

# **Pulse Energy Scaling of Thulium-Doped Fiber Lasers for Nonlinear Conversion into the Mid-Infrared**

by  
Julian Schneider

Karlsruher Institut für Technologie  
Institut für Regelungs- und Steuerungssysteme

Pulse Energy Scaling of Thulium-Doped Fiber Lasers  
for Nonlinear Conversion into the Mid-Infrared

Zur Erlangung des akademischen Grades eines Doktors der Ingenieurwissenschaften von der KIT-Fakultät für Elektrotechnik und Informationstechnik des Karlsruher Instituts für Technologie (KIT) genehmigte Dissertation

von Julian Schneider, M.Sc

Tag der mündlichen Prüfung: 8. Januar 2026

Prof. Dr. rer. nat. habil. Marc Eichhorn

Prof. Dr. rer. nat. habil. Uli Lemmer

## Impressum



Karlsruhe Institute of Technology (KIT)  
Kaiserstraße 12  
76131 Karlsruhe  
Institute of Control Systems  
[www.irs.kit.edu](http://www.irs.kit.edu)



*This document – excluding parts marked otherwise, the cover, pictures and graphs – is licensed under a Creative Commons Attribution-Share Alike 4.0 International License (CC BY-SA 4.0): <https://creativecommons.org/licenses/by-sa/4.0/deed.en>*



*The cover page is licensed under a Creative Commons Attribution-No Derivatives 4.0 International License (CC BY-ND 4.0): <https://creativecommons.org/licenses/by-nd/4.0/deed.en>*

2026

ISSN 2943-2308

DOI 10.5445/IR/1000190171





# **Pulse Energy Scaling of Thulium-Doped Fiber Lasers for Nonlinear Conversion into the Mid-Infrared**

Zur Erlangung des akademischen Grades eines  
DOKTORS DER INGENIEURWISSENSCHAFTEN (Dr.-Ing.)

von der KIT-Fakultät für Elektrotechnik und Informationstechnik des  
Karlsruher Instituts für Technologie (KIT)  
angenommene

DISSERTATION

von

**Julian Stefan Schneider, M.Sc**

geboren am 12.05.1995 in Emmendingen

Tag der mündlichen Prüfung: 08.01.2026

Hauptreferent: Prof. Dr. rer. nat. habil. Marc Eichhorn

Korreferent: Prof. Dr. rer. nat. habil. Uli Lemmer



# Kurzfassung

Gepulste Hochleistungslaserquellen im Spektralbereich um  $2\ \mu\text{m}$  eignen sich für zahlreiche Anwendungen in den Bereichen der Fernerkundung, Materialbearbeitung und der Medizin. Neben ihrem direkten Einsatz stellen diese Laser ideale Pumpquellen für die nichtlineare Frequenzkonversion dar, um Hochenergiestrahlung im mittleren Infrarot (mid-IR) zu erzeugen. Der Bereich des mid-IR von  $3\text{--}5\ \mu\text{m}$  bedient wiederum wichtige Anwendungen in der Spektroskopie, der minimalinvasiven Chirurgie und der Verteidigungstechnik. Diese Anwendungen stellen hohe Anforderungen an den  $2\ \mu\text{m}$ -Laser: Um maximale Effektivität zu erzielen, ist oft eine Kombination aus hoher Ausgangsleistung und Pulsenergie bei gleichzeitig hervorragender Strahlqualität und spektraler Reinheit erforderlich. Das Erreichen von langen Emissionswellenlängen oberhalb von  $2\ \mu\text{m}$  ist hierbei von besonderer Bedeutung, da in diesem Spektralbereich eine höhere atmosphärische Transmission sowie eine geringere Hintergrundabsorption im nichtlinearen Kristall  $\text{ZnGeP}_2$  (ZGP) vorzufinden sind.

Thulium-dotierte Faserlaser stellen eine vielversprechende Technologie zur Adressierung dieses Spektralbereichs dar. Sie erreichen hohe Ausgangsleistungen mit nahezu beugungsbegrenzter Strahlqualität, wobei sie sich gleichzeitig durch die Möglichkeit einer kompakten und zuverlässigen Systemintegration auszeichnen. Die primäre Herausforderung der Faserlasertechnologie liegt jedoch in deren eingeschränkter Leistungsfähigkeit im Pulsbetrieb, verursacht durch intensitätsabhängige nichtlineare Effekte sowie die Begrenzung der maximal erreichbaren Verstärkung durch parasitäre Oszillationen und verstärkte spontane Emission. Folglich stellt die Skalierung der Pulsenergie unter Erhalt der spektralen Reinheit ein Kernthema aktueller Forschung an Thulium-dotierten Faserlasern dar.

Diese Arbeit befasst sich mit der zentralen Herausforderung der Pulsenergieskalierung in Nanosekunden-gepulsten Thulium-dotierten Faserlasern. Ausgehend von gezielten ex-

perimentellen Untersuchungen erfolgt die Entwicklung eines semi-analytischen Modellierungsansatzes zur quantitativen Analyse und Optimierung dieser Lasersysteme. Anhand dieser Analyse werden fundamentale Einschränkungen im Faserlaserdesign identifiziert und Strategien zur Überwindung bisheriger Leistungsgrenzen entwickelt sowie experimentell validiert. Die Arbeit kulminiert schließlich in der Demonstration eines Thulium-dotierten Photonic-Crystal-Fiber-(PCF)-Lasers, der einen neuen Maßstab für die 2  $\mu\text{m}$ -Lasertechnologie setzt.

Der optimierte PCF-Oszillator erreicht eine maximale Pulsenergie von 1.9 mJ bei einer langen Emissionswellenlänge von 2050 nm und einer hohen mittleren Ausgangsleistung von 114 W. Der Laser weist dabei eine nahezu beugungsbegrenzte Strahlqualität ( $M^2 < 1.3$ ) sowie eine schmale 10-dB-Linienbreite von 340 pm auf. Diese Ergebnisse stellen nahezu eine Verdopplung der bisherigen Pulsenergie von Nanosekunden-Faserlasern dar, für den Betrieb bei Wellenlängen oberhalb von 2  $\mu\text{m}$ . Eine anschließende kollaborative Arbeit zur Entwicklung eines PCF-Verstärkers demonstriert zudem das enorme Potential von Faserlasern zum Pumpen von optisch-parametrischen Oszillatoren (OPO). Der ZGP-OPO erreicht eine Ausgangsleistung von 25.8 W im mid-IR mit einer Rekord-Konversionseffizienz von 69 %. Diese Ergebnisse ebnen den Weg für künftige Faserlaser-gepumpte mid-IR-Quellen mit Ausgangsleistungen von über 100 W.

# Abstract

High-power, pulsed laser sources operating at wavelengths around  $2\ \mu\text{m}$  are in demand for numerous applications in remote sensing, material processing, and medicine. Beyond their direct application, these  $2\ \mu\text{m}$  lasers serve as pump sources for nonlinear frequency conversion into the mid-infrared (mid-IR), which in turn is ideally suited for spectroscopy, minimally invasive surgery, and defense technology. To maximize the impact and efficiency of the  $2\ \mu\text{m}$  laser in these applications, it must combine high output power and pulse energy with excellent spatial beam quality and spectral purity. Moreover, the advantageous atmospheric transmission and reduced background absorption of the nonlinear crystal  $\text{ZnGeP}_2$  (ZGP) have directed recent efforts in laser development to emission wavelengths longer than  $2\ \mu\text{m}$ .

Thulium-doped fiber lasers represent a compact and reliable technology for generating high-power laser radiation with nearly diffraction-limited beam quality in this spectral range. However, in pulsed operation, their performance is fundamentally constrained by intensity-dependent nonlinear effects and gain limitations, such as parasitic lasing and amplified spontaneous emission. Consequently, ongoing research faces the challenge of scaling the pulse energy in thulium-doped fiber lasers while maintaining high spectral purity and beam quality.

This thesis addresses the central challenge of pulse energy scaling in nanosecond-pulsed thulium-doped fiber lasers. Supported by dedicated experimental investigations, a general framework for quantitative modeling of these systems is developed. Based on this model, the fundamental constraints and trade-offs in fiber laser design are analyzed and quantified. From this analysis, strategies to overcome previous performance barriers were identified and experimentally validated. The work culminates in the demonstration of a thulium-doped photonic crystal fiber (PCF) laser that successfully sets a new benchmark for  $2\ \mu\text{m}$  laser technology.

This optimized PCF oscillator demonstrates a pulse energy of 1.9 mJ at a long emission wavelength of 2050 nm with a high average output power of 114 W. The laser exhibits nearly diffraction-limited beam quality ( $M^2 < 1.3$ ) and a narrow 10-dB linewidth of 340 pm. These results represent a significant advancement beyond the state of the art, nearly doubling the pulse energy reported from previous nanosecond-pulsed fiber lasers at wavelengths beyond 2  $\mu\text{m}$ . Furthermore, subsequent collaborative work on the development of a PCF amplifier confirms the enormous potential of fiber lasers for pumping nonlinear converters, demonstrating 25.8 W of mid-IR output power from a ZGP optical parametric oscillator with a record conversion efficiency of 69 %. These results pave the way for future fiber-laser-pumped mid-IR sources with output powers exceeding 100 W.

# Contents

<b>Kurzfassung</b> . . . . .	<b>i</b>
<b>Abstract</b> . . . . .	<b>iii</b>
<b>1 Introduction</b> . . . . .	<b>1</b>
<b>2 Theoretical Foundation</b> . . . . .	<b>7</b>
2.1 Fundamental Principles of Light Propagation and Interaction . . . . .	8
2.1.1 Laser Light: Beam Propagation and Characteristics . . . . .	8
2.1.2 Linear Propagation in Dielectric Media . . . . .	16
2.1.3 Absorption and Emission . . . . .	31
2.1.4 Nonlinear Interactions . . . . .	42
2.2 Principles of Optical Amplification and Oscillation . . . . .	64
2.2.1 Fundamentals of Optical Oscillators . . . . .	64
2.2.2 Laser Amplifiers and Oscillators . . . . .	70
2.2.3 Optical Parametric Oscillators . . . . .	80
2.3 Thulium-doped Fiber Lasers . . . . .	88
2.3.1 Spectroscopy of Thulium-doped Silica . . . . .	89
2.3.2 Fiber Waveguide Geometry and Specialty Fibers . . . . .	95
2.3.3 Fiber Nonlinearities . . . . .	107
2.3.4 Fiber Laser Architectures . . . . .	123
2.4 Pulse Generation in Fiber Lasers . . . . .	128
2.4.1 Active Q-switching . . . . .	133
2.4.2 Pulse Amplification in Fiber Amplifiers . . . . .	140
2.4.3 Pulse Energy Scaling and State of the Art . . . . .	144

2.5	Mid-Infrared Generation via Optical Parametric Oscillators . . . . .	150
2.5.1	The Nonlinear Crystal ZnGeP <sub>2</sub> . . . . .	151
2.5.2	Pump Source Requirements . . . . .	153
2.5.3	State of the Art in Fiber-Laser-Pumped ZGP OPOs . . . . .	158
<b>3</b>	<b>Investigation of Pulse Energy Limits and Nonlinear Conversion . . . . .</b>	<b>163</b>
3.1	Q-switched Fiber Oscillator . . . . .	164
3.1.1	Experimental Setup and Procedure . . . . .	164
3.1.2	Experimental Results and Discussion . . . . .	166
3.2	Pumping of a ZGP OPO . . . . .	181
3.2.1	Experimental Setup . . . . .	181
3.2.2	Experimental Results and Discussion . . . . .	182
3.3	Conclusion . . . . .	186
<b>4</b>	<b>Analysis and Optimization of Pulse Energy Extraction . . . . .</b>	<b>189</b>
4.1	Analysis of Gain Limitations . . . . .	191
4.1.1	Modeling of Gain Saturation and Parameter Calibration . . . . .	192
4.1.2	Analysis of Pulse Extraction . . . . .	198
4.2	Analysis of Fiber Nonlinearities . . . . .	205
4.3	Conclusion . . . . .	209
<b>5</b>	<b>Investigation of a Large-Mode-Area Photonic Crystal Fiber . . . . .</b>	<b>211</b>
5.1	Experimental Setup . . . . .	212
5.2	Results and Discussion . . . . .	214
5.2.1	Initial Experimental Characterization . . . . .	214
5.2.2	Model Calibration and Optimization Strategy . . . . .	216
5.2.3	Validation and Refinement . . . . .	221
5.2.4	Power Scaling of the Q-switched Photonic Crystal Fiber Oscillator . . . . .	226
5.3	Conclusion . . . . .	228
<b>6</b>	<b>Conclusion and Outlook . . . . .</b>	<b>231</b>
6.1	Thesis Summary . . . . .	231
6.2	General Fiber Laser Design Approach . . . . .	234
6.3	Implementation of a Photonic Crystal Fiber Amplifier . . . . .	236
6.4	Comparison with the State of the Art . . . . .	238
6.5	Outlook . . . . .	243

<b>References</b> . . . . .	<b>247</b>
<b>Publications and Conference Contributions</b> . . . . .	<b>273</b>
<b>List of Acronyms</b> . . . . .	<b>277</b>
<b>Danksagung</b> . . . . .	<b>281</b>



# 1 Introduction

Since the first experimental demonstration by Maiman in 1960, the laser has evolved into an integral component of the modern technological landscape [1]. Lasers are ubiquitous in all areas of society, including application fields in measurement and safety technology, medical surgery and diagnostics, industrial material processing, and fundamental science. They form the basis of global information transfer and networking, indispensable for the modern Internet. Furthermore, lasers actively push technological frontiers, whether through the generation of extreme ultraviolet (EUV) radiation for next-generation semiconductor manufacturing or by offering a promising pathway for sustainable energy generation from nuclear fusion [2, 3].

Responsible for this widespread success are the unique properties of laser light. Coherent laser radiation exhibits minimal divergence, forming a directed beam that can either be transmitted over long distances onto a receiving target, or be focused on small spots to achieve the high intensities required for precise material processing or to initiate intensity-dependent nonlinear effects in matter. Moreover, lasers offer precisely defined spectral characteristics often with high spectral purity. This allows them to address specific molecular absorption lines for sensing or medical applications, or to align with atmospheric transmission bands for low-loss, free-space propagation. The exact output characteristics required from a laser in the spatial, spectral, and temporal domain are dictated by the specific application.

The class of high-power lasers provides the signal strengths necessary for long-range information transfer with high signal-to-noise ratio (SNR) and the high intensities for industrial processing or driving nonlinear effects. To maximize impact and efficiency of a laser beam for a specific application, these lasers must combine high output power with excellent spatial beam quality and emission at a specific wavelength with high spectral purity.

The emergence of the fiber laser has revolutionized high-power laser technology, continuously supplanting competing CO<sub>2</sub> and bulk solid-state lasers in both industrial and medical applications [4–6]. Fiber lasers offer crucial advantages in terms of performance as well as practical applicability: their geometry-related excellent thermal management makes them ideally suited for high-power operation, and the integration into an all-in-fiber architecture allows for exceptionally compact, robust, and reliable laser systems. The most mature fiber laser technology is based on Yb<sup>3+</sup>-doped silica fibers which emit at wavelengths around 1 μm. Yb<sup>3+</sup>-doped fiber lasers have demonstrated more than 10 kW of average output power in continuous-wave (CW) operation with close to diffraction-limited beam quality [7]. However, for many applications, longer emission wavelengths are either required or highly beneficial. Consequently, the focus of current laser research has increasingly shifted to the spectral regions around 2 μm and the mid-infrared (mid-IR) between 3–5 μm.

High-power laser radiation at wavelengths around 2 μm is required for numerous applications as a result of several distinct features in this spectral region. In the field of medical laser surgery, the high water absorption at 2 μm results in a minimal penetration depth in biological tissue, making the wavelength ideal for minimally invasive operations. Furthermore, this wavelength provides a coagulation effect that mitigates bleeding during operations. Consequently, 2 μm lasers are widely employed for lithotripsy, ophthalmic surgery, dermatology, and the removal of tumors [6, 8]. For many of these applications, pulsed lasers in the micro- to nanosecond regime are beneficial, as they allow for precise ablation while minimizing thermal diffusion to the surrounding tissue [9].

In material processing, 2 μm laser radiation is particularly attractive for the cutting and welding of polymers, especially for materials that are transparent at shorter wavelengths of Yb<sup>3+</sup>-based lasers [8, 10, 11]. Similarly to medical procedures, pulsed lasers can increase the precision by reducing the lateral heat diffusion.

Furthermore, the 2 μm region offers several advantages for free-space applications such as sensing and spectroscopy. First, this wavelength is in the "eye-safe" region, which means that the threshold for retinal damage is substantially higher than at wavelengths shorter than 1.4 μm. This simplifies the safety requirements for free-space application of these lasers. Second, for propagation over long distances, the atmosphere offers a transmission window at wavelengths above 2 μm, as shown in fig. 1.1. The combination of eye-safety and low atmospheric propagation loss enables applications such as range measurement, object detection, and 3D imaging via LIDAR (Light Detection and Ranging) techniques [8, 12]. In addition,

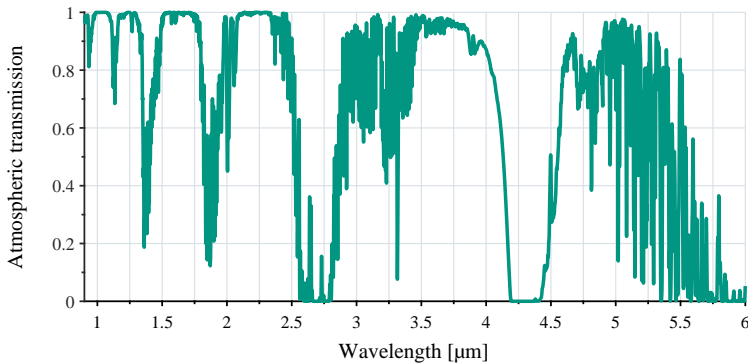


Figure 1.1: Atmospheric transmission versus wavelength. There are transmission bands at  $\sim 2.0\text{--}2.5\ \mu\text{m}$ ,  $\sim 3.5\text{--}4\ \mu\text{m}$ , and  $\sim 4.5\text{--}5\ \mu\text{m}$  relevant for the coherent radiation sources developed in this work. These data produced using the program IRTRANS4, were obtained from the UKIRT worldwide web pages [14].

this spectral window also contains distinct absorption lines for many gases, such as  $\text{H}_2\text{O}$ ,  $\text{CO}_2$ , and  $\text{N}_2\text{O}$ , which allows for their detection and analysis in atmospheric spectroscopy [8]. For these applications, pulsed lasers offer improved distance resolution, while high pulse energies enhance the SNR and allow for measurements over longer ranges [13].

High-power laser systems operating in the  $2\ \mu\text{m}$  range are typically based on  $\text{Tm}^{3+}$ -doped or  $\text{Ho}^{3+}$ -doped bulk crystals or optical fibers. While  $\text{Ho}^{3+}$ -based systems are often preferred for generating longer emission wavelengths in the range of  $\sim 2.09\text{--}2.2\ \mu\text{m}$ ,  $\text{Tm}^{3+}$ -based lasers offer the crucial advantage of being efficiently pumped by readily available, high power AlGaAs laser diodes at  $793\ \text{nm}$  [15]. Consequently,  $\text{Tm}^{3+}$ -doped fiber lasers have emerged as a widely employed and continuously growing technology in all areas of application [5, 6, 11]. They have been shown to generate  $1\ \text{kW}$  of output power with nearly diffraction-limited beam quality, thus representing the fiber laser technology with the second-highest power capabilities after  $\text{Yb}^{3+}$ -doped systems [16–21]. This high-power capability combined with a widely tunable emission range (typically  $\sim 1.9\text{--}2.1\ \mu\text{m}$ ) in the amorphous silica host and the inherent advantages of the fiber laser architecture in compactness, robustness, and reliability have placed them at the center stage of current laser research. In addition to their direct application,  $\text{Tm}^{3+}$ -doped fiber lasers have also been demonstrated to serve as pump sources for nonlinear frequency conversion into the mid-IR [22].

Many specific applications demand coherent radiation sources emitting at wavelengths even longer than the  $2\ \mu\text{m}$  region. The mid-IR spectral range from  $3\text{--}5\ \mu\text{m}$  is of particular interest as it

is known as the "molecular fingerprint region". Because the ro-vibrational absorption signatures of many chemical compounds are located here, mid-IR laser sources are ideally suited for highly-sensitive spectroscopy [23]. Furthermore, this spectral range contains two atmospheric transmission windows, located at approximately 3.5–4  $\mu\text{m}$  and 4.5–5  $\mu\text{m}$ , offering low propagation loss for free-space applications (see fig. 1.1). Taking these features together, high-power mid-IR radiation provides the ability to remotely measure and analyze chemical compounds, enabling applications such as atmospheric spectroscopy of greenhouse gases or the detection of hazardous or explosive substances from a safe distance [24, 25].

Mid-IR laser sources are also highly attractive for medical applications. The even stronger water absorption in this spectral range than at 2  $\mu\text{m}$  allows for minimally invasive surgery with reduced collateral thermal damage [26, 27]. In addition, the mid-IR radiation can be used for non-invasive diagnostics by identifying biomarkers in spectroscopic breath analysis [28, 29].

However, the generation of coherent, high-power mid-IR radiation is challenging. Mid-IR fiber lasers based on rare-earth dopants such as  $\text{Er}^{3+}$  (emission at  $\sim 2.8 \mu\text{m}$  and  $\sim 3.5 \mu\text{m}$ ),  $\text{Dy}^{3+}$  ( $\sim 2.9 \mu\text{m}$ ), and  $\text{Ho}^{3+}$  ( $\sim 2.9 \mu\text{m}$ ,  $\sim 3.2 \mu\text{m}$ , and  $\sim 3.9 \mu\text{m}$ ), have made significant progress in recent years, typically providing output powers in the tens of watt [30, 31]. These lasers, however, rely on rather inefficient lasing schemes and on fragile and moisture-sensitive fluoride fiber hosts, making reliable, long-term operation at high-power levels a challenge [32, 33]. Quantum cascade lasers and interband cascade lasers represent another valuable technology for mid-IR generation, but they are limited in their energy storage capacity, which restricts their use for generating high pulse energies [34, 35].

Beyond direct mid-IR laser emission, nonlinear frequency conversion offers a highly attractive and well-established avenue for generating high-power radiation in this spectral range. A widely-adopted approach is the conversion of a 2  $\mu\text{m}$  pump beam in an optical parametric oscillator (OPO) to generate two mid-IR beams, referred to as the signal and idler. This quasi-instantaneous conversion process is governed by energy and momentum conservation, making the mid-IR output characteristics primarily dependent on the properties of the 2  $\mu\text{m}$  pump source. Consequently, 2  $\mu\text{m}$ -pumped OPOs represent highly versatile mid-IR sources that combine high output power and high pulse energy with a widely tunable emission wavelength covering the entire 3–5  $\mu\text{m}$  range.

The traditionally standard pump sources for high-power mid-IR OPOs have been nanosecond-pulsed  $\text{Ho}^{3+}$ -doped  $\text{Y}_3\text{Al}_5\text{O}_{12}$  (YAG) solid-state laser systems. Scaling of this approach has demonstrated mid-IR output powers of more than 150 W [36, 37]. However, to achieve such power levels, the  $\text{Ho}^{3+}$ -based bulk laser system rapidly gains in complexity. Multiple  $\text{Ho}^{3+}$ :YAG amplifier stages are required, and each of them must, in turn, be pumped by another 1.9  $\mu\text{m}$  high-brightness laser, making the overall system inefficient, difficult to integrate, and less robust. A potential solution is the application of a compact, robust, and efficient  $\text{Tm}^{3+}$ -doped fiber laser as the pump source [22]. However, this approach faces a central challenge: the generation of sufficiently high pulse energies from the fiber laser to efficiently drive the nonlinear conversion process.

This thesis addresses the central challenge of pulse energy scaling in 2  $\mu\text{m}$   $\text{Tm}^{3+}$ -doped fiber lasers, specifically focusing on meeting the requirements for efficient nonlinear conversion into the 3–5  $\mu\text{m}$  mid-IR. The pulse energy limitations in  $\text{Tm}^{3+}$ -doped fiber lasers are identified and analyzed based on a comprehensive literature review, dedicated experimental investigations, and the development of a semi-analytical theoretical model. Building on this, fundamental constraints and trade-offs in the laser design are detailed and quantified, considering the performance impacts of fiber characteristics, laser architecture, and operating conditions. From this analysis, strategies to overcome these performance limitations are derived and experimentally validated. Thus, this work provides a comprehensive framework for understanding and optimizing high-energy, nanosecond-pulsed  $\text{Tm}^{3+}$ -doped fiber lasers.

The theoretical foundation of this thesis is laid in chapter 2. A detailed review of the literature establishes a comprehensive overview of the fundamental optical principles and technological concepts upon which this work is built. From this broad perspective, relevant theoretical expressions are introduced, and the research gap that will be addressed is gradually detailed, finally motivating the approach of this work.

Chapter 3 presents the initial experimental investigations that test and refine the established theoretical basics. This comprises experiments on pulse energy scaling of Q-switched  $\text{Tm}^{3+}$ -doped fiber lasers and their application as OPO pump sources for mid-IR generation. These experiments highlight not only the relevant performance limitations but also the mechanisms that can be exploited to enhance the pulse energy extraction.

Based on these experimental findings, chapter 4 develops a theoretical model for quantitatively analyzing and optimizing the performance of nanosecond-pulsed  $\text{Tm}^{3+}$ -doped fiber lasers.

The analysis focuses on the primary limiting factors that have been identified experimentally: gain limitation by parasitic lasing and the intensity limitation by modulation instability. Other potential limitations, such as amplified spontaneous emission (ASE) and pump bleaching, are shown to be not relevant under the operation conditions considered in this work. This focused approach yields a powerful and computationally efficient tool for optimizing specific design parameters, such as fiber length, and paves the way for overcoming existing pulse energy barriers.

Substantial improvement of the pulsed fiber laser performance requires a strategic choice of the active fiber itself. Chapter 5 therefore investigates a  $\text{Tm}^{3+}$ -doped photonic crystal fiber (PCF) for generating high pulse energies in a Q-switched fiber oscillator configuration. The active PCF combines two key features: First, it exhibits a significantly larger core diameter of  $50\ \mu\text{m}$  compared to conventional large-mode-area (LMA) fibers, resulting in a higher saturation energy and reducing the intensity to mitigate nonlinear effects. Second, in contrast to rigid large pitch fiber (LPF) rods, the PCF is flexible, which enables the use of a longer fiber length to provide higher gain at long emission wavelengths. Despite this potential, previous work on  $\text{Tm}^{3+}$ -doped PCFs had been restricted to short emission wavelengths  $< 2\ \mu\text{m}$  and had not surpassed the pulse energies of conventional LMA fibers [38, 39]. Using the theoretical framework developed in the previous chapter, the specific challenges of the PCF were identified and addressed with an optimized fiber length. This approach enabled the experimental demonstration of  $1.9\ \text{mJ}$  of pulse energy with a high average output power of  $114\ \text{W}$  at a long emission wavelength of  $2050\ \text{nm}$ . This almost doubles the previous state of the art in pulse energy in the spectral range beyond  $2\ \mu\text{m}$ , which is ideally suited for free-space applications and nonlinear frequency conversion to the mid-IR.

Finally, the thesis is concluded in chapter 6, summarizing and evaluating the findings and results of this work. After a summary, a general fiber laser design approach is synthesized that can provide guidance for future  $\text{Tm}^{3+}$ -doped fiber laser designs. Furthermore, the results of a subsequent, shared first-authorship work on a PCF amplifier are briefly presented. The results achieved in this thesis and in the subsequent collaborative project are then compared with the state of the art, highlighting the impact of this work. The thesis ends with an outlook for future investigations.

## 2 Theoretical Foundation

This chapter establishes the theoretical framework this work is based on and reviews the technological concepts that are applied and refined in the course of this thesis. Starting from fundamental optical principles, the two primary topics of this work are gradually detailed from the literature and linked together: the generation of high-energy pulses in Thulium-doped fibers and their application for mid-infrared (mid-IR) generation in optical parametric oscillators (OPOs). By developing critical concepts, insights, and conclusions from a broad perspective, a compelling argument is constructed for the approach of this work.

The foundation of this argument begins in section 2.1 with the fundamental principles of light propagation and interaction, providing essential vocabulary and describing the underlying physical mechanisms for techniques and components used throughout this work. Building on this, section 2.2 elaborates on the generation and amplification of coherent light in optical oscillators and amplifiers, emphasizing the distinct features, challenges, and design concepts of lasers and OPOs. This provides the formal framework that is later applied for their optimization. Section 2.3 narrows the focus to the laser technology investigated in this work—Thulium-doped fiber lasers—detailing the physical and practical considerations regarding spectroscopy, waveguiding, architecture, and performance limitation for their employment. Subsequently, section 2.4 presents methods for pulse generation in fiber lasers and reviews the state of the art in this current field of research, highlighting the open scientific questions and technological challenges that are addressed in this work. Finally, section 2.5 considers the application of Thulium-doped fiber lasers for pumping mid-IR OPOs. This concluding section synthesizes and connects the physical principles and design criteria for fiber lasers and OPOs and culminates in the formulation of the demands that motivate the approach of this work.

## **2.1 Fundamental Principles of Light Propagation and Interaction**

Generation and manipulation of light are based on fundamental physical principles governing the interactions of light and matter that constitute the field of optics. The following chapter provides an overview of the optical fundamentals relevant to this work.

The chapter begins by introducing the physical properties of laser light and its practical characterization metrics. It then explores linear propagation in dielectric media, covering concepts like passive material response, optical anisotropy, inhomogeneities, and dispersion, along with describing important optical components that are based on these mechanisms. Following this, the fundamental interactions of absorption and emission are considered, with a special focus on rare-earth transitions in amorphous solids. Finally, relevant principles and concepts of nonlinear optics are discussed, including parametric second- and third-order effects, as well as non-parametric interactions.

### **2.1.1 Laser Light: Beam Propagation and Characteristics**

Lasers generate and amplify light with unique properties. Like any form of light, laser radiation is described by electromagnetic waves. However, in contrast to other light sources, the light emitted from a laser is not a superposition of many different and unrelated waveforms, but rather propagates as a single, coherent waveform. As a result, highly coherent laser light exhibits a precisely defined narrow spectrum and interferes constructively primarily along its propagation axis to form a directed beam with low divergence and high focusability.

## Electromagnetic Waves and the Helmholtz Equation

The fundamental relations to describe electromagnetism in media are given by the macroscopic Maxwell equations in SI units:

$$\nabla \cdot \mathbf{D} = \rho_f \quad (2.1)$$

$$\nabla \cdot \mathbf{B} = 0 \quad (2.2)$$

$$\nabla \times \mathbf{E} = -\frac{\partial \mathbf{B}}{\partial t} \quad (2.3)$$

$$\nabla \times \mathbf{H} = \mathbf{J}_f + \frac{\partial \mathbf{D}}{\partial t} \quad (2.4)$$

in which  $\rho_f$  is the density of free charges and  $\mathbf{J}_f$  the free current density [40].

The effects of bound charges and currents in a medium are considered by the constitutive relations connecting the electric field to the electric displacement  $\mathbf{D}$  and the magnetic field  $\mathbf{H}$  to the magnetic flux-density  $\mathbf{B}$ :

$$\mathbf{D} = \epsilon_0 \mathbf{E} + \mathbf{P} \quad (2.5)$$

$$\mathbf{B} = \mu_0 (\mathbf{H} + \mathbf{M}) \quad (2.6)$$

where  $\mathbf{P}$  is the polarization and  $\mathbf{M}$  is the magnetization in the medium induced by the electric and magnetic fields, respectively,  $\epsilon_0$  is the vacuum permittivity, and  $\mu_0$  is the vacuum permeability [40]. Assuming a linear, nonmagnetic ( $\mathbf{M} = 0$ ), isotropic, and homogeneous dielectric medium, these relations can be simplified to direct proportionalities:

$$\mathbf{D} = \epsilon_0 \epsilon_r \mathbf{E} \quad (2.7)$$

$$\mathbf{B} = \mu_0 \mathbf{H} \quad (2.8)$$

where  $\epsilon_r$  is the scalar relative permittivity taking into account a linear polarization.

Maxwell's equations formulate the dynamic interplay between electric and magnetic fields. Due to their linearity, any field in the time domain, e.g.  $\mathbf{E}(\mathbf{r}, t)$  or  $\mathbf{H}(\mathbf{r}, t)$ , can be represented by superposition of a series of monochromatic waves. This allows for a separate treatment of the individual components oscillating at a single angular frequency  $\omega$  and yields the complex phasor notation:

$$\mathbf{E}(\mathbf{r}, t) = \mathbf{E}(\mathbf{r})e^{j\omega t} \quad (2.9)$$

$$\mathbf{H}(\mathbf{r}, t) = \mathbf{H}(\mathbf{r})e^{j\omega t} \quad (2.10)$$

where  $\mathbf{E}(\mathbf{r})$  and  $\mathbf{H}(\mathbf{r})$  are complex vector amplitudes depending only on the position  $\mathbf{r}$  in space.

Using this notation corresponds to a Fourier transformation of the Maxwell eqs. (2.1) to (2.4) providing their frequency domain representations ( $\partial/\partial t \rightarrow j\omega$ ). Moreover, assuming the absence of free sources ( $\rho_f = 0$ ,  $\mathbf{J}_f = 0$ ), taking the curl ( $\nabla \times$ ) of Faraday's law (2.3), using the vector identity  $\nabla \times (\nabla \times \mathbf{E}) = \nabla(\nabla \cdot \mathbf{E}) - \nabla^2 \mathbf{E}$ , and substituting with eqs. (2.1) and (2.4) yields the linear Helmholtz equation for the electric field in isotropic and homogeneous dielectrics [40]:

$$\nabla^2 \mathbf{E}(\mathbf{r}) + k^2 \mathbf{E}(\mathbf{r}) = 0 \quad (2.11)$$

where  $k$  is the wavenumber that describes the spatial frequency with a period of the wavelength  $\lambda$  in the medium:

$$k = \omega \sqrt{\mu_0 \epsilon_0 \epsilon_r} = \frac{2\pi}{\lambda} = |\mathbf{k}|. \quad (2.12)$$

The wavenumber represents the magnitude of the wave vector  $\mathbf{k}$  pointing in the direction of wave propagation.

The Helmholtz equation is an eigenvalue problem whose solutions are the modes defined by the eigenvalues  $k^2$ . The solutions are plane waves of the form

$$\mathbf{E}(\mathbf{r}) = \mathbf{E}_0 e^{-j\mathbf{k}\mathbf{r}} = \mathbf{E}_0 e^{-j(k_x x + k_y y + k_z z)} \quad (2.13)$$

where  $\mathbf{E}_0$  is a complex vector that describes the polarization and amplitude of the electric field. Maxwell's eqs. (2.1) to (2.4) imply that the vectors of the electric field  $\mathbf{E}_0$ , the magnetic field  $\mathbf{H}_0$ , and the wave vector  $\mathbf{k}$  are mutually orthogonal to each other and therefore form a transverse electromagnetic (TEM) wave. Plane waves traveling in different directions with certain wavelengths serve as eigenmodes for the construction of arbitrary fields via superposition, e.g. a general spherical wave that diverges uniformly in all directions from a light source.

## Paraxial Approximation and Gaussian Beams

In contrast to general spherical wave propagation, a coherent laser beam exhibits high spectral purity and propagates predominantly along one axis, meaning its wave vector  $\mathbf{k}$  points primarily in one direction. To derive an appropriate description for laser beams, the paraxial approximation is applied to the general Helmholtz equation (2.11) [41]. Assuming a beam traveling primarily along the  $z$ -axis, the  $z$ -propagation and the normalized transverse beam profile  $\psi(x, y, z)$  can be separated:

$$\mathbf{E}(\mathbf{r}) = \mathbf{E}_0 \psi(x, y, z) e^{-jkz} . \quad (2.14)$$

Substituting this into the scalar Helmholtz equation analogously to (2.11) yields

$$\nabla_T^2 \psi + \frac{\partial^2 \psi}{\partial z^2} - 2jk \frac{\partial \psi}{\partial z} = 0 \quad (2.15)$$

where  $\nabla_T^2 = \partial^2/\partial x^2 + \partial^2/\partial y^2$  is the transverse Laplacian. Furthermore, as the remaining  $z$ -dependence of the transverse beam profile is slow compared to the underlying carrier wave  $\exp(-jkz)$ , the slowly varying envelope approximation (SVEA) is justified which neglects the second partial derivative in  $z$  with respect to the other terms [41]. Removal of the term  $\partial^2 \psi/\partial z^2$  then yields the paraxial wave equation

$$\nabla_T^2 \psi - 2jk \frac{\partial \psi}{\partial z} = 0 . \quad (2.16)$$

The paraxial approximation is considered valid for laser beams that diverge (or converge) with angles up to about  $30^\circ$  [41]. Solutions of the paraxial wave equation are Hermite-Gaussian functions in Cartesian coordinates and Laguerre-Gaussian functions in cylindrical coordinates which represent a basis of eigenmodes to describe laser beams [41, 42]. The fundamental mode is the Gaussian beam with a field profile in one transverse axis  $x$  of [41]

$$\psi(x, z) = \left(\frac{2}{\pi}\right)^{1/4} \frac{w_{0x}}{w_x(z)} \exp\left(-\frac{x^2}{w_x(z)^2}\right) \exp\left(-j\left[\frac{kx^2}{2R_x(z)} - \phi_x(z)\right]\right) . \quad (2.17)$$

The total transverse beam profile is then the product of the orthogonal solutions:

$$\psi(x, y, z) = \psi(x, z)\psi(y, z) . \quad (2.18)$$

According to eq. (2.17), the fundamental Gaussian mode exhibits a Gaussian field distribution in transverse  $x$ -direction with a standard deviation of  $w_x/\sqrt{2}$  around the optical  $z$ -axis. Therefore,

$$w_x(z) = w_{0x} \sqrt{1 + \left( \frac{z - z_{0x}}{z_{Rx}} \right)^2} \quad (2.19)$$

is defined as the beam radius in transverse  $x$ -direction that changes its size along the propagation axis  $z$  [41]. For the Gaussian beam, the beam radius corresponds to the distance at which the transverse Gaussian field envelope drops to  $1/e$  of its peak value. Along  $z$ , the evolution of the beam radius reaches its minimum,  $w_{0x}$ , at  $z = z_{0x}$ . The phase fronts of a Gaussian beam are characterized by their radius of curvature [41]

$$R_x(z) = (z - z_{0x}) + \frac{z_{Rx}^2}{z - z_{0x}} \quad (2.20)$$

and the Gouy phase shift [41]

$$\phi_x(z) = \arctan \left( \frac{z - z_{0x}}{z_{Rx}} \right) \quad (2.21)$$

where  $z_{Rx}$  is the Rayleigh length given by

$$z_{Rx} = \frac{\pi \omega_{0x}^2}{\lambda}. \quad (2.22)$$

Figure 2.1 illustrates the evolution of the beam radius  $w_x$ , the phase front radius  $R_x$  and the Gouy phase shift  $\phi_x$  around  $z_{0x}$  over a  $z$ -propagation of several Rayleigh lengths  $z_{Rx}$ . The beam radius evolves symmetrically around its minimum  $w_{0x}$ , which is termed the beam waist. At the waist position, the field exhibits plane phase fronts ( $R_x \rightarrow \infty$ ). Along the propagation axis, the Rayleigh length defines the distance from the waist at which the beam radius has increased by  $\sqrt{2}$ , meaning a doubling in mode field area. The phase fronts exhibit maximum curvature at these points ( $z - z_{0x} = \pm z_{Rx}$ ). Consequently, their radius of curvature decreases rapidly within a distance of  $\pm z_{Rx}$  around  $z_{0x}$  followed by a continuous increase in magnitude, approaching  $R_x(z) \approx z - z_{0x}$  in the far field ( $|z - z_{0x}| \gg z_{Rx}$ ). In the far field, the divergence of the beam radius approaches a linear expansion with a divergence angle of

$$\theta_x = \arctan \left( \frac{w_{0x}}{z_{Rx}} \right) \quad (2.23)$$

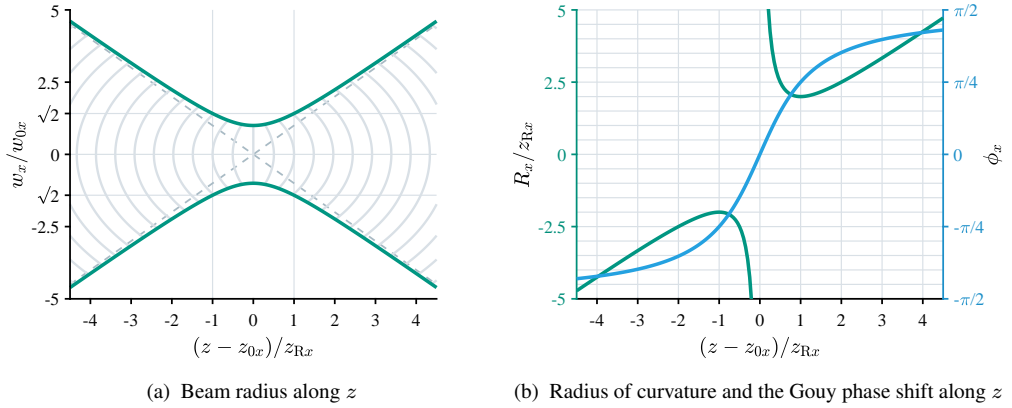


Figure 2.1: Characteristics of the Gaussian beam. In (a), the gray arcs illustrate the form of the phase fronts and the gray dashed lines refer to the far field divergence.

which is indicated by the gray dashed line in fig. 2.1a. The Gouy phase shift  $\phi_x$  depicted in fig. 2.1b accounts for the difference in phase between the Gaussian beam and a plane wave that accumulates its phase solely by the term  $\exp(-jkz)$ . Due to its transverse confinement, the Gaussian beam has nonzero transverse wave vector components  $k_x$  and  $k_y$  leading to a slower phase accumulation in  $z$ -direction ( $k_z < k$ ). Consequently, the Gouy phase shift shows the greatest impact around the waist, where the beam is most confined, resulting in a slightly larger axial spacing of wave fronts in this region compared to a plane wave. The total Gouy shift from  $z = -\infty$  to  $z = +\infty$  adds an extra phase of  $\pi$ .

### Characterization of Real Laser Beams

The fundamental Gaussian mode represents an ideal laser beam in terms of spatial confinement and divergence [41]. This means that any other arbitrary laser beam pattern exhibits a larger divergence when confining it to the same focus size. The propagation of a Gaussian beam in one transverse axis  $x$  along  $z$  is fully described by its wavelength and the beam parameters  $w_{0x}$  or  $z_{Rx}$ . This provides a benchmark against which any real laser beam can be compared to quantify its quality. For this comparison, the beam radius  $w$  of an arbitrary beam is defined in the same way as for the Gaussian beam, as the second moment of its transverse intensity profile ( $\sqrt{2}$  times the standard deviation of the transverse field pattern). This definition is equivalent to

the  $D4\sigma$  diameter ( $2w$ ) according to the ISO standard [43]. Using this definition, the effective Rayleigh length in which the beam radius expands by  $\sqrt{2}$  with respect to its waist is reduced by a factor  $1/M^2$ :

$$z_{R,x,\text{eff}} = \frac{1}{M_x^2} \frac{\pi w_{0x}^2}{\lambda}, \quad (2.24)$$

which results in an evolution of the beam radius along  $z$  given by

$$w_x(z) = w_{0x} \sqrt{1 + \left( M_x^2 \frac{\lambda}{\pi w_{0x}^2} \right)^2 (z - z_{0x})^2} \quad (2.25)$$

where  $M^2$  is the beam propagation factor—a dimensionless metric that quantifies the beam quality of an arbitrary laser beam [44]. An  $M^2 = 1$  represents an ideal Gaussian beam (eqs. (2.24) and (2.25) agree with eqs. (2.19) and (2.22)), which states a diffraction-limited beam quality, i.e. the transverse spatial confinement  $\Delta w_x$  and directionality  $\Delta k_x$  of the beam are Fourier transform limited. As a result, an  $M^2 > 1$  of a non-ideal beam quantifies how close its relation between spatial confinement and angular divergence comes to the fundamental diffraction limit [42]

$$w_{0x} \theta_x = M_x^2 \frac{\lambda}{\pi}. \quad (2.26)$$

This relation is referred to as the beam parameter product.

The power transported by a laser beam is described by the complex Poynting vector of its complex field amplitudes [40]

$$\mathbf{S} = \frac{1}{2} \mathbf{E} \times \mathbf{H}^* \quad (2.27)$$

where  $\mathbf{H}^*$  denotes the complex conjugate of the magnetic field. The real part of the complex Poynting vector  $\text{Re}\{\mathbf{S}\}$  describes the vector field of the time-averaged power flow whose magnitude corresponds to the intensity. Within an isotropic, homogeneous and non-magnetic medium, the intensity of a laser beam is given by

$$I = |\text{Re}\{\mathbf{S}\}| = \frac{1}{2} \sqrt{\frac{\epsilon_0 \epsilon_r}{\mu_0}} |\mathbf{E}|^2 \quad (2.28)$$

which, for a Gaussian beam with optical power  $P(z)$  along its propagation direction  $z$ , leads to

$$I(x, y, z) = \frac{2P(z)}{\pi w_y(z) w_x(z)} \exp\left(-2 \frac{x^2}{w_x(z)^2}\right) \exp\left(-2 \frac{y^2}{w_y(z)^2}\right) \quad (2.29)$$

where the optical power is the integral over the entire cross-sectional area  $A$  of a beam, perpendicular to the propagation direction  $z$ :

$$P(z) = \iint I(x, y, z) dA . \quad (2.30)$$

Experimentally, laser beam characteristics are determined by measuring the irradiance on a sensor surface. Using a detector array placed perpendicular to the propagation axis, the intensity profile  $I(x, y, z)$  of the beam can be spatially resolved with the pixel size. From this profile, the beam radius  $w_x$  in one transverse axis  $x$  corresponds to twice the standard deviation of the intensity profile, in agreement with the ISO standard  $D4\sigma = 2w$  [43]. The optical power  $P$  is typically measured by integrating the irradiance over the surface of a power sensor.

To characterize the beam quality of a laser in terms of  $M^2$ , its transverse beam radius can be measured along the propagation axis. Fitting eq. (2.25) to the measured radii then yields the  $M^2$  of the laser beam in one transverse axis. It should be noted that the beam characteristics  $w_0$ ,  $z_0$ , and  $z_R$  can differ between the transverse axes  $x$  and  $y$ . To account for ellipticity and astigmatism, factors  $M_x^2$  and  $M_y^2$  are determined for both elliptical beam axes  $x$  and  $y$ , respectively. Furthermore, the  $M^2$  factor is defined for a monochromatic laser beam with a wavelength  $\lambda$ , however, real laser light exhibits a wider spectrum that needs to be taken into account. To determine an  $M^2$  factor that characterizes a non-monochromatic laser beam, the central wavelength  $\lambda_c$  of a laser can be determined by calculating the spectral mean

$$\lambda_c = \frac{\int_{-\infty}^{\infty} \lambda S(\lambda) d\lambda}{\int_{-\infty}^{\infty} S(\lambda) d\lambda} \quad (2.31)$$

where  $S(\lambda)$  describes the spectral power density.

Generally, laser light exhibits high spectral purity with a spectrum often consisting of a single peak referred to as a laser line. Therefore, another widely used way to characterize a laser spectrum is to specify its peak wavelength  $\lambda_{\text{peak}}$ . The spectral purity of a laser can be expressed by means of the linewidth measured at levels of 3 dB, 10 dB, or 20 dB of the spectral power density  $S(\lambda)$  with respect to its peak.

## 2.1.2 Linear Propagation in Dielectric Media

In homogeneous media, solutions to the Helmholtz equation, whether in its general form eq. (2.11) yielding plane waves or in its paraxial approximation eq. (2.16) describing Gaussian beams, are characterized by a wavenumber  $k$  specific to the medium. These solutions represent TEM waves exhibiting temporal oscillations with angular frequencies  $\omega$  and spatial propagation described by a wave vector  $\mathbf{k}$  with a magnitude (the wavenumber) and a direction. Spatial propagation is associated with a wavelength  $\lambda$  that represents the spatial period of the TEM wave along its propagation direction that oscillates with a period of  $T = 2\pi/\omega$  in time.

While the temporal oscillation  $\omega$  of an electromagnetic wave is independent of the surrounding medium, the spatial oscillation results from the propagation of phase fronts in the medium with the phase velocity

$$v_p = \frac{\omega}{k} = \lambda f \quad (2.32)$$

where  $f = \omega/(2\pi)$  is the temporal frequency. Eq. (2.32) provides the dispersion relation. It describes the connection  $\omega(k)$  between the temporal and spatial frequency by the phase velocity  $v_p$  that depends on the local reaction of a specific medium that can vary with frequency (dispersion) and polarization direction (anisotropy) of the interacting electromagnetic wave (and even with intensity; see sec. 2.1.4). This interaction reduces the phase velocity  $v_p$  in a medium compared to the phase velocity of light in vacuum

$$c_0 = \frac{1}{\sqrt{\mu_0\epsilon_0}} = \frac{\omega}{k_0} = \lambda_0 f \quad (2.33)$$

where  $k_0$  is the vacuum wavenumber and  $\lambda_0$  is the vacuum wavelength that is commonly used for the characterization of laser spectra independently of the medium.

As a consequence of the dispersion relation, the properties of the medium dictate the phase velocity  $v_p$  and thus the wave vector  $\mathbf{k}$  (or wavenumber  $k$ ) of each mode. The total electromagnetic field results from the superposition of the individual modes. Spatial variations within the propagation medium (inhomogeneities) lead to changes in magnitude and direction of the wave vectors thereby affecting the propagation path and spatial distribution of the wave. This influence of dielectric media on wave propagation is described in the following.

## Polarization in Dielectric Material

In the absence of free charges ( $\rho_f = 0$ ), an electromagnetic wave propagating through a dielectric medium displaces the bound charges within the atoms or molecules of the material, inducing microscopic dipole moments. These oscillating dipoles themselves represent radiation sources that transmit the wave through the medium. However, because the response of the dipoles is slightly inert compared to wave propagation in vacuum, the contribution of the oscillating dipoles to the electric field leads to a continuous phase retardation across the medium, resulting in a total electromagnetic wave that propagates slower than in vacuum ( $v_p < c_0$ ). Consequently, for a given oscillation frequency  $f$ , the corresponding wavelength is shorter within the medium ( $\lambda < \lambda_0$ ).

On a macroscopic scale, the displacement of bound charges  $\rho_b$  is described by the electric polarization  $\mathbf{P}$  of the medium

$$\nabla \cdot \mathbf{P} = -\rho_b \quad (2.34)$$

analogously to the electric displacement  $\mathbf{D}$  of free charges, according to Gauss law eq. (2.1) [40]. The different sign arises because the polarization is defined as the cause for the displacement of the bound charges, i.e. in contrast to the electric field  $\mathbf{E}$  and displacement  $\mathbf{D}$ , it points from negative to positive bound charges. Polarization represents the response of the dielectric material to the electric field and modifies the wave propagation compared to the vacuum, according to the constitutive relation eq. (2.5).

## Linear Susceptibility, Permittivity, and Refractive Index

For small displacements of the bound charges, the restoring forces can be approximated to be linearly dependent on the displacements corresponding to the description of the dipoles as harmonic oscillators. This results in a linear relationship between the total macroscopic electric field and the polarization. Considering the Fourier transforms  $\tilde{\mathbf{E}}(\mathbf{r}, \omega)$  and  $\tilde{\mathbf{P}}_L(\mathbf{r}, \omega)$  of the electric field  $\mathbf{E}(\mathbf{r}, t)$  and the linear polarization  $\mathbf{P}_L(\mathbf{r}, t)$  in the time domain, the connection between the electric field and the linear polarization in the frequency domain is given by

$$\tilde{\mathbf{P}}_L(\mathbf{r}, \omega) = \epsilon_0 \chi^{(1)}(\mathbf{r}, \omega) \tilde{\mathbf{E}}(\mathbf{r}, \omega) \quad (2.35)$$

where  $\chi^{(1)}$  is the linear electric susceptibility that characterizes a dielectric medium in its ability to polarize [40].

In general, the linear susceptibility is a  $(3 \times 3)$ -matrix to account for anisotropic media where the induced polarization might not be parallel to the electric field. The elements of this matrix are generally complex to describe a possible phase shift between polarization and the electric field in the medium that results in attenuation or amplification in the medium. These effects of the imaginary part of  $\chi^{(1)}$  are described in sec. 2.1.3. For the case of a lossless (and gainless) medium, the susceptibility is real, leading to a polarization that is in phase with the electric field in the medium. The connection of the linear susceptibility to the relative permittivity tensor is

$$\epsilon_r = \mathbf{I} + \chi^{(1)} \quad (2.36)$$

where  $\mathbf{I}$  is the identity matrix [40].

The description simplifies for the case of isotropic materials, where the susceptibility is independent of the direction of the electric field and can be described as a scalar  $\chi^{(1)}(\mathbf{r}, \omega)$ , resulting in a polarization  $\mathbf{P}$  that is always parallel to the electric field. This allows for the definition of a local refractive index (which is real in the lossless case discussed here) in a linear, non-magnetic, and isotropic medium:

$$n(\mathbf{r}, \omega) = \sqrt{\epsilon_r(\mathbf{r}, \omega)} = \sqrt{1 + \chi^{(1)}(\mathbf{r}, \omega)}, \quad (2.37)$$

which describes the frequency-dependent decrease of the phase velocity in the medium

$$v_p = \frac{c_0}{n}. \quad (2.38)$$

Within a homogeneous medium, susceptibility  $\chi^{(1)}(\omega)$ , relative permittivity  $\epsilon_r(\omega)$ , and refractive index  $n(\omega)$  become independent of location  $\mathbf{r}$ . Consequently, the dispersion relation which connects  $\omega$  and  $k$  via  $n(\omega)$  is also spatially uniform.

## Wave Propagation in Anisotropic Media

Anisotropic media, such as non-cubic crystals, are characterized by tensor forms of the electric susceptibility  $\chi^{(1)}$  and the relative permittivity  $\epsilon_r$  to account for their directional dependence.

This means that the dispersion relation depends on the direction of the wave vector  $\mathbf{k}$ . To analyze wave propagation in a periodic crystal lattice of a homogeneous, anisotropic material, it is convenient to define principal axes  $X$ ,  $Y$ , and  $Z$  that form an orthogonal coordinate system along which the crystal exhibits constant refractive indices  $n_x$ ,  $n_y$ , and  $n_z$ . Within this coordinate system the relative permittivity tensor  $\epsilon_r$  takes on a diagonal form with the elements  $n_x^2$ ,  $n_y^2$ ,  $n_z^2$ .

Because the medium polarizes differently in these directions, the wave propagates with different direction-dependent phase velocities and thus wavelengths depending on its orientation within this coordinate system. The wave undergoes different phase shifts in different directions resulting in a change of its polarization state. This phenomenon is known as birefringence.

In the simplest case, if a plane wave propagates along one of the principal axes, its electric field can be decomposed into two orthogonal linearly polarized components aligned with the other principal axes. Because these axes feature different refractive indices,  $n_f < n_s$ , they are designated as the fast and slow axis, respectively. If the wave is already linearly polarized along one of the principal axes, its polarization state is maintained during propagation. Otherwise, it changes because of the resulting phase difference

$$\Delta\phi = \frac{2\pi L}{\lambda_0}(n_s - n_f) \quad (2.39)$$

between the two components over the propagation distance  $L$  due to the different phase velocities along the slow and fast axis [40].

This birefringence is utilized in optical components, such as half-wave plates, to manipulate the polarization direction of an optical wave. A half-wave plate is designed to introduce a phase difference of  $\pi$ . This means that a linearly polarized incident wave remains linearly polarized, but with a rotated polarization direction depending on its relative orientation to the principal axes.

If the propagation direction does not coincide with one of the principal axes of the anisotropic medium, the situation becomes more complex. In this case, the directions of the electric field  $\mathbf{E}$  and the polarization  $\mathbf{P}$  are no longer in the same transverse plane perpendicular to the wave vector  $\mathbf{k}$ . As a consequence, according to the constitutive relation eq. (2.5), only the electric displacement is still orthogonal to  $\mathbf{k}$ , but  $\mathbf{E}$  is not. Moreover, as  $\mathbf{E}$  is not or-

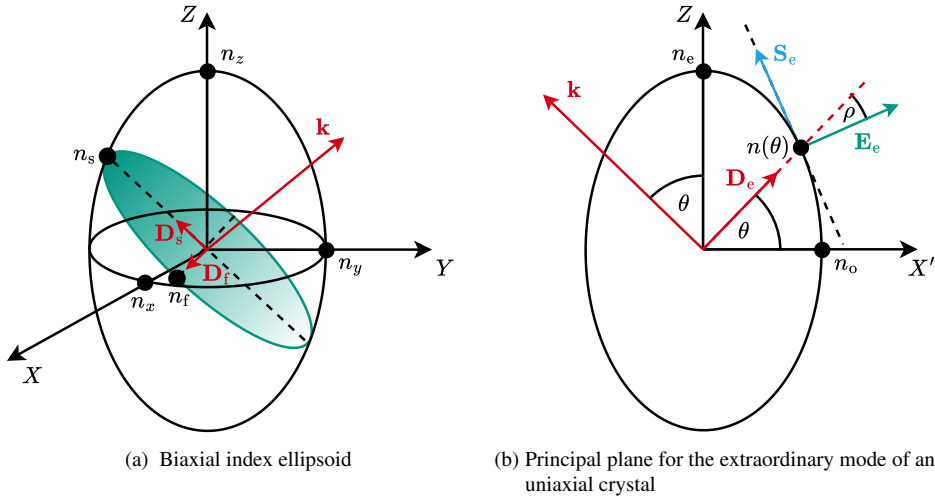


Figure 2.2: Geometric construction of the field quantities in anisotropic media. The electric displacement  $\mathbf{D}$  can be separated into normal modes that lie on an index ellipse orthogonal to the wave vector  $\mathbf{k}$ . Rotational symmetry in uniaxial crystals enables simplification of the three dimensional index ellipsoid (a) to a principal plane (b).

thogonal to  $\mathbf{k}$ , the complex Poynting vector according to eq. (2.27) is no longer parallel to  $\mathbf{k}$ .

If the direction of the wave vector  $\mathbf{k}$  is known, the normal polarization modes of the electric displacement in a biaxial material system ( $n_x \neq n_y \neq n_z$ ) can be determined using the index ellipsoid

$$\frac{X^2}{n_x^2} + \frac{Y^2}{n_y^2} + \frac{Z^2}{n_z^2} = 1 \quad (2.40)$$

defined in the coordinate system of the principal axes (see fig. 2.2a) [40]. As the electric displacement  $\mathbf{D}$  is orthogonal to  $\mathbf{k}$ , its normal polarization modes  $\mathbf{D}_s$  and  $\mathbf{D}_f$  lie along the semi-axes of an ellipse orthogonal to  $\mathbf{k}$  within the ellipsoid. The lengths of the semi-axes of this ellipse determine the refractive indices  $n_s$  and  $n_f$  of the slow and fast axis, respectively. These refractive indices characterize the birefringence for these two normal modes of the  $\mathbf{D}$ -field to determine their phase difference according to eq. (2.39) along the propagation through the anisotropic medium.

At any point, the electric field can be determined from the electric displacement using the relation  $\mathbf{E} = \epsilon_0^{-1} \epsilon_r^{-1} \mathbf{D}$ , i.e. [40]

$$\begin{pmatrix} E_x \\ E_y \\ E_z \end{pmatrix} = \frac{1}{\epsilon_0} \begin{pmatrix} \frac{1}{n_x^2} & 0 & 0 \\ 0 & \frac{1}{n_y^2} & 0 \\ 0 & 0 & \frac{1}{n_z^2} \end{pmatrix} \begin{pmatrix} D_x \\ D_y \\ D_z \end{pmatrix}. \quad (2.41)$$

In a uniaxial crystal such as ZnGeP<sub>2</sub> (ZGP), rotational symmetry allows for the definition of an ordinary axis with refractive index  $n_o = n_x = n_y$  and an extraordinary axis  $n_e = n_z$ , designated as the optical axis. One of the normal modes always sees the refractive index  $n_o$  independent of the propagation direction and is hence termed the ordinary mode  $\mathbf{D}_o$ . The electric field  $\mathbf{E}_o$  of the ordinary mode is always parallel to the electric displacement  $\mathbf{D}_o$ , and thus the Poynting vector  $\mathbf{S}_o$  is parallel to the wave vector  $\mathbf{k}$ . For the other mode, commonly termed the extraordinary mode  $\mathbf{D}_e$ , the refractive index changes with the propagation direction, the electric field  $\mathbf{E}_e$  is not parallel to  $\mathbf{D}_e$ , and the Poynting vector  $\mathbf{S}_e$  is not parallel to  $\mathbf{k}$ .

However, rotational symmetry allows for the choice of a coordinate system so that all field quantities of the extraordinary mode lie within a principal plane  $Z - X'$  by rotating the principal axes around  $Z$  [40]. Therefore, the ellipsoid simplifies to a two-dimensional ellipse depicted in fig. 2.2b. The refractive index  $n(\theta)$  of the extraordinary mode  $\mathbf{D}_e$  is described by the ellipse equation

$$\frac{1}{n^2(\theta)} = \frac{\cos^2(\theta)}{n_o^2} + \frac{\sin^2(\theta)}{n_e^2} \quad (2.42)$$

where  $\theta$  is the angle of the wave vector with respect to the optical axis  $Z$  [40]. For a wave that propagates along the optical axis ( $\theta = 0$ ) the crystal behaves isotropic. Birefringence increases with the angle to the optical axis and becomes maximum for orthogonal propagation to it  $n(\theta = \pi/2) = n_e$ . As illustrated in figure 2.2b, the electric field  $\mathbf{E}_e$  is perpendicular to the surface of the index ellipsoid at the point indicated by  $\mathbf{D}_e$  corresponding to  $n(\theta)$ .

The walk-off angle  $\rho$  between the extraordinary Poynting vector  $\mathbf{S}_e$  and the wave vector agrees with the angle between the extraordinary electric field  $\mathbf{E}_e$  and displacement  $\mathbf{D}_e$  and is given by

$$\rho = \mp \theta \pm \arctan \left( \frac{n_o^2}{n_e^2} \tan(\theta) \right) \quad (2.43)$$

where the upper signs apply for negative uniaxial crystals ( $n_e < n_o$ ) and the lower signs apply for positive uniaxial crystals ( $n_e > n_o$ ) [45].

## Reflection and Refraction at Optical Interfaces

Within homogeneous media, the directions of the wave vector, and thus also the directions of linearly polarized field components, remain constant during propagation. However, at optical inhomogeneities described by a spatial variation in the refractive index, the electromagnetic wave can change its propagation direction. According to Fermat's principle, light travels along propagation paths with stationary propagation time with respect to variations in the path. Along these paths, the light that can be considered in any point on the wave front as an elementary spherical wave according to Huygens' principle, superimposes constructively. For a TEM wave, such as a plane wave or a collimated laser beam, the coherent light exhibits a primary propagation direction given by the wave vector  $\mathbf{k}$  along which it interferes constructively. Any other path is canceled out by destructive interference. If the wave passes from an isotropic medium with refractive index  $n_1$  at an angle of incidence of  $\theta_i$  through an interface into another isotropic medium with refractive index  $n_2 > n_1$ , its path is split into a reflected and a transmitted wave at the interface. Because the reflected wave propagates within the same medium as the incident wave, its phase fronts travel with the same speed  $v_{p,1} = c_0/n_1$  and interfere constructively in direction of a reflection angle  $\theta_r$  that agrees with the incident angle  $\theta_i$  relative to the surface normal

$$\theta_r = \theta_i . \quad (2.44)$$

For the transmitted wave, the phase fronts travel at different speeds  $v_{p,2} = c_0/n_2 < v_{p,1}$  leading to a shorter wavelength. Therefore, the phase-shifted phase fronts along the interface interfere constructively in direction of an angle  $\theta_t < \theta_i$  to maintain phase continuity. The change in propagation direction of a wave by passing an optical inhomogeneity is known as refraction and is described by Snell's law:

$$n_1 \sin \theta_i = n_2 \sin \theta_t . \quad (2.45)$$

For the electric and magnetic field the following interface conditions result from the Maxwell equations:

$$\mathbf{n}_{12} \times (\mathbf{E}_2 - \mathbf{E}_1) = 0 \quad (2.46)$$

$$\mathbf{n}_{12} \times (\mathbf{H}_2 - \mathbf{H}_1) = 0 \quad (2.47)$$

where  $\mathbf{n}_{12}$  is the unit vector normal to the interface [40]. Therefore, the field components tangential to the interface have to match continuously across the boundary. Applying these conditions to the incident, reflected, and transmitted wave yields the Fresnel coefficients for reflection and transmission

$$r_s = \frac{E_{r,s}}{E_{i,s}} = \frac{n_1 \cos \theta_i - n_2 \cos \theta_t}{n_1 \cos \theta_i + n_2 \cos \theta_t} \quad (2.48)$$

$$t_s = \frac{E_{t,s}}{E_{i,s}} = \frac{2n_1 \cos \theta_i}{n_1 \cos \theta_i + n_2 \cos \theta_t} \quad (2.49)$$

$$r_p = \frac{E_{r,p}}{E_{i,p}} = \frac{n_2 \cos \theta_i - n_1 \cos \theta_t}{n_2 \cos \theta_i + n_1 \cos \theta_t} \quad (2.50)$$

$$t_p = \frac{E_{t,p}}{E_{i,p}} = \frac{2n_1 \cos \theta_i}{n_2 \cos \theta_i + n_1 \cos \theta_t} \quad (2.51)$$

where the indices denote s- and p-polarization describing the perpendicular and parallel polarization modes with respect to the plane of refraction, respectively [40].

Figure 2.3 shows the directions of  $\mathbf{E}$ ,  $\mathbf{H}$ , and  $\mathbf{k}$  of a TEM wave for refraction and reflection at an optical interface between two isotropic and homogeneous media for s- and p-polarization. The Fresnel coefficients relate the complex field amplitudes between two linear, isotropic, homogeneous, non-magnetic and lossless media to each other and are therefore complex numbers themselves, meaning they describe a change in magnitude and phase. For external reflection ( $n_1 < n_2$ ) s-polarized light always undergoes a phase shift of  $\pi$ . Its reflected magnitude is minimal for normal incidence ( $\theta_i = 0$ ) and increases with the angle of incidence. For p-polarization the reflection vanishes for incidence at the Brewster angle [40]:

$$\theta_B = \arctan \left( \frac{n_2}{n_1} \right). \quad (2.52)$$

For angles of incidence smaller than the Brewster angle p-polarized light undergoes a phase shift of  $\pi$ , and for larger angles it does not undergo a phase shift.

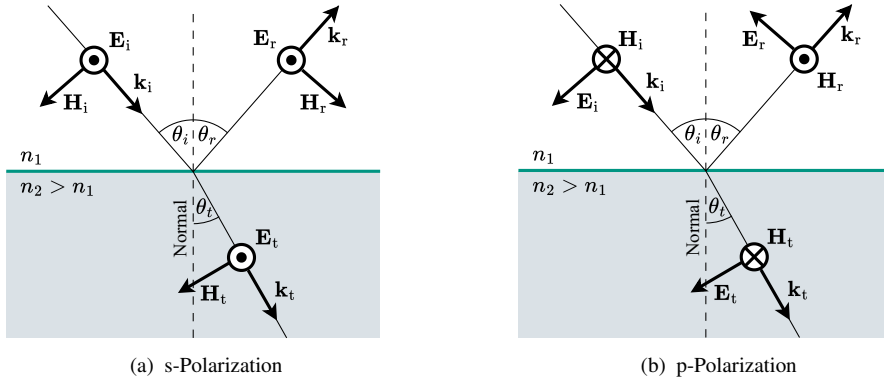


Figure 2.3: Refraction and reflection of a wave on an interface between media with different refractive index.

For internal reflection ( $n_1 > n_2$ ), Snell's law eq. (2.45) implies  $\theta_i < \theta_t$  up to a critical angle

$$\theta_c = \arcsin\left(\frac{n_2}{n_1}\right). \quad (2.53)$$

For angles of incidence smaller than  $\theta_c$ , s-polarized light is reflected without phase shift and with a magnitude increasing with  $\theta_i$ . The reflection of p-polarized light below the critical angle is not phase shifted for angles of incidence smaller than the Brewster angle, where the reflected magnitude vanishes, and is associated with a phase shift of  $\pi$  for angles of incidence  $\theta_B < \theta_i < \theta_c$ .

For angles of incidence greater than  $\theta_c$ , both s- and p-polarized light enter the state of total internal reflection [40]. In this case, the normal component of the incident wave vector  $k_{i,n} = n_1 k_0 \cos(\theta_i)$  cannot match with a real normal component  $k_{i,t} = n_2 k_0 \cos(\theta_t)$  of the transmitted wave vector. Therefore,  $\cos \theta_t$  becomes imaginary, resulting in magnitudes of the reflection coefficients of  $|r_s| = |r_p| = 1$  and an evanescent transmitted wave, decaying exponentially into medium 2. The phase shift of the reflected wave increases continuously with the angle of incidence for s-polarization and decreases continuously with the angle of incidence for p-polarization. The effect of total internal reflection provides the basis for the design of waveguides such as optical fibers.

The fraction of power or intensity that is reflected or transmitted at the interface between two lossless media are given by the reflectance  $R$  and the transmittance  $T$ :

$$R = \frac{I_r}{I_i} = |r|^2 \quad (2.54)$$

$$T = \frac{I_t}{I_i} = 1 - R = \frac{n_2 \cos \theta_t}{n_1 \cos \theta_i} |t|^2 \quad (2.55)$$

where the prefactor in the transmittance accounts for the change in impedance ( $\mathbf{E}/\mathbf{H}$ ) and beam area projection when entering a different medium.

The effects of reflection and refraction are used for the design of various passive optical components such as mirrors, beam splitters, polarization filters, and lenses to manipulate laser beams in direction, intensity, polarization, diameter, and divergence. As they consist of polished flat or continuously curved surfaces, these elements generally modify the beam parameters without changing the mode content or the  $M^2$  parameter of a laser beam.

## Photonic Crystals and Periodic Structures

According to the dispersion relation eq. (2.32) and eq. (2.38), the refractive index depends on the frequency at which the medium is excited by the electromagnetic wave, leading to a frequency-dependent phase velocity. Material dispersion, as discussed earlier, denotes the spectrally dependent response of a medium described by its frequency-dependent susceptibility  $\chi(\omega)$ , permittivity  $\epsilon_r(\omega)$  and refractive index  $n(\omega)$ . Due to dispersion, non-perpendicular incidence on a boundary surface into a dispersive medium results in spectral fragmentation of light, as different wavelengths are refracted at different angles. Dispersion must be taken into account, in particular, for transmitting optical components, e.g. lenses whose dispersive focal length can cause chromatic aberrations. Strongly dispersive elements, such as optical gratings or coatings, are based on the superposition of the effects of multiple periodically alternating refractive index sequences or layers. Such periodically structured optical elements are called photonic crystals.

A one-dimensional photonic crystal is characterized by a periodically alternating refractive index profile  $n(z)$  along one spatial axis  $z$  with a period  $\Lambda$ . An electromagnetic wave propagating in  $z$ -direction through a lossless, linear medium with a periodically modulated refractive index experiences a constant phase shift of

$$\Phi = K\Lambda \quad (2.56)$$

per period  $\Lambda$  due to the periodicity, where  $K$  is the Bloch wavenumber. The modes propagating with this effective wavenumber in the periodic medium are called Bloch waves. If the period of index modulation  $\Lambda$  is on the order of the magnitude of the effective wavelength  $\lambda = 2\pi/K$ , the medium behaves strongly dispersive. The dispersion relation of a one-dimensional photonic crystal is related to the amplitude transmission coefficient  $t_\Lambda(\omega)$  of a unit cell of the periodic structure by [40]

$$\cos(K\Lambda) = \text{Re} \left\{ \frac{1}{t_\Lambda(\omega)} \right\}. \quad (2.57)$$

If  $|\text{Re}\{1/t_\Lambda\}| \leq 1$ , a wave with an angular frequency  $\omega$  can pass any number of unit cells without decaying. In this case a Bloch wave with a real wavenumber  $K$  exists within the total periodic structure. If  $|\text{Re}\{1/t_\Lambda\}| > 1$ , the wavenumber  $K$  becomes imaginary corresponding to an evanescent wave. The frequencies for which no real Bloch wavenumbers  $K$  exist form a photonic band gap. Within these spectral ranges the reflections from each periodic unit cell interfere constructively, resulting in total reflection. The band gaps represent discontinuities in the nonlinear dispersion relation  $K(\omega)$  of a photonic crystal between frequencies at the band edges that lead to the same Bloch wavenumber for which the condition  $\cos(K\Lambda) = \pm 1$  is met [40]. Thus, in terms of vacuum wavelengths, the band gaps emerge around the Bragg wavelengths  $\lambda_B$  which are integer multiples of the grating period  $\Lambda$ , given by the Bragg condition

$$m\lambda_B = 2n_{\text{avg}}\Lambda \cos \theta_i, \quad m = 1, 2, 3, \dots \quad (2.58)$$

where  $n_{\text{avg}}$  is the average refractive index along the periodic structure [40].

The bandwidth of the photonic band gap is determined by the number of unit cell repetitions and their reflectances. Figure 2.4 shows two reflection characteristics of periodically structured, highly dispersive optical components with a broad and a narrow reflection bandwidth, typical for dielectric mirrors and Bragg gratings, respectively. Dielectric mirrors are usually characterized by a broad reflection bandwidth, as shown in fig. 2.4a. They are manufactured by depositing a series of thin film layers that form an optical coating alternating between higher and lower refractive indices  $n_L$  and  $n_H$  on a substrate. Typically, the thicknesses of the layers correspond to  $d_L = \lambda_B/(4n_L)$  and  $d_H = \lambda_B/(4n_H)$  for the low- and high-index layers, respectively [40]. To obtain a broad reflection bandwidth, the difference in refractive index  $\Delta n = n_H - n_L$  between the layers is chosen large, leading to strong reflections of the unit cells. The total reflection

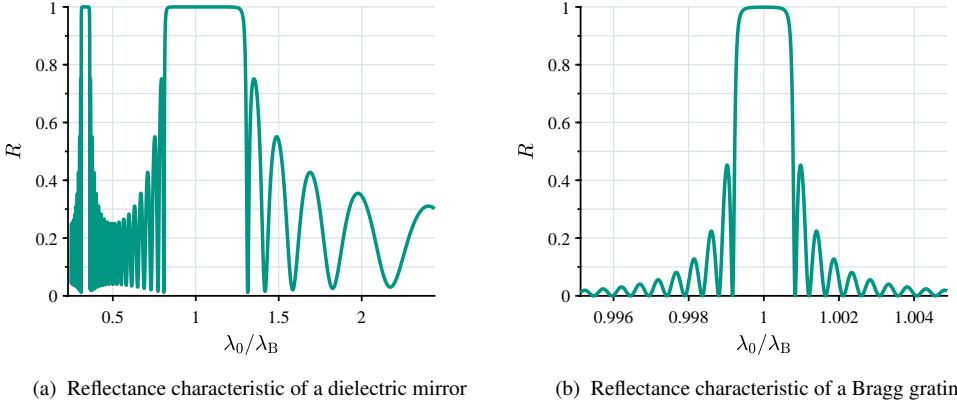


Figure 2.4: Reflectance characteristics of one-dimensional photonic crystals with a periodically varying refractive index. In (a), ten periods of discrete alternating layers with a large refractive index difference of  $\Delta n = 1.5$  result in a broad photonic band gap where light gets totally reflected. In contrast, a larger number of two thousand periods of harmonic refractive index modulation with low depth  $\Delta n = 2 \cdot 10^{-3}$  leads to a narrower band gap depicted in (b).

characteristic can be determined using the transfer matrix method considering a stack of identical discrete segments by calculating their matrix product [40]. For the reflectance spectrum plotted in fig. 2.4a, a high reflective (HR) coating consisting of ten periods with discrete layers having refractive indices of  $n_L = 1.5$  and  $n_H = 3$  is assumed resulting in a broad band gap around the first order ( $m = 1$ ) Bragg wavelength. For anti-reflective (AR) coatings, the layers are designed to provide destructive extinction of the reflected wave.

In contrast to broadband HR mirrors, a Bragg grating usually offers a narrow reflectance bandwidth, for example, to provide high resolutions in spectrometers or a precise spectral selection as a dispersive resonator mirror. To realize a Bragg grating, a periodic refractive index pattern is inscribed in a photosensitive material, for example, via ultraviolet (UV) lithography or femtosecond lasers [46, 47]. This leads to a nearly sinusoidal index modulation of the grating substrate with a low modulation depth  $\Delta n$ :

$$n(z) \approx n_{\text{avg}} + \frac{1}{2} \Delta n \sin(Gz) \quad (2.59)$$

where  $G = 2\pi/\Lambda$  is the lattice wavenumber. The harmonic modulation prevents reflections at higher orders of the Bragg wavelengths and the low reflection per period enables a narrow bandwidth. To achieve a high peak reflectance despite the weak unit cell reflections, Bragg

gratings extend over many grating periods with lengths of several millimeters to centimeters.

The total reflectance of a sinusoidal index-modulation can be calculated using the approach of coupled mode theory [48, 49]. In this, the forward and backward propagating modes are coupled by scattering on the continuous index grating. The coupling coefficient

$$\kappa = \frac{\pi}{\lambda_B} \Delta n \quad (2.60)$$

is therefore related to the modulation depth  $\Delta n$  of the refractive index and to the Bragg wavelength  $\lambda_B$  that is connected to the grating period  $\Lambda$  via the Bragg condition eq. (2.58) [48]. To enable an efficient coupling between the forward and backward propagating waves, the continuous scattering interactions with the index grating have to add up constructively along the entire length of the grating, which poses the requirement of *phase matching*:

$$\frac{\Delta K}{2} = \frac{2\pi n_{\text{avg}}}{\lambda} - \frac{\pi}{\Lambda} \quad (2.61)$$

where  $\Delta K$  denotes the detuning between the wavenumbers of nominal forward and backward traveling waves defined by the average refractive index  $n_{\text{avg}}$  of the grating, and the lattice wavenumber  $G = 2\pi/\Lambda$  [48]. Thus, ideal phase matching ( $\Delta K = 0$ ) occurs at the Bragg wavelength  $\lambda_B$ . The exponential decay rate of a forward traveling wave that arises from the interaction with the grating to couple into the backward traveling wave is given by:

$$\gamma = \sqrt{\kappa^2 - \left(\frac{\Delta K}{2}\right)^2} \quad (2.62)$$

leading to a total reflectance over the grating length  $L$  of [48]

$$R = \frac{\kappa^2 \sinh^2(\gamma L)}{\kappa^2 \cosh^2(\gamma L) - \left(\frac{\Delta K}{2}\right)^2}. \quad (2.63)$$

Fig. 2.4b shows the reflectance characteristic of a sinusoidal index modulation with a modulation depth of  $\Delta n = 2 \cdot 10^{-3}$  over a length of two thousand periods. Stronger side lobe suppression can be obtained by apodized gratings that have a varying modulation depth over their length, for example, by a Gaussian-apodized or raised-cosine-apodized envelope [48]. Bragg gratings

exist in several realizations, e.g. as volume Bragg gratings (VBGs) made of bulk glass or fiber Bragg gratings (FBGs) inscribed in fibers.

## Material Dispersion and Group Velocity Dispersion

Photonic crystals exhibit a strongly nonlinear dispersion relation given by eq. (2.57) caused by resonant scattering in their periodic index structure. In general, the dispersion relation  $k(\omega)$  of (homogeneous) dielectric materials related to their spectral dependent susceptibility  $\chi^{(1)}(\omega)$  or refractive index  $n(\omega)$  is also not linear. In contrast, this nonlinear spectral dependency does not arise from macroscopic index structures but from the resonant excitation of the microscopic dipole moments that cause the polarization  $\mathbf{P}$  in the material. For dielectric optical materials like glasses, these resonances are typically located at UV frequencies corresponding to the excitation of bound electronic oscillation states, and mid- to far-IR corresponding to vibrational and rotational molecular oscillations.

Similar to the band gaps in photonic crystals, these resonances disturb or prevent propagation in these spectral regions. In this case, resonant excitation of the material is associated with absorption described by the imaginary part of the susceptibility which is discussed in the next section. However, even in transparent spectral regions apart from the resonance frequencies, the dispersion relation is influenced by these resonances leading to a nonlinear relationship between  $k$  and  $\omega$ .

The connection between the real and imaginary part of the linear electric susceptibility is given by the Kramers-Kronig relation:

$$\operatorname{Re}\{\chi^{(1)}(\omega)\} = -\frac{2}{\pi} \mathcal{P} \int_0^\infty \frac{\omega' \operatorname{Im}\{\chi^{(1)}(\omega')\}}{\omega'^2 - \omega^2} d\omega' \quad (2.64)$$

$$\operatorname{Im}\{\chi^{(1)}(\omega)\} = \frac{2\omega}{\pi} \mathcal{P} \int_0^\infty \frac{\operatorname{Re}\{\chi^{(1)}(\omega')\}}{\omega'^2 - \omega^2} d\omega' \quad (2.65)$$

where  $\mathcal{P}$  denotes the Cauchy principal value around the pole  $\omega'$  [45].

Within the transparency range of a dielectric material, i.e. far away from its resonance frequencies, the resonance lines can be approximated by a series of delta functions:

$$\operatorname{Im}\{\chi^{(1)}(\omega)\} \approx \sum_i \delta(\omega - \omega_i) \quad (2.66)$$

where  $\omega_i$  denotes the resonant frequencies. Using eq. (2.64) to obtain the corresponding real part and consider the associated refractive index by eq. (2.37) this yields the Sellmeier equation

$$n^2(\lambda_0) = 1 + \sum_i \frac{B_i \lambda_0^2}{\lambda_0^2 - \lambda_i^2} \quad (2.67)$$

where  $\lambda_i$  are the corresponding vacuum wavelengths of the resonant frequencies  $\omega_i$  and  $B_i$  are the Sellmeier coefficients of the specific resonance. For fused silica the Sellmeier coefficients are  $B_1 = 0.6961663$ ,  $B_2 = 0.4079426$ , and  $B_3 = 0.8974794$  at the corresponding vacuum wavelengths  $\lambda_1 = 0.0684043 \mu\text{m}$ ,  $\lambda_2 = 0.1162414 \mu\text{m}$ , and  $\lambda_3 = 9.896161 \mu\text{m}$  [50].

The nonlinear dispersion relation can be expanded by a Taylor series around a central frequency  $\omega_0$

$$k(\omega) = \sum_{m=0}^{\infty} \frac{(\omega - \omega_0)^m}{m!} \left. \frac{d^m k}{d\omega^m} \right|_{\omega=\omega_0} \quad (2.68)$$

Because the magnitude of the terms in the Taylor series decreases with increasing order  $m$ , it depends on the application to which order the expansion must be considered [51]. While the first term  $k(\omega_0)$  accounts for the phase of a monochromatic wave, the first derivative  $k' = (dk/d\omega)|_{\omega_0}$  in the second term causes a group delay  $T_g = Lk'$  over a propagation distance  $L$  of a waveform spanning over a wider spectrum, such as a laser pulse. It is related to the refractive index by

$$k' = \frac{1}{c_0} \left( n + \omega \frac{dn}{d\omega} \right) = \frac{1}{v_g} \quad (2.69)$$

where  $v_g$  is the group velocity that describes the velocity of the envelope of the wave packet [51].

In linear propagation, the terms  $k(\omega_0)$  and  $k'$  do not affect the shape of a pulse [52]. Pulse broadening or compression is mainly caused by the second derivative  $k''$  that describes the group velocity dispersion (GVD). The relation of the GVD to the refractive index is given by [51]

$$k'' = \frac{1}{c_0} \left( 2 \frac{dn}{d\omega} + \omega \frac{d^2 n}{d\omega^2} \right) = \frac{\lambda_0^3}{2\pi c_0^2} \frac{d^2 n}{d\lambda_0^2}. \quad (2.70)$$

Figure 2.5 shows the refractive index and GVD of fused silica calculated by the Sellmeier equation (2.67) and eq. (2.70) over the vacuum wavelength. The GVD is related to the curvature of the wavelength dependency of the refractive index described by the second derivative

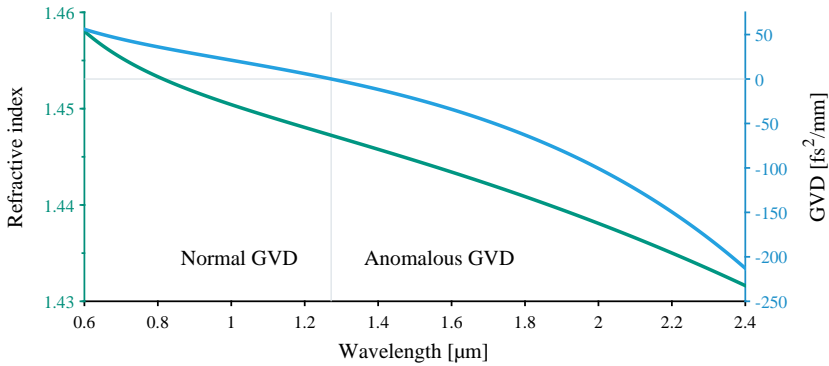


Figure 2.5: Refractive index of fused silica calculated by the Sellmeier equation and the corresponding group velocity dispersion (GVD) versus the wavelength. The gray lines indicate the zero dispersion wavelength (ZDW) that separates the spectral regimes of normal and anomalous GVD. The Sellmeier coefficients are taken from [50].

$d^2n/d\lambda_0^2$ . At the inflection point it vanishes. The corresponding wavelength is termed the zero dispersion wavelength (ZDW), indicated by the gray lines in fig. 2.5. For fused silica, the ZDW is around  $1.27 \mu\text{m}$ . At wavelengths shorter than the ZDW, the GVD has a positive sign denoted as normal GVD meaning that shorter wavelengths travel slower than longer wavelengths through the medium. Longer wavelengths than the ZDW are subject to anomalous GVD (negative sign of  $k''$ ) which causes shorter wavelengths to propagate faster than longer wavelengths.

The consideration of higher-order dispersive terms, i.e.  $k'''$ ,  $k''''$  becomes necessary for dispersion compensation in the generation of ultrashort pulses, propagation over long distances, and in the vicinity of the ZDW [51, 52].

### 2.1.3 Absorption and Emission

The linear response of a dielectric material to an electric field is characterized by its linear electric susceptibility  $\chi^{(1)}$  leading to a macroscopic polarization  $\mathbf{P}$  in the material that represents the sum of induced microscopic dipole moments. These dipole moments can be described as Lorentz oscillators with resonant frequencies determined by their charge that is displaced within the electric potential [40]. The sharpness of the resonance lines is influenced by damping forces

as a result of fast interactions with the surrounding crystal lattice or with other dipoles, leading to broadened line shapes of the dipole ensemble.

Due to causality, the total macroscopic response of the dipole ensemble,  $\mathbf{P}$ , is generally phase-shifted relative to the driving electric field. This non-instantaneous response is described by a complex electric susceptibility in the frequency domain whose real and imaginary parts are connected by the Kramers-Kronig relation (see eqs. (2.64) and (2.65)). Within the spectral transparency range, the material response described by the magnitude of the electric susceptibility is weak and quasi-instantaneous leading to a retardation of the wave without a net transfer of energy to the medium. Approaching the resonance frequency, the material response increases and causes an increasing phase shift of the induced polarization to the electromagnetic wave. Right at the resonance, the phase shift is  $90^\circ$  which corresponds to a predominantly imaginary electric susceptibility. The electric field resonantly drives the alteration of the polarization ( $d\mathbf{P}/dt$ ), resulting in a transfer of energy to the medium, i.e. absorption. Because the associated excited dipole moments emit radiation that interferes destructively with the driving electromagnetic wave, the wave is attenuated along its propagation direction. Conversely, if a medium contains an ensemble of dipoles already oscillating in an excited state, an incident electromagnetic wave of appropriate frequency can stimulate them to radiate in phase with the electromagnetic wave, resulting in constructive interference and thus amplification of the wave.

In a homogeneous, isotropic, and non-magnetic medium, a complex scalar susceptibility  $\chi^{(1)} = \chi_r^{(1)} + j\chi_i^{(1)}$  is associated with a complex relative permittivity  $\epsilon_r = \epsilon_{r,r} - j\epsilon_{r,i}$  and a complex refractive index  $\underline{n} = n - jn_i$  analogous to eq. (2.37). This leads to attenuation or amplification of a propagating plane wave along the  $z$ -direction through the medium:

$$\mathbf{E}(z) = \mathbf{E}_0 e^{-jkz} = \mathbf{E}_0 e^{-j(n-jn_i)k_0 z} = \mathbf{E}_0 e^{-n_i k_0 z} e^{-jn k_0 z} . \quad (2.71)$$

With the definition of the absorption coefficient

$$\alpha = 2n_i k_0 , \quad (2.72)$$

this leads to an exponentially decaying or growing intensity

$$I(z) \propto |\mathbf{E}(z)|^2 \propto e^{-\alpha z} . \quad (2.73)$$

Therefore, attenuation is associated with positive signs of the absorption coefficient  $\alpha$  and the imaginary parts of the refractive index  $n_i$ , and the relative permittivity  $\epsilon_{r,i}$ , as well as a negative sign of the imaginary part of the electric susceptibility  $\chi_i^{(1)}$ . The reverse signs, on the other hand, correspond to amplification.

## Energy Levels of Dielectric Materials and Rare-Earth Dopants

Atoms, molecules and solid-state materials have permitted oscillation states defined by the rules of quantum mechanics. These states represent solutions to the Schrödinger equation and correspond to energy eigenvalues that form discrete energy levels or continuous bands dependent on the surrounding potential [40].

For single atoms, discrete energetic states arise from the allowed configurations of the electrons within the electrostatic potential with respect to the positive charged nucleus and the other electrons. The occupation of allowed states follows the Pauli principle, according to which the individual electrons must not match in all four quantum numbers  $n$ ,  $l$ ,  $m$ , and  $s$ . This causes the electrons to arrange in shells according to the principal quantum number  $n$ , and orbitals determined by the azimuthal quantum number  $l$ , which are denoted as  $s$ ,  $p$ ,  $d$ , and  $f$  orbitals depending on their allowed spatial orientations described by the magnetic quantum numbers  $m$ . A further distinction is made by the spin  $s$ , which can be up or down ( $\pm 1/2$ ). Because electrons typically fill orbitals in order of increasing energy, optical transitions usually involve the valence electrons in the lowest not fully occupied orbital, as they are weaker bound to the nucleus and their energetic distance to the next higher unoccupied states is small. Molecules consisting of several atoms exhibit not only electronic states, but also vibrational and rotational states that are associated with typically smaller energy spacings. [40]

Solid-state materials consist of a lattice of closely spaced atoms that exhibit a periodic long range order in the case of crystals and a short range order in the case of amorphous glasses. The close spacing between the atoms leads to coupling between their electronic states [40]. Therefore, the electrons become delocalized and form electronic Bloch waves within the periodic potential of the atom lattice. These electronic Bloch waves exhibit a dispersion relation  $E(\mathbf{k})$  relating their energy to their crystal momentum, similar to electromagnetic waves in a photonic crystal as described in the previous section 2.1.2. Analogously, the dispersion relation of the electronic Bloch waves yields a band structure of quasi-continuous energy bands separated by band gaps with energy spacing  $\Delta E$  in which no allowed Bloch wave states exist.

Without any excitation, the bands are either fully occupied or unoccupied by the electrons. The energetically highest occupied band is denoted as the valence band and the energetically lowest unoccupied band is the conduction band. Excitation of an electron from the valence into the conduction band can occur if the energy of an interacting electromagnetic wave is sufficient to bridge the band gap  $hf > \Delta E$ , where  $h$  is Planck's constant that relates the frequency of an electromagnetic wave to its quantized photon energy. Therefore, the band gap characterizes the transparency range towards high frequencies (short wavelengths). The lower frequency border of the transparency range is determined by phonon absorption corresponding to lattice vibration states.

Real materials exhibit some degree of optical losses even within their spectral transparency range because of lattice defects and impurities. These defects in the crystal structure create states within the band gap to which electrons from the valence band can be excited or from which they can be excited to the conduction band. Amorphous materials such as silica inherently have structural defects due to their missing long-range order. Deviation from periodicity in the lattice potential therefore causes the sharp band edges to smear out. In silica glass, OH impurities are the main contributor to absorption losses in the infrared range [51]. For optimized IR transmission, special precautions are taken in the manufacturing process to reduce these impurities [53]. In silica fibers, Rayleigh scattering arising from density fluctuations within the material represents another fundamental loss mechanism that scales with  $\lambda^{-4}$  [51].

Figure 2.6 compares the spectral attenuation of silica glasses with different degrees of purity. While the silica fiber, designed for operation in the range of 1850–2200 nm [54], contains Ge-doping to provide guiding, the main difference between the high-purity synthetic silica glasses Infrasil 301/302 and Suprasil 3001/3002 is their OH content [55]. This becomes evident from the absorption peaks at around 1.4  $\mu\text{m}$  and 2.25  $\mu\text{m}$  where overtones of the fundamental OH vibration peak at 2.73  $\mu\text{m}$  are located.

In order to achieve specific absorption and emission characteristics required for the realization of solid-state lasers, the host matrix of the solid material is intentionally doped with foreign ions. Typical dopants are trivalent rare-earth ions, or more precisely Lanthanides, such as  $\text{Yb}^{3+}$ ,  $\text{Er}^{3+}$ ,  $\text{Tm}^{3+}$ , and  $\text{Ho}^{3+}$ . Lanthanides have the special feature that their incompletely occupied  $4f$  shell has a smaller radius than the fully occupied  $5s$  and  $5p$  shells which shields the  $4f$  valence electrons from the influence of the crystal field [53, 56]. Their trivalent ionization involves the donation of two  $6s$  electrons and either a  $4f$  or  $5d$  electron, leaving a Xenon nucleus with  $N$

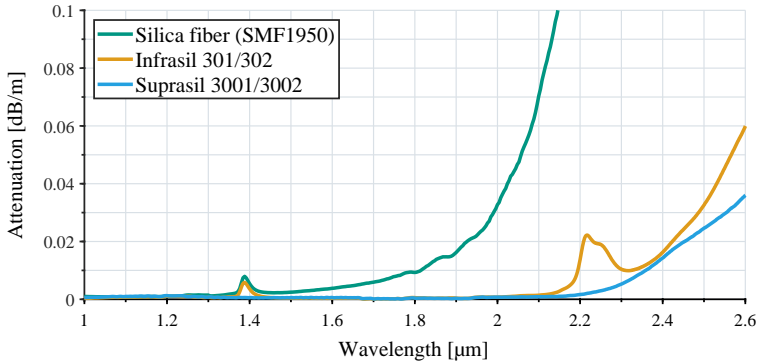


Figure 2.6: Attenuation in silica glasses with different degrees of purity versus the wavelength. The silica fiber is designed for single mode operation between 1850–2200 nm (SMF1950 from Thorlabs) and has a Ge-doped core. Infrasil 301/302 and Suprasil 3001/3002 are high-purity synthetic silica glasses manufactured by Heraeus Covantics. Data from [54, 55].

$4f$  electrons [53]. Within a crystal or glass host, the shielding by the  $5s^25p^6$  shells prevents strong coupling of the  $4f$  electrons with the host lattice. Thus, the electrons largely retain their sharp atomic energy levels [40, 53].

Figure 2.7 illustrates the splitting of the energy level of the  $N$   $4f$  electrons of a trivalent Lanthanide ion in a crystal. The main splitting is caused by the inner atomic forces of mutual electrostatic repulsion between the  $4f$  electrons and spin-orbit coupling. These interactions lift the degeneracy of the  $4f^N$  configuration, resulting in a series of energy terms denoted by the Russel-Saunders notation  $^{2S+1}L_J$  [53]. The weak perturbation by the crystal field refines these terms into multiple closely spaced Stark levels that form manifolds. The optical transitions of these rare-earth dopants are characterized by sharp spectral lines corresponding to intra- $4f^N$ -transitions. These parity-forbidden transitions are assisted by static or dynamic crystal field asymmetry, magnetic dipole radiation and electric quadrupole radiation [57]. The intensities of these forced dipole transitions between the Stark level manifolds can be calculated by Judd-Ofelt theory [58, 59].

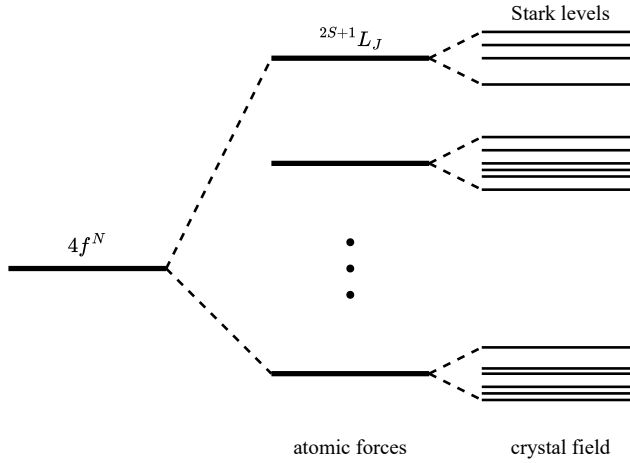


Figure 2.7: Energy level splitting of the  $4f^N$  states of Lanthanide ions in a crystal. Inner atomic forces split the  $4f^N$  orbital into  $^{2S+1}L_J$  terms. The significantly weaker influence of the crystal field results in additional splitting into a fine structure of Stark levels.

## Optical Transitions and Spectroscopic Cross-Sections

The energy levels of a material represent the allowed oscillation states of its microscopic dipoles. Considering a material system that has two discrete states  $|1\rangle$  and  $|2\rangle$  with corresponding energy levels  $E_1 < E_2$ , there is a local population density of dipoles  $N_1$  that occupies state  $|1\rangle$  and a local population density  $N_2$  for state  $|2\rangle$ . Optical transitions change the state occupation of the local dipole ensemble by transferring energy between the material and an interacting electromagnetic wave. These transitions can be described by three types of fundamental interactions with light: absorption, stimulated emission, and spontaneous emission.

The three interactions are illustrated in fig. 2.8. In absorption, dipoles are resonantly excited by an electromagnetic wave from an energetic lower oscillation state  $|1\rangle$  into a higher oscillation state  $|2\rangle$ , taking the quantized photon energy  $hf = \Delta E$  to bridge the energy gap. For the two-level system depicted in fig. 2.8a, this results in a change in population densities

$$\left(\frac{dN_2}{dt}\right)_{\text{abs}} = -\left(\frac{dN_1}{dt}\right)_{\text{abs}} = B_{12}u(f)N_1 \quad (2.74)$$

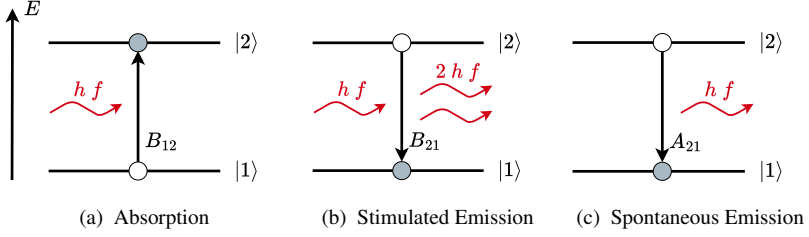


Figure 2.8: Fundamental optical interactions.

where  $u(f)$  is the spectral energy density per unit volume and per unit frequency interval of the electromagnetic wave, and  $B_{12}$  is a proportionality constant that describes the transition strength [42]. In a classical picture, the radiation emitted by the excited dipole oscillations interferes destructively with the coherent initiating wave, resulting in attenuation.

Stimulated emission is the counteracting process depicted in fig. 2.8b, in which the electromagnetic wave induces resonant state transitions from the higher to the lower energy level. This is accompanied by the emission of photons that are coherent to the initiating electromagnetic wave. The associated transition rate for a two-level system is given by

$$\left(\frac{dN_2}{dt}\right)_{\text{stim}} = -\left(\frac{dN_1}{dt}\right)_{\text{stim}} = -B_{21}u(f)N_2. \quad (2.75)$$

proportional to the transition strength  $B_{21}$  [42]. Stimulated emission forces already excited dipoles to radiate in phase with the electromagnetic wave, leading to constructive interference and amplification.

The third fundamental interaction is spontaneous emission, depicted in fig. 2.8c, resulting in a transition from state  $|2\rangle$  to  $|1\rangle$  under the release of a photon that matches the energy difference. In contrast to stimulated emission, spontaneous emission is a random process leading to incoherent emission with arbitrary phase and direction, which is called fluorescence. The associated transition rate in a two-level system

$$\left(\frac{dN_2}{dt}\right)_{\text{spon}} = -\left(\frac{dN_1}{dt}\right)_{\text{spon}} = -A_{21}N_2 \quad (2.76)$$

is proportional to the constant  $A_{21}$  that can be associated with a time constant  $\tau_{21} = A_{21}^{-1}$  of an exponential radiative decay [42]. Spontaneous emission is a direct consequence of the quantization of the electromagnetic field. The commutation of the electric and magnetic field operators leads to a ground state with non-zero energy  $(1/2)hf$  of the Hamiltonian of their harmonic oscillation. This corresponds to vacuum fluctuations of the electromagnetic field around the expectation value of zero. These randomly appearing and disappearing virtual photons represent a perturbation that couples excited dipole moments with the available modes of the electromagnetic field thereby stimulating incoherent emission with random directions and phases [42].

The three constants  $B_{12}$ ,  $B_{21}$ , and  $A_{21}$  each relating to one of the fundamental light-matter interactions are the Einstein coefficients. The total rate of state transitions in a two-level system results from the contribution of all three processes:

$$\frac{dN_2}{dt} = -\frac{dN_1}{dt} = B_{12}u(f)N_1 - (B_{21}u(f) + A_{21})N_2 . \quad (2.77)$$

For any constant energy density  $u(f)$  of the interacting electromagnetic wave, the two-level system must enter a steady state, i.e.  $dN_2/dt = 0$  and  $dN_1/dt = 0$ . This requires

$$B_{12} = B_{21} , \quad (2.78)$$

which means that absorption and stimulated emission are equivalent to each other. Because spontaneous emission is initiated by vacuum fluctuations, it relates to the same transition strength

$$A_{21} = \frac{8\pi n^3 hf^3}{c_0^3} B_{21} , \quad (2.79)$$

where the pre-factor accounts for the spectral and spatial power density of the vacuum fluctuations given by the photon energy  $hf$  times the mode density per volume and frequency in the medium with refractive index  $n$  [42].

In general, the lifetime of an excited state described by the time constant  $\tau$  is determined by radiative as well as non-radiative decay:

$$\frac{1}{\tau} = \frac{1}{\tau_{21}} + \frac{1}{\tau_{nr}} \quad (2.80)$$

where  $\tau_{21}$  is the radiative lifetime connected to the Einstein  $A_{21}$  coefficient and  $\tau_{nr}$  the non-radiative lifetime. In solids, non-radiative decay mainly occurs through energy transfer to the surrounding lattice exciting vibrational states. Typically, these discrete vibration states have smaller energy spacings than electronic states. Their excitation can be described by the generation of quantized phonons. Generation or recombination of one or multiple phonons can directly cause non-radiative transitions or assist radiative transitions by compensating for an energy mismatch of the interacting photon. The probability of a transition decreases with an increasing number of involved phonons. The density of phonons in a material system depends on the temperature and their maximum energies on the lattice structure and composition. Silica has a maximum phonon energy of about  $1100 \text{ cm}^{-1}$  at room temperature [60].

Due to the finite lifetime  $\tau$  of excited states, optical transitions do not exhibit infinite sharp resonance frequencies, as a consequence of the energy-time uncertainty. To account for a spectrally dependent transition intensity, the Einstein coefficients can be multiplied with a normalized line-shape function  $\rho_f(f)$ . Moreover, for practical application, it is convenient to relate the transition rates to intensities  $I$  instead of the energy density  $u(f)$ . Thus, the Einstein coefficients of a two-level system can be converted into spectroscopic cross-sections

$$\sigma_{12}(f) = \frac{hf}{v_g} B_{12} \rho_f(f) \quad (2.81)$$

$$\sigma_{21}(f) = \frac{hf}{v_g} B_{21} \rho_f(f) \quad (2.82)$$

where  $\sigma_{12}(f)$  is the absorption cross-section and  $\sigma_{21}(f)$  is the emission cross-section of the two-level system [53]. For narrow line widths  $\rho_f(f)$ , the group velocity  $v_g$  according to eq. (2.69) is often assumed to be  $v_g \approx c_0/n$ .

The spectroscopic cross-sections have the units of areas to quantify the strength of optical transitions with regard to optical intensities. Because they take into account the spectral dependence of optical transitions, they can also characterize the transition intensity over several states, while each of the states can have a different population density. This enables the determination of emission and absorption cross-sections of entire manifolds of closely spaced energy sub-levels, such as those formed by Stark splitting of electronic states of rare-earth ions.

The spectroscopic cross-sections of the manifolds  $|1\rangle$  and  $|2\rangle$  result from the summation of the individual cross sections  $\sigma_{m_1, m_2}(f)$  and  $\sigma_{m_2, m_1}(f)$  between each of the sublevels  $m_1$  and  $m_2$  within the two manifolds

$$\sigma_a(f) = \sum_{m_1, m_1} \left( \frac{\exp\left(-\frac{E_{m_1}}{k_B T}\right)}{Z_1} \right) \sigma_{m_1, m_2}(f) \quad (2.83)$$

$$\sigma_e(f) = \sum_{m_1, m_2} \left( \frac{\exp\left(-\frac{E_{m_2}}{k_B T}\right)}{Z_2} \right) \sigma_{m_2, m_1}(f) \quad (2.84)$$

where the preceding term describes the population of the individual levels by means of the Boltzmann distribution depending on the temperature  $T$  related to the partition functions

$$Z_i = \sum_{m_i} \exp\left(\frac{-E_{m_i}}{k_B T}\right) \quad (2.85)$$

representing the sum of all populations in the respective manifold [61]. The parameter  $k_B$  is the Boltzmann constant.

These spectroscopic cross-sections of emission  $\sigma_e(f)$  and absorption  $\sigma_a(f)$  or their equivalent descriptions for vacuum wavelengths  $\sigma_e(\lambda_0)$  and  $\sigma_a(\lambda_0)$  are usually determined experimentally. In contrast to the cross-sections between two discrete levels  $\sigma_{12}$  and  $\sigma_{21}$ , the line-shapes of the emission and absorption cross-sections of the entire manifolds differ from each other due to the different population within the sublevels. With the assumption of a stationary population distribution within the manifolds according to the thermal equilibrium, the absorption and emission cross-section are related by the McCumber equation:

$$\frac{\sigma_e(\lambda_0)}{\sigma_a(\lambda_0)} = \exp\left(-\frac{hc_0}{k_B T} \left(\frac{1}{\lambda_0} - \frac{1}{\lambda_\mu}\right)\right) \quad (2.86)$$

where

$$\lambda_\mu = \frac{hc_0}{k_B T} \left(\ln \frac{Z_1}{Z_2}\right)^{-1} \quad (2.87)$$

describes the wavelength of the chemical potential corresponding to the intersection point of the absorption and emission cross-sections [42, 62]. The radiative lifetime of the upper manifold is given by the Füchtbauer-Ladenburg relation

$$\frac{1}{\tau_{21}} = \frac{8\pi n^2}{c_0^2} \int \sigma_e(f) f^2 df = 8\pi n^2 c_0 \int \frac{\sigma_e(\lambda_0)}{\lambda_0^4} d\lambda_0 \quad (2.88)$$

which can be used to experimentally determine the emission cross-section by measuring the radiative lifetime  $\tau_{21}$  [42].

For rare-earth ions, the weak parity-forbidden transition intensities within the  $4f$  shell result in long radiative lifetimes of the Stark manifolds [53]. Thus, the radiative lifetime of a manifold is much longer than the non-radiative lifetimes of its upper Stark levels, leading to a rapid adaptation of the population distribution to the thermal equilibrium by phonon relaxations. The spectroscopic cross-sections of rare-earth ions therefore show a good agreement with the McCumber relation (2.86). Within a silica host, the line-shapes of the manifolds are affected by homogeneous and inhomogeneous broadening. Homogeneous broadening is caused by dephasing and the finite lifetime due to radiative and non-radiative interactions, resulting in a Lorentzian line-shape [42]. Inhomogeneous broadening arises from different environments of the individual states, which leads to a spectral and spatial decoupling of the state ensemble. The sum of these individually shifted lines results in an inhomogeneous Gaussian line-shape [42]. A combination of homogeneous and inhomogeneous broadening typically results in a Voigt profile [42]. In silica, the high phonon energy leads to a strong homogeneous broadening of the individual Stark levels, causing them to overlap. Inhomogeneous broadening between the local sites in the amorphous glass further diffuses the individual peaks to merge into smooth and broad absorption and emission profiles [63].

The spectroscopic cross-sections represent the spectral transition strength to quantify the transition rates for absorption and emission dependent on the population densities and the interacting optical intensity. Considering eqs. (2.72) and (2.73) for the attenuation or amplification within a dielectric material derived from the complex electric susceptibility, the absorption coefficient  $\alpha$  can be connected with the spectroscopic cross-sections:

$$\alpha = \sigma_a(\lambda_0)N_1 - \sigma_e(\lambda_0)N_2 . \quad (2.89)$$

Thus, the optical gain along the  $z$ -direction through a material with two contributing manifolds having the populations  $N_1$  and  $N_2$  can be expressed by

$$G(z, \lambda_0) = \frac{\tilde{I}(z, \lambda_0)}{\tilde{I}(0, \lambda_0)} = e^{(\sigma_e(\lambda_0)N_2 - \sigma_a(\lambda_0)N_1)z} \quad (2.90)$$

where  $\tilde{I}(z, \lambda_0)$  denotes the spectral intensity connected by a Fourier transform to the temporal intensity  $I(z, t)$ . An optical gain  $G > 1$  means amplification and an optical gain  $G < 1$  means attenuation of the optical intensity.

### 2.1.4 Nonlinear Interactions

The treatment of dipole moments in dielectric materials as harmonic oscillators assumes a displacement of charges within a parabolic potential, resulting in restoration forces that are linearly dependent on the displacement. This yields the linear relationship between the induced polarization and the electric field, described by the linear electric susceptibility (see eq. (2.35)). However, the actual electrostatic potential experienced by bound charges deviates from this ideal parabolic shape. Consequently, strong electric fields, such as those from intense laser radiation, can induce large displacements where the anharmonicity of the potential becomes significant. This results in a nonlinear material response.

Figure 2.9 illustrates this concept for a one-dimensional displacement. The orange curve shows an anharmonic potential  $U(x)$ , which approximates the harmonic potential (green dashed line), only for small displacements. For larger displacements caused by strong electric fields, the deviation from the harmonic potential becomes significant. Thus, the dipoles experience a restoring force  $F_R = -dU/dx$  in the anharmonic potential that becomes nonlinear dependent on the charge displacement. If a strong sinusoidal electric field drives the dipoles far below their resonance frequency, their quasi-instantaneous displacement yields a macroscopic polarization  $P(t) \propto x$  that deviates from the sinusoidal course of the driving electric field. This is illustrated in the lower part of figure 2.9. The polarization contains higher harmonics of the driving frequency as a result of the nonlinear material response to the harmonic electric field. Furthermore, since the illustrated anharmonic potential is asymmetric, the polarization  $P(t)$  responds asymmetrically to positive and negative field amplitudes. Such an asymmetry is a characteristic of media with non-centrosymmetric lattice structures. In contrast, centrosymmetrical materials exhibit symmetric anharmonic potentials.

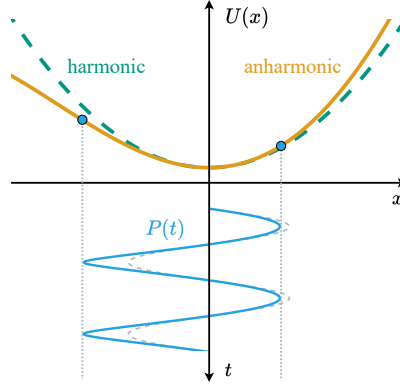


Figure 2.9: Displacement of bound charges in an anharmonic potential driven by a sinusoidal electric field at a frequency far below resonance. Because the restoring force does not linearly depend on the displacement, the corresponding nonlinear polarization contains higher harmonics of the driving frequency.

To account for its nonlinearity, the polarization needs to be expanded over several powers of the electric field vectors while considering optical anisotropy in the medium. This leads to a description of the polarization as a sum of several orders

$$\mathbf{P} = \sum_{n=1}^{\infty} \mathbf{P}^{(n)} = \mathbf{P}_L + \mathbf{P}_{NL} \quad (2.91)$$

where  $\mathbf{P}^{(n)}$  denotes the polarization of  $n$ -th order depending on the electric field vector to the power of  $n$  i.e.  $\mathbf{E}$ ,  $\mathbf{E}\mathbf{E}$ ,  $\mathbf{E}\mathbf{E}\mathbf{E}$ , and so on. While the first order polarization  $\mathbf{P}^{(1)}$  corresponds to the linear polarization  $\mathbf{P}_L$ , the higher-order terms constitute the nonlinear polarization  $\mathbf{P}_{NL}$ .

The description by power series emphasizes that the nonlinear interaction of light with the propagation medium is accompanied by the emergence of new frequency components. To analyze these effects in the frequency domain, it is convenient to express the electric field as a superposition of monochromatic components

$$\mathbf{E}(t) = \frac{1}{2} \sum_{m=-M}^M (1 + \delta_{m,0}) \mathbf{E}(\omega_m) e^{j\omega_m t} \quad (2.92)$$

where  $\mathbf{E}(\omega_m)$  is the complex vector amplitude of the monochromatic wave in the time-domain oscillating with the frequency  $\omega_m$  according to the complex phasor notation eq. (2.9) [45].

The summation includes all positive and negative frequencies  $\omega_m$ ,  $m = -M \dots M$  using the conventions  $\omega_{-m} = -\omega_m$  and  $\mathbf{E}(\omega_{-m}) = \mathbf{E}^*(\omega_m)$ , as well as a DC component with  $\omega_0 = 0$ . The factor of  $1/2$  appears because the field amplitude is divided between positive and negative frequency components, and the term  $(1 + \delta_{m,0})$  provides a correction for the DC field as it has no positive and negative frequency components, where  $\delta_{m,0}$  denotes the Kronecker delta. Analogously, the polarization is expressed by

$$\mathbf{P}(t) = \frac{1}{2} \sum_{m=-M}^M (1 + \delta_{m,0}) \mathbf{P}(\omega_m) e^{j\omega_m t}. \quad (2.93)$$

Within this framework, an  $n$ -th order polarization component  $\mathbf{P}^{(n)}(\omega_p)$  at a frequency  $\omega_p$  arises, if the incident electric field contains a combination of  $n$  frequencies whose sum is  $\omega_p$ :

$$\omega_p = \omega_{m_1} + \omega_{m_2} + \dots + \omega_{m_n} \quad (2.94)$$

as a result of the product of the  $n$  monochromatic waves at these frequencies in the power expansion. This condition is equivalent to energy conservation. Each resulting polarization component  $\mathbf{P}^{(n)}(\omega_p)$  is then related to the product of the  $n$  interacting electric field amplitudes  $\mathbf{E}(\omega_{m_1}) \mathbf{E}(\omega_{m_2}) \dots \mathbf{E}(\omega_{m_n})$  through the  $n$ -th order nonlinear susceptibility tensor  $\chi^{(n)}(\omega_p : \omega_{m_1}, \dots, \omega_{m_n})$ , which has a rank of  $n + 1$ . The general expression for the  $n$ -th order polarization is

$$\begin{aligned} \mathbf{P}^{(n)}(\omega_p) &= \frac{1}{2^{n-1}} \epsilon_0 \sum_{\mathbb{S}(\omega_p)} \frac{(1 + \delta_{m_1,0}) \dots (1 + \delta_{m_n,0})}{1 + \delta_{p,0}} \\ &\quad \chi^{(n)}(\omega_p : \omega_{m_1}, \dots, \omega_{m_n}) : \mathbf{E}(\omega_{m_1}) \dots \mathbf{E}(\omega_{m_n}) \end{aligned} \quad (2.95)$$

where

$$\mathbb{S}(\omega_p) = \{(m_1, \dots, m_n) \mid \omega_{m_1} + \dots + \omega_{m_n} = \omega_p\} \quad (2.96)$$

describes the set of all pairs  $(m_1, \dots, m_n)$  that fulfill the condition eq. (2.94) [45].

## Nonlinear Wave Propagation and Susceptibility Symmetries

The nonlinear interaction of a strong electric field with a dielectric material results in a polarization that contains new frequency components  $\omega_p$ . The underlying ensemble of microscopic

dipole moments in turn re-radiates at these nonlinearly excited oscillation frequencies. This response evolves in a propagating wave with a new frequency  $\omega_l$  corresponding to a frequency component  $\omega_p$  of the induced polarization, if the emission of the spatially distributed induced dipole moments superimposes coherently for this frequency. Efficient generation of this new wave at  $\omega_l$  requires phase matching, ensuring a constructive build-up of the field from the polarization source over a significant interaction length.

The propagation of these emerging modes within the nonlinear medium is governed by a wave equation analogous to the linear Helmholtz equation (2.11), but extended to include the nonlinear interaction. Its derivation from Maxwell's eqs. (2.1) to (2.4) is largely parallel to the linear wave equation (see sec. 2.1.1) but involves the general constitutive relation eq. (2.5) that incorporates the nonlinear polarization:

$$\mathbf{D} = \epsilon_0 \mathbf{E} + \mathbf{P}_L + \mathbf{P}_{NL} = \epsilon_0 \epsilon_r \mathbf{E} + \mathbf{P}_{NL} . \quad (2.97)$$

Thus, in contrast to the linear approximation, the first term on the right-hand side of the vector identity  $\nabla \times (\nabla \times \mathbf{E}) = \nabla(\nabla \cdot \mathbf{E}) - \nabla^2 \mathbf{E}$  does not vanish anymore. However, for the practical case of small nonlinearities it is usually neglected, in particular if the SVEA is valid [64]. With this approximation, the nonlinear Helmholtz equation is obtained

$$\nabla^2 \mathbf{E}(\mathbf{r}, \omega_m) + k_m^2 \mathbf{E}(\mathbf{r}, \omega_m) = -\omega_m^2 \mu_0 \mathbf{P}_{NL}(\mathbf{r}, \omega_m) \quad (2.98)$$

where the nonlinear polarization  $\mathbf{P}_{NL}(\mathbf{r}, \omega_m)$  acts as a source term for wave propagation at frequencies  $\omega_m$  and with wavenumbers  $k_m$  [64].

Considering a plane wave with a frequency  $\omega_l$  and wavenumber  $k_l$  propagating in  $z$ -direction

$$\mathbf{E}(z, \omega_l) = \mathbf{A}(z, \omega_l) e^{-jk_l z} \quad (2.99)$$

with the slowly varying amplitude  $\mathbf{A}(z, \omega_l)$  and substituting into eq. (2.98), the SVEA allows for neglecting the second derivative  $d^2 \mathbf{A}/dz^2$  resulting in the relation

$$2jk_l \frac{d\mathbf{A}(z, \omega_l)}{dz} e^{-jk_l z} = \omega_l^2 \mu_0 \mathbf{P}_{NL}(z, \omega_l) . \quad (2.100)$$

Inserting eq. (2.95) to consider the  $n$ -th order polarization effects yields the relation

$$\frac{d\mathbf{A}(z, \omega_l)}{dz} = -j \frac{\omega_l^2 \mu_0}{2^n k_l} \sum_{\mathbb{S}(\omega_p)} \frac{(1 + \delta_{m_1,0}) \cdots (1 + \delta_{m_n,0})}{1 + \delta_{p,0}} \chi^{(n)}(\omega_p : \omega_{m_1}, \cdots, \omega_{m_n}) : \mathbf{A}(z, \omega_{m_1}) \cdots \mathbf{A}(z, \omega_{m_n}) e^{-j\Delta k z} \quad (2.101)$$

where  $\mathbf{A}(z, \omega_m)$  are the slowly varying amplitudes at the frequency components  $\omega_m$  of the electric field and

$$\Delta k = k_p - k_l = k_{m_1} + \cdots + k_{m_n} - k_l \quad (2.102)$$

denotes the phase mismatch between the wavenumbers  $k_l$  and  $k_p$  of the emerging wave oscillating at  $\omega_l$  and the polarization resulting from the sum of the wavenumbers  $k_m$  of the monochromatic field components  $\mathbf{E}(z, \omega_m)$  [45]. Thus, eq. (2.101) describes the spatial evolution of the amplitude of a wave at frequency  $\omega_l$  as a result of mode coupling via the nonlinear polarization of order  $n$ . Efficient coupling requires proper phase matching  $\Delta k \approx 0$ , which corresponds to conservation of momentum.

Optical nonlinearity represents a material response to an electric field that depends on the electric field itself, more precisely on the field strength, polarization, and frequency of its individual components. A complete description of the interaction involves consideration of all possible permutations of polarization directions and frequency components of the electric field. The material response to each of these permutations is characterized by a specific tensor element  $\chi_{q_0:q_1 \cdots q_n}^{(n)}(\omega_p : \omega_{m_1}, \cdots, \omega_{m_n})$  of the anisotropic nonlinear susceptibility of order  $n$ , with the Cartesian coordinates  $q_0, q_1, \cdots, q_n \in \{x, y, z\}$  [45].

This large number of complex tensor elements can be reduced drastically by exploiting general as well as material specific symmetries of the nonlinear susceptibility. In general, the elements of the susceptibility tensor exhibit intrinsic permutation symmetry,

$$\chi_{q_0:q_1 \cdots q_i q_j \cdots q_n}^{(n)}(\omega_p : \omega_1, \cdots, \omega_i, \omega_j, \cdots, \omega_n) = \chi_{q_0:q_1 \cdots q_j q_i \cdots q_n}^{(n)}(\omega_p : \omega_1, \cdots, \omega_j, \omega_i, \cdots, \omega_n) \quad (2.103)$$

as a result of the commutativity within the product of the complex field amplitudes and its positive- and negative-frequency components are the complex conjugate of each other,

$$\chi_{q_0:q_1 \cdots q_n}^{(n)}(\omega_p : \omega_1, \cdots, \omega_n) = \chi_{q_0:q_1 \cdots q_n}^{(n)}(-\omega_p : -\omega_1, \cdots, -\omega_n)^* \quad (2.104)$$

because of the reality of the fields in the time domain [45, 64]. For lossless media, the elements are real, enabling full permutation symmetry [45, 64]:

$$\chi_{q_0:q_1 \dots q_i \dots q_n}^{(n)}(\omega_p : \omega_1, \dots, \omega_i, \dots, \omega_n) = \chi_{q_i:q_1 \dots q_0 \dots q_n}^{(n)}(\omega_i : -\omega_1, \dots, \omega_p, \dots, -\omega_n). \quad (2.105)$$

Nonlinear interactions that rely only on the real part of the susceptibility are termed parametric processes. In these processes, energy is exchanged between the optical field components, without involving energy transfer with the medium. In contrast, non-parametric processes entail an energy exchange of the field with the medium associated with the excitation of energy levels or phonon interactions. These interactions are related to the imaginary part of the susceptibility.

For frequencies far below the lowest resonance frequency of the material system, its response can be assumed to be lossless and instantaneous. Under these conditions, Kleinman's symmetry can be applied, which neglects the frequency dependence of the susceptibility [65]. Further symmetries can be found within specific crystals and material systems [66, 67]. For centrosymmetric media including amorphous glasses, the symmetric potential results in a vanishing second-order susceptibility  $\chi^{(2)}$  [68]. Because the magnitude of the susceptibility decreases with order, nonlinearities in these materials are mainly attributed to third-order effects. In non-centrosymmetric crystals such as ZGP, the second-order effects are dominant.

## Second-Order Nonlinear Effects and Parametric Amplification

Second-order nonlinear effects arise from the interaction of three waves in a non-centrosymmetric material characterized by the tensor  $\chi^{(2)}$  of rank three. The vector components of the resulting second-order polarization  $\mathbf{P}^{(2)}$ , derived from the general expression eq. (2.95) for  $n = 2$ , are

$$P_q^{(2)}(\omega_p) = \frac{\epsilon_0}{2} \sum_{rs} \sum_{\mathbb{S}(\omega_p)} \frac{(1 + \delta_{m_1,0})(1 + \delta_{m_2,0})}{1 + \delta_{p,0}} \chi_{q:rs}^{(2)}(\omega_p : \omega_{m_1}, \omega_{m_2}) E_r(\omega_{m_1}) E_s(\omega_{m_2}) \quad (2.106)$$

where the indices  $qrs \in \{xyz\}$  refer to the Cartesian vector components [45]. The second-order nonlinear polarization  $P_q^{(2)}(\omega_p)$  leads to the emergence of new frequency components through parametric second-order nonlinear effects such as second-harmonic generation (SHG), optical rectification (OR), sum-frequency generation (SFG), and difference-frequency gen-

eration (DFG). An efficient occurrence of these processes requires adherence with energy conservation eq. (2.94) and phase matching  $\Delta k \approx 0$  according to eq. (2.102). In SHG, a degenerate input wave  $\omega_{m_1} = \omega_{m_2}$  results in the generation of a wave with double frequency  $\omega_p = 2\omega_{m_1}$ ; OR creates a constant DC field  $\omega_p = 0$  from frequency components  $\omega_{m_1} = -\omega_{m_2}$ ; in SFG, two distinct frequencies  $\omega_{m_1} \neq \omega_{m_2}$  generate a wave with  $\omega_p = \omega_{m_1} + \omega_{m_2}$ ; and DFG leads to the creation of two waves at lower frequencies  $\omega_p$  and  $\omega_{m_2}$  under the depletion of a wave  $\omega_{m_1}$ , fulfilling the condition  $\omega_p = \omega_{m_1} - \omega_{m_2}$ . In general, these processes do not all occur efficiently in a medium, as the phase-matching condition favors specific interactions [64].

For waves with fixed polarization and propagation directions, the complex field amplitudes can be written as

$$\mathbf{E}(\omega_m) = E(\omega_m)\mathbf{e}_m, \quad (2.107)$$

where  $E(\omega_m)$  is the complex scalar amplitude and  $\mathbf{e}_m$  is the unit vector pointing in the polarization direction of the wave at frequency  $\omega_m$ . The strengths of the nonlinear interaction for specific polarizations then be described by the scalar effective coefficient

$$d_{\text{eff}} = \frac{1}{2} \frac{(1 + \delta_{m_1,0})(1 + \delta_{m_2,0})}{1 + \delta_{p,0}} \sum_{qrs} e_{p,q} \chi_{q:r,s}^{(2)}(\omega_p : \omega_{m_1}, \omega_{m_2}) e_{m_1,r} e_{m_2,s}, \quad (2.108)$$

which relates the scalar amplitudes of the fields to the scalar amplitude of the second-order polarization

$$P^{(2)}(\omega_p) = \epsilon_0 d_{\text{eff}} E(\omega_{m_1}) E(\omega_{m_2}), \quad (2.109)$$

where  $\mathbf{P}^{(2)}(\omega_p) = P^{(2)}(\omega_p)\mathbf{e}_p$  analogous to eq. (2.107) [45, 64].

For the determination of the effective coefficient  $d_{\text{eff}}$ , the second-order nonlinearity of a material is often given in the form of a contracted notation. This notation reduces the second-order susceptibility tensor  $\chi^{(2)}$  into a  $3 \times 6$  matrix  $\mathbf{d}$  for SHG by exploiting the intrinsic permutation symmetry [69]. For frequencies far below resonance, Kleinman's symmetry enables the application of the contracted notation also for SFG and DFG, since the vector indices  $qrs$  become freely permutable [65].

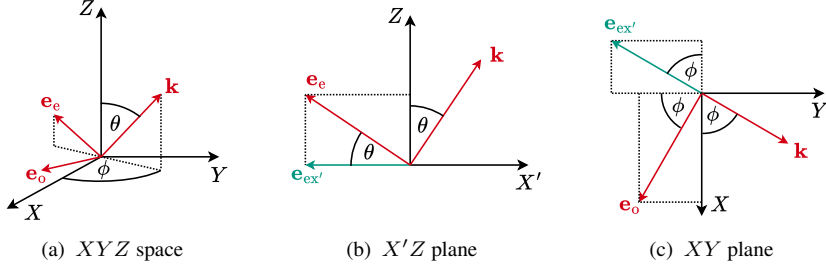


Figure 2.10: Directions of the wave vector  $\mathbf{k}$  and the polarization vectors  $\mathbf{e}_o$  and  $\mathbf{e}_e$  for ordinary and extraordinary polarization within the principal axes  $XYZ$  of a uniaxial crystal. The ordinary mode is defined by the angle  $\phi$  in the  $XY$  plane and the extraordinary mode by the angles  $\phi$  and  $\theta$  in all three dimensions  $XYZ$ .

The effective nonlinearity then results from the simple matrix multiplication  $d_{\text{eff}} = \mathbf{e}_p \mathbf{d} \mathbf{F}$ , i.e.:

$$d_{\text{eff}} = \begin{pmatrix} e_{p,x} \\ e_{p,y} \\ e_{p,z} \end{pmatrix} \begin{pmatrix} d_{11} & d_{12} & d_{13} & d_{14} & d_{15} & d_{16} \\ d_{21} & d_{22} & d_{23} & d_{24} & d_{25} & d_{26} \\ d_{31} & d_{32} & d_{33} & d_{34} & d_{35} & d_{36} \end{pmatrix} \begin{pmatrix} e_{m_1,x} e_{m_2,x} \\ e_{m_1,y} e_{m_2,y} \\ e_{m_1,z} e_{m_2,z} \\ e_{m_1,y} e_{m_2,z} + e_{m_1,z} e_{m_2,y} \\ e_{m_1,x} e_{m_2,z} + e_{m_1,z} e_{m_2,x} \\ e_{m_1,x} e_{m_2,y} + e_{m_1,y} e_{m_2,x} \end{pmatrix}. \quad (2.110)$$

Within a uniaxial crystal, the polarization vectors of the field components can be expressed by ordinary and extraordinary modes  $\mathbf{e}_o$  and  $\mathbf{e}_e$  by means of the polar coordinate angles  $\theta$  and  $\phi$  with respect to the principal axes  $XYZ$ . The definitions are illustrated in fig. 2.10. In cartesian coordinates, the polarization vectors  $\mathbf{e}_o$  and  $\mathbf{e}_e$  are given by

$$\mathbf{e}_o = \begin{pmatrix} \sin \phi \\ -\cos \phi \\ 0 \end{pmatrix}, \quad \mathbf{e}_e = \begin{pmatrix} -\cos \theta \cos \phi \\ -\cos \theta \sin \phi \\ \sin \theta \end{pmatrix}. \quad (2.111)$$

For the case of DFG, the input wave is referred to as the pump with the frequency  $\omega_{\text{pump}}$ , and the two output waves generated or amplified by the parametric process are called signal and idler with the frequencies  $\omega_{\text{idl}} \leq \omega_{\text{sig}} < \omega_{\text{pump}}$ . For a positive uniaxial crystal of the point group  $\bar{4}2m$ , such as ZGP, all matrix elements of  $\mathbf{d}$  vanish, except for  $d_{14}$ ,  $d_{25}$ , and  $d_{36}$ , which are equal under the assumption of Kleinman symmetry ( $d_{14} = d_{25} = d_{36}$ ) [66]. Assuming that all three

waves have a collinear propagation direction, while signal and idler are extraordinarily polarized and parallel to each other  $\mathbf{e}_{\text{sig}} = \mathbf{e}_{\text{idl}} = \mathbf{e}_e$ , and the pump is ordinarily polarized  $\mathbf{e}_{\text{pump}} = \mathbf{e}_o$  (type I phase matching), eq. (2.110) yields an effective nonlinearity of

$$d_{\text{eff}} = d_{14} \sin(2\theta) \sin(2\phi) . \quad (2.112)$$

Using the scalar effective nonlinearity  $d_{\text{eff}}$ , DFG can be expressed by three scalar coupled amplitude equations according to eq. (2.101), which describe the evolution of the three waves along their propagation direction  $z$  through the nonlinear crystal

$$\frac{dA(z, \omega_{\text{pump}})}{dz} = -j \frac{\omega_{\text{pump}}}{c_0 n(\omega_{\text{pump}})} d_{\text{eff}} A(z, \omega_{\text{sig}}) A(z, \omega_{\text{idl}}) e^{-j\Delta k z} , \quad (2.113)$$

$$\frac{dA(z, \omega_{\text{sig}})}{dz} = -j \frac{\omega_{\text{sig}}}{c_0 n(\omega_{\text{sig}})} d_{\text{eff}} A(z, \omega_{\text{pump}}) A^*(z, \omega_{\text{idl}}) e^{j\Delta k z} , \quad (2.114)$$

$$\frac{dA(z, \omega_{\text{idl}})}{dz} = -j \frac{\omega_{\text{idl}}}{c_0 n(\omega_{\text{idl}})} d_{\text{eff}} A(z, \omega_{\text{pump}}) A^*(z, \omega_{\text{sig}}) e^{j\Delta k z} , \quad (2.115)$$

where  $n(\omega)$  is the refractive index of the anisotropic crystal for the frequencies and polarizations of the pump, the signal, and the idler, respectively [64].

These equations can be expressed in terms of intensities  $I \propto |A|^2$  (see eq. (2.28))

$$\frac{dI_{\text{pump}}(z)}{dz} = -\epsilon_0 \omega_{\text{pump}} d_{\text{eff}} \text{Im} \{ A^*(z, \omega_{\text{sig}}) A^*(z, \omega_{\text{idl}}) A(z, \omega_{\text{pump}}) e^{j\Delta k z} \} , \quad (2.116)$$

$$\frac{dI_{\text{sig}}(z)}{dz} = \epsilon_0 \omega_{\text{sig}} d_{\text{eff}} \text{Im} \{ A^*(z, \omega_{\text{sig}}) A^*(z, \omega_{\text{idl}}) A(z, \omega_{\text{pump}}) e^{j\Delta k z} \} , \quad (2.117)$$

$$\frac{dI_{\text{idl}}(z)}{dz} = \epsilon_0 \omega_{\text{idl}} d_{\text{eff}} \text{Im} \{ A^*(z, \omega_{\text{sig}}) A^*(z, \omega_{\text{idl}}) A(z, \omega_{\text{pump}}) e^{j\Delta k z} \} , \quad (2.118)$$

where  $I_i(z)$  represents the intensities of the waves oscillating at the frequencies  $\omega_{\text{pump}}$ ,  $\omega_{\text{sig}}$  and  $\omega_{\text{idl}}$  [64]. These imply the Manley-Rowe relation

$$\frac{d}{dz} \left( \frac{I_{\text{sig}}(z)}{\hbar \omega_{\text{sig}}} \right) = \frac{d}{dz} \left( \frac{I_{\text{idl}}(z)}{\hbar \omega_{\text{idl}}} \right) = - \frac{d}{dz} \left( \frac{I_{\text{pump}}(z)}{\hbar \omega_{\text{pump}}} \right) , \quad (2.119)$$

with  $\hbar = h/(2\pi)$ , which indicates that each annihilation of a pump photon  $\hbar \omega_{\text{pump}}$  is accompanied by the generation of a signal photon  $\hbar \omega_{\text{sig}}$  and an idler photon  $\hbar \omega_{\text{idl}}$ .

A simple analytical solution of the coupled wave equations can be found under the undepleted pump approximation, which assumes a strong pump wave that remains constant over a short interaction length  $z$ , i.e.  $A(z, \omega_{\text{pump}}) \approx A(0, \omega_{\text{pump}}) = A_{\text{pump}}$  or in terms of pump intensity  $I_{\text{pump}}(z) \approx I_{\text{pump}}(0) = I_{\text{pump}}$ . Differentiating eq. (2.114) and inserting eq. (2.115) and then eq. (2.114) again, yields an ordinary differential equation (ODE) with constant coefficients

$$\frac{d^2}{dz^2} A(z, \omega_{\text{sig}}) - j\Delta k \frac{d}{dz} A(z, \omega_{\text{sig}}) - \kappa^2 A(z, \omega_{\text{sig}}) = 0 \quad (2.120)$$

with the coupling coefficient  $\kappa$  given by [45]

$$\kappa^2 = \frac{\omega_{\text{sig}}\omega_{\text{idl}}d_{\text{eff}}^2}{c_0^2 n(\omega_{\text{sig}})n(\omega_{\text{idl}})} |A_{\text{pump}}|^2 = \frac{2\omega_{\text{sig}}\omega_{\text{idl}}d_{\text{eff}}^2}{\epsilon_0 c_0^3 n(\omega_{\text{sig}})n(\omega_{\text{idl}})n(\omega_{\text{pump}})} I_{\text{pump}}. \quad (2.121)$$

The ODE for the idler can be derived analogously.

With the initial values  $A(0, \omega_{\text{sig}}) = A_{\text{sig},0}$  and  $A(0, \omega_{\text{idl}}) = A_{\text{idl},0}$  the solutions for signal and idler are

$$A(z, \omega_{\text{sig}}) = \left[ A_{\text{sig},0} \left( \cosh(gz) - j\frac{\Delta k}{2g} \sinh(gz) \right) - j\frac{\omega_{\text{sig}}d_{\text{eff}}}{n(\omega_{\text{sig}})c_0g} A_{\text{pump}} A_{\text{idl},0}^* \sinh(gz) \right] \exp\left(j\frac{\Delta k}{2}z\right) \quad (2.122)$$

$$A(z, \omega_{\text{idl}}) = \left[ A_{\text{idl},0} \left( \cosh(gz) - j\frac{\Delta k}{2g} \sinh(gz) \right) - j\frac{\omega_{\text{idl}}d_{\text{eff}}}{n(\omega_{\text{idl}})c_0g} A_{\text{pump}} A_{\text{sig},0}^* \sinh(gz) \right] \exp\left(j\frac{\Delta k}{2}z\right) \quad (2.123)$$

where

$$g = \sqrt{\kappa^2 - \left(\frac{\Delta k}{2}\right)^2} \quad (2.124)$$

is the parametric gain coefficient [64].

The parametric gain for the intensities of signal and idler can be derived from the absolute value squared of the complex amplitude ratios  $G(z) = I(z)/I(0) = |A(z)/A(0)|^2$ . Assuming weak dispersion, i.e.  $n(\omega_{\text{sig}}) = n(\omega_{\text{idl}})$ , and losses, which implies that signal and idler have the same number of photons at any location  $z$  along the propagation direction as a consequence of the Manley–Rowe relation (2.119), i.e.  $I_{\text{sig}}(z) = (\omega_{\text{sig}}/\omega_{\text{idl}})I_{\text{idl}}(z)$ , results in a parametric gain of

$$G(z) = 1 + \frac{2\kappa^2}{g^2} \sinh^2(gz) + \frac{\kappa}{g} \sinh(2gz) \sin(\Delta\phi) + \frac{\kappa\Delta k}{g^2} \sinh^2(gz) \cos(\Delta\phi) \quad (2.125)$$

where

$$\Delta\phi = \phi_{\text{pump}} - \phi_{\text{sig}} - \phi_{\text{idl}} \quad (2.126)$$

is the phase difference between the slowly varying amplitudes  $A_i = |A_i|e^{-j\phi_i}$  of the pump, the signal, and the idler. While for ideal phase matching the relative phase between the waves remains at this initial value, a wavenumber mismatch  $\Delta k > 0$  causes the waves to change their phase relationship along the propagation direction  $z$ .

DFG in a nonlinear medium results in parametric amplification of the signal and the idler depending on the pump intensity  $I_{\text{pump}}$  incorporated in the coupling coefficient  $\kappa$  according to eq. (2.121), sufficient phase matching  $\Delta k$ , and the relative phases of the three waves  $\Delta\phi$ . As a consequence of the Manley–Rowe relation (2.119), signal and idler experience the same parametric gain according to eq. (2.125) under the assumption of a constant undepleted pump along  $z$ . A gain  $G > 1$  corresponds to parametric amplification, and a gain  $G < 1$  leads to backconversion to the pump. For ideal phase matching ( $\Delta k = 0$ ), the first term  $1 + 2\kappa^2/g^2 \sinh^2(gz)$  is always positive and the last term proportional to  $\Delta k$  vanishes. The middle term proportional to  $\sin(\Delta\phi)$  can be positive or negative depending on the phase difference  $\Delta\phi$  between the slowly varying amplitudes. The gain becomes maximum for  $\sin(\pi/2) = 1$ . Since ideal phase matching implies  $g = \kappa$  according to eq. (2.124), using the hyperbolic identity  $1 + 2\sinh^2(x) + \sinh(2x) = e^{2x}$ , simplifies eq. (2.125) to

$$G_{\text{max}}(z, \Delta k = 0) = e^{2\kappa z} \quad (2.127)$$

meaning an exponential growth of the signal and idler along  $z$  for the case of an ideal phase relationship  $\Delta\phi = \pi/2$  with the pump, as long as pump depletion can be neglected. A larger phase mismatch  $\Delta k > 0$  results in a reduction of the parametric gain, but can be partly compensated by a favorable initial phase relationship  $\Delta\phi$  between signal, idler, and the pump.

Figure 2.11 illustrates the relationship between parametric gain  $G$ , phase mismatch of the wavenumbers  $\Delta k$ , and initial phase difference between the complex amplitudes  $\Delta\phi$ , according to eq. (2.125). In figure 2.11a, the parametric gain versus the propagation distance  $z$  normalized

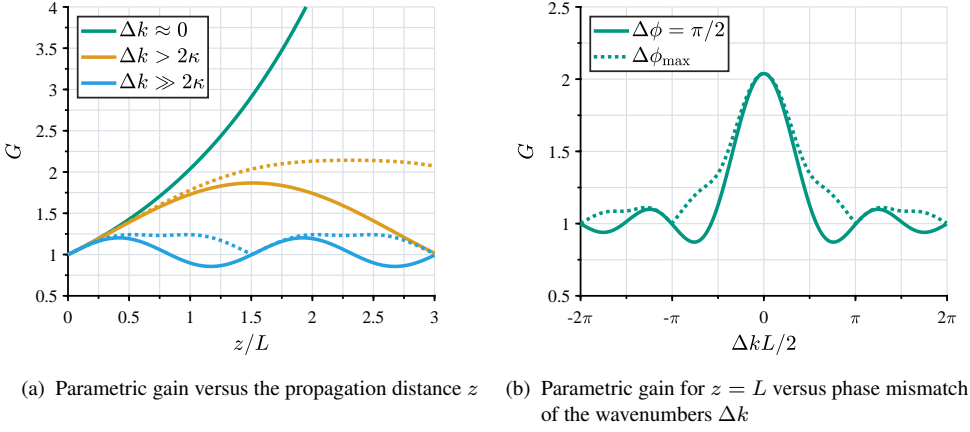


Figure 2.11: Parametric gain dependent on the propagation distance  $z$  within the nonlinear medium, the phase mismatch of the wavenumbers  $\Delta k$ , and the phase difference between the complex amplitudes  $\Delta \phi$ . The solid curves correspond to a initial phase difference  $\Delta \phi = \pi/2$  to the pump, and the dotted curves to an optimally altering phase difference  $\Delta \phi_{\max}(z)$  resulting in maximum gain at each distance  $z$ . An optimal phase difference  $\Delta \phi_{\max}$  can still provide gain for phase mismatches  $|\Delta k L/2| > \pi/2$ , which allows for a spectrally broader parametric amplification.

by a length  $L$  within the nonlinear medium is plotted for different phase mismatches  $\Delta k$ . For the solid curves an initial phase difference  $\Delta \phi = \pi/2$  is chosen. While phase matching  $\Delta k \approx 0$  results in an exponential gain according to eq. (2.127), a phase mismatch  $\Delta k > 2\kappa$ , yields a complex gain coefficient according to eq. (2.124) leading to a parametric gain that oscillates between amplification and backconversion along  $z$ , because the waves progressively change their relative phase relationship. An increasing phase mismatch  $\Delta k \gg 2\kappa$  decreases the period of the gain oscillation and reduces the gain even for short interaction lengths.

Over a propagation distance  $z$ , the gain  $G(z)$  results from the relative phase evolution over the entire interaction length, which depends on the phase change by the wavenumber mismatch  $\Delta k z$ , but also on the initial phase difference  $\Delta \phi$ . Thus, there is an ideal initial phase difference  $\phi_{\max}(z)$  that maximizes the gain over a specific propagation distance  $z$  [70]. The dotted curves in fig. 2.11a show the gain with optimally adapted phase differences  $\Delta \phi_{\max}(z)$  versus the propagation distance  $z$ . Compared to the gain with a fixed phase relation and the same phase mismatches  $\Delta k$  illustrated in the same color, respectively, the ideal phase difference provides a higher gain over most interaction lengths and avoids backconversion. This reduces the influence of a phase mismatch  $\Delta k$  of the wavenumbers, in particular for short interaction lengths and low

gain levels, as illustrated in fig. 2.11b. The diagram shows the parametric gain over an interaction length  $z = L$  versus the phase mismatch  $\Delta kL/2$  for a fixed and an optimal phase difference  $\Delta\phi$  between the waves. An optimal phase difference  $\Delta\phi_{\max}$  relaxes the sensitivity of the gain to a wavenumber mismatch  $\Delta k$ , allowing parametric amplification within a broader spectral range. This is in particular important for optical parametric oscillators (OPOs), as it will be discussed in sec. 2.2.3, where small parametric single-pass gain levels over short resonator lengths result in generation of broad signal and idler spectra by parametric amplification from noise. Although the phase-matching condition can be slightly extended under specific constraints, it remains a sensitive requirement for parametric processes.

### Angular Phase Matching in Birefringent Crystals

Phase matching ensures that the interacting waves in a nonlinear process remain coherent throughout their propagation in the nonlinear medium to enable effective parametric energy transfer. For DFG, this requires that the pump wave vector equals the sum of the wave vectors of signal and idler

$$\Delta\mathbf{k} = \mathbf{k}_{\text{pump}} - \mathbf{k}_{\text{sig}} - \mathbf{k}_{\text{idl}} = 0, \quad (2.128)$$

which simplifies for the case of collinearity between the three waves to the same relation in terms of wavenumbers. In addition, the phase difference  $\Delta\phi$  of the slowly varying amplitudes of signal and idler to the pump wave determines whether signal and idler are amplified by a DFG or converted back by an SFG process. Because phase matching concerns the spatial periodicity of the waves in the nonlinear medium, it can be expressed in terms of vacuum wavelengths and dispersive refractive indices

$$\frac{n(\lambda_{\text{pump}})}{\lambda_{\text{pump}}} - \frac{n(\lambda_{\text{sig}})}{\lambda_{\text{sig}}} - \frac{n(\lambda_{\text{idl}})}{\lambda_{\text{idl}}} = 0 \quad (2.129)$$

for the case of three collinear waves. Within their transparency range below resonances, dielectric materials exhibit normal dispersion ( $dn/d\lambda < 0$ ) which prevents fulfilling eq. (2.129) in media that are homogeneous and isotropic [64]. Thus, to achieve phase matching in nonlinear crystals, special techniques are usually applied, exploiting birefringence or a periodic structure of alternating nonlinearity (quasi-phase-matching, QPM; see [64]).

Birefringent phase matching utilizes the polarization-dependent refractive index in anisotropic materials, described in sec. 2.1.2. In uniaxial crystals, there are two methods to achieve

birefringent phase matching [66]: In type I phase matching, the two lower frequency waves have the same polarization direction and the higher frequency wave is orthogonally polarized to them. For DFG in a positive uniaxial crystal, this means an ordinarily polarized pump and extraordinarily polarized signal and idler waves ( $o \rightarrow e + e$ ), and vice versa for a negative uniaxial crystal ( $e \rightarrow o + o$ ). In contrast, Type II phase matching involves two orthogonally polarized lower frequency waves, i.e.  $o \rightarrow e + o$  for DFG in positive crystals and  $e \rightarrow o + e$  in negative ones.

For the case of non-critical phase matching, the waves propagate perpendicular to the optical axis, resulting in phase matching at specific wavelengths determined by the refractive indices of the ordinary and extraordinary axis. Temperature tuning allows for adjusting the generated wavelengths by exploiting the temperature dependence of the refractive index in the nonlinear material [71]. In critical phase matching, propagation is at an angle to the principal crystal axes. This provides the possibility for angle tuning, in which the refractive index of the extraordinary mode is adjusted by tilting the crystal relative to the incident pump beam. The dependency of the refractive index of the extraordinary mode on the angle  $\theta$  between the wave vector and the optical axis is given by eq. (2.42).

Figure 2.12 shows an example for critical type I phase matching in ZGP for DFG. Since ZGP is a positive uniaxial crystal, the linear polarization of the pump is aligned to the ordinary mode in the crystal; thus, its wavenumber  $k_{\text{pump}} = n_o(\lambda_{\text{pump}})/\lambda_{\text{pump}}$  is determined by the ordinary refractive index, depicted by the green curve in fig. 2.12a. The extraordinarily polarized signal and idler experience the refractive index  $n(\lambda_0, \theta)$ , depicted in light blue, depending on their vacuum wavelengths  $\lambda_{\text{sig}}$ ,  $\lambda_{\text{idl}}$  and the angle  $\theta$  according to eq. (2.42). Thus, a pump wave with a given wavelength  $\lambda_{\text{pump}}$  propagating in an angle  $\theta$  to the optical axis, leads to collinear DFG of a specific pair of signal and idler wavelengths that satisfy the phase-matching condition eq. (2.129).

Fig. 2.12b shows the signal and idler wavelengths that achieve phase matching for a pump wavelength of 2050 nm versus the angle  $\theta$ . For a fixed pump wavelength, the signal and idler wavelengths can be tuned by tilting the crystal angle. For example, an angle tilt of  $56.5^\circ$  leads to signal and idler wavelengths of 3665 nm and 4652 nm for a pump wavelength of 2050 nm, indicated by the purple, orange and green markers in fig. 2.12. At the apex ( $\theta \approx 56.85^\circ$ ), signal and idler are degenerate, i.e.  $\lambda_{\text{sig}} = \lambda_{\text{idl}}$ . At this point, the DFG is very sensitive to angle deviations, which can cause a broad output spectrum.

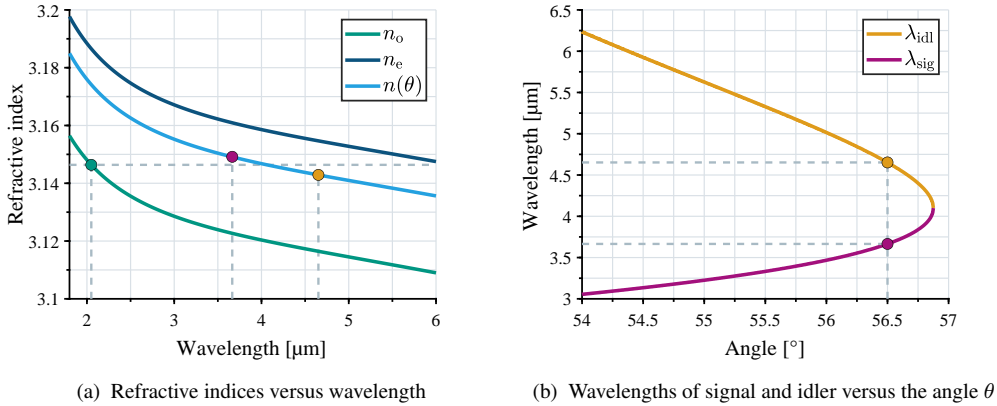


Figure 2.12: Angular type I phase matching in ZGP for collinear propagation. The pump experience the ordinary refractive index  $n_o$  and signal and idler the refractive index  $n(\theta)$  dependent on the angle  $\theta$  between the collinear wave vectors and the optical axis  $Z$ . The markers indicate an example of DFG in which a pump with a wavelength of 2050 nm and an angle of  $56.5^\circ$  to the optical axis generates signal and idler at wavelengths of 3665 nm and 4652 nm. The refractive index data are taken from [72].

Angular phase matching in birefringent crystals offers flexible wavelength tuning within a broad spectral range, but comes with the drawback of spatial walk-off between the Poynting vectors of the ordinary and extraordinary mode described by the angle  $\rho$  according to eq. (2.43). Unlike plane waves, real laser beams possess spatially confined transverse mode and intensity profiles as discussed in sec. 2.1.1. Due to walk-off, the intensity profiles of the ordinary and extraordinary modes lose spatial overlap as they propagate through the birefringent crystal. For parametric amplification by type I phase matching, this reduces the effective pump intensity that couples with the signal and idler beams via the coupling coefficient  $\kappa$  defined by eq. (2.121), leading to a reduced parametric gain along the nonlinear crystal length.

### Third-Order Nonlinear Effects and Optical Kerr Effect

Third-order nonlinear effects rely on the fourth-rank susceptibility tensor  $\chi^{(3)}$  describing the interaction of four waves in a nonlinear material. They occur in non-centrosymmetric as well as centrosymmetric media, including silica glass. Thus, third-order nonlinear effects are the dominant nonlinearities in optical silica fibers. In general, the third-order susceptibility tensor  $\chi^{(3)}$  consists of 81 separate elements  $\chi_{ijkl}^{(3)}$  [64]. However, for isotropic media, such as

Table 2.1: Overview of parametric third-order nonlinear effects

Nonlinear effect	Abbreviation	Involved Frequencies
Third-harmonic generation	THG	$\omega_{m_1} = \omega_{m_2} = \omega_{m_3}$
Self-phase modulation	SPM	$\omega_{m_1} = \omega_{m_2} = -\omega_{m_3}$
Cross-phase modulation	XPM	$\omega_{m_1} \neq \omega_{m_2} = -\omega_{m_3}$
Degenerate four-wave mixing	DFWM	$\omega_{m_1} \neq \omega_{m_2} = \omega_{m_3}$
Four-wave mixing	FWM	$\omega_{m_1} \neq \omega_{m_2} \neq \omega_{m_3}$

amorphous silica, only three of these elements are independent of each other, which can be used to express all tensor elements by the relation

$$\chi_{ijkl}^{(3)} = \chi_{xxyy}^{(3)}\delta_{ij}\delta_{kl} + \chi_{xyxy}^{(3)}\delta_{ik}\delta_{jl} + \chi_{yyyx}^{(3)}\delta_{il}\delta_{jk} \quad (2.130)$$

where  $\delta_{ij}$  denotes the Kronecker delta function [64]. Moreover, for parametric processes within the spectral transparency range of the material that rely on non-resonant electronic response, the three elements can be assumed to be identical, i.e.  $\chi_{xxyy}^{(3)} = \chi_{xyxy}^{(3)} = \chi_{yyyx}^{(3)}$  [64]. This enables the description of parametric third-order nonlinear effects by means of a scalar effective susceptibility

$$\chi_{\text{eff}}^{(3)} = \frac{3}{4}\epsilon_0\chi_{xxxx}^{(3)} = \frac{9}{4}\epsilon_0\chi_{xxyy}^{(3)}. \quad (2.131)$$

According to eq. (2.95), the third-order nonlinear polarization  $\mathbf{P}^{(3)}(t)$  contains the frequency components

$$\omega_p = \omega_{m_1} + \omega_{m_2} + \omega_{m_3} \quad (2.132)$$

that arise from the interaction of three monochromatic waves with the medium. Table 2.1 gives an overview of the parametric third-order nonlinear effects and the relations between the involved frequencies  $\omega_{m_1}$ ,  $\omega_{m_2}$ , and  $\omega_{m_3}$  of the electric field that induce a nonlinear polarization at the frequency  $\omega_p$  according to eq. (2.132) in the material. The nonlinear polarization changes the slowly varying amplitude at a frequency  $\omega_l$  if the phase-matching condition

$$\Delta k = k_{m_1} + k_{m_2} + k_{m_3} - k_l = 0 \quad (2.133)$$

is satisfied as described by the coupled mode equation (2.101).

Third-harmonic generation (THG), degenerate four-wave mixing (DFWM), and four-wave mixing (FWM) lead to the emergence of new frequency components if phase matching is

provided. In contrast, self-phase modulation (SPM) and cross-phase modulation (XPM) are intrinsically phase-matched, because the terms  $\mathbf{E}(\omega_{m_2})\mathbf{E}(\omega_{m_3}) = \mathbf{E}(\omega_{m_2})\mathbf{E}^*(\omega_{m_2})$  imply  $\omega_p = \omega_{m_1}$  and  $k_p = k_{m_1}$ . These effects cause a nonlinear phase shift on the interacting waves, leading to spectral broadening [73]. They can be described by means of an intensity-dependent refractive index, which is known as the optical Kerr effect [51].

Using the definition of  $\chi_{\text{eff}}^{(3)}$  from eq. (2.131) for a parametric interaction within an isotropic medium, the third-order nonlinear polarization  $\mathbf{P}^{(3)}(\omega_p = \omega_{m_1})$  according to eq. (2.95) is given by

$$\mathbf{P}^{(3)}(\omega_{m_1}) = \chi_{\text{eff}}^{(3)} \left( \left[ \mathbf{E}_1 \mathbf{E}_1^* + \frac{2}{3} \mathbf{E}_2 \mathbf{E}_2^* \right] \mathbf{E}_1 + \frac{2}{3} \mathbf{E}_2 \mathbf{E}_1 \mathbf{E}_2^* + \frac{2}{3} \mathbf{E}_2^* \mathbf{E}_1 \mathbf{E}_2 \right) \quad (2.134)$$

where the complex amplitudes  $\mathbf{E}_1 = E(\omega_{m_1})\mathbf{e}_1$  and  $\mathbf{E}_2 = E(\omega_{m_2})\mathbf{e}_2$  of the electric field components oscillating at the frequencies  $\omega_{m_1}$  and  $\omega_{m_2}$  are assumed to be linearly polarized in the direction of the unit vectors  $\mathbf{e}_1$  and  $\mathbf{e}_2$ , respectively. For the case of parallel polarization of all electric field components  $\mathbf{e}_1 = \mathbf{e}_2$ , the complex vector amplitudes can be permuted and the equation simplifies to

$$\mathbf{P}^{(3)}(\omega_{m_1}) = \chi_{\text{eff}}^{(3)} (|E(\omega_{m_1})|^2 + 2|E(\omega_{m_2})|^2) \mathbf{E}_1, \quad (2.135)$$

where the first term proportional to  $|E(\omega_{m_1})|^2$  describes the effect of SPM and the second term proportional to  $2|E(\omega_{m_2})|^2$  describes the effect of XPM.

Considering the total polarization  $\mathbf{P}(\omega_{m_1}) = \mathbf{P}_L(\omega_{m_1}) + \mathbf{P}^{(3)}(\omega_{m_1})$  at the frequency  $\omega_{m_1}$ , the third-order polarization component  $\mathbf{P}^{(3)}(\omega_{m_1})$  can be interpreted to cause a change in refractive index  $\Delta n$ , leading to the relation

$$(n + \Delta n)^2 = 1 + \chi^{(1)} + \frac{\chi_{\text{eff}}^{(3)}}{\epsilon_0} (|E(\omega_{m_1})|^2 + 2|E(\omega_{m_2})|^2). \quad (2.136)$$

Because the effective third-order susceptibility  $\chi_{\text{eff}}^{(3)}$  has a small magnitude typically on the order of  $\sim 1 \cdot 10^{-22} \text{ m}^2 \text{ V}^{-2}$ , the term  $\Delta n^2$  can be neglected [64]. Thus, since the linear refractive index  $n$  is defined by eq. (2.37), the refractive index change  $\Delta n$  caused by SPM and XPM is given by

$$\Delta n = \frac{1}{2\epsilon_0 n} \chi_{\text{eff}}^{(3)} (|E(\omega_{m_1})|^2 + 2|E(\omega_{m_2})|^2). \quad (2.137)$$

Assuming  $n(\omega_{m_1}) \approx n(\omega_{m_2})$ , the total refractive index  $\tilde{n} = n + \Delta n$  can be described in terms of intensities

$$\tilde{n} = n + n_2 (I_1 + 2I_2) \quad (2.138)$$

where  $I_1$  and  $I_2$  are the intensities of the waves oscillating at the frequencies  $\omega_{m_1}$  and  $\omega_{m_2}$ , respectively, and

$$n_2 = \frac{\chi_{\text{eff}}^{(3)}}{c_0 \epsilon_0^2 n^2} \quad (2.139)$$

is the nonlinear Kerr index. For fused silica, the nonlinear index is  $n_2 \approx 2.8 \cdot 10^{-20} \text{ m}^2 \text{ W}^{-1}$  at wavelengths around  $2 \mu\text{m}$  [74]. Eq. (2.138) reveals that the spatial propagation of a wave  $\mathbf{E}(\omega_{m_1})$  is determined by a refractive index  $\tilde{n}$  that is influenced by the intensity  $I_1$  of the wave itself (SPM) and by the intensity  $I_2$  of a wave at a different frequency  $\omega_{m_2} \neq \omega_{m_1}$  (XPM). For the case of parallel polarization and different frequencies, the effect of XPM is twice as large as the effect of SPM.

If the two electric fields are orthogonally polarized, i.e.  $\mathbf{e}_1 \perp \mathbf{e}_2$ , the two latter terms in eq. (2.134) vanish. Assuming two plane wave components with the amplitudes  $E_x$  and  $E_y$  polarized in  $x$  and  $y$  direction, respectively, both propagating in  $z$ -direction and oscillating at the same frequency  $\omega_m$ , the third-order polarization components at this frequency are

$$P_x^{(3)}(\omega_m) = \chi_{\text{eff}}^{(3)} \left( |E_x(\omega_m)|^2 + \frac{2}{3} |E_y(\omega_m)|^2 \right) E_x(\omega_m) \quad (2.140)$$

$$P_y^{(3)}(\omega_m) = \chi_{\text{eff}}^{(3)} \left( |E_y(\omega_m)|^2 + \frac{2}{3} |E_x(\omega_m)|^2 \right) E_y(\omega_m) . \quad (2.141)$$

In this case, the optical Kerr effect leads to anisotropic refractive indices  $\tilde{n}_x$  and  $\tilde{n}_y$  induced by the intensities  $I_x$  and  $I_y$  in the polarization directions  $x$  and  $y$

$$\tilde{n}_x = n + n_2 \left( I_x + \frac{2}{3} I_y \right) \quad (2.142)$$

$$\tilde{n}_y = n + n_2 \left( I_y + \frac{2}{3} I_x \right) . \quad (2.143)$$

This effect is known as nonlinear birefringence. The refractive index for one polarization axis  $n_x$  is modified by the intensity in this polarization direction  $I_x$  as a result of SPM and by the intensity  $I_y$  in the other polarization axis through degenerate XPM. The effect of degenerate

XPM is  $2/3$  times weaker than the effect of SPM. Thus, eqs. (2.142) and (2.143) imply that circular polarized light ( $I_x = I_y$ ) induces a weaker nonlinear index change  $\Delta n = (5/6)n_2I$  than linearly polarized light of the same intensity  $\Delta n = n_2I$ .

The optical Kerr effect affects the propagation of laser beams in nonlinear media in various ways. When propagating over a length  $L$  in the nonlinear medium, SPM and XPM impact the phase evolution

$$\Delta\phi = \frac{2\pi}{\lambda_0}\tilde{n}L = \Delta\phi_L + \Delta\phi_{\text{NL}} \quad (2.144)$$

by a nonlinear phase shift  $\Delta\phi_{\text{NL}} = 2\pi\Delta nL/\lambda_0$  that delays the spatial propagation and induces spectral changes [51]. For ultra-short laser pulses in the time scale of picoseconds to femtoseconds that are significantly shorter than the coherence time of the laser, these spectral changes are due to the change in pulse shape caused by the intensity-dependent phase delay [73]. For laser signals that change significantly slower in intensity than the coherence time, the linewidth is not directly related to the dynamics. In this case, nonlinear phase-modulation degrades temporal coherence, resulting in intensity-dependent spectral broadening [75]. The induced nonlinear birefringence of a laser beam that is not linearly polarized causes a change in its polarization state known as nonlinear polarization rotation [76].

Moreover, the optical Kerr effect also has a spatial impact on the propagation of laser beams. The intensity profile  $I(x, y, z)$  of a laser beam induces a refractive index variation proportional to the intensity distribution in the nonlinear material. For a typical Gaussian beam profile according to eq. (2.29), the modified refractive index profile  $\tilde{n}(x, y, z)$  forms a positive lens that leads to self-focusing of the beam [77]. If the beam reduces in diameter and thereby intensifies via self-focusing, the mechanism reinforces itself, which can result in optical damage to the material.

In addition to these direct effects of the optical Kerr nonlinearity on the properties of a laser beam, several phenomena arise from the interplay between nonlinear refraction and GVD [51]. For the case of anomalous GVD ( $k'' < 0$ ), GVD and SPM counteract each other: While SPM induces an intensity-dependent delay of higher frequency components, anomalous GVD causes higher frequencies to propagate faster than lower frequencies. As a consequence, SPM can provide phase matching in combination with anomalous GVD to enable DFWM [51]. For optical silica fibers, this concerns the spectral range with wavelengths longer than  $\sim 1.3\ \mu\text{m}$  (see fig. 2.5). The occurrence of DFWM in the context of optical fibers is discussed in more detail in sec. 2.3.3.

## Non-Parametric Nonlinear Effects

Non-parametric interactions between an optical wave and a dielectric material involve the exchange of energy between the electromagnetic field and the material. This is associated with electronic transitions or phonon interactions in the material. Due to the causality of the energy transfer from the electromagnetic field to the medium and back again, these interactions proceed not instantaneous and are described by the imaginary part of the electric susceptibility. Non-parametric nonlinear effects are mainly related to the imaginary part of third-order susceptibility  $\chi^{(3)}$ .

In the previous section, the nonlinear refractive index is introduced under the assumption of a real third-order susceptibility by the eqs. (2.138) and (2.139) for optical frequencies far below resonance. To take into account the typically small imaginary part of  $\chi_{\text{eff}}^{(3)}$  for an isotropic material in its transparency range, a nonlinear absorption coefficient  $\alpha_2$  is introduced:

$$\alpha_2(\omega) = \frac{\omega}{c_0 \epsilon_0 n_0} \text{Im}\{\chi_{\text{eff}}^{(3)}\} \quad (2.145)$$

leading to an intensity-dependent attenuation in the material

$$\tilde{\alpha} = \alpha + \alpha_2 |E|^2 \quad (2.146)$$

analogous to the intensity-dependent refractive index [51]. This nonlinear attenuation is associated with the absorption of two photons by the material to excite an electronic state (two-photon absorption) [78].

Nonlinear effects that involve the creation or annihilation of phonons in a material can be described as inelastic scattering processes between photons and phonons [51]. Depending on their energy, a distinction is made between optical and acoustic phonons in the material: Optical phonons correspond to molecular vibrations and exhibit higher frequencies leading to a non-parametric process with significant energy transfer. The interaction of the electromagnetic field with optical phonons is called Raman scattering. In contrast, acoustic phonons describe sound waves propagating through the medium inducing macroscopic refractive index patterns by electrostriction. Because of their low acoustic frequencies, the interaction with acoustic phonons is associated with a much smaller and often negligible energy transfer. This process is termed Brillouin scattering.

The interaction between acoustic and electromagnetic waves is used in acousto-optical modulators (AOMs). Fig. 2.13 illustrates the functional principle of an AOM for the case of Bragg diffraction. An AOM consists of an acousto-optical crystal, such as tellurium dioxide ( $\text{TeO}_2$ ), with an attached piezoelectric transducer driven by an electric signal. The electric signal leads to a periodic expansion of the piezo element with a frequency  $\Omega$ , which induces acoustic pressure waves in the crystal. The induced density variations correspond to a modulation of the refractive index  $\Delta n$  according to the propagating sound wave with frequency  $\Omega$  and wave vector  $\mathbf{q}$ :

$$\Delta n = \Delta n_0 \cos(\Omega t - \mathbf{q}\mathbf{r}) \quad (2.147)$$

where the amplitude  $\Delta n_0$  depends on the photo-elastic tensor elements of the crystal [79].

If a laser beam with an optical frequency  $\omega_s$  and a wave vector  $\mathbf{k}_0$  crosses the crystal, it interacts with the acoustic wave via Brillouin scattering. The coupled mode has a wave vector  $\mathbf{k}_1$  that meets the phase-matching condition

$$\mathbf{k}_1 = \mathbf{k}_0 \pm \mathbf{q} . \quad (2.148)$$

Because the acoustic wavelength  $\Lambda_a = 2\pi/|\mathbf{q}|$  is much longer than the optical wavelength  $\lambda_s = 2\pi/k_0$  of the laser beam, the optical wave vector remains approximately unaffected in its magnitude  $|\mathbf{k}_1| \approx |\mathbf{k}_0|$ , but changes its direction by the interaction with the acoustic phonon. Similarly, the change in the optical frequency of the deflected mode can be neglected, i.e.  $\omega_s \pm \Omega \approx \omega_s$ .

If the interaction length  $L$  of the laser beam with the AOM is sufficiently long, meeting the condition

$$L \tan \theta_B \gg \Lambda_a , \quad (2.149)$$

the beam interacts with a large number of acoustic wave fronts in the form of Bragg scattering [64]. Here, the Bragg angle  $\theta_B$  denotes the incident angle of the beam with respect to the acoustic wave fronts for which the coupled mode  $\mathbf{k}_1$  is deflected at the same angle, corresponding to natural reflection according to Snell's law (2.45). In this case, the phase-matching condition becomes

$$\sin \theta_B = \frac{\lambda_s}{2n\Lambda_a} \quad (2.150)$$

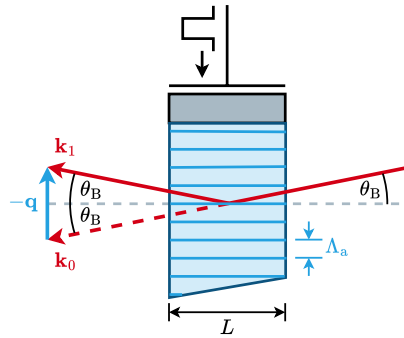


Figure 2.13: Bragg diffraction in an acousto-optic modulator (AOM). A piezoelectric transducer generates an acoustic wave that travels with a wavelength  $\Lambda_a$  through a transparent crystal. The acoustic wave deflects a transmitting laser beam efficiently if the beam is incident with the Bragg angle  $\theta_B$

which is equivalent to the Bragg-condition (2.58) for  $\theta_i = \pi/2 - \theta_B$ . Thus, for this angle of incidence, the scattering with the acoustic wave adds up coherently, resulting in a high deflection efficiency into a beam with a wave vector  $\mathbf{k}_1$ . AOMs that provide Bragg diffraction serve as optical switches for applications like Q-switched lasers (see sec. 2.4.1).

Within optical fibers, intense laser light guided over long interaction lengths can become subject to stimulated phonon-scattering processes. In these processes, an intense pump wave is resonantly coupled into a Stokes wave via spontaneously generated optical or acoustic phonons from the wave itself [51]. Stimulated Brillouin scattering (SBS) with acoustic phonons causes a counter-propagating Stokes wave with small frequency shift. For stimulated Raman scattering (SRS), the interaction with optical phonons generates Stokes waves with a larger frequency shift in co- and counter-propagating direction to the initiating pump wave. These processes are discussed in more detail in sec. 2.3.3.

## 2.2 Principles of Optical Amplification and Oscillation

A laser is an optical oscillator that serves as a source of coherent light. Laser light exhibits the characteristic properties of substantial spatial and spectral confinement that have been introduced in sec. 2.1.1 as a consequence of its coherence. To generate coherent light, an optical oscillator is stimulated at its resonant frequency, resulting in the emission of a coherent wave at this frequency. The essential concept of an optical oscillator is the amplification of light within a resonator that defines the emission properties [41]. In a laser, this amplification is based on the process of stimulated emission described in sec. 2.1.3. Besides lasers, OPOs represent another form of optical oscillators, which utilize the nonlinear parametric amplification discussed in sec. 2.1.4. The following sections will first introduce the general principles of optical oscillators before detailing the specific physics of lasers and OPOs.

### 2.2.1 Fundamentals of Optical Oscillators

An optical oscillator generally consists of a saturable amplifier within a damped feedback loop that forms a resonator. Figure 2.14 shows the principle of this system as a block diagram. The closed control circuit contains four elements that affect the magnitude and phase of an electromagnetic wave. Within one loop pass, a wave undergoes a phase shift of  $\phi$  when propagating through the optical resonator, corresponding to the multiplication of the complex field amplitude by a factor  $e^{j\phi}$ . In addition, an amplifier element provides a wavelength-dependent power gain  $G(\lambda_0)$  and two types of damping elements reduce the circulating power by factors of  $R_{OC}$  and  $R_{HR}(1 - \Lambda)$ , respectively. To provide optical gain, the pump power  $P_{\text{pump}}$  is supplied to the amplifier. The damping element on the right side of the amplifier is the output coupler (OC), which extracts part of the circulating power to obtain the output signal of the oscillator with the power  $P_{\text{out}}$ . The other damping element accounts for the losses in the system, corresponding to a power  $P_{\text{loss}}$ .

The feedback mechanism of an optical resonator is practically realized by arranging multiple mirrors to redirect the light to perform round trips in the resonator. The geometry, dimensions and relative position of the resonator mirrors define a cavity in which only certain resonator modes are able to propagate. These modes have complex amplitudes, which are eigenfunctions of the Helmholtz equation (2.11) under consideration of the resonator geometry as the boundary

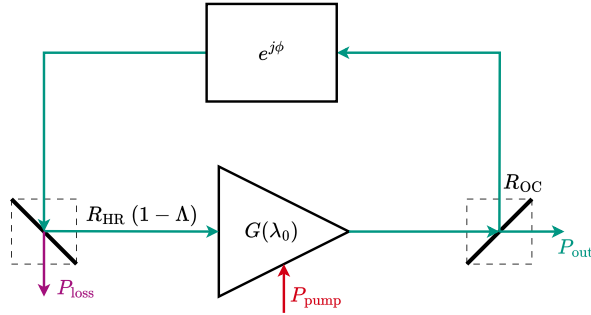


Figure 2.14: Block diagram of an optical oscillator. The oscillator consists of an amplifier, an output coupler, and resonator losses within a positive feedback loop accompanied by a phase shift.

condition and therefore represent field distributions that reproduce themselves when they undergo feedback.

In the simplest case of a Fabry-Pérot resonator, the cavity is formed by two opposing plane-parallel mirrors that reflect the propagating light back and forth. One of the mirrors is usually partially reflective with a reflectivity  $R_{OC}$  to act as the OC, decoupling an amount of  $T_{OC} = 1 - R_{OC}$  of the power within the resonator per round trip. The opposite mirror usually has a high reflectivity  $R_{HR} \approx 1$  and is called the high reflector (HR). This resonator confines the propagating field in one spatial dimension  $z$ , forming a linear cavity within the distance  $L$  between the mirrors. A monochromatic wave having a wavenumber  $k$  undergoes a phase shift of  $\phi = k2L$  when propagating one round trip along the longitudinal axis  $z$  of the resonator. Because the circulating wave interferes with itself after each round trip, the resonator only preserves the modes that reproduce during feedback, which requires a phase shift by a multiple of  $2\pi$  per cycle. Thus, the eigenmodes of a linear resonator are given by the wavenumbers [40]

$$k = m \frac{\pi}{L}, \quad m = 1, 2, 3, \dots \quad (2.151)$$

Note that in an oscillator containing an optical amplifier and mirrors, amplification and reflection also induce phase shifts that contribute to the total phase shift per round trip determining the eigenmodes [41].

For linear propagation within a lossless and gainless resonator that is filled with a homogeneous medium characterized by a constant refractive index  $n$ , the modes have discrete frequencies which are periodically spaced in the free spectral range (FSR)

$$\Delta f_{\text{FSR}} = \frac{c_0}{2nL} = \frac{1}{\tau_{\text{rt}}}, \quad (2.152)$$

which is reciprocal to the round trip time  $\tau_{\text{rt}}$  of the light in the cavity [40]. Real resonators are damped by their intended out-coupling as well as by losses due to imperfect mirror reflectivities, scattering and absorption in the cavity filling medium, and diffraction [40]. This results in a decay of the energy stored in the resonator, described by the photon lifetime  $\tau_c$ . For the resonator system shown in fig. 2.14, the photon lifetime is given by

$$\tau_c = -\frac{\tau_{\text{rt}}}{\ln(R_{\text{OC}}R_{\text{HR}}(1 - \Lambda))} \quad (2.153)$$

where all losses apart from the mirror reflectivities  $R_{\text{OC}}$  and  $R_{\text{HR}}$  are incorporated into the term  $\Lambda$  [42]. At one of its resonance frequencies  $f_0 = m\Delta f_{\text{FSR}}$  with  $m \in \mathbb{N}^*$ , the resonator can be characterized by its quality factor (Q-factor) [40]

$$Q = 2\pi \frac{\text{stored energy}}{\text{energy loss per period}} = 2\pi f_0 \tau_c. \quad (2.154)$$

The Q-factor accounts for the damping in the resonator, whereby a high Q-factor corresponds to weak damping.

To obtain an oscillating system, the damping is counteracted by the gain of the amplifier within the feedback loop. For the system depicted in fig. 2.14, the net round-trip gain is

$$G_{\text{rt}} = G(\lambda_0)R_{\text{OC}}R_{\text{HR}}(1 - \Lambda). \quad (2.155)$$

In steady-state operation of the oscillator, the gain exactly compensates for the resonator losses ( $G_{\text{rt}} = 1$ ), resulting in a constant power within the resonator and a constant output power  $P_{\text{out}}$ . Figure 2.15 shows the normalized spectral power density  $S_N/S_0$  after 2, 5, and 15 resonator round trips  $N$ . The spectrum shows an interference pattern resulting from the phase-shifted feedback of the waves at frequencies  $f$ . As the number of round trips increases, the interference peaks at the resonance frequencies  $m\Delta f_{\text{FSR}}$  increase in height and narrow in width. The coherence time over which a wave can interfere with itself by circulating through the resonator is given by the cavity lifetime of the photons  $\tau_c$ . Thus, an optical signal can effectively perform  $N_{\text{eff}} = \tau_c/\tau_{\text{rt}}$  round trips, which determines the sharpness of the longitudinal resonator modes as illustrated in fig. 2.15. The spectral 3-dB width (FWHM) of the longitudinal

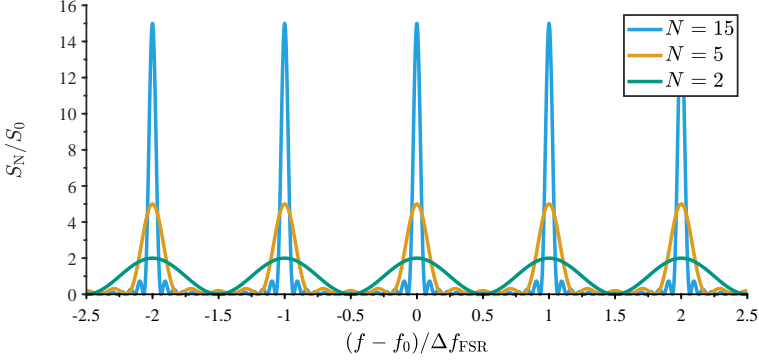


Figure 2.15: Normalized spectral power density of a steady state oscillator ( $G_{\text{rt}} = 1$ ) after  $N$  round trips.

resonator modes  $\Delta f_c$  is hence connected with the photon lifetime and the Q-factor by the relation [40]

$$\Delta f_c = \frac{f_0}{Q} = \frac{1}{2\pi\tau_c} \quad (3\text{-dB width}). \quad (2.156)$$

For a lossless resonator ( $Q \rightarrow \infty \Leftrightarrow \tau_c \rightarrow \infty \Leftrightarrow N_{\text{eff}} \rightarrow \infty$ ), the longitudinal modes become a series of delta functions  $\delta(f - m\Delta f_{\text{FSR}})$ .

The finite diameter of the resonator mirrors constrains the resonator modes to propagate mainly along the longitudinal z-axis in the resonator, as deviating propagation directions escape the resonator and are therefore not preserved. This justifies the paraxial approximation to derive the transverse modes of the one-dimensional resonator from the paraxial wave equation (2.16). The solutions are the Gaussian modes described in sec. 2.1.1. Because Gaussian modes of different order exhibit different beam parameter products according to eq. (2.26), they experience different diffraction losses in the resonator. This can be utilized for transversal mode selection by the resonator design [41, 80]. To adapt the resonator to low diffraction losses for the fundamental Gaussian mode (see eq. (2.17)), curved mirrors that match the radius of curvature of the wave fronts according to eq. (2.20) are beneficial. Due to the Gouy phase shift, the different transverse modes also differ slightly in their resonance frequencies [40].

To generate a signal from the optical oscillator, the round-trip gain must be  $G_{\text{rt}} > 1$  to build up a field in the resonator starting from vacuum fluctuations. For  $G_{\text{rt}} < 1$  the resonator field is not preserved and decays over time, preventing a continuous oscillation. Thus, to enable an oscillation, the amplifier must exceed the threshold gain  $G_{\text{th}}$  to compensate the resonator losses

and ensure  $G_{\text{rt}} \geq 1$  [41]. Considering eq. (2.155) for the system from fig. 2.14, the threshold gain is given by:

$$G_{\text{th}} = \frac{1}{R_{\text{OC}}R_{\text{HR}}(1 - \Lambda)}. \quad (2.157)$$

The unsaturated small-signal gain  $G_{\text{ss}}$  of the amplifier, given by the eqs. (2.90) and (2.125) for laser and parametric amplifiers, respectively, can exceed the threshold gain  $G_{\text{th}}$  by supplying sufficient pump power higher than the corresponding threshold pump power  $P_{\text{th}}$ . Exceeding the threshold results in effective amplification of the initial noise in the cavity and a growing resonator field defined by the resonator modes. Part of this field is extracted by the OC as the output signal. The optical amplifier thereby converts the supplied pump power into signal power within the resonator modes. As the resonator field grows, it reaches a power level where the pump power is no longer sufficient to provide the small-signal gain, resulting in gain saturation of the amplifier [81]. This reduces the gain of the amplifier compared to the small-signal gain, until the oscillator reaches a steady state, which eventually clamps the gain to the threshold level  $G_{\text{th}}$ . An important quantity to characterize gain saturation is the saturation power  $P_{\text{sat}}$  (or the corresponding saturation intensity  $I_{\text{sat}}$ ), defined as the power (intensity) within the resonator for which the gain coefficient of the amplifier  $g = \ln G/L$  drops to half of the small-signal gain coefficient  $g_{\text{ss}} = \ln G_{\text{ss}}/L$  [40].

Figure 2.16 shows the characteristic curves of the output power  $P_{\text{out}}$  and the gain coefficient  $g$  versus the pump power  $P_{\text{pump}}$  for steady-state operation of an optical oscillator. Two characteristic regions below and above the oscillation threshold can be distinguished. Below the threshold, no stationary field can be preserved in the resonator, resulting in an output power  $P_{\text{out}} \approx 0$ . In this region, the gain increases with the pump power, depending on the efficiency of the amplifier pump process. For a pump power  $P_{\text{pump}} = P_{\text{th}}$ , the amplifier provides the threshold gain  $G_{\text{th}} = e^{g_{\text{th}}L}$  that enables steady state oscillation. Above the threshold, an increase in pump power leads to a linear increase in output power that constantly saturates the gain to the threshold level. The characteristic power curve is given by

$$P_{\text{out}} = \eta_s(P_{\text{pump}} - P_{\text{th}}) \quad (2.158)$$

where  $\eta_s = dP_{\text{out}}/dP_{\text{pump}}$  is the slope efficiency, which includes the efficiency of the amplifier and the outcoupling efficiency of the resonator. The resonator outcoupling efficiency  $\eta_R$  results from the ratio of the outcoupling rate to the total cavity photon decay rate including losses,

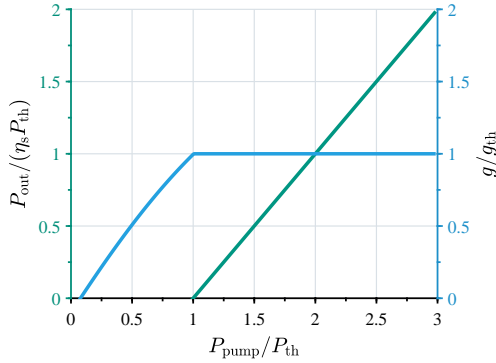


Figure 2.16: Output power and gain coefficient characteristics of an optical oscillator in steady state. Below the oscillator threshold, the output power is zero and the gain increases with the pump power. Above the threshold, the output power increases linearly with the slope efficiency  $\eta_s$  and the gain coefficient is clamped at the threshold level  $g_{\text{th}} = \ln G_{\text{th}}/L$ .

which yields

$$\eta_R = \frac{\ln(R_{\text{OC}})}{\ln(R_{\text{OC}}R_{\text{HR}}(1 - \Lambda))}. \quad (2.159)$$

The efficiencies of the amplification processes for lasers and OPOs are discussed in the following sections, respectively.

A sudden change in pump power or in the properties of the resonator causes the oscillator to react dynamically to transition into a new state of equilibrium. As the amplification processes are generally very fast, the inertia and hence the stability of the oscillator is mainly defined by the Q-factor of the resonator given by eq. (2.154). The resonator acts as a low pass. A high Q-factor corresponds to a highly inert field in the resonator, and hence an inert oscillator output. Thus, a high-Q oscillator remains stable against noise, but also reacts with stronger overshoot to significant operation changes.

The stability of the oscillator also determines the linewidth of the output signal. The finite spectral width of the resonator modes  $\Delta f_c$  depending on the Q-factor according to eq. (2.156), leads to phase fluctuations in the generated output signal with a temporal uncertainty  $\Delta t_c$ . In an ideal case without technical noise, the relationship between bandwidth and time is Fourier limited, resulting in the minimum Schawlow-Townes linewidth [82]

$$\Delta f_L \geq \frac{2\pi h f \Delta f_c^2}{P_{\text{out}}}. \quad (2.160)$$

In real oscillator systems that suffer from technical noise, for example by mechanical vibrations that lead to fluctuations in the resonance frequencies, the linewidth is further broadened, but still related to the reciprocal of the Q-factor [83]. The low-pass filter characteristic of the resonator thereby determines the noise transfer function.

## 2.2.2 Laser Amplifiers and Oscillators

The acronym *laser* stands for *light amplification by stimulated emission of radiation*. As described in section 2.1.3, stimulated emission is one of the three fundamental interactions of light and matter that causes an optical transition from an excited to a lower state by releasing a coherent photon. The optical gain that results from stimulated emission and the counteracting process of absorption is described by eq. (2.90). It depends on the spectroscopic emission and absorption cross-sections  $\sigma_e$  and  $\sigma_a$  resulting from the energy levels of the material and the population densities in these levels. An active solid-state laser medium with specific absorption and emission characteristics is obtained by doping a host material with active ions that introduce the energy levels for the laser transition. To achieve amplification in the active medium, an optical gain  $G(\lambda_s) > 1$  at the signal wavelength  $\lambda_s$  is required, which demands the rate of stimulated emission to be higher than the rate of absorption:

$$\sigma_e(\lambda_s)N_2 > \sigma_a(\lambda_s)N_1 \quad \Leftrightarrow \quad N_2 > \frac{\sigma_a(\lambda_s)}{\sigma_e(\lambda_s)}N_1, \quad (2.161)$$

which implies a population distribution between the upper and lower laser level according to the latter expression known as *effective population inversion* [42]. Because this condition cannot be fulfilled in thermal equilibrium, the active medium must be pumped to obtain amplification [42]. To realize a laser oscillator, a pumped active medium is placed in a resonator.

### Quasi-Three-Level Laser Amplification

Stationary laser amplification requires permanent preservation of population inversion through continuous pumping. For optical pumping, population inversion is built up by absorption of the pump radiation in the active medium. This means that continuous laser operation requires an energy level configuration in the active medium, which simultaneously provides permanent

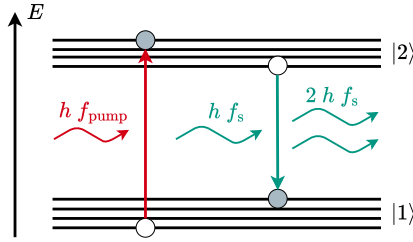


Figure 2.17: Laser operation in a quasi-three-level scheme.

absorption  $G(\lambda_{\text{pump}}) < 1$  at the pump wavelength  $\lambda_{\text{pump}}$  and permanent amplification  $G(\lambda_s) > 1$  at the signal wavelength  $\lambda_s$ . A two-level system does not allow continuous laser operation because a steady state  $dN_2/dt = -dN_1/dt = 0$  implies an equilibrium between absorption and emission processes for constant irradiation (see eq. (2.77)), meaning  $G \leq 1$ . Thus, continuous laser operation requires at least three involved energy levels (three-level laser)—or more efficient four involved energy levels (four-level laser)—to separate the pump and signal transitions [41, 42]. In rare-earth-doped solids, the optical transitions occur between manifolds that consist of closely spaced Stark levels. Such an energy level scheme represents an intermediate form between three- and four-level lasers: a quasi-three-level laser.

Figure 2.17 shows the operation principle of a quasi-three-level laser that involves two manifolds  $|1\rangle$  and  $|2\rangle$ . The laser signal is generated by stimulated emission at a frequency  $f_s = c_0/\lambda_s$  and the pump light is supplied at a higher frequency  $f_{\text{pump}}$  (shorter wavelength  $\lambda_{\text{pump}}$ ) to build up inversion. In steady-state operation, the excitement rate of the higher manifold balances the recombination rate into the lower manifold, resulting in a constant population of the manifolds, i.e.,  $dN_2/dt = dN_1/dt = 0$ . Within the manifolds, fast phonon interactions lead to a thermal population distribution, resulting in emission and absorption cross-sections according to the McCumber relation (2.86). Thus, in contrast to a two-level system, the spectroscopic cross-sections of absorption and emission are spectrally shifted relative to each other. This allows the medium to be pumped efficiently at the pump wavelength  $\lambda_p$  while simultaneously providing net gain at the signal wavelength  $\lambda_s$ , which enables continuous laser operation.

Instead of dealing with individual population densities  $N_1$  and  $N_2$  of the manifolds, the population difference can be considered by the single quantity of inversion  $\Delta N = N_2 - N_1$ . The total density of states, i.e. the local doping concentration, is given by  $N = N_2 + N_1$ . In

general, the inversion  $\Delta N$  and the total density of states  $N$  vary spatially throughout the active medium. However, if pump and signal are assumed to propagate collinearly along the  $z$  axis through the medium, it is often convenient to consider the axial averages  $\langle \Delta N \rangle$  and  $\langle N \rangle$  defined by

$$\langle \cdot \rangle = \frac{1}{L} \int_0^L \cdot dz, \quad (2.162)$$

where  $L$  is the length of the active medium in the direction  $z$ . Using these definitions the optical gain according to eq. (2.90) along the active medium can be rewritten to [42]

$$G(\lambda_0) = \exp \left( \frac{1}{2} \Gamma L ([\sigma_a(\lambda_0) + \sigma_e(\lambda_0)] \langle \Delta N \rangle - [\sigma_a(\lambda_0) - \sigma_e(\lambda_0)] \langle N \rangle) \right). \quad (2.163)$$

Here  $\Gamma$  is the overlap factor of the transverse intensity profile of the signal or the pump with the doping distribution, given by the overlap integral in a cylindrical coordinate system

$$\Gamma(z) = 2\pi \int_0^\infty \frac{I(r, z)}{P(z)} \frac{n(r)}{\langle N \rangle} r dr, \quad (2.164)$$

where a radial symmetric intensity profile  $I(r, z)$  with a power  $P(z)$  and a radial symmetric doping profile  $n(r)$  with a constant average density  $\langle N \rangle$  is assumed [53]. The overlap factor is important, in particular, for fiber lasers, where the intensity profile is larger than the actively doped core area. Otherwise, it is  $\Gamma = 1$ .

The optical gains  $G(\lambda_{\text{pump}})$  for the pump and  $G(\lambda_s)$  for the signal depend on the same population inversion  $\langle \Delta N \rangle$ , which is built up by absorption and depleted by stimulated emission and spontaneous decay. Supplied pump light is absorbed with the pump absorption efficiency

$$\eta_{\text{abs}} = 1 - G(\lambda_{\text{pump}}) \quad (2.165)$$

along the amplifier. In a quasi-three-level laser, the pump absorption is reduced by reemission  $\sigma_e(\lambda_{\text{pump}})N_1 = \sigma_e(\lambda_{\text{pump}})(N + \Delta N)/2$  at the pump wavelength, which increases with the build-up of inversion. Without depletion by a signal, the change in inversion by pump absorption and spontaneous decay is given by the small-signal rate equation

$$\frac{d \langle \Delta N \rangle_{\text{ss}}}{dt} = 2 \frac{\lambda_{\text{pump}}}{hc_0} \frac{P_{\text{pump}}}{V} \eta_{\text{abs}} \eta_{\text{q}} - \frac{\langle \Delta N \rangle_{\text{ss}} + \langle N \rangle}{\tau}, \quad (2.166)$$

where  $\langle \Delta N \rangle_{ss}$  is the small-signal inversion,  $V$  is the volume of the active medium that is excited by the pump and  $\eta_q$  is the quantum yield.

The quantum yield considers the number of state excitations into the lasing level per pump photon, taking into account radiative and non-radiative energy transfer processes with other levels. Such energy transfer processes can cause a reduction in efficiency ( $n_q < 1$ ) by quenching the inversion, but also an improvement in efficiency ( $n_q > 1$ ) by assisting excitations of the laser level [84, 85]. The energy transfer processes in  $\text{Tm}^{3+}$ -doped silica are discussed in sec. 2.3.1.

In steady state  $d\langle \Delta N \rangle_{ss}/dt = 0$ , the pump rate is in equilibrium with the spontaneous decay leading to a constant small-signal inversion  $\langle \Delta N \rangle_{ss}$ . Inserting  $\langle \Delta N \rangle_{ss}$  in eq. (2.163) yields the small-signal gain  $G_{ss}(\lambda_s)$ .

An input signal with a power  $P_{in}$  is amplified by stimulated emission in the pumped amplifier to an output power  $P_{out} = G(\lambda_s)P_{in}$ . In a quasi-three-level laser, the gain by stimulated emission is reduced by reabsorption  $\sigma_a(\lambda_s)N_1 = \sigma_e(\lambda_s)(N - \Delta N)/2$ , which becomes higher the lower the inversion is. The optical gain  $G(\lambda_s)$  an input signal experiences in the amplifier is reduced compared to the small-signal gain  $G_{ss}$ , because the stimulated emission depletes the inversion  $\langle \Delta N \rangle$  compared to the small-signal inversion  $\langle \Delta N \rangle_{ss}$ . This effect, known as gain saturation, decreases the local gain coefficient by the relation

$$g(z) = \frac{g_{ss}}{1 + \frac{P_s(z)}{P_{sat}}} \quad (2.167)$$

where the saturation power  $P_{sat}$  defines the signal power  $P_s(z)$  for which the gain coefficient  $g(z)$  drops to half of its small-signal value [40]. Integrating the relation  $dP/dz = g(z)P$  along the amplifier length  $L$  yields the total extracted power  $P_{ext} = P(L) - P(0)$  by an input signal  $P_{in} = P(0)$ :

$$P_{ext} = P_{sat}(\ln G_{ss} - \ln G) . \quad (2.168)$$

Thus, the saturation power  $P_{sat}$  connects the stored and hence extractable energy in a laser amplifier to the gain [41]. Extraction of the saturation power leads to a reduction in gain by a factor  $1/e$ . With the saturation power

$$P_{sat} = \frac{hc_0}{\lambda_s} \frac{A}{\Gamma_s \tau [\sigma_a(\lambda_s) + \sigma_e(\lambda_s)]} \quad (2.169)$$

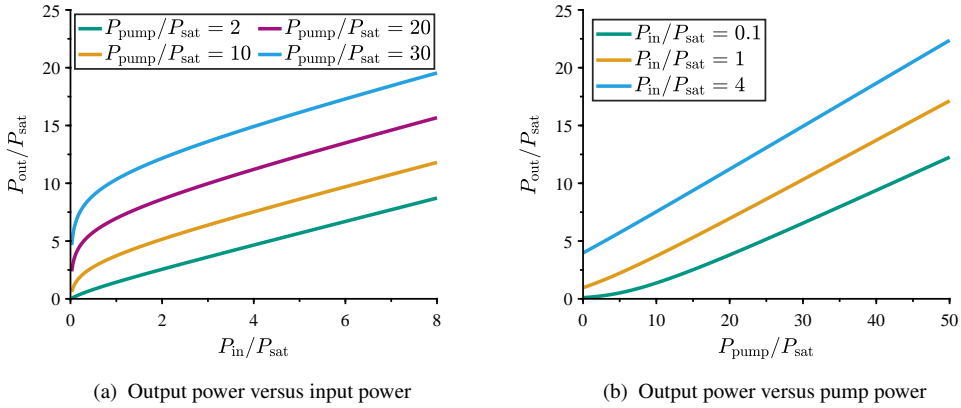


Figure 2.18: Characteristic curves of a laser amplifier. For input powers larger than the saturation power  $P_{\text{sat}}$  the amplifier saturates, resulting in a linear output power characteristic.

including the excited doped area  $A$  and the overlap factor  $\Gamma_s$  of the signal, the amplifier output power  $P_{\text{out}}$  is derived using eqs. (2.163), (2.166) and (2.168):

$$P_{\text{out}} = G(\lambda_s)P_{\text{in}} = P_{\text{in}} + \frac{\lambda_p}{\lambda_s}\eta_{\text{abs}}\eta_q P_{\text{pump}} - \frac{hc_0}{\lambda_s}L \frac{\langle \Delta N \rangle + \langle N \rangle}{2\tau}. \quad (2.170)$$

Because  $\langle \Delta N \rangle$  is included in  $G(\lambda_s)$ ,  $\eta_{\text{abs}}$ , and the spontaneous decay rate in the last term, this represents a transcendental equation that can be solved numerically to obtain the inversion, the gain, and the output power for a given pump and input power.

Figure 2.18 shows the characteristic power curves of a laser amplifier obtained from eq. (2.170). The input, output, and pump power are normalized by the saturation power, respectively. In figure 2.18a, the output power is plotted versus the input power for different pump powers. For small pump powers, e.g.  $P_{\text{pump}}/P_{\text{sat}} = 2$  (green curve), the output power corresponds approximately to the input power, as the amplifier provides no net gain. For higher pump powers, the curves exhibit an unsaturated and a saturated section: At input powers below the saturation power the energy extraction is low, resulting in a weak but rapidly increasing gain. Once the input power exceeds the saturation power, the curves continue with a saturated linear characteristic between input and output power.

Figure 2.18b depicts the output power characteristics versus the pump power for three constant input powers. For input powers at around the saturation power and below (orange and green

curves), the output power characteristics exhibit a flat course at the beginning where the energy extraction is low. In contrast, input powers significantly above the saturation power (blue curve) attain nearly linear amplification right from the beginning. For larger pump powers, the power extraction saturates the gain in all three cases, resulting in a nearly linear increase in gain and output power proportional to the supplied pump power. In this region, the increase in output power is mainly determined by the pump rate, leading to a slope efficiency of

$$\eta_s = \frac{dP_{\text{out}}}{dP_{\text{pump}}} \approx \eta_{\text{abs}}\eta_Q \quad (2.171)$$

where

$$\eta_Q = \eta_q \lambda_{\text{pump}} / \lambda_s \quad (2.172)$$

is the quantum efficiency consisting of the quantum yield  $n_q$  and the Stokes efficiency  $\lambda_p / \lambda_s$ .

Because the gain and hence the inversion increase with the pump power, the absorption efficiency is reduced, resulting in a deviation from a linear slope. Thus, high pump powers can lead to pump saturation when the inversion approaches the bleaching level

$$\langle \Delta N \rangle_{\text{bleach}} = \frac{\sigma_a(\lambda_{\text{pump}}) - \sigma_e(\lambda_{\text{pump}})}{\sigma_a(\lambda_{\text{pump}}) + \sigma_e(\lambda_{\text{pump}})} \langle N \rangle \quad (2.173)$$

where the amplifier becomes transparent for additional pump power. This limits the achievable gain and flattens the output power curve. The deviation from a linear slope efficiency by pump saturation can be avoided by using high doping concentrations and a long amplifier length that provides high gain at low inversion.

Local inversion  $\Delta N(z)$ , signal power  $P_s(z)$ , and pump power  $P_{\text{pump}}(z)$  can vary substantially along the amplifier length. Thus, accurate numerical modeling requires dividing the amplifier into length segments. Furthermore, to describe amplifiers with high gain, such as fiber amplifiers, amplified spontaneous emission (ASE) must be considered [53]. ASE represents a broadband signal according to the fluorescence spectrum that travels in the forward and backward directions through the amplifier. It causes additional losses and inversion depletion proportional to the amplifier gain. The propagation equation for the ASE power in one direction is

$$\frac{dP_{\text{ASE}}(\lambda_0)}{dz} = g(\lambda_0)P_{\text{ASE}}(\lambda_0) + \Gamma_s \sigma_e(\lambda_0) \frac{\Delta N + N}{2} P_{\text{noise}}^0(\lambda_0) \quad (2.174)$$

with the source term of noise per bandwidth  $\Delta\lambda_0$

$$P_{\text{noise}}^0 = M_f \frac{hc^2}{\lambda_0^3} \Delta\lambda_0, \quad (2.175)$$

where  $M_f$  is the number of modes in the amplifier [53].

## Laser Oscillators

A laser oscillator is realized by placing an amplifying laser medium into an optical resonator. Pumping the active medium leads to an increase of the amplifier small-signal gain until the laser threshold is reached, which enables the build-up of a coherent laser field in the cavity initiated from spontaneous emission. For a linear cavity consisting of two opposing mirrors, the laser signal passes the amplifier two times per round trip in forward and backward direction. Thus, the optical gain per round trip is  $G^2(\lambda_s)$ , leading to a single-pass threshold gain of

$$G_{\text{th}} = \frac{1}{\sqrt{R_{\text{OC}}R_{\text{HR}}(1-\Lambda)}}. \quad (2.176)$$

To provide the threshold gain  $G_{\text{th}}$ , a corresponding threshold inversion  $\langle\Delta N\rangle_{\text{th}}$  must be available in the laser amplifier, which is yielded from the optical gain equation (2.163) to be

$$\langle\Delta N\rangle_{\text{th}} = \frac{2 \ln G_{\text{th}}}{[\sigma_a(\lambda_s) + \sigma_e(\lambda_s)]\Gamma_s L} + \frac{\sigma_a(\lambda_s) - \sigma_e(\lambda_s)}{\sigma_a(\lambda_s) + \sigma_e(\lambda_s)} \langle N \rangle. \quad (2.177)$$

The accumulation of the threshold inversion  $\langle\Delta N\rangle_{\text{th}}$  within the active medium requires the supply of the threshold pump power  $P_{\text{th}}$ . Inserting eq. (2.177) into the amplifier equation (2.170) and solving for the pump power  $P_{\text{pump}}$  for  $P_{\text{in}} = P_{\text{out}} = 0$  yields the optical pump threshold of a quasi-three-level laser oscillator:

$$P_{\text{th}} = \frac{P_{\text{sat}}}{\eta_Q \eta_{\text{abs}}} (\ln G_{\text{th}} + \sigma_a(\lambda_s) \langle N \rangle L). \quad (2.178)$$

By supplying the threshold pump power into the active medium, the laser starts oscillating, enabling the generation of a laser signal according to the resonator modes. As described in sec. 2.2.1, the resonator field emerging above the oscillation threshold saturates the gain to the threshold level  $G_{\text{th}}$  in steady-state operation. Consequently, the axial average of the population inversion  $\langle\Delta N\rangle$  in a laser operated above threshold is clamped to the threshold

level  $\langle \Delta N \rangle_{\text{th}}$  by stimulated emission. Thus, the supplied pump power above the threshold  $P_{\text{th}}$  is converted into laser output power according to eq. (2.158), with a constant slope efficiency

$$\eta_s = \frac{dP_{\text{out}}}{dP_{\text{pump}}} = \eta_R \eta_Q \eta_{\text{abs}} \quad (2.179)$$

that is composed of the resonator efficiency  $\eta_R$  (see eq. (2.159)) and the efficiency of the laser amplifier (see eq. (2.171)) for a constant inversion  $\langle \Delta N \rangle_{\text{th}}$ . The steady-state operation of a laser above threshold is termed continuous-wave (CW) operation.

The output spectrum of a laser oscillator is determined by the longitudinal resonator modes and the optical gain spectrum of the active medium depending on the spectroscopic cross-sections and the population inversion. For an ideally homogeneous medium, the spectral amplification by the state ensemble can be described by one homogeneously broadened gain spectrum. As illustrated in figure 2.19, the longitudinal modes that are preserved in the resonator experience different amplification according to this gain spectrum. Thus, the mode that first reaches the threshold gain  $G_{\text{th}}$  saturates the gain in the laser oscillator, which prevents other modes from reaching the threshold.

However, lasers usually still oscillate at multiple longitudinal modes due to the mechanisms of spatial and spectral hole burning [42]. Spatial hole burning results from the standing-wave character of the longitudinal modes in a linear resonator. Because these standing waves exhibit locally static maxima and minima in their intensity, other standing waves can co-exist by achieving gain at the unsaturated minima regions. Spectral hole burning occurs in inhomogeneously broadened gain media, where the individual active states are decoupled from each other and exhibit slightly different gain spectra. Thus, an oscillating mode does not saturate the entire inhomogeneously broadened gain spectrum, because it affects only a subset of the excited states. The mode locally "burns a hole" in the gain spectrum. Excited states with different gain spectra can independently amplify other modes. To achieve laser emission with a narrow linewidth, wavelength-selective elements are introduced in the resonator that constrain the oscillating longitudinal modes to a narrow bandwidth. A common method is the use of Bragg gratings (see sec. 2.1.2) as resonator mirrors.

The population inversion and the laser field control each other in the laser oscillator to achieve equilibrium in a steady state. Changes in the pump power or the resonator characteristics that affect the Q-factor (see eq. (2.154)) cause a transition to a new equilibrium state, which is accompanied by dynamics in population inversion and laser power. The laser dynamics are

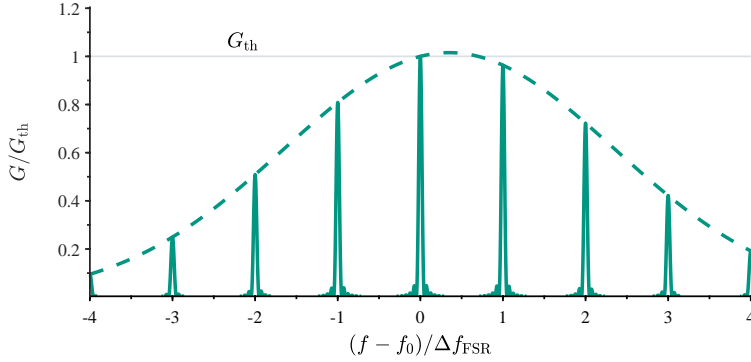


Figure 2.19: Gain spectrum of the longitudinal modes for an ideal homogeneous laser medium. The mode that first reaches the threshold gain  $G_{\text{th}}$  saturates the gain.

given by the rate equations of inversion  $\Delta N$  and intensity  $I_s$  in the oscillator. According to [42], they are:

$$\begin{aligned} \frac{d \langle \Delta N \rangle}{dt} = & 2 \frac{\lambda_{\text{pump}} P_{\text{pump}}}{h c_0 V} \eta_{\text{abs}} \eta_{\text{q}} - \frac{\langle \Delta N \rangle + \langle N \rangle}{\tau} \\ & + \Gamma_s \frac{\lambda_s}{h c_0} ([\sigma_a(\lambda_s) - \sigma_e(\lambda_s)] \langle I_s N \rangle - [\sigma_a(\lambda_s) + \sigma_e(\lambda_s)] \langle I_s \Delta N \rangle) \end{aligned} \quad (2.180)$$

$$\frac{d \langle I_s \rangle}{dt} = \Gamma_s \frac{c_0}{2n} ([\sigma_a(\lambda_s) + \sigma_e(\lambda_s)] \langle I_s \Delta N \rangle - [\sigma_a(\lambda_s) - \sigma_e(\lambda_s)] \langle I_s N \rangle) - \frac{\langle I_s \rangle}{\tau_c} \quad (2.181)$$

where the axial averages  $\langle \Delta N \rangle$  and  $\langle I_s \rangle$  along the resonator length are considered. The laser rate equations form a set of coupled differential equations that generally cannot be solved analytically. The first equation describes the change in inversion, accounting for the pump rate, spontaneous decay, and depletion via stimulated emission. The second rate equation relates the intensity change to the gain by stimulated emission and losses characterized by the cavity lifetime  $\tau_c$ .

For most solid-state and fiber lasers the inversion recovery time given by the pump rate and the lifetime  $\tau$  of the laser level is much longer than the cavity lifetime  $\tau_c$  determining the inertia of the laser field. Thus, perturbations from the steady state result in an oscillation behavior of inversion and laser power [41].

For small perturbations from the steady state, the dynamics of inversion and laser power can be described by relaxation oscillations that result from the approximation of linearized rate

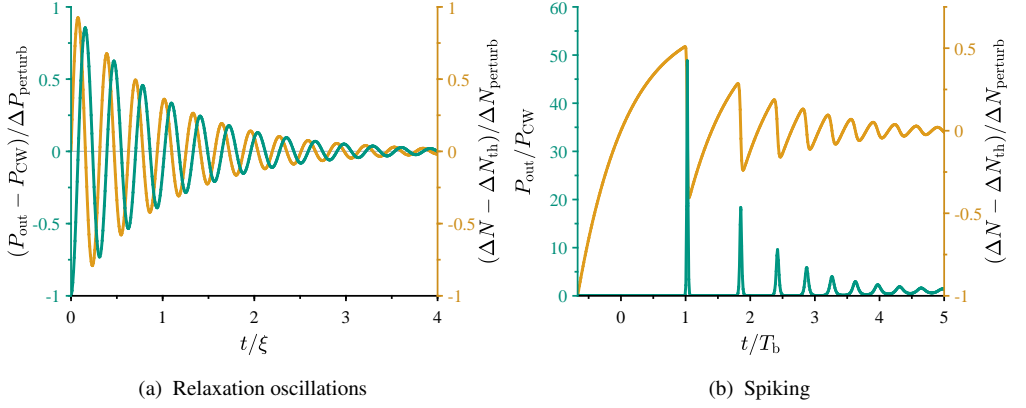


Figure 2.20: Dynamics of a laser oscillator. Small perturbations to the steady state lead to relaxation oscillations, while a large perturbation results in spiking characterized by large anharmonic overshooting in power and inversion above the steady state.

equations [41, 42]. In this case, inversion and laser power respond with a transient behavior similar to that of a damped harmonic oscillator to approach the new steady state characterized by the CW output power  $P_{\text{CW}}$  and the threshold inversion  $\Delta N_{\text{th}}$ . Figure 2.20a shows the relaxation oscillations of the output power  $P_{\text{out}}$  and the inversion  $\Delta N$  for a small increase in pump power. For this case, the induced laser dynamic settles into a new steady state characterized by a slightly higher output power, while the inversion returns to its clamped threshold value  $\Delta N_{\text{th}}$ . The oscillations of inversion and power exhibit a phase shift of about  $\pi/2$  as they react to each other. The initial amplitudes of the perturbations  $\Delta P_{\text{perturb}}$  and  $\Delta N_{\text{perturb}}$  from the new steady state  $P_{\text{CW}}$  and  $\Delta N_{\text{th}}$  undergo exponential damping  $e^{\xi t}$  over time  $t$  with the temporal damping constant [42]:

$$\xi = \frac{1}{2\tau} \left[ (1 + \sigma_a(\lambda_s) \langle N \rangle c\tau_c) \left( \frac{P_{\text{pump}}}{P_{\text{th}}} - 1 \right) + 1 \right]. \quad (2.182)$$

Large perturbations result in an anharmonic laser dynamic, called spiking [41, 42]. Spiking typically occurs when a laser is turned on, as the oscillator undergoes a large perturbation from below to above the threshold. Figure 2.20b shows the temporal oscillation behavior of the output power and the inversion during spiking. At the beginning of the process the population inversion is below the threshold  $\Delta N_{\text{th}}$  and there is no laser field in the resonator ( $I_s = 0$ ). Thus, supplying a pump power  $P_{\text{pump}} > P_{\text{th}}$  leads to an inversion build-up according to the small-signal rate equation (2.166).

After reaching the threshold inversion  $\Delta N_{\text{th}}$  ( $t = 0$  in fig. 2.20b), the laser field builds up, but requires the build-up time  $T_b$  to be amplified from noise to the CW power  $P_{\text{CW}}$ . During the build-up time  $T_b$ , inversion depletion by the laser field is still negligible. Thus, the still increasing inversion accumulates a significant excess above the threshold level. Once the laser field has built up ( $t = T_b$ ), the high inversion leads to a strong amplification of the laser power, resulting in an output power  $P_{\text{out}}$  multiple times higher than the CW level  $P_{\text{CW}}$ . This in turn rapidly depletes the inversion below the threshold level  $\Delta N_{\text{th}}$  again. The laser power forms a short spike. The process repeats until the spiking turns into relaxation oscillations and finally reaches the steady state.

### 2.2.3 Optical Parametric Oscillators

An OPO is a form of optical oscillator that differs from a laser in terms of its amplification mechanism: instead of stimulated emission, an OPO relies on nonlinear interactions between light and matter. The optical amplifier in an OPO is based on the second-order nonlinear parametric gain given by eq. (2.125) in a nonlinear dielectric medium, which was discussed in sec. 2.1.4. Because the nonlinear parametric amplification results from DFG, an OPO converts pump light into signal and idler at lower frequencies (longer wavelengths). The nonlinear amplifier consists of a non-centrosymmetric crystal with a non-vanishing second-order susceptibility  $\chi^{(2)}$ . For a fixed polarization geometry of the involved fields in the crystal, the second-order nonlinearity can be characterized by a scalar effective nonlinear coefficient  $d_{\text{eff}}$ . A crystal that exhibits a high nonlinearity  $d_{\text{eff}}$  provides a strong coupling between signal, idler, and pump. This results in a large gain for the generation of signal and idler along the nonlinear crystal, if proper phase matching is achieved ( $\Delta k \approx 0$ ). To accomplish phase matching, birefringent nonlinear crystals or, for the case of quasi-phase-matching, periodically poled nonlinear crystals are required. Using temperature or angle tuning, the signal and idler wavelengths that fulfill the phase-matching condition in the crystal can be tuned within a broad spectral range. By placing the nonlinear crystal in an optical resonator, an OPO is realized. OPOs are generally used to generate coherent radiation in spectral regions where no suitable laser transitions exist.

The resonator classifies OPOs into two main types: singly-resonant oscillators (SROs), where either the signal or the idler are resonant, and doubly-resonant oscillators (DROs), which are resonant for both. While DROs have a lower threshold, SROs are generally more stable in

their oscillation frequency and exhibit a smoother tuning characteristic [64, 86]. Both OPO types generate signal and idler, when the parametric gain reaches the threshold that enables a stable oscillation of the resonator field. In contrast to a laser, the parametric gain does not rely on energy storage, but on the quasi-instantaneous material response to a pump signal that induces a nonlinear polarization. Thus, the generation of signal and idler in an OPO is an instantaneous conversion process of the pump that performs in compliance with the conservation of energy and momentum. This means that the output characteristics of an OPO are directly dependent on the properties of the pump light, which places high demands on the pump laser sources.

To establish some fundamental OPO relations, in the following, a linear DRO consisting of a nonlinear medium of length  $L$  between two opposing mirrors that provide equivalent feedback for signal and idler along the resonator axis  $z$  is considered. A collinear propagating pump wave leads to a parametric small-signal gain (see eq. (2.125)) along the nonlinear crystal that depends directly on the instantaneous pump intensity  $I_{\text{pump}}$  through the coupling coefficient  $\kappa$  (see eq. (2.121) and hence also the gain coefficient  $g$  (see eq. (2.124)). Due to momentum conservation, signal and idler waves are only amplified when traveling in the same direction as the pump wave [86]. The OPO starts oscillating when the parametric small-signal gain reaches the threshold according to eq. (2.157), enabling the build-up of signal and idler fields in the resonator. For the ideal case of perfect phase matching ( $\Delta k = 0$ ), eq. (2.127) for the maximum parametric small-signal gain can be set equal to the threshold gain, which yields the ideal minimum pump threshold

$$P_{\text{th}} = \frac{A_{\text{pump}} \epsilon_0 n_{\text{sig}}^2 n_{\text{idl}}^2 n_{\text{pump}} \lambda_{\text{sig}} \lambda_{\text{idl}}}{8\pi^2 c_0 d_{\text{eff}}^2} \frac{1}{\tau_c} \quad (2.183)$$

where  $A_{\text{pump}}$  is the area of the pump beam and  $\tau_c$  is the cavity photon lifetime given by eq. (2.153).

Because signal and idler are built up from vacuum noise with random phase, the OPO chooses an ideal phase relationship  $\Delta\phi = \Delta\phi_{\text{max}}$  that maximizes the gain along the nonlinear crystal [70, 87]. Modes that differ from ideal phase matching experience a lower small-signal gain given by eq. (2.125) and hence have a higher pump threshold.

Figure 2.21 illustrates the longitudinal cavity modes of signal and idler in a DRO within the parametric gain spectrum. On the  $x$ -axis, the frequency difference from degeneracy  $\Omega = \omega - \omega_{\text{pump}}/2$  is plotted, normalized by the frequency difference of the oscillation frequency

from degeneracy  $\Omega_{\text{osc}} = \omega_{\text{osc}} - \omega_{\text{pump}}/2$ . A DRO without wavelength-selective elements generally begins to oscillate at the signal and idler mode pair with the highest gain that satisfies energy conservation. According to eq. (2.152), the frequency spacing between the modes depends on the refractive index  $n$  of the nonlinear crystal, which is dispersive and therefore not constant when considering a wide spectral range. However, energy conservation requires an equidistant frequency difference  $\Omega$  from the degeneracy frequency  $\omega_{\text{pump}}/2$ . This constrains DROs to specific mode pairs that are able to oscillate, as illustrated in fig. 2.21, where the signal and idler gain modes coincide only at  $\pm\Omega_{\text{osc}}$  in frequency difference  $|\Omega|$ . Note that the mode spacing is exaggerated for the purpose of illustration.

In reality, technical noise causes the cavity modes to fluctuate in their resonance frequencies. Thus, the oscillation in a DRO continuously jumps between different mode pairs that form oscillation clusters [64, 88]. The bandwidth of these clusters, within which the OPO oscillates quasi-simultaneously, determines the effective linewidth of the signal:

$$\Delta\omega_{\text{L}} \approx \frac{n_{\text{idl}}}{n_{\text{idl}} - n_{\text{sig}}} \Delta\omega_{\text{noise}} \quad (2.184)$$

where  $\Delta\omega_{\text{noise}}$  is the frequency change caused by technical noise due to fluctuations in the pump frequency, temperature, or mechanical vibrations [64]. The idler linewidth is obtained analogously by interchanging the refractive indices. For type I phase matching, this linewidth expression formally diverges at degeneracy ( $n_{\text{idl}} = n_{\text{sig}}$ ), which means that the oscillation cluster extends over the entire gain bandwidth [64]. In this case, oscillation occurs at all modes that exceed the threshold. Thus, eq. (2.183) represents a good approximation for the pump threshold of the first oscillation in a DRO operated close to degeneracy with type I phase matching. For the general case, excitation of different unstable longitudinal modes with non-ideal phase matching requires a more comprehensive analysis of the threshold [87].

Above the threshold, the parametric gain along the crystal is clamped at the level  $G_{\text{th}}$ . Because the parametric gain depends directly on the instantaneous pump intensity, the OPO has two ways to react to an increase in pump power above the pump threshold  $P_{\text{th}}$  to keep the gain constant: depletion of the pump power by conversion into the signal and idler resonator field or modulation of the relative phase difference  $\Delta\phi$  of the complex amplitudes of pump, signal, and idler given by eq. (2.126). The latter is related to backconversion, which can limit the output power of an OPO [89, 90].

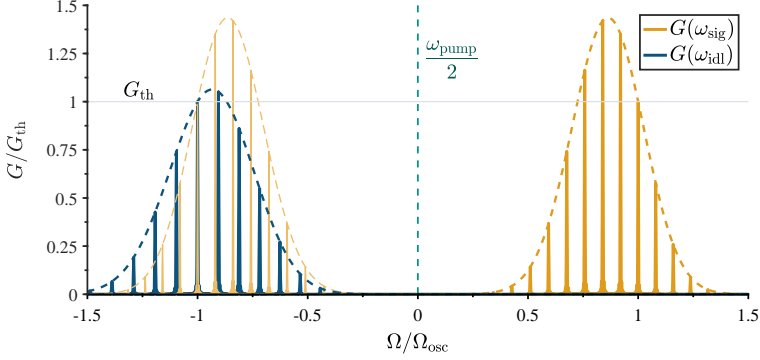


Figure 2.21: Gain spectrum of the longitudinal signal and idler modes of a doubly resonant OPO. Pairs of signal and idler modes must satisfy energy conservation to be able to oscillate, i.e., they must have the same frequency separation  $\pm\Omega$  from the degeneracy frequency  $\omega_{\text{pump}}/2$ . The gain spectrum of the signal modes projected from  $+\Omega$  to  $-\Omega$  is illustrated in light orange. The OPO oscillates at the mode pair, where an idler mode coincides with a projected signal mode.

The conversion of pump power above threshold occurs with instant energy conservation, which means an ideal quantum efficiency  $n_Q = \lambda_{\text{pump}}/(\lambda_{\text{sig}} + \lambda_{\text{idl}}) = 1$ . The efficiency of the pump process in an OPO is therefore only reduced by scattering and background absorption at optics and in the nonlinear crystal. Thus, the slope efficiency of a single signal and idler mode pair ideally corresponds to the resonator efficiency ( $\eta_s \approx \eta_R$ ) given by eq. (2.159). Each mode pair has the same slope efficiency but a different threshold. When the pump power is increased above the threshold of the first oscillating mode pair, the small-signal gain reaches the thresholds of further mode pairs within the oscillation cluster. Due to the inherent instability of the DRO, these mode pairs are equally excited. Thus, the pump power is distributed across several channels representing the individual mode pairs, with the individual channels varying in efficiency due to their different pump thresholds. However, as the number of newly excited modes per pump power decreases in relation to the modes that already oscillate in the cluster, the slope efficiency of the output power quickly converges to the resonator efficiency.

In steady state, the sum of the phases of signal and idler  $\phi_{\text{sig}} + \phi_{\text{idl}}$  adapts to the pump phase  $\phi_{\text{pump}}$  adiabatically [91, 92]. This results in a fixed relative phase difference  $\Delta\phi$  according to eq. (2.126) at each location in the OPO cavity, although the individual phases  $\phi_{\text{pump}}(z)$ ,  $\phi_{\text{sig}}(z)$ , and  $\phi_{\text{idl}}(z)$  of the slowly varying amplitudes may vary. A low-intensity signal and idler mode pair right above the threshold exhibit an ideal phase relationship that maximizes the gain at the OPO output, i.e.  $\Delta\phi = \Delta\phi_{\text{max}}(L)$  (see fig. 2.11). However, if the intensity becomes high,

signal and idler can backconvert into the pump through an SFG process that creates a wave at the pump frequency with a phase shift of  $\pi$  relative to the original pump [89, 90]. Superposition of the pump waves in combination with frequency fluctuations  $\Delta\omega_{\text{pump}}$  results in phase modulation of the pump, which in turn also modulates the phases of signal and idler. This changes the relative phase difference  $\Delta\phi$ , resulting in a reduced gain. Thus, after reaching the threshold for backconversion, an increase in pump power is no longer converted to output power, but leads to pure phase modulation that keeps the gain at the threshold level  $G_{\text{th}}$  despite the increase in pump power [93]. In this case, the output power characteristic shows a plateau [94, 95]. Once the minimum relative phase difference  $\Delta\phi$  is reached, a further increase in pump power will again increase the output power. Note that in a linear resonator, backconversion can also occur in the backward direction, which also reduces the round-trip gain [86].

The occurrence of backconversion is found to be closely related to the group velocity mismatch (GVM) between the pump, signal, and idler [94, 95]. As introduced in eq. (2.69), the group velocity  $v_g$  results from the linear approximation of the material dispersion relation  $k(\omega)$  that can be described by a frequency-dependent refractive index  $n(\omega)$ . Figure 2.22 illustrates the linearly approximated dispersion characteristic for small fluctuations of wavenumber and frequency  $\Delta k$  and  $\Delta\omega$  for the pump, signal, and idler in an OPO. Signal and idler are assumed to be not too far from degeneracy to have the same group velocity, resulting in the same linear dispersion  $n(\omega)$  illustrated by the blue slope.

Figure 2.22a shows the case for a matched group velocity of the pump, corresponding to a parallel dispersion characteristic depicted in green. In contrast, the case of mismatched group velocities with different slopes is shown in fig. 2.22b. For comparison with type I phase matched ZGP, see fig. 2.12a.

Modulation of the pump phase  $\phi_{\text{pump}}(L) = \phi_{\text{pump}}(0) + \Delta k_{\text{pump}}L$  along the OPO length  $L$  that can reduce the gain requires a fluctuation in the wave number  $\Delta k_{\text{pump}}$ , which is associated with a spectral fluctuation  $\Delta\omega_{\text{pump}}$  via the dispersion relation of the nonlinear crystal. Both fluctuations are provided by the back-converting SFG process from signal and idler. As illustrated by the equally sized yellow triangles, an OPO with matched group velocities can perform a phase modulation in compliance with the conservation of momentum ( $\Delta k_{\text{pump}} = \Delta k_{\text{sig}} + \Delta k_{\text{idl}}$ ) and energy ( $\Delta\omega_{\text{pump}} = \Delta\omega_{\text{sig}} + \Delta\omega_{\text{idl}}$ ). Therefore, the relative phase difference  $\Delta\phi$  can be modulated without a net energy transfer to keep the gain constant at the level  $G_{\text{th}}$ . In contrast, for the case of mismatched group velocities depicted in fig. 2.22b, momentum conservation for a given pump phase shift  $\Delta k_{\text{pump}}L$  requires a larger corresponding frequency shift for the signal

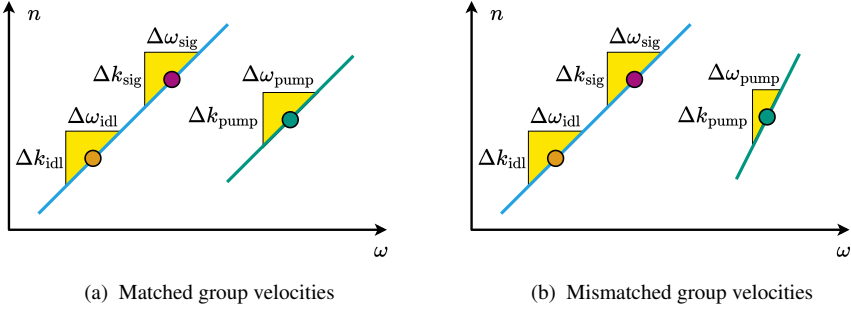


Figure 2.22: Phase and frequency diffusion for matched and mismatched group velocities between pump and signal plus idler. In an OPO, the sum of the signal and idler phase is locked to the pump phase, i.e.  $\Delta k_{\text{pump}}L = (\Delta k_{\text{sig}} + \Delta k_{\text{idl}})L$ . Apparently, pure phase modulation without a net energy transfer ( $\Delta\omega_{\text{pump}} = \Delta\omega_{\text{sig}} + \Delta\omega_{\text{idl}}$ ) is only possible for matched group velocities. Deviating group velocities lead to spectral broadening of signal and idler, which avoids strong backconversion.

and idler than for the pump, i.e.  $\Delta\omega_{\text{pump}} < \Delta\omega_{\text{sig}} + \Delta\omega_{\text{idl}}$ , resulting in an energetic imbalance. This means that pump phase modulation entails pump power consumption by the signal and idler to broaden their spectra. Therefore, an OPO with GVM of the pump does not exhibit an output power plateau caused by a backconversion regime where additional pump power induces pure phase modulation. Instead, such an OPO undergoes spectral broadening to maintain a linear output power characteristic.

Consideration of an OPO with a large GVM between pump and signal plus idler allows for a simplified description of the conversion process. Increasing the pump power leads to strong spectral broadening, which means the continuous excitation of a large number of additional modes when the small-signal gain reaches their thresholds. As phase modulation is avoided, each mode pair maintains the ideal fixed relative phase difference  $\Delta\phi = \Delta\phi_{\text{max}}$  that results in maximum gain at the OPO output end. This allows the build-up of modes with phase mismatches  $|\Delta kL| > \pi$ , as illustrated by the dotted gain spectrum fig. (2.11b). The fixed phase results in a fixed intensity distribution in the resonator for each mode, which reproduces itself in each round trip and scales linearly above its individual pump threshold. Figure 2.23 shows the normalized spectral broadening and the resulting intensity distribution along the OPO cavity for different pump power levels above threshold. For higher pump powers, the normalized spectral power density of signal and idler  $S/S_{\text{max}}$  is distributed across increasingly broad spectra on each side of the degeneracy wavelength  $\lambda_d$ . The nonlinear conversion along the length  $L$  of the OPO takes place in a progressively shorter section at the beginning of the nonlinear crystal. For

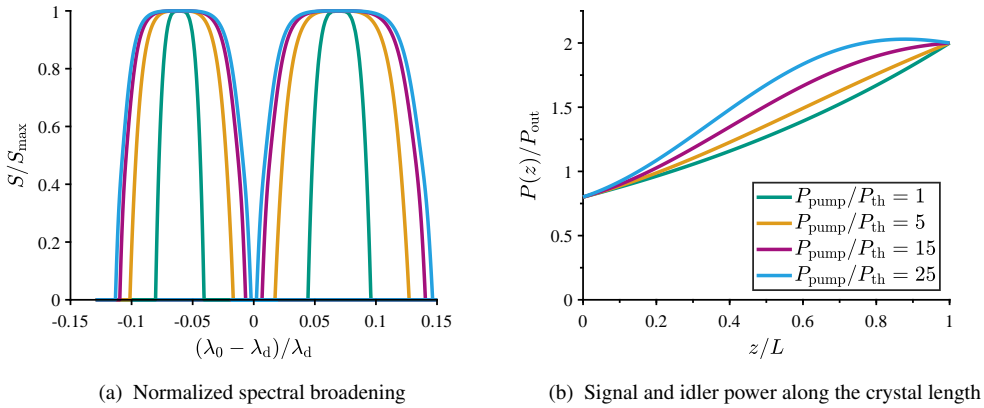


Figure 2.23: Nonlinear conversion in an OPO with GVM between pump and signal and idler. Increasing the pump power leads to substantial spectral broadening, utilizing the entire parametric gain spectrum. The excitation of modes with oscillating gain along the OPO results in a concentration of the nonlinear conversion toward the front region of the crystal.

$P_{\text{pump}}/P_{\text{th}} = 25$ , the power is even partially backconverted at the end of the crystal. Substantial spectral broadening is accompanied by the amplification of modes with phase mismatches  $\Delta k \gg 2\kappa$ , which do not continuously increase in intensity along the oscillator, but exhibit an oscillating amplification (see fig. 2.11a). At high pump powers, these modes already contribute enough to the total power to have a significant influence on the axial power distribution in the OPO. The transverse field distributions of the pump, signal, and idler beams, as well as the finite narrow linewidth of the pump, are not taken into account in this consideration. Transverse spatial effects can even enhance the spectral broadening due to angular dispersion. Despite simplification, the qualitative observations shown in fig. 2.23 agree with more comprehensive models for this special case of a large GVM [94].

Real pump laser beams generally exhibit a non-uniform intensity profile as discussed in sec. 2.1.1. For a Gaussian pump beam in which the intensity is concentrated at the center, the beam center may exceed the pump threshold while its peripheral region remains below. Thus, parts of the pump power cannot contribute to the nonlinear conversion, which leads to a reduction in efficiency. Furthermore, the transverse signal and idler fields in the resonator are spatially confined to the region of high intensity and even further focused for increasing pump intensities, as they experience disproportionate gain in the beam center. This effect is referred to as gain guiding or gain lensing and must be considered when designing the resonator. Moreover,

spatial walk-off in birefringent crystals (see eq. (2.43)) can further reduce the efficiency and beam quality.

To achieve the high intensities required for operating an OPO, pulsed pump lasers are typically used. Typical pulse widths are in the nanosecond time scale, which is much longer than the OPO cavity length. Although the parametric processes are quasi-instantaneous, the OPO must re-establish its resonator field from the vacuum noise for each pump pulse after reaching the threshold. During this build-up time, the pump power of the pulse is not depleted and no power conversion takes place. As a result, this reduces the efficiency of the OPO.

According to [86], the build-up time of the OPO is given by

$$T_b = \frac{\tau_c}{\sqrt{\frac{P_{\text{pump}}}{P_{\text{th}}} - 1}} \ln \left( \frac{P_{\text{CW}}}{P_{\text{noise}}^0} \right) \quad (2.185)$$

where the ratio of the steady-state power  $P_{\text{CW}}$  to the vacuum noise power  $P_{\text{noise}}^0$  (one photon per resonator mode) is typically on the order of  $1 \cdot 10^8$ . The exponential growth process is not critically dependent on the exact value of this ratio, meaning that a variance of two orders of magnitude does not affect the outcome of eq. (2.185) significantly [86]. The equation assumes an ideal rectangular pump pulse that provides the pump power  $P_{\text{pump}}$  in an abrupt step. To obtain an approximation for Gaussian-shaped pump pulses, the ratio  $\sqrt{P_{\text{pump}}/P_{\text{th}}}$  can be multiplied by a factor of 0.88 as long as the pump pulse width is longer than the rise time [86].

## 2.3 Thulium-doped Fiber Lasers

$\text{Tm}^{3+}$ -doped fiber lasers represent an ideal source for generating high-power laser radiation at wavelengths around  $2\ \mu\text{m}$ . Compared to  $\text{Ho}^{3+}$ -doped solid-state and fiber lasers that can also address this spectral range, they offer a crucial advantage: the possibility of being directly pumped with high-power laser diodes at  $793\ \text{nm}$ , thereby reaching slope efficiencies up to  $70\%$  [96, 97]. A high efficiency of the laser process is essential for achieving high output powers, as losses result in a heat load of the system, which ultimately limits power scaling.

Fiber lasers have outstanding properties for power scaling due to their special geometry: Compared to bulk solid-state lasers, doped fibers constitute active media with considerably longer lengths and smaller cross-sections. The large surface-to-volume ratio of this geometry improves heat dissipation, enabling efficient conduction cooling. Because the mode field in the fiber is determined by its waveguide geometry, fiber lasers typically provide ideal beam quality, largely independent of external influences and heat load, even up to high power levels. Furthermore, the long fiber length facilitates high gain levels (see eq. (2.163)) as well as high pump absorption efficiency (see eq. (2.165)). The combination of high gain and small fiber cross-sections, meaning a low saturation power according to eq. (2.169), enables the realization of high-gain fiber amplifiers that can amplify low-power signals by multiple orders of magnitude.

The amorphous glass host inhomogeneously broadens the gain spectrum, resulting in a wide amplification bandwidth—a feature particularly prominent for  $\text{Tm}^{3+}$ -doped fibers. Besides offering a wide range of possible emission wavelengths, this offers great potential for generating and amplifying ultrashort laser pulses. Silica glass is the most widely used and mature material for drawing fibers. It is characterized by high mechanical flexibility, excellent chemical and mechanical stability, a high optical damage threshold ( $\sim 480\ \text{GW cm}^{-2}$ ), and low transmission losses up to wavelengths of  $2.2\ \mu\text{m}$  (see fig. 2.6) [15, 98]. Finally, the ability to fusion-splice various fiber components allows for the construction of highly compact, robust, and alignment-free all-in-fiber systems. Taken together, these characteristics make fiber lasers ideal for applications in industry, medicine, and defense.

While  $\text{Yb}^{3+}$ -doped single-mode fiber lasers have demonstrated output powers of up to  $10\ \text{kW}$  at  $1\ \mu\text{m}$  [7, 99], Thulium is the rare-earth ion with the second highest output power achieved

in fiber lasers. A single-mode output power of 1 kW at 2  $\mu\text{m}$  has been reported in several publications [16–21].

However, the properties that make fiber lasers so advantageous also introduce challenges. The high gain over a broad spectral range can amplify undesired spectral artifacts and noise. Amplified spontaneous emission (ASE) can constitute a significant power fraction in high-gain fiber amplifiers. Furthermore, the small fiber cross-sections lead to high optical intensities in the amorphous glass. When guided over the long fiber length, this results in a high gain for third-order nonlinear effects, which can significantly distort the temporal and spectral properties of the laser output.

The following section first describes the spectroscopic properties of  $\text{Tm}^{3+}$ -doped silica for laser emission at 2  $\mu\text{m}$ , including the relevant radiative and non-radiative transitions and energy-transfer processes that influence the efficiency. Subsequently, the double-clad fiber geometry essential for high-power fiber lasers is introduced, and special fibers such as polarization-maintaining (PM), large-mode-area (LMA), and photonic crystal fibers (PCFs) are discussed. This is followed by an overview of the fiber nonlinearities relevant to this work. Finally, some general fiber laser and amplifier architectures are introduced.

### 2.3.1 Spectroscopy of Thulium-doped Silica

As described in section 2.1.3, the optical gain spectrum of rare-earth-doped solids originates from electronic transitions within the  $4f$  shell of the triply ionized dopant. In amorphous silica, the discrete energy levels of the ion split into closely spaced, locally varying Stark levels that form broad manifolds. This inhomogeneous broadening results in wide and smooth spectroscopic cross-sections that describe the optical transitions in the macroscopic active medium. Section 2.2.2 assumed a two-manifold scheme depicted in fig. 2.17 to discuss quasi-three-level lasers. This corresponds to the situation in 1  $\mu\text{m}$   $\text{Yb}^{3+}$ -doped fiber lasers, achieving slope efficiencies of around 90 % when pumped with 976 nm pump diodes, which almost agrees with the Stokes limit  $\lambda_{\text{pump}}/\lambda_s$  [15]. In contrast,  $\text{Tm}^{3+}$ -doped silica fibers exhibit a more complex laser scheme, involving the participation of multiple manifolds in the vicinity of the 2  $\mu\text{m}$  laser transition. Consequently, the overall quantum efficiency  $\eta_Q$  (see eq. (2.172))—and hence the final slope efficiency  $\eta_s$  (see eq. (2.179))—is determined by the combined rates of all competing radiative and non-radiative transitions and energy transfer processes between these energy levels.

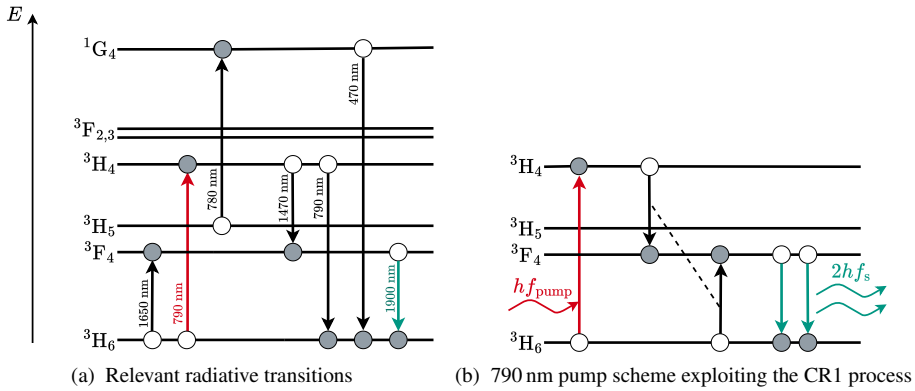


Figure 2.24: Energy levels and radiative transitions in  $\text{Tm}^{3+}:\text{SiO}_2$  for  $2\ \mu\text{m}$  laser emission according to [101]. Pumping at  $790\ \text{nm}$  can provide efficiencies above the Stokes limit  $\lambda_{\text{pump}}/\lambda_s$  thanks to the cross relaxation process CR1.

Figure 2.24a shows the relevant energy levels and radiative transitions of  $\text{Tm}^{3+}$ -doped silica for laser operation at  $2\ \mu\text{m}$ . The optical  $2\ \mu\text{m}$  laser transition occurs between the  ${}^3\text{F}_4$  level and the  ${}^3\text{H}_6$  ground level. The lifetime  $\tau$  of the  ${}^3\text{F}_4$  level in silica fibers is typically around  $200\text{--}650\ \mu\text{s}$ , and strongly dominated by non-radiative multiphonon decay due to the high maximum phonon energies in silica [100, 101]. The exact lifetime depends on the doping composition, including co-dopants that influence the local phonon energy around the  $\text{Tm}^{3+}$  ions [102, 103]. In-band pumping of the  ${}^3\text{F}_4$  manifold is feasible within a broad spectral range from  $1550\text{--}1910\ \text{nm}$ , using  $\text{Er}^{3+}$ -doped fiber lasers, Raman fiber lasers, or other  $\text{Tm}^{3+}$ -doped fiber lasers [104, 105]. However, high-power laser diodes are not readily available within this wavelength range. Therefore, the most common approach is out-of-band pumping. This method employs available  $790\ \text{nm}$  high-power laser diodes to pump the  ${}^3\text{H}_4$  level. The high absorption cross-section at  $790\ \text{nm}$  of around  $1 \cdot 10^{-25}\ \text{m}^2$  provides a high pump absorption efficiency [106].

Although the Stokes efficiency  $\lambda_{\text{pump}}/\lambda_s$  for  $790\ \text{nm}$  pumping is only around  $40\%$ , diode-pumped  $\text{Tm}^{3+}$ -doped fiber lasers can achieve slope efficiencies of  $60\text{--}70\%$  [101]. The reason is the "two-for-one" cross-relaxation process (CR1) of Thulium, which increases the quantum yield per pump photon and hence enables slope efficiencies above the Stokes limit [107]. Figure 2.24b illustrates the  $790\ \text{nm}$  pump scheme exploiting the CR1 process. In  $\text{Tm}^{3+}$ -doped silica, the  ${}^3\text{H}_4 \rightarrow {}^3\text{F}_4$  emission spectrum has a high degree of spectral overlap with the  ${}^3\text{H}_6 \rightarrow {}^3\text{F}_4$  absorption spectrum, enabling a resonant energy transfer process [85]. The CR1 process does

not require additional phonon interactions and is therefore highly probable. Thus, if there are two spatially close  $\text{Tm}^{3+}$  ions in the fiber, one in the  $^3\text{H}_6$  ground level and one excited in the  $^3\text{H}_4$  pump level, they perform an energy exchange that brings both to the  $^3\text{F}_4$  laser level. This means that the absorption of one pump photon results in the excitation of two ions to the laser level, ending in the generation of two laser photons through stimulated emission. Thus, CR1 enables a quantum yield  $\eta_q > 100\%$ .

However, CR1 is not the only pathway for an ion in the  $^3\text{H}_4$  pump level. It competes with multiphonon decay to the intermediate  $^3\text{H}_5$  level. From there, the ion typically relaxes further to the  $^3\text{F}_4$  laser level, yielding only a single excited ion per pump photon. A less probable but detrimental alternative is excited-state absorption (ESA) of another pump photon, which elevates the ion from  $^3\text{H}_5$  to the higher  $^1\text{G}_4$  level, from where it can decay under emission of blue fluorescence. In both cases, multiphonon decay of the  $^3\text{H}_4$  pump level reduces the overall efficiency and contributes to the heat load of the fiber laser. [108]

In addition to the CR1 process, there are other energy transfer processes in  $\text{Tm}^{3+}$ -doped silica that influence the quantum yield. An overview is given in figure 2.25. A second cross-relaxation process CR2 involves the transitions  $^3\text{H}_4 \rightarrow ^3\text{H}_5$  and  $^3\text{H}_6 \rightarrow ^3\text{F}_4$ . However, due to its small spectral overlap, this process requires the assistance of several phonons and therefore has a minor impact [85]. Energy migration (EM) proceeds much faster than other transfer processes because of its large spectral overlap. The process leads to a spatial distribution of the energy between the active ions in the medium, which potentially enhances the CR1 process [109]. In contrast, the energy transfer upconversion processes ETU1 and ETU2 decrease the quantum yield by quenching the  $^3\text{F}_4$  level. Although both processes require multi-phonon assistance and are therefore weaker than CR1, ETU was found to have a non-negligible effect in reducing the lifetime of the  $^3\text{F}_4$  level [85, 110].

The transition rates of these processes are strongly dependent on the doping composition. To obtain high efficiency for the  $^3\text{F}_4 \rightarrow ^3\text{H}_6$  laser transition, the CR1 rate must predominate over the multiphonon decay of the  $^3\text{H}_4$  level, which is achieved by a high  $\text{Tm}^{3+}$  concentration to minimize the ion separation [111]. However, the formation of ion clusters at high  $\text{Tm}^{3+}$  concentrations leads to quenching of the  $^3\text{F}_4$  level by enhancing the ETU processes [110]. For this reason,  $\text{Al}^{3+}$  is added in the fabrication of  $\text{Tm}^{3+}$ -doped silica fibers as a co-dopant. The  $\text{Al}^{3+}$  ions form a network around the  $\text{Tm}^{3+}$  ions that avoids clustering and reduces the phonon energy in the local environment [102]. The lower phonon energy not only reduces the rate of the ETU processes but also the multiphonon decay of the  $^3\text{H}_4$  level [102]. A doping ratio  $\text{Al}^{3+}:\text{Tm}^{3+}$  of

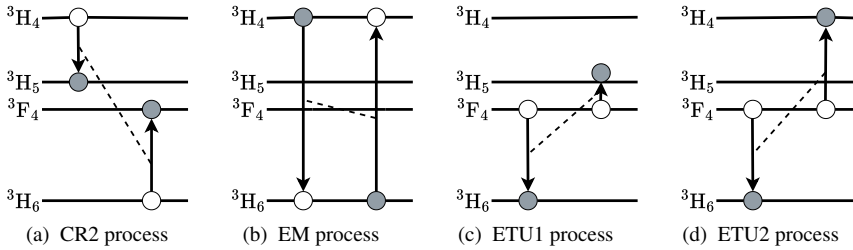


Figure 2.25: Relevant energy transfer processes in  $\text{Tm}^{3+}:\text{SiO}_2$  besides the CR1 process. Given a compatible energy gap between two transitions, two ions perform a mutual energy exchange. Energy mismatches between the transitions can be compensated by phonon interactions, which, however, reduces the probability of the process.

10:1 minimizes concentration quenching and enables enhanced efficiencies for higher  $\text{Tm}^{3+}$  concentrations [109]. Numerous studies reviewed in [101] show that  $\text{Tm}^{3+}$  concentrations of more than 2 wt.% are required to benefit from the CR1 process. The highest slope efficiencies are achieved for doping concentrations  $> 3.5$  wt.% [96, 97].

Figure 2.26 shows the spectroscopic cross-sections of the  $2\ \mu\text{m}$  laser transition in  $\text{Tm}^{3+}$ -doped aluminosilicate glass. The solid curves are based on data from Jackson [100]. Note that the absorption cross-section is modified in this illustration compared to the measured data from [100] by removing an apparent non-physical offset at short wavelengths from  $1.4\text{--}1.55\ \mu\text{m}$  and long wavelengths  $> 1.89\ \mu\text{m}$ . This baseline correction is justified by the expectation of zero absorption far from the resonance peak. The dashed curves show cross-section data from Jirickova et al. [106]. Data from [106] also consider the temperature dependence of the spectroscopic cross-sections. As temperature increases, the population distribution within the Stark manifolds changes, populating higher energy levels. This leads to a spectral shift of the absorption cross-section to longer wavelengths and of the emission cross-section to shorter wavelengths [106, 112]. Higher temperature also enhances phonon interactions, which leads to stronger inhomogeneous broadening of the cross-sections entailing a reduction in height [106, 112]. The data presented in fig. 2.26 are for room temperature. As can be seen in the figure, the data from the different references differ significantly from each other. Measurements from earlier publications reveal similar variations [112–115]. This emphasizes that the spectroscopic cross-sections strongly rely on the exact material and doping composition of the specific fiber under investigation.

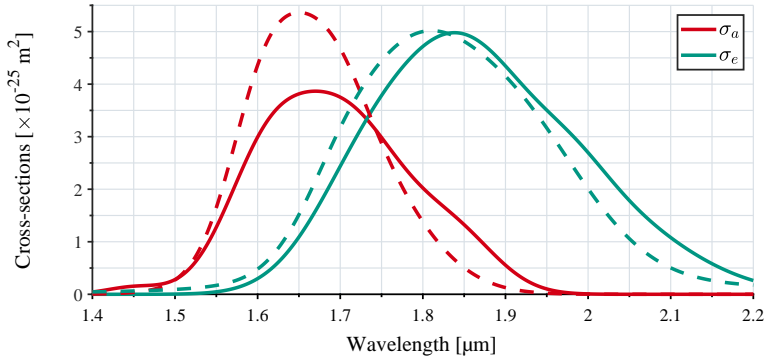


Figure 2.26: Spectroscopic absorption and emission cross-sections of  $\text{Tm}^{3+}$ -doped aluminosilicate glass at room temperature. Data plotted as solid lines are taken from [100], and have been baseline-corrected to remove an offset. Data plotted as dashed lines are from [106].

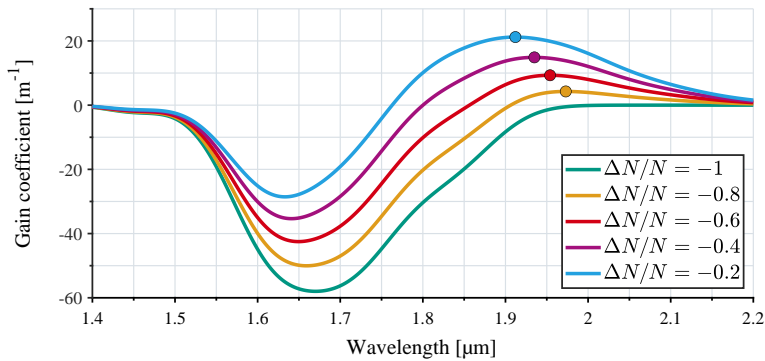


Figure 2.27: Gain coefficient of  $\text{Tm}^{3+}$ -doped silica for different inversion level versus the wavelength. The markers indicate the maxima of the gain spectra. The spectroscopic cross-sections were taken from [100].

The gain spectrum of a  $\text{Tm}^{3+}$ -doped silica fiber results from the spectroscopic cross-sections and the population inversion  $\Delta N$ , as defined in eq. (2.163). Figure 2.27 illustrates the gain coefficient  $g(\lambda_0)$  for several population inversion levels  $\Delta N$  relative to the doping concentration  $N$ . While a ratio  $\Delta N/N = -1$  means no excitation, a ratio  $\Delta N/N = -0.2$  corresponds to an inversion close to the bleaching level. Optical gain  $G > 1$  is achieved in the spectral range with a gain coefficient  $g > 0$ . The markers indicate the maxima of the spectral gain curves for the respective inversion ratio  $\Delta N/N$ . A higher population inversion ( $\Delta N = N_2 - N_1$ ) increases the rate of stimulated emission ( $\propto \sigma_e N_2$ ) and decreases reabsorption ( $\propto \sigma_a N_1$ ). Because the

absorption cross-section is located at shorter wavelengths, the reduction in reabsorption at high inversions enhances the gain in particular at short wavelengths, leading to a blue shift of the gain spectrum.

The wide gain spectrum of  $\text{Tm}^{3+}$ -doped silica fibers allows laser operation within a broad spectral range. The operation wavelength of a laser can be selected within the gain bandwidth  $g > 1$  by using strongly dispersive resonator mirrors, such as Bragg gratings (see sec. 2.1.2). This provides selective feedback within a narrow bandwidth and avoids oscillations at other wavelengths in the gain spectrum. For amplifiers, an input spectrum with high signal-to-noise ratio is required to avoid the build-up of undesired spectral artifacts within the gain bandwidth. Because the gain  $G = \exp(gL)$  grows exponentially with the gain coefficient along the fiber length, the gain spectrum of a fiber laser has a high dynamic range. If a fiber laser or amplifier is operated too far away from its gain maximum, the gain at the maximum can become several orders of magnitude higher than at the intended operation wavelength. This can cause substantial ASE that builds up in accordance with the gain spectrum (see eq. (2.174)). Furthermore, the peak gain can become high enough that even minor reflections in the laser system provide sufficient feedback to cause a parasitic laser oscillation. The occurrence of parasitic lasing saturates the gain in the fiber, preventing laser oscillation or further amplification at wavelengths with lower gain. When designing a fiber laser or amplifier, it is therefore important to ensure operation close to the gain maximum.

As illustrated in figure 2.27, the gain maximum can be spectrally shifted by controlling the inversion in the fiber. For long emission wavelengths, a low inversion is required. This can be achieved by using a long fiber length, because the distribution of the excited states over a longer length results in a lower inversion density while providing the same gain. A high doping concentration is also beneficial for operation at long wavelengths, as it increases the number of unexcited states and thus enhances the red shift of the gain through reabsorption. Furthermore, to operate fiber oscillators at long wavelengths it is crucial to have a high Q-factor, meaning a sufficiently high OC reflectivity to ensure a low threshold inversion according to eq. (2.177). An emission wavelength of up to  $2.2\mu\text{m}$  has been demonstrated for a  $\text{Tm}^{3+}$ -doped fiber oscillator using an FBG-based resonator in which the OC had a reflectivity of 50 % [116].

### 2.3.2 Fiber Waveguide Geometry and Specialty Fibers

An optical fiber is a cylindrical optical waveguide comprising a circular core with a radius  $r_{\text{core}}$  surrounded by a cladding with a radius  $r_{\text{clad}}$ . Core and cladding are both made of transparent glass, most commonly silica, with the core having a higher refractive index than the cladding ( $n_{\text{core}} > n_{\text{clad}}$ ). This index step enables light guidance in the core via total internal reflection (see sec. 2.1.2). The fiber is coated with one or more protective polymer layers to make it flexible and resistant to the environment.

To act as an active laser medium, the core is doped with active ions, such as  $\text{Yb}^{3+}$ ,  $\text{Tm}^{3+}$ , or  $\text{Ho}^{3+}$ . For amplification, a laser signal must be guided in the core, where the waveguide geometry defines the transverse mode field. This allows for a transverse mode selection by the fiber design to achieve a high output beam quality. However, generating optical gain in the fiber core also requires the supply of pump light. Guiding the pump light in the same core would require a beam quality similar to that of the laser signal. The realization of high-power fiber lasers, on the other hand, relies on high optical pump powers from multimode light sources. This conflict between beam quality and power is resolved by the invention of the double-clad fiber [117].

#### Wave Guidance in Double-Clad Fibers

A double-clad fiber confines pump and laser light to different layers of the waveguide. Figure 2.28 shows the design concept of this fiber geometry. The fiber is surrounded by a polymer coating with a refractive index lower than the cladding ( $n_{\text{clad}} > n_{\text{coat}}$ ). Thus, the low-index coating acts as a second cladding that allows pump light to be guided in the transparent inner cladding. During propagation in the cladding, the pump light intersects the actively doped core, where it is absorbed. The generated laser light remains guided in the core. This separation of pump and laser light guidance enables coupling of high-power multimode pump diodes into the cladding while maintaining excellent beam quality of the laser output in the core.

To facilitate the coupling of multimode pump light, the diameter of the cladding is large compared to the wavelength. Therefore, the pump light propagation in the cladding can be

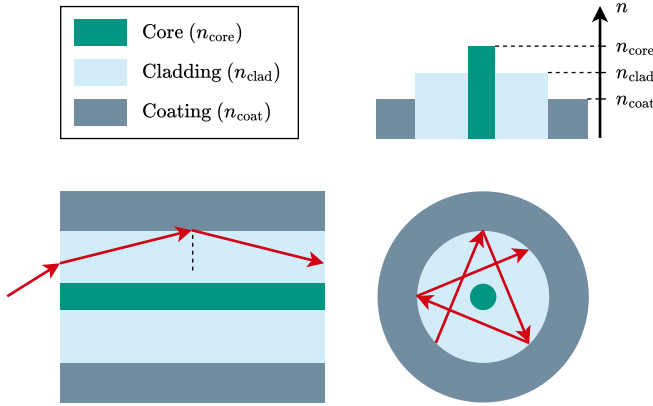


Figure 2.28: Geometry of the double-clad fiber. The refractive index decreases stepwise from the core to the coating. The pump light (red arrows) can be coupled into the cladding to be guided there. To get absorbed, the pump light must intersect the active core.

accurately described by geometric ray optics. A ray is guided in the cladding when it satisfies the condition for total internal reflection at the interface to the coating. This requires its angle of incidence to be greater than the critical angle  $\theta_c$  defined by eq. (2.53) with respect to the interface normal. This guidance condition, in turn, defines an acceptance angle  $\theta_a$  for light entering the fiber endface, which is typically specified by the numerical aperture (NA)

$$\text{NA}_{\text{clad}} = n_0 \sin \theta_a \stackrel{n_0=1}{=} \sqrt{n_{\text{clad}}^2 - n_{\text{coat}}^2}, \quad (2.186)$$

where  $n_0$  is the refractive index of the incident medium (usually 1 for air) [15]. Thus, the numerical aperture  $\text{NA}_{\text{clad}}$  defines the acceptance cone for pump coupling and depends solely on the refractive indices  $n_{\text{clad}}$  and  $n_{\text{coat}}$  of the cladding and coating.

The absorption efficiency of the pump light  $\eta_{\text{abs}}$  depends on the overlap factor  $\Gamma_{\text{pump}}$  between the pump field and the doped area (see eqs. (2.163) to (2.165)). For a uniformly doped core, the overlap factor  $\Gamma_{\text{pump}}$  can be estimated by the ratio of the core area  $A_{\text{core}}$  to the cladding area  $A_{\text{clad}}$ :

$$\Gamma_{\text{pump}} \approx \frac{A_{\text{core}}}{A_{\text{clad}}} = \frac{r_{\text{core}}^2}{r_{\text{clad}}^2}. \quad (2.187)$$

In reality, however, the pump field comprises numerous cladding modes, each with a different degree of overlap with the core [118]. These modes can be described as rays that follow helical

paths within the cladding, as illustrated in fig. 2.28 by the red arrows. Rays with large reflection angles at the cladding-coating interface travel in wide cycles with less core intersection; some "skew" modes may not intersect the core at all.

The overlap of the pump light is directly related to the fill factor of the cladding NA. The fill factor describes how the angular distribution of the launched pump light fills the acceptance cone of the fiber. Pump light concentrated within a smaller NA is better absorbed than light that uniformly fills the entire acceptance NA. Therefore, a better beam quality of the pump diodes is generally advantageous. Furthermore, the absorption efficiency can be improved by mode mixing, causing modes with poor core overlap to transfer to modes with better overlap [118]. Strategies for improved mode mixing include bending the fiber and the use of special fiber designs with D-shaped or octagonal claddings that break the circular symmetry [119, 120].

The propagation of the laser light is governed by the core geometry, which has dimensions comparable to the wavelength. This requires a wave optics description. At the dielectric core-cladding interface, the field distribution confined to the core merges into an evanescent field in the cladding. Under these boundary conditions, Maxwell's eqs. (2.1) to (2.4) yield certain modes that can propagate in the cylindrical waveguide [121]. The modes propagate along the  $z$ -axis of the waveguide and are transversely confined to the core region. In a cylindrical coordinate system, the solutions for the electric field are of the form

$$\mathbf{E}(R, \varphi, z) = \mathbf{E}_0 \psi(R, \varphi) e^{-j\beta z}, \quad (2.188)$$

where  $\psi(R, \varphi)$  is the normalized transverse field amplitude depending on the normalized radius  $R = r/r_{\text{core}}$  and the angular coordinate  $\varphi$ . The propagation constant  $\beta$  characterizes the propagation of a monochromatic mode along the waveguide. It is defined as

$$\beta = n_{\text{eff}} k_0, \quad (2.189)$$

where  $n_{\text{eff}}$  is the effective refractive index experienced by the mode in the waveguide, depending on its transverse field distribution in the core and the cladding. Thus, the propagation constant  $\beta$  replaces the wavenumber  $k$  in the inhomogeneous waveguide geometry and takes values within the interval  $n_{\text{core}} k_0 \geq \beta \geq n_{\text{clad}} k_0$ .

Substituting eq. (2.188) into the Helmholtz equation (2.11) yields the wave equations for the core and cladding regions

$$\left( \frac{\partial^2}{\partial R^2} + \frac{1}{R} \frac{\partial}{\partial R} + \frac{1}{R^2} \frac{\partial^2}{\partial \varphi^2} + U^2 \right) \psi(R, \varphi) = 0 \quad 0 \leq R < 1, \quad (2.190)$$

$$\left( \frac{\partial^2}{\partial R^2} + \frac{1}{R} \frac{\partial}{\partial R} + \frac{1}{R^2} \frac{\partial^2}{\partial \varphi^2} - W^2 \right) \psi(R, \varphi) = 0 \quad 1 \leq R < \infty, \quad (2.191)$$

where the cladding is assumed to have an infinite radial extension compared to the much smaller core [15]. The parameters  $U$  and  $W$  characterize the transverse propagation at the core-cladding interface and are defined as

$$U^2 = r_{\text{core}}^2 (n_{\text{core}}^2 k_0^2 - \beta^2), \quad (2.192)$$

$$W^2 = r_{\text{core}}^2 (\beta^2 - n_{\text{clad}}^2 k_0^2). \quad (2.193)$$

Separation of the variables  $\psi(R, \varphi) = F(R)f(\varphi)$  yields the normalized transverse modes  $\psi_l$  ( $l = 0, 1, 2, \dots$ ):

$$\psi_l(r) = \begin{cases} \frac{J_l(U R)}{J_l(U)} f_l(\varphi) & 0 \leq R < 1, \\ \frac{K_l(W R)}{K_l(W)} f_l(\varphi) & 1 \leq R < \infty, \end{cases} \quad (2.194)$$

where  $J_l$  is the Bessel function and  $K_l$  is the modified Hankel function of order  $l$ , respectively [122]. The functions  $f_l(\varphi)$  can take the orthogonal solutions

$$f_l(\varphi) = \begin{cases} \cos(l\varphi) \\ \sin(l\varphi) \end{cases} \quad (2.195)$$

which means a two-fold degeneracy of the modes  $\psi_l$  for  $l > 0$ .

In general, the boundary conditions require all transverse and longitudinal field components to be continuous at the core-cladding interface [117]. However, for the most common case of weakly guiding fibers where  $(n_{\text{core}} - n_{\text{clad}})/n_{\text{clad}} \ll 1$ , the longitudinal field components can be neglected, i.e.  $E_z \approx 0$  and  $H_z \approx 0$  [122]. Thus, the waveguide modes become linearly polarized quasi-TEM modes, which are referred to as  $\text{LP}_{lm}$  modes ( $m = 1, 2, 3, \dots$ ) [122]. Each  $\text{LP}_{lm}$  mode has two degenerate polarization states for p- and s-polarization. Combined with the azimuthal degeneracy  $f_l(\varphi)$ , this results in a four-fold degeneracy for  $l > 0$ , and a two-fold

degeneracy for  $l = 0$ . For weakly guiding fibers, continuity of the transverse fields at  $R = 1$  can be expressed by a single characteristic equation [123]

$$U \frac{J_{l-1}(U)}{J_l(U)} = -W \frac{K_{l-1}(W)}{K_l(W)}. \quad (2.196)$$

This equation yields the eigenvalues  $\beta_{lm}$  corresponding to the  $\text{LP}_{lm}$  modes of the waveguide. With the definition of the normalized frequency

$$V = \sqrt{U^2 + W^2} = k_0 r_{\text{core}} \sqrt{n_{\text{core}}^2 - n_{\text{clad}}^2} = \frac{2\pi}{\lambda_s} r_{\text{core}} \text{NA}_{\text{core}}, \quad (2.197)$$

the normalized cutoff frequencies  $V_{lm}^c$  of the  $\text{LP}_{lm}$  can be determined by setting  $W = 0$  to minimize  $\beta$  [122]. At cutoff, eq. (2.196) yields the conditions

$$J'_0(V_{0m}^c) = 0, \quad \text{for } l = 0, \quad (2.198)$$

$$J_{l-1}(V_{lm}^c) = 0, \quad \text{for } l > 0, \quad (2.199)$$

where  $J'_0$  is the first derivative of the zero-order Bessel function  $J_0$ , which arises from the identity  $J_{-1} = -J_1 = J'_0$  for  $l = 0$ .

Figure 2.29 shows the curves  $J_{l-1}(U)$  for  $l = 1, 2, 3$ . The normalized cutoff frequencies for the modes  $\text{LP}_{lm}$  are indicated by the dashed lines at the roots of the functions  $J_0$ ,  $J_1$ , and  $J_2$ , and the extrema of  $J_0$  according to the eqs. (2.198) and (2.199). For normalized frequencies below the  $\text{LP}_{11}$  cutoff ( $V < 2.405$ ) only the fundamental  $\text{LP}_{01}$  mode can propagate in the fiber. The fiber is termed single-mode in this case.

The normalized transverse intensity profile of the fundamental  $\text{LP}_{01}$  mode is circularly symmetric because  $f_0(\varphi) = 1$ . Its radial intensity profile is proportional to  $|J_0(r)|^2$  within the core, and proportional to  $|K_0(r)|^2$  outside of the core. For normalized frequencies  $V > 1.5$ , the intensity of the  $\text{LP}_{01}$  mode can be approximated by a Gaussian field distribution [124, 125]. This allows determining the mode field radius  $w_0$  of a step-index fiber from the equation [125]:

$$w_0 = r_{\text{core}} \left( 0.65 + \frac{1.619}{V^{3/2}} + \frac{2.879}{V^6} \right). \quad (2.200)$$

Because of their nearly Gaussian beam profiles, single-mode fibers provide a close to diffraction-limited beam quality, characterized by an  $M^2 \approx 1$ .

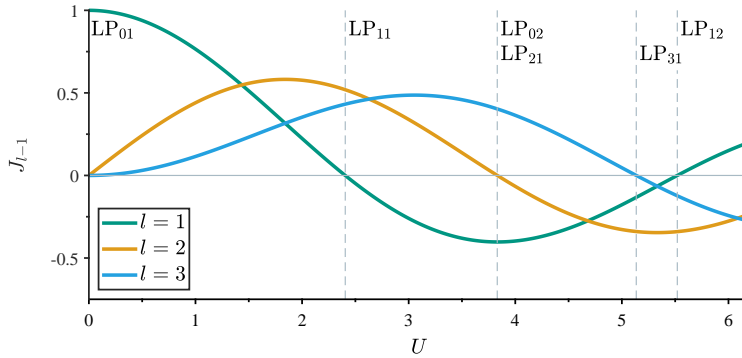


Figure 2.29: Illustration of the normalized cutoff frequencies of the  $LP_{lm}$  Modes in weakly guiding fibers. At cutoff, the normalized cutoff frequencies  $V_{lm}^c$  correspond to the values of  $U$  at the locations indicated by the dashed lines.

The optical gain (see eq. (2.163)) in an active fiber depends on the overlap factor  $\Gamma_s$  (see eq. (2.164)) of the laser mode field with the doped core. Using the Gaussian approximation of the fundamental  $LP_{01}$  mode, the overlap factor  $\Gamma_s$  in a single mode fiber with a uniformly doped core is given by

$$\Gamma_s = 1 - \exp\left(-2\frac{r_{\text{core}}^2}{w_0^2}\right). \quad (2.201)$$

## Specialty Fiber Designs and Photonic Crystal Fibers

There are a variety of special fiber designs that modify the standard double-clad fiber for specific applications. Figure 2.30 shows two common fiber designs that address specific issues: polarization-maintaining (PM) fibers and large-mode-area (LMA) fibers. Despite their advantages, special fiber designs generally come at the expense of complicating splice connections to standard fiber components.

Standard fibers induce polarization changes in the guided signal. As described above, the fundamental  $LP_{01}$  mode of a single-mode fiber is composed of two orthogonal polarization states. Optical anisotropy along the fiber causes different propagation constants  $\beta_x$  and  $\beta_y$  for the two polarization states, leading to modal birefringence with a strength [126]

$$B_m = \frac{|\beta_x - \beta_y|}{k_0} = |n_x - n_y|. \quad (2.202)$$

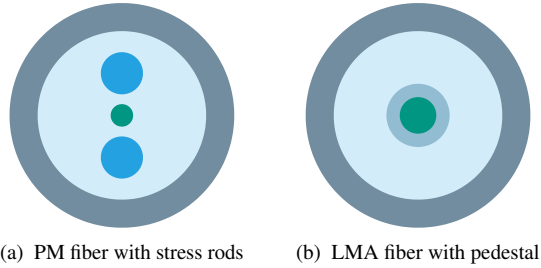


Figure 2.30: Specialty fibers. Adding of stress rods makes a fiber polarization-maintaining (PM). The combination of large-mode-area (LMA) with nearly diffraction-limited beam quality is enabled by a pedestal that reduces the NA of the core.

Modal birefringence causes a periodic coupling between the polarization states with a period of the beat length [126]

$$L_B = \frac{\lambda}{B_m}. \quad (2.203)$$

In real fibers, small irregularities in the circular core or anisotropic stress by bending or twisting result in random variations of the modal birefringence  $B_m$  along the fiber. Due to these random perturbations, linearly polarized light changes its polarization state towards random polarization when propagating in a standard fiber.

PM fibers are designed to preserve the polarization state of a guided signal [127, 128]. One common approach is to add two rods of boron-doped silica glass along one cross-sectional axis of the fiber, as shown in fig. 2.30a. The stress induced by these rods introduces a large amount of intentional birefringence in a defined axis. The induced birefringence depends on the shape and thickness of the stress rods, and is typically on the order of  $B_m \sim 10^{-4}$  leading to a beat length  $L_B$  of a few centimeters [128]. The transverse axis with the stress rods is referred to as the slow axis, because of its higher refractive index. Consequently, the orthogonal axis is referred to as the fast axis. To maintain the linear polarization of a signal, its polarization direction must coincide with the slow or fast axis of the PM fiber. The defined birefringence leads to large phase mismatch between the orthogonal polarization modes, which avoids effective coupling by small perturbations. Thus, the linear polarization of the guided signal is maintained in the fiber.

Power scaling of fiber lasers leads to the occurrence of high intensities in the small fiber core, which can cause severe temporal and spectral distortion by nonlinear effects. This issue becomes even more pronounced in pulsed operation of the fiber laser, where the pulse peak power can be multiple times higher than in CW operation. An essential countermeasure to reduce the intensity in the fiber is the use of LMA fibers. Compared to standard single-mode fibers, LMA fibers have a larger core diameter while still providing nearly ideal beam quality. In general, equation (2.197) indicates that the core diameter  $r_{\text{core}}$  of a single-mode fiber ( $V < 2.405$ ) can be increased, if the NA of the core is reduced simultaneously [129]. However, realizing a very low  $\text{NA}_{\text{core}}$  demands precise control of the refractive index step between core and cladding during the fiber manufacturing process. The numerical apertures of  $\text{Tm}^{3+}$ -doped step-index fibers are typically limited to minimum values in the range of 0.07–0.1 [130, 131]. This means that the core diameter of a true single-mode fiber at a wavelength of  $2\ \mu\text{m}$  is limited to less than  $20\ \mu\text{m}$ . To scale the core diameter beyond this limit, LMA fibers are therefore usually designed to be slightly multimoded. Single-mode operation is then enforced by coiling the fiber, which induces high bending losses for the undesired higher-order modes [132]. This approach utilizes the fact that the fundamental  $\text{LP}_{01}$  mode is more confined to the core and therefore most resistant to bending losses [133].

$\text{Tm}^{3+}$ -doped LMA fibers require a high doping concentration of  $\text{Tm}^{3+}$  and  $\text{Al}^{3+}$  ions to enable high efficiencies by the CR1 process, as described in sec. 2.3.1. However, the high doping concentrations substantially increase the refractive index of the core compared to the undoped cladding, which would limit the minimum  $\text{NA}_{\text{core}}$  to values around 0.18–0.24 [134]. For this reason, a pedestal typically surrounds the core in a  $\text{Tm}^{3+}$ -doped LMA fiber, as illustrated in fig. 2.30b. The pedestal is a passive region with an intermediate refractive index between core and cladding to achieve a low  $\text{NA}_{\text{core}}$ .

The diameter of the pedestal must be carefully designed. On the one hand, the pedestal must be large enough to fully contain the evanescent field of the guided mode. If the pedestal is too small, the mode can become leaky and couple into unwanted pedestal modes, causing loss and a distorted beam profile. On the other hand, the pedestal should not be too large to trap pump light in pedestal skew modes. Furthermore, a large pedestal means higher manufacturing costs. [134]

Standard  $\text{Tm}^{3+}$ -doped LMA fibers have core diameters of 20–25  $\mu\text{m}$ , limited by the minimum  $\text{NA}_{\text{core}}$  that can be achieved by a conventional refractive index gradient [130, 131]. One approach to overcome this limitation is the use of photonic crystal fibers (PCFs). In a PCF, the core is

surrounded by a two-dimensional photonic crystal, which acts as the cladding. As described in sec. 2.1.2, photonic crystals are periodic dielectric structures that behave highly dispersive, if their period is on the order of the wavelength. The dispersion relation of the micro-structured cladding can be described by means of an effective refractive index. In index-guiding PCFs, this effective refractive index is lower than that of the core, resulting in light guidance via total internal reflection [135]. Designing the photonic crystal cladding allows for precise control of the effective refractive index, which enables the realization of a low  $NA_{\text{core}}$  and hence larger single-mode diameters. Another class of PCFs are photonic band gap fibers. In contrast to index-guiding PCFs, these fibers can have a lower refractive index in the core than in the cladding by utilizing the photonic band gap effect. This enables the realization of hollow-core fibers (HCFs). The following discussion focuses on index-guiding PCFs, which are ideal for scaling the core area of active fibers.

Figure 2.31 shows the cross-section of an index-guiding PCF. The photonic crystal cladding is formed by a two-dimensional lattice of air holes, typically arranged in a periodic hexagonal pattern [136]. The air holes are drawn lengthwise through the silica fiber to provide constant guiding properties. In the center of this air hole matrix, one or more omitted air holes form a hexagonal region of solid silica that acts as the fiber core. The design parameters determining the guiding properties of the PCF are the hole diameter  $d$  and the pitch  $\Lambda$  that separates the holes. The core diameter corresponds to a multiple of the pitch  $\Lambda$ , depending on the number of air-hole cells omitted in the center.

Double-clad PCFs are typically realized with an air cladding that confines the pump light [137, 138]. The air cladding consists of a ring of air-filled cells that are separated by thin silica bridges. These bridges act as slab waveguides for the pump field that penetrates the air cladding boundary [139]. If their width is narrower than the pump wavelength, the evanescent pump field strongly extends into the air on both sides of the thin bridge. This creates a low effective refractive index for the air cladding boundary, which confines the pump light to the enclosed area. Thus, a small ratio of bridge width to pump wavelength leads to a large NA of the air cladding that facilitates efficient pump coupling [139]. Furthermore, the air cladding isolates high pump powers from the polymer coating, offering improved reliability in high-power operation [140].

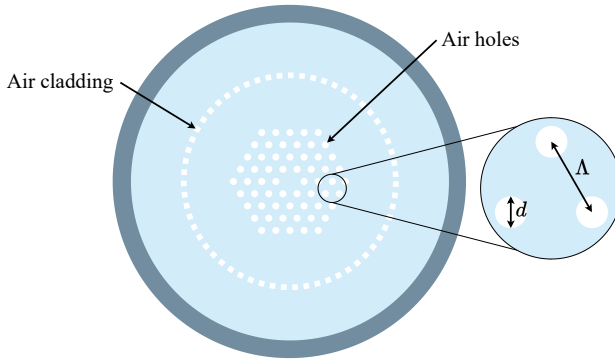


Figure 2.31: Schematic of a photonic crystal fiber (PCF). The double-clad design features two main structures: a central periodic air hole lattice that creates low-NA guidance for the signal core, and an outer air cladding that provides high-NA pump light guidance. The guiding properties of the core are determined by the air hole diameter  $d$  and the pitch  $\Lambda$ .

For guiding in the core via total internal reflection, a core mode must have a propagation constant  $\beta$  that cannot couple to the available modes in the cladding, i.e.

$$k_0 n_{\text{core}} > \beta > \beta_{\text{FSM}} \quad (2.204)$$

where  $\beta_{\text{FSM}}$  is the propagation constant of the fundamental space-filling mode (FSM) of the photonic crystal cladding [135]. The description of the guiding properties in the core therefore requires the determination of  $\beta_{\text{FSM}}$ .

The FSM is the mode with the highest  $\beta$  that extends across the entire photonic crystal cladding. Its transverse field is represented by two-dimensional periodic Bloch waves, leading to a field distribution that repeats in each unit cell. This periodicity allows to determine  $\beta_{\text{FSM}}$  by analyzing a single unit cell. A unit cell is defined by a hexagon centered on an air hole with a distance of  $\Lambda/2$  from the center to the corners. Symmetry between unit cells requires the transverse field amplitude  $\psi_{\text{FSM}}$  to satisfy the boundary condition  $\partial\psi_{\text{FSM}}/\partial s = 0$  at the edge of each cell, where  $s$  is a spatial coordinate normal to the edge. Taking into account this boundary condition, the propagation constant  $\beta_{\text{FSM}}$  can be determined by numerical field calculation within a unit cell. By approximating the hexagonal shape of the unit cell with a circle, the transverse field corresponds to zero-order Bessel functions. [135]

To find the modes in the PCF core, parameters  $U$  and  $W$  can be defined in analogy to a step-index fiber (see eqs. (2.192) and (2.193)) to match the transverse fields of the core and the

cladding. For a PCF with a one-cell core ( $r_{\text{core}} = \Lambda$ ), this leads to a total radial phase shift in the core described by the normalized frequency

$$V_{\text{PCF}} = \sqrt{U^2 + W^2} = k_0 \Lambda \sqrt{n_{\text{core}}^2 - n_{\text{clad,eff}}^2} \quad (2.205)$$

where the effective refractive index of the cladding

$$n_{\text{clad,eff}} = \frac{\beta_{\text{FSM}}}{k_0} \quad (2.206)$$

results from the propagation constant of the FSM. For PCF cores consisting of several unit cells, the V-number can be calculated using the respective multiple of the pitch  $\Lambda$ . This definition of the core radius leads to a normalized cutoff frequency  $V_{\text{PCF}} < \pi$  for single-mode operation [141].

Despite the hexagonal core shape, the radial intensity distribution of the fundamental mode in a PCF can also be well approximated by a Gaussian profile. From this, the mode field radius can be determined by a similar equation as for a step-index fiber [142]:

$$w_0 = \Lambda \left( \frac{0.7078}{V_{\text{PCF}}^{1/5}} + \frac{0.2997}{V_{\text{PCF}}^{3/2}} + \frac{0.0037}{V_{\text{PCF}}^6} \right). \quad (2.207)$$

The relationship between the normalized frequency  $V_{\text{PCF}}$  and the highly dispersive effective refractive index  $n_{\text{clad,eff}}$  opens up special possibilities in the design of PCFs. The effective refractive index arises from the intensity distribution of the FSM in air and silica. Thus, it depends on the ratio of air hole size to pitch length  $d/\Lambda$ , and the wavelength. For shorter wavelengths, the FSM concentrates more strongly in the silica regions of the cladding. This causes the effective refractive index  $n_{\text{clad,eff}}$  to increase towards the index of silica, which in turn reduces the NA between the core and the cladding. This reduction in  $\text{NA}_{\text{core}}$  compensates for the dependence on  $k_0 = 2\pi/\lambda$  in eq. (2.205), leading to a plateau of the V-number in the short wavelength limit [135]. Numerical calculations show that a PCF design  $d/\Lambda < 0.45$  leads to a normalized frequency  $V_{\text{PCF}} < \pi$  for all wavelengths [143]. PCFs meeting this criterion are therefore termed "endlessly single-mode".

The endlessly single mode condition implies that the core size of a PCF can be arbitrarily scaled without losing its single-mode property, as long as  $d/\Lambda < 0.45$ . This behavior can be qualitatively understood by considering the photonic crystal cladding as a "modal sieve" [144].

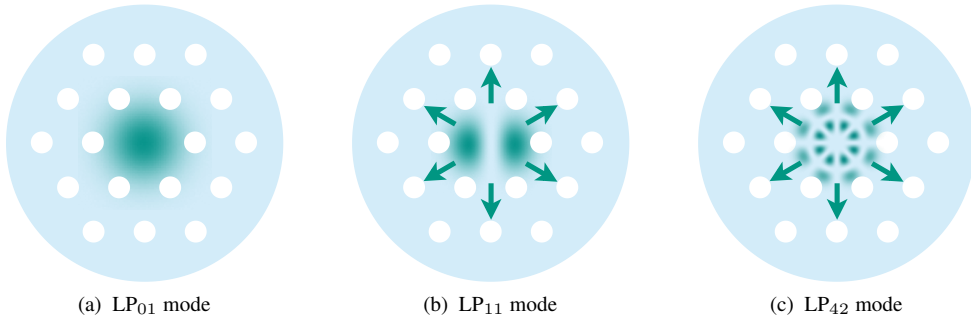


Figure 2.32: Illustration of the transverse mode selection in a PCF. The photonic crystal cladding acts as a modal sieve. In (a), the fundamental mode is confined in the core, because its effective transverse wavelength is too large to fit in the gaps between the holes. In contrast, the higher-order modes depicted in (b) and (c) have shorter transverse wavelengths and therefore leak through the gaps, preventing them from being guided in the core.

Figure 2.32 depicts the transverse intensity profiles of the fundamental  $LP_{01}$  mode, and of the higher-order modes  $LP_{11}$  and  $LP_{42}$  in the PCF air hole structure to illustrate the principle. Because of their significantly lower refractive index, the air holes represent strong barriers to light propagating in silica. They form a mesh that confines the fundamental mode to the enclosed core. Higher-order modes have a lower propagation constant  $\beta$ , which corresponds to a larger transverse component of their wavevector  $k_T^2 = (n_{\text{core}}k_0)^2 - \beta$ . This leads to a shorter effective wavelength in the transverse direction, creating a more complex mode pattern with smaller intensity lobes. If the gaps between the air holes are wide enough, these lobes can leak through the gaps, preventing the mode from being guided. By scaling the entire PCF structure, the proportions between the gaps and the mode fields remain the same. Thus, the mode field area of the fundamental mode can be increased, while higher order modes are still filtered out by the modal sieve.

The practical limit for the endlessly single-mode behavior is the weakening of light guidance when the mesh dimensions become large compared to the wavelength. An increase of the pitch  $\Lambda$  causes the effective refractive index  $n_{\text{clad,eff}}$  to approach the index of silica, resulting in a diminishing numerical aperture  $NA_{\text{core}}$ . This makes the guiding more and more sensitive to perturbations, such as fiber bending or scattering at inhomogeneities [145]. The guiding losses become substantial, below a critical bending radius  $R_c$  that follows the relation [135]

$$R_c \propto \frac{\Lambda^3}{\lambda_s^2}. \quad (2.208)$$

In order to realize very large mode field diameters, this led to the development of non-bendable PCF rods, called large pitch fibers (LPFs) [146]. The LPF technology enables core diameters of more than 100  $\mu\text{m}$  for  $\text{Yb}^{3+}$ -doped fiber lasers operating at an emission wavelength of 1  $\mu\text{m}$  with a close to diffraction limited beam quality [147, 148]. The active fibers are usually designed slightly multimode, as the large pitch delocalizes the higher-order modes from the actively doped core region. This results in a lower gain for higher-order modes and ensures a high beam quality of the laser mode. However, because the straight LPF rods cannot be coiled, their practical length is typically restricted to around 1 m. Thus, they lose some of the special features of the fiber geometry. For instance, the short fiber length generally leads to a laser operation at higher inversion, which limits the gain at long wavelengths (see fig. 2.27).

The realization of active PCFs requires careful control of the refractive index in the core. To exploit the PCF guiding effect, the core index  $n_{\text{core}}$  must closely match the index of the pure silica in the cladding. However, high doping of rare-earth ions and co-dopants such as  $\text{Al}^{3+}$  raise the refractive index of the core. To counteract this, index-depressing elements like fluorine are typically added to the doping composition [143]. The stack-and-draw fabrication process also allows for more advanced techniques to design the core index profile [138]: highly doped silica rods can be placed alongside pure silica rods in the preform. After being drawn together, they form a core with a fine-structured refractive index that appears homogeneously reduced to guided light.

### 2.3.3 Fiber Nonlinearities

Nonlinear effects in optical fibers influence the temporal and spectral output characteristics of fiber lasers and amplifiers. As a quasi-centrosymmetric material, silica fibers are mainly affected by third-order nonlinear effects and non-parametric scattering processes such as stimulated Brillouin scattering (SBS) and SRS, as described in sec. 2.1.4. Exploiting these effects enables the development of various fiber-based radiation sources, such as Raman lasers, parametric fiber oscillators and amplifiers, and supercontinuum sources [51]. However, for high-power  $\text{Tm}^{3+}$ -doped fiber lasers, nonlinear effects are usually detrimental because they limit the optical intensity that can be generated while maintaining a narrow linewidth.

The evolution of a guided laser signal is determined by the interplay of nonlinear effects and dispersion in the fiber. Assuming a linearly polarized signal propagating in a PM fiber, the electric field can be expressed within the SVEA as

$$\mathbf{E}(\mathbf{r}, t) = \mathbf{e}_x \psi(x, y) A(z, t) \exp(j(\omega_0 t - \beta_0 z)), \quad (2.209)$$

where  $\mathbf{e}_x$  is the unit vector in transverse  $x$  direction,  $\psi(x, y)$  is the transverse field distribution in the fiber, and  $A(z, t)$  is the slowly varying amplitude. In general, the signal can consist of various spectral components with frequencies  $\omega$  around the central frequency  $\omega_0$  corresponding to a propagation constant  $\beta_0 = \beta(\omega_0)$ . The temporal amplitude  $A(z, t)$  of a signal with a finite spectral bandwidth then represents, for instance, the envelope of a laser pulse. In the frequency domain, the signal is described by the corresponding Fourier transforms of the electric field  $\tilde{\mathbf{E}}$  and the slowly varying amplitude  $\tilde{A}$ , i.e.

$$\tilde{\mathbf{E}}(\mathbf{r}, \omega - \omega_0) = \mathbf{e}_x \psi(x, y) \tilde{A}(z, \omega - \omega_0) \exp(-j\beta_0 z). \quad (2.210)$$

In first-order perturbation theory, the optical Kerr effect is treated as a small perturbation  $\Delta n$  to the refractive index. This perturbation is assumed to not affect the modal distribution  $\psi(x, y)$ , but to modify the slowly varying amplitude by inducing an intensity-dependent nonlinear phase shift (see eq. (2.144)) [51]. This corresponds to a change  $\Delta\beta$  in the propagation constant, i.e.  $\tilde{\beta}(\omega) = \beta(\omega) + \Delta\beta$ , where  $\Delta\beta$  is assumed to be frequency independent for small perturbation. The dispersion relation of the propagation constant  $\beta(\omega)$  can be expanded in a Taylor series around the central frequency  $\omega_0$ , analogously to the wavenumber  $k(\omega)$  (see eq. (2.68)):

$$\beta(\omega) = \sum_{m=0}^{\infty} \frac{(\omega - \omega_0)^m}{m!} \beta_m, \quad (2.211)$$

where  $\beta_m = (d^m \beta / d\omega^m)|_{\omega_0}$ . Thus, when propagating along the fiber, each frequency component  $\omega$  within the signal envelope acquires a phase shift that is both frequency and intensity dependent [51]:

$$\frac{\partial \tilde{A}}{\partial z} \approx -j(\beta(\omega) + \Delta\beta - \beta_0) \tilde{A}. \quad (2.212)$$

In the time domain, the evolution of the slowly varying envelope  $A(z, t)$  in an active fiber is governed by the propagation equation

$$\frac{\partial A}{\partial z} - \frac{j}{2}\beta_2 \frac{\partial^2 A}{\partial T^2} + j\gamma|A|^2 A = \frac{1}{2}g(z, T) \left( A + T_2^2 \frac{\partial^2 A}{\partial T^2} \right) - \frac{\alpha}{2}A, \quad (2.213)$$

where  $\gamma$  is the nonlinear parameter,  $\alpha$  is the absorption coefficient, and  $g$  is the laser gain coefficient of the active fiber, with a gain dispersion described by the parameter  $T_2^2$  [149]. For practical convenience, the time dependence in eq. (2.213) is referenced to a retarded time frame  $T = t - z/v_g$  moving with the group velocity  $v_g$  of the signal envelope  $A$ . Furthermore,  $A$  can be normalized to units of  $\sqrt{W}$ , such that  $|A|^2$  corresponds to the optical power (see eqs. (2.28) and (2.30)). With this normalization, the nonlinear parameter  $\gamma$  is given by

$$\gamma = \frac{\omega_0 n_2}{c_0 A_{\text{eff}}}, \quad (2.214)$$

where  $n_2$  is the nonlinear Kerr index (see eq. (2.139)), and

$$A_{\text{eff}} = \frac{\left( \iint_{-\infty}^{\infty} |\psi(x, y)|^2 dx dy \right)^2}{\iint_{-\infty}^{\infty} |\psi(x, y)|^4 dx dy} \quad (2.215)$$

is the effective mode area of the intensity profile  $|\psi(x, y)|^2$  [51]. For a Gaussian beam profile, the effective area is  $A_{\text{eff}} = \pi w^2$ , which approximately also applies for the LP<sub>01</sub> mode field in a single-mode fiber using eq. (2.200). For a fiber without gain or losses, i.e.  $\alpha = 0$ ,  $g = 0$ ,  $T_2^2 = 0$ , eq. (2.213) is referred to as the nonlinear Schrödinger equation (NLSE) [51].

The intensity, pulse width, and optical gain or loss along the fiber determine whether the signal propagation is dominated by the nonlinear Kerr effect, dispersion effects, both, or neither. To identify these propagation regimes, three characteristic length scales are introduced: the nonlinear length  $L_{\text{NL}}$ , the dispersion length  $L_{\text{D}}$ , and the effective fiber length  $L_{\text{eff}}$ , defined as

$$L_{\text{NL}} = \frac{1}{\gamma P_0}, \quad L_{\text{D}} = \frac{T_0^2}{|\beta_2|}, \quad L_{\text{eff}} = \int_0^L \frac{P(z)}{P_{\text{out}}} dz, \quad (2.216)$$

where  $P_0$  is the peak power and  $T_0$  is the characteristic pulse duration of the input signal at  $z = 0$  [51]. For constant absorption and gain coefficients along the fiber length  $L$ , the effective length can be written as

$$L_{\text{eff}} = \frac{1 - e^{(g-\alpha)L}}{\alpha - g} . \quad (2.217)$$

For an effective length  $L_{\text{eff}} \ll L_{\text{NL}}$  and  $L_{\text{eff}} \ll L_{\text{D}}$ , the effects of nonlinearity and dispersion on signal propagation are negligible. Conversely, these effects become significant when the effective fiber length  $L_{\text{eff}}$  is on the order of or exceeds  $L_{\text{D}}$  and  $L_{\text{NL}}$ , respectively.

In this work, laser pulses with durations in the nanosecond regime ( $T_0 \sim 10$  ns) and peak powers of several kilowatts ( $P_0 \sim 10$  kW) are studied. For such pulses, the dispersion length is immense  $L_{\text{D}} \sim 1 \cdot 10^9$  m, while the nonlinear length is of the order  $L_{\text{NL}} \sim 1$  m, indicating that the propagation of these pulses is dominated by the nonlinear Kerr effect.

However, while dispersion has a negligible direct impact on the nanosecond pulse envelope, it can facilitate another nonlinear effect: Because the emission wavelength of Tm<sup>3+</sup>-doped fiber lasers around 2  $\mu\text{m}$  is located in the anomalous GVD regime (see fig. 2.5), it counteracts the nonlinear phase shift induced by the Kerr effect. This interplay leads to phase matching for DFWM, resulting in parametric gain for spectral sidebands that lie outside the narrow linewidth of the nanosecond pulse. Thus, instabilities within the nanosecond pulse envelope are amplified, which can cause the pulse to break up into ultrashort pulses. This effect is referred to as modulation instability (MI).

In the following, the nonlinear effects relevant for nanosecond pulses at wavelengths of 2  $\mu\text{m}$  are discussed in more detail. First, spectral broadening by SPM is described, followed by a discussion on MI. Finally, the influence of the stimulated inelastic scattering processes SRS and SBS is considered.

### **Spectral Broadening by Self-Phase Modulation**

For the case of nanosecond pulses where  $L_{\text{D}} \gg L_{\text{eff}} \sim L_{\text{NL}}$ , the generalized propagation equation (2.213) can be simplified by neglecting dispersion ( $\beta_2 = 0$ ) [51]. Furthermore, because the optical bandwidth of nanosecond pulses is typically much narrower than the broad gain spectrum of a Tm<sup>3+</sup>-doped fiber, gain dispersion can also be neglected ( $T_2^2 = 0$ ). This reduces the propagation equation to:

$$\frac{\partial A}{\partial z} = -j\gamma|A|^2 A + \frac{A}{2}(g(z, T) - \alpha) . \quad (2.218)$$

Substituting the ansatz

$$A(z, T) = A(0, T) \exp\left(j\phi_{\text{NL}}(z, T) + \frac{g(z, T) - \alpha}{2}z\right) \quad (2.219)$$

into eq. (2.218) and equating the imaginary parts yields the expression for the accumulated nonlinear phase shift along the fiber length  $L$

$$\phi_{\text{NL}}(L, T) = -\gamma|U(0, T)|^2 \int_0^L P(z) dz = -|U(0, T)|^2 \frac{L_{\text{eff}}}{L_{\text{NL}}} \quad (2.220)$$

where  $U(0, T) = A(0, T)/\sqrt{P_0}$  is the normalized temporal input pulse shape [150].

Because the nonlinear phase shift  $\phi_{\text{NL}}$  is directly proportional to the normalized intensity profile  $|U(0, T)|^2$ , the pulse acquires a temporally varying phase at the output. This corresponds to a change in the instantaneous frequency throughout the pulse, while the pulse shape remains unaffected [51]. The temporal frequency shift from the central frequency  $\omega_0$  is given by

$$\delta\omega(T) = \frac{\partial\phi_{\text{NL}}}{\partial T} = \frac{L_{\text{eff}}}{L_{\text{NL}}} \frac{\partial}{\partial T}|U(0, T)|^2 \quad (2.221)$$

and is referred to as frequency chirp [51].

Figure 2.33 shows the nonlinear phase shift  $\phi_{\text{NL}}$  and the induced frequency chirp  $\delta\omega$  for a Gaussian input pulse. The negative temporal phase shift  $\phi_{\text{NL}}$  directly follows the Gaussian intensity profile, reaching its maximum magnitude  $\phi_{\text{max}} = \gamma P_0 L_{\text{eff}}$  at the pulse peak. Because the frequency chirp  $\delta\omega$  is proportional to the derivative of the Gaussian pulse shape, it is negative on the leading edge of the pulse, corresponding to a red shift, and becomes positive at the trailing edge, meaning a blue shift. The magnitude of the chirp depends on the rising and falling slopes of the pulse and is thereby related to the pulse duration  $T_0$ .

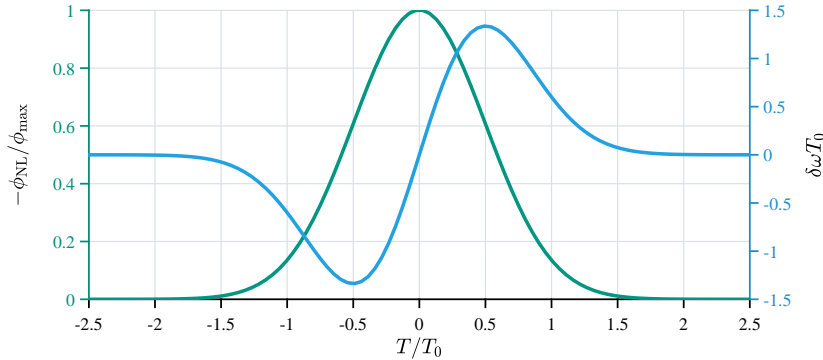


Figure 2.33: Nonlinear phase shift and induced frequency chirp for a Gaussian input pulse versus normalized time  $T/T_0$ . For the characteristic pulse duration  $T_0$ , the  $1/e^2$ -width of the Gaussian intensity profile is used.

For pulse widths in the nanosecond regime, the maximum chirp is in the MHz-range corresponding to wavelength shifts on the order of  $\sim 0.1$  pm around  $2 \mu\text{m}$ . A transform-limited nanosecond pulse would also have a bandwidth on this scale. However, real nanosecond-pulsed lasers exhibit much larger linewidths, because of their limited coherence time due to a finite resonator lifetime and technical noise (see sec. 2.2). Therefore, the coherent frequency chirp induced by SPM on the nanosecond pulse envelope is generally negligible. The linewidth of a nanosecond-pulsed laser is mainly determined by the effect of partial coherence.

The spectral power density  $S(\omega)$  of a partially coherent signal corresponds to the Fourier transform of its coherence function  $\Gamma(z, \tau)$

$$S(z, \omega) = \int_{-\infty}^{\infty} \Gamma(z, \tau) e^{j\omega\tau} d\tau \quad (2.222)$$

where

$$\Gamma(z, \tau) = \langle A^*(z, T) A(z, T + \tau) \rangle . \quad (2.223)$$

is defined as the autocorrelation function of the statistically fluctuating amplitude  $A$  [51]. A perfectly coherent CW signal would have a correlation function whose magnitude  $|\Gamma(z, \tau)| = P(z)$  is constant and non-decaying, resulting in a discrete spectral power density peak at  $\omega_0$ . In contrast, partial coherence corresponds to a decay of  $\Gamma(z, \tau)$  characterized by a  $1/e$  time constant defined as the coherence time [151]. A shorter coherence time leads to a wider bandwidth  $S(z, \omega)$ , according to the properties of the Fourier transform.

A partial coherent signal exhibits intensity and phase fluctuations in its envelope  $A$ . During propagation along a fiber, the intensity fluctuations induce additional phase fluctuations via the nonlinear phase shift  $\phi_{\text{NL}}$ , making the signal progressively less coherent. This SPM-induced degradation of coherence causes spectral broadening of the output signal [75, 151].

Assuming an initially Gaussian power spectrum  $S(0, \omega)$ , its Fourier transform yields an input coherence function that also has a Gaussian profile

$$\Gamma(0, \tau) = P_0 \exp\left(-\frac{\tau^2}{2T_c^2}\right), \quad (2.224)$$

where  $T_c$  is the coherence time of the input signal. For this specific case, the ensemble average in eq. (2.223) can be performed analytically, resulting in a coherence function

$$\Gamma(Z, \tau) = \frac{\Gamma(0, \tau)}{\left[1 + Z^2 \left(1 - \left|\frac{\Gamma(0, \tau)}{P_0}\right|^2\right)\right]^2} \quad (2.225)$$

that evolves along the normalized propagation distance  $Z = L_{\text{eff}}/L_{\text{NL}}$  [151]. With an increase in  $Z$ , the coherence function changes in shape and becomes narrower corresponding to a shorter coherence time. This in turn corresponds to a broadened output spectrum according to eq. (2.222).

Figure 2.34 shows the spectral broadening by SPM-induced coherence degradation for an initially Gaussian input spectrum at  $Z = 0$ . In fig. 2.34a, the normalized output spectra are plotted on a logarithmic scale for several values of  $Z$ . The initial linewidth  $\Delta\omega_0$  of the Gaussian input spectrum is substantially broadened for larger values of the normalized propagation distance  $Z$ . The characteristics of this spectral broadening are illustrated in fig. 2.34b, where the relative increase in 3-dB, 10-dB, and 20-dB linewidth is plotted versus  $Z$ . The relative increase in linewidth is independent of the initial linewidth  $\Delta\omega_0$  and approaches a linear dependence for large  $Z$ . The nonlinear phase shift thus causes the fiber to act effectively as a bandwidth amplifier for partially coherent light.

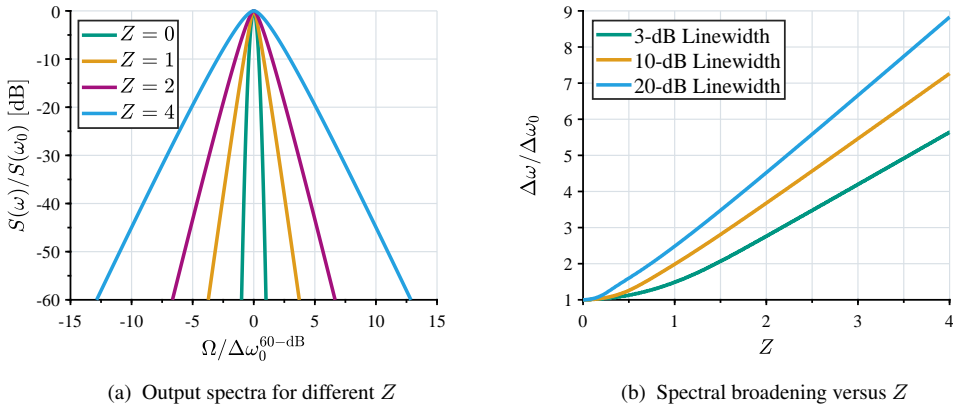


Figure 2.34: Spectral broadening of a partial coherent Gaussian laser line due to SPM. An initially Gaussian input spectrum with a linewidth  $\Delta\omega_0$  becomes progressively less coherent under the influence of SPM. This results in spectral broadening depending on the parameter  $Z = L_{\text{eff}}/L_{\text{NL}}$ .

## Modulation Instability

Although GVD is negligible for a nanosecond pulse envelope  $A(z, T)$ , it critically affects intensity and phase fluctuations that occur on a much shorter time scale. In the anomalous GVD regime at wavelengths longer than the ZDW (see fig. 2.5), higher frequency components propagate faster than lower ones through the fiber. Considering a small and short intensity ripple slightly distorting the much longer pulse envelope, the SPM-induced chirp creates lower frequencies at its leading edge and higher frequencies at its trailing edge (see fig. 2.33). Consequently, anomalous GVD causes both frequency parts to move toward the center of the ripple, leading to a growing fluctuation. This amplification of perturbations in the anomalous GVD regime can eventually result in a break up of the pulse envelope into ultra-short sub-pulses; a phenomenon known as modulation instability (MI) [152].

To analyze the instability of a nanosecond pulse envelope during propagation, a small perturbation  $a(z, T)$  is added to the steady-state solution from eq. (2.219)

$$A(z, T) = (A(0, T) + a) \exp \left( -j\gamma \int_0^L P(z, T) dz + \frac{g(z, T) - \alpha}{2} z \right) \quad (2.226)$$

where the nonlinear phase shift from eq. (2.220) was used. Substituting into the generalized propagation equation (2.213) and neglecting higher powers to the small perturbation  $a$  yields

$$\frac{\partial a}{\partial z} - \frac{j}{2}\beta_2 \frac{\partial^2 a}{\partial T^2} + j\gamma P(z, T)(a + a^*) = \frac{1}{2}g(z, T)T_2^2 \frac{\partial^2 a}{\partial T^2}. \quad (2.227)$$

By introducing  $a = u + jv$ , the separation of the real and imaginary parts results in two coupled equations

$$\frac{\partial u}{\partial z} + \frac{1}{2}\beta_2 \frac{\partial^2 v}{\partial T^2} = \frac{1}{2}gT_2^2 \frac{\partial^2 u}{\partial T^2} \quad (2.228)$$

$$\frac{\partial v}{\partial z} - \frac{1}{2}\beta_2 \frac{\partial^2 u}{\partial T^2} = \frac{1}{2}gT_2^2 \frac{\partial^2 v}{\partial T^2} - 2\gamma P(z, T)u, \quad (2.229)$$

which can be solved approximately by the ansatz [150]

$$u(z, T) = u_0(z) \exp \left[ j \left( \Omega T - \int K(z) dz \right) \right] \quad (2.230)$$

$$v(z, T) = v_0(z) \exp \left[ j \left( \Omega T - \int K(z) dz \right) \right]. \quad (2.231)$$

The perturbations  $u$  and  $v$  have the frequency  $\Omega = \omega_0 \pm \omega$  and a wavenumber  $K$ , which depends on the propagation distance  $z$ , because of gain and losses in the active fiber. Substituting the ansatz from the eqs. (2.230) and (2.231) into the coupled eqs. (2.228) and (2.229) and assuming  $\partial u_0/\partial z = 0$  and  $\partial v_0/\partial z = 0$  (SVEA), provides a set of two linear equations

$$\begin{pmatrix} \frac{g}{2}T_2^2\Omega^2 - jK(z) & -\frac{\beta_2}{2}\Omega^2 \\ \frac{\beta_2}{2}\Omega^2 + 2\gamma P(z, T) & \frac{g}{2}T_2^2\Omega^2 - jK(z) \end{pmatrix} \begin{pmatrix} v_0 \\ u_0 \end{pmatrix} = \begin{pmatrix} 0 \\ 0 \end{pmatrix}. \quad (2.232)$$

A nontrivial solution is obtained for a dispersion relation

$$K(\Omega, z) = -\frac{j}{2}g(z, T)T_2^2\Omega^2 \pm \frac{1}{2}|\beta_2\Omega| \sqrt{\Omega^2 + \text{sgn}(\beta_2)\Omega_c^2}, \quad (2.233)$$

where  $\text{sgn}(\beta_2) = \pm 1$  depending on the sign of  $\beta_2$ , and

$$\Omega_c^2(z, T) = \frac{4\gamma P(z, T)}{|\beta_2|} \quad (2.234)$$

is the characteristic frequency shift that refers to the bandwidth of the MI process [150]. Perturbations at frequencies  $\pm\Omega$  from the central carrier frequency  $\omega_0$  grow during propagation, if their wavenumber has a positive imaginary part.

In the normal GVD regime ( $\beta_2 > 0$ ), the term under the square root in eq. (2.233) is positive, meaning the parametric gain responsible for MI is absent. Any amplification or attenuation of perturbations is therefore governed by the first term  $-\frac{j}{2}g(z, T)T_2^2\Omega^2$ , which describes the dispersion of the laser gain around  $\omega_0$ . In this expression, the laser gain dispersion is approximated by a symmetric quadratic function of  $\Omega$  in the vicinity of the central signal frequency  $\omega_0$ , whose width is determined by the time constant  $T_2$  [149]. If the center frequency  $\omega_0$  is not at the gain maximum, the term  $-(1/2)gT_2^2\Omega^2$  can be replaced by  $g(z, T) (T_1\Omega - (1/2)T_2^2\Omega^2)$ , where the linear term  $T_1\Omega$  leads to an asymmetry of the gain curve around  $\omega_0$ . A positive value of  $T_1$  corresponds to an  $\omega_0$  on the lower-frequency side of the gain peak. In this case, perturbations at  $\omega_0 - \Omega$  are slightly attenuated, while perturbations at  $\omega_0 + \Omega$  are slightly amplified in relation to the pulse envelope  $A$  at  $\omega_0$ . While laser gain dispersion can provide a small gain to one side of the spectrum, it generally does not cause large instabilities in the pulse envelope. Thus, the signal is considered to be inherently stable in the normal GVD regime.

For anomalous GVD ( $\beta_2 < 0$ ), the term under the square root in eq. (2.233) becomes negative in the frequency range  $|\Omega| < \Omega_c$ . This results in a positive imaginary part of the wavenumber  $K$  for perturbation frequencies  $\pm\Omega$  on both sides of the central frequency  $\omega_0$ . Thus, the perturbations grow exponentially, depending on the local power  $P(z)$  of the laser signal, resulting in MI of the nanosecond pulse envelope. This results in a power gain of MI along the active fiber length  $L$

$$G_{\text{MI}} = \left| \frac{a(L)}{a(0)} \right|^2 = \exp(g_{\text{MI}}L) \quad (2.235)$$

with the gain coefficient

$$g_{\text{MI}} = \frac{2}{L} \text{Im} \left\{ \int_0^L K(z) dz \right\}. \quad (2.236)$$

The gain coefficient  $g_{\text{MI}}$  results from the imaginary part of the integrated perturbation wavenumber  $K(z)$ , which varies along the propagation direction  $z$  due to laser gain and losses in the active fiber [150]. This is illustrated in figure 2.35. In fig. 2.35a, three different signal power distributions  $P(z)$  along the fiber length  $L$  are shown, resulting from laser gain saturation in the active fiber. The temporal power of the nanosecond pulse is assumed to be constant.

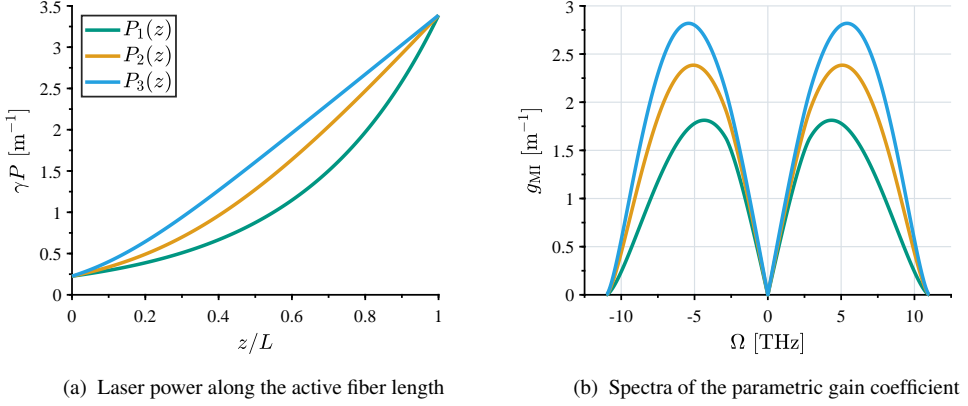


Figure 2.35: Parametric gain for MI. The laser power distributions  $P_1(z)$ ,  $P_2(z)$ , and  $P_3(z)$  shown in (a) cause the parametric gain spectra depicted in (b). The gain spectrum exhibits characteristic side peaks that increase in magnitude and frequency shift  $\Omega = \omega_0 \pm \omega$  for a higher integrated power along the active fiber length  $L$ .

The gain spectrum varies locally with the power  $P(z)$ . Depending on the local nonlinear phase shift  $\gamma P(z)$ , the gain spectrum extends symmetrically to different frequencies  $\Omega_c(z)$  (see eq. (2.234)), and becomes maximum at the frequencies [51]

$$\Omega_{\max}(z) = \pm \sqrt{\frac{2\gamma P(z)}{|\beta_2|}}. \quad (2.237)$$

Integrating the local gain  $2 \cdot \text{Im}\{K(\Omega, z)\}$  along the fiber length  $L$  yields the total gain spectra plotted in fig. 2.35b for the three power distributions  $P_1(z)$ ,  $P_2(z)$ , and  $P_3(z)$  from fig. 2.35a. The spectra exhibit two characteristic lobes located symmetrically around the center frequency  $\omega_0$  [152]. Although the input and output power  $P(0)$  and  $P(L)$  are identical in all three cases, the gain spectra differ in magnitude and frequency of their maxima—a consequence of their different integrated powers  $\int P(z) dz$ . The effect of laser gain dispersion is neglected in these plots but, as previously discussed, can cause a slight asymmetry in the parametric gain spectrum. More significant asymmetries in the parametric gain spectrum can arise in combination with other nonlinear effects, such as SRS [51].

MI can be interpreted as a DFWM process that converts two pump photons at the frequency  $\omega_0$  into a signal (anti-Stokes) and an idler (Stokes) photon at equidistant frequencies

$\omega_0 \pm \Omega$  in compliance with energy conservation [51]. Phase matching is achieved under consideration of the nonlinear phase shift  $\Delta k_{\text{NL}} = 2\gamma P(z)$  and material dispersion in the fiber

$$\Delta k_{\text{MD}} = \beta(\omega_0 + \Omega) + \beta(\omega_0 - \Omega) - 2\beta(\omega_0) \approx \beta_2 \Omega^2 \quad (2.238)$$

where the propagation constant  $\beta$  was expanded up to the second-order term ( $m = 2$ ) of eq. (2.211). In the anomalous dispersion regime, the negative  $\Delta k_{\text{MD}}$  can perfectly balance the positive nonlinear phase shift  $\Delta k_{\text{NL}}$ . The phase-matching condition  $\Delta k = \Delta k_{\text{NL}} + \Delta k_{\text{MD}} = 0$  is equivalent to eq. (2.237), defining the signal and idler frequencies with maximum parametric gain. Assuming an undepleted pump, the parametric small-signal gain of DFWM can be expressed analogously to the eqs. (2.124) and (2.125) with the coupling constant  $\kappa = 2\gamma P(z)$  and a relative phase difference  $\Delta\phi = 2\phi_{\text{pump}} - \phi_{\text{sig}} - \phi_{\text{idl}}$  [153]. The parametric gain of DFWM becomes equivalent to MI when signal and idler are initiated from noise with random phase distributions [154].

In addition to material dispersion, phase matching in optical fibers can also be achieved by transverse mode dispersion or birefringence [155, 156]. The latter can cause vector modulation instability, as a result of coupling between the polarization modes by XPM [51]. A rigorous treatment of polarization mode dispersion generally requires a full vector analysis of the propagation using coupled NLS equations [51].

For PM fibers with large birefringence  $B_m \sim 10^{-4}$ , the corresponding phase mismatch  $|\Delta\beta_{\text{B}}| = k_0 B_m \sim 300 \text{ m}^{-1}$  between the slow and the fast axis is much larger than the nonlinear phase shift  $\gamma P \sim 3 \text{ m}^{-1}$  for the case of nanosecond pulses at  $2 \mu\text{m}$ . Thus, phase matching between the fast and the slow axis requires the GVD to counteract the polarization dispersion. In the anomalous GVD regime, a pump that is polarized along the fast axis can be phase-matched to signal and idler polarized in the slow axis, with a frequency shift  $\Omega_s = \sqrt{2k_0 B_m / |\beta_2|}$  [157]. Several other phase-matching conditions exist for different polarization configurations [157]. The gain of these processes is determined by the nonlinear coupling between the polarization modes by SPM and degenerate XPM (see eqs. (2.142) and (2.143)). Because coupling by degenerate XPM between the polarization axes is  $2/3$  times weaker than coupling within the same polarization axis, the gain of vector MI is generally lower than for the scalar case. Consequently, in high-birefringence PM fibers, scalar MI remains the dominant process in the anomalous dispersion regime.

For a circularly polarized pump ( $I_x = I_y$ ), each polarization component induces a nonlinear phase shift to itself by SPM and to the other axis by degenerate XPM (see eqs. (2.142) and (2.143)). Due to the symmetrical nonlinear index change  $\Delta n = (5/6)n_2(I_x + I_y)$ , MI can be treated analogous to the scalar case with an effective nonlinear parameter that is reduced by the factor 5/6 compared to a linearly polarized pump with the same total intensity  $I = I_x + I_y$ .

The impact of MI on the temporal and spectral characteristics of a laser signal becomes significant when the power within the spectral side bands grows to a non-negligible fraction of the total output power, for instance,  $> 1\%$ . The power of MI depends on the initial noise that seeds the process and the total parametric gain  $G_{\text{MI}}$  resulting from the power distribution  $P(z)$  along the fiber length  $L$  (see eqs. (2.235) and (2.236)). Assuming an initial noise level of one photon per mode (see eq. (2.175)), the growth of MI power along the fiber can be calculated.

Figure 2.36 illustrates this exponential amplification versus fiber length  $L$ , for the three power distributions  $P_1(z)$ ,  $P_2(z)$ , and  $P_3(z)$  depicted in fig. 2.35a with linear polarization (solid curves) and circular polarization (dotted curves), respectively. Depending on the nonlinear gain (see fig. 2.35b), MI becomes significant ( $P_{\text{MI}}/P_{\text{out}} > 0.01$ ) when the fiber length exceeds a critical length. The threshold for circularly polarized light is higher than for linearly polarized light, corresponding to a longer critical length. To suppress significant MI, a fiber laser design must consider the power distribution  $P(z)$  in the fiber, the effective mode field area  $A_{\text{eff}}$  given by the waveguide geometry, and the fiber length  $L$ .

Further amplification of MI causes the propagating signal to approach a new steady-state solution of the propagation equation (2.213). As the perturbations grow, the pump is depleted and the propagation is governed by the peak power and durations of the perturbations rather than by the initial nanosecond pulse envelope. The pulse envelope finally breaks up into a train of ultra-short pulses with a temporal period  $T_m = 2\pi/\Omega_{\text{max}}$ , corresponding to the creation of higher-order sidebands located at  $\omega_0 \pm m\Omega_{\text{max}}$  ( $m = 2, 3, \dots$ ) in the output spectrum [51]. These individual pulses evolve during propagation until the effects of nonlinear phase shift and anomalous dispersion achieve a dynamic balance, resulting in a pulse shape that remains constant or changes in a periodic manner. Such pulses are termed solitons, representing eigensolutions of the NLSE [51]. The formation and subsequent dynamic of these solitons are accompanied by substantial spectral broadening, leading to the generation of a supercontinuum that is further expanded by SRS [158].

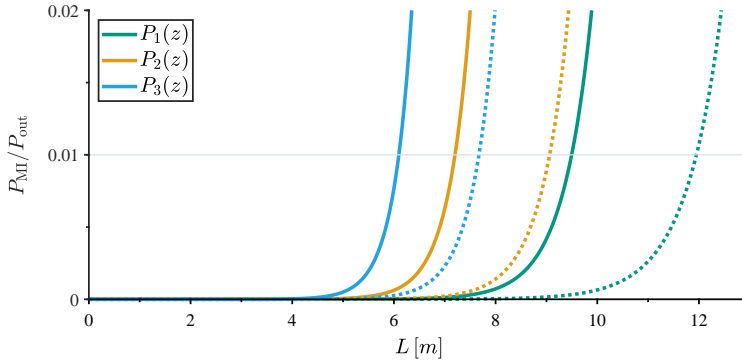


Figure 2.36: Power content within the spectral side bands  $P_{\text{MI}}$  induced by MI in relation to the total output power  $P_{\text{out}}$  versus the fiber length  $L$ . The curves show the amplification of MI for the laser power distributions  $P(z)$  depicted in fig. 2.35a with linear polarization (solid curves), and circular polarization (dotted curves), respectively. A longer fiber length leads to an exponential increase of the MI power content, which becomes significant ( $P_{\text{MI}}/P_{\text{out}} > 0.01$ ) above a critical fiber length.

## Stimulated Inelastic Scattering Processes

The most relevant stimulated inelastic scattering processes, SBS and SRS, have already been introduced in sec. 2.1.4 as examples of non-parametric nonlinear effects related to the imaginary part of the third-order susceptibility  $\chi^{(3)}$  in the nonlinear material. In both processes, a pump photon is inelastically scattered on a phonon in the material, thereby converting into a frequency-downshifted Stokes photon and another phonon with the same energy as the initiating one. This results in a resonant energy transfer process from the pump field to the Stokes field with a gain depending on the properties of the material and the intensity of the pump field. The two processes exhibit distinct gain spectra as a result of the different energy of the involved phonons; while SBS occurs with acoustic phonons, SRS involves optical phonons. In the context of optical fibers, the high intensities and long interaction lengths can cause high gain levels for both stimulated scattering processes, resulting in the generation of substantial Stokes signals seeded by vacuum noise when the pump power exceeds a certain threshold [159].

In SBS, the transition of the pump wave into the Stokes wave creates an acoustic wave with a wavevector  $\mathbf{k}_A = \mathbf{k}_{\text{pump}} - \mathbf{k}_{\text{Stokes}}$  and an acoustic frequency  $\Omega_{\text{SBS}} = \omega_{\text{pump}} - \omega_{\text{Stokes}}$ , satisfying conservation of energy and momentum. Because the acoustic frequency is much lower than the optical frequency ( $\Omega_{\text{SBS}} \ll \omega_p$ ), the magnitude of the pump and Stokes wavevectors are

nearly identical, i.e.  $|\mathbf{k}_{\text{pump}}| \approx |\mathbf{k}_{\text{Stokes}}|$ . This leads to the dispersion relation of the acoustic wave

$$\Omega_{\text{SBS}} = v_A |\mathbf{k}_A| \approx 2v_A |\mathbf{k}_{\text{pump}}| \sin\left(\frac{\theta}{2}\right) \quad (2.239)$$

where  $v_A$  is the velocity of sound in the fiber and  $\theta$  is the angle between the pump and the Stokes field [51]. Because the waves can only propagate in two directions in a single-mode fiber, i.e.  $\theta = \pi$  or  $\theta = 0$ , the generation of a Stokes wave by SBS is significant only in the counter-propagating direction to the pump ( $\theta = \pi$ ), as  $\Omega_{\text{SBS}}$  vanishes in forward direction ( $\theta = 0$ ). Using the sound velocity of  $5.96 \text{ km s}^{-1}$  in silica results in a Brillouin frequency shift of  $\Omega_{\text{SBS}}/2\pi \approx 8.5 \text{ GHz}$  for a pump wavelength of  $2 \mu\text{m}$ .

The small-signal gain for SBS in the backward direction of an active fiber is defined as

$$G_{\text{SBS}} = \frac{I_{\text{Stokes}}(0)}{I_{\text{Stokes}}(L)} = \exp\left(g_{\text{SBS}} \frac{P_0 L_{\text{eff}}}{A_{\text{eff}}} + (g - \alpha)L\right) \quad (2.240)$$

where the undepleted pump approximation is used and the Stokes intensity  $I_{\text{Stokes}}$  is assumed to experience the same laser gain  $g$  and propagation losses  $\alpha$  in the active fiber as the pump [51]. The Brillouin gain coefficient  $g_{\text{SBS}}(\Omega)$  has a narrow spectral width of typically  $\Delta f_{\text{SBS}} \sim 13 \text{ MHz}$ , related to the fast decay time of the acoustic phonons  $\tau_A < 10 \text{ ns}$  in the waveguide [51, 160]. Its peak value  $g_p$  at  $\Omega = \Omega_{\text{SBS}}$  is in the range  $3\text{--}5 \cdot 10^{-11} \text{ m W}^{-1}$  and nearly independent of the pump wavelength [51]. The exact Brillouin gain spectrum depends on the fiber design and can exhibit several side peaks corresponding to different guided acoustic modes [161]. Moreover, if the pump spectrum is wider than the Brillouin linewidth  $\Delta f_{\text{SBS}}$ , the effective SBS gain spectrum results from the convolution of the Brillouin gain coefficient  $g_{\text{SBS}}(\Omega)$  with the pump spectrum  $S_{\text{pump}}(\Omega)$  [51]. Consequently, for a pump linewidth  $\Delta f_{\text{pump}} \gg 13 \text{ MHz}$ , the effective Brillouin gain spectrum  $g_{\text{SBS}}^{\text{eff}}(\Omega)$  approaches the width of the pump spectrum. This effectively reduces the peak gain to  $g_p^{\text{eff}} \approx (\Delta f_{\text{SBS}}/\Delta f_{\text{pump}})g_p$  [51].

The critical pump power for which the Stokes signal builds up to a significant level from vacuum noise can be found, by considering the amplification of noise power (see eq. (2.175)) with the small-signal gain (see eq. (2.240)) and integrating over the effective gain spectrum. In a passive fiber without laser gain, this results in an estimated pump power threshold for SBS given by [159]

$$P_{\text{th}}^{\text{SBS}} \approx 21 \frac{A_{\text{eff}}}{g_p^{\text{eff}} L_{\text{eff}}}. \quad (2.241)$$

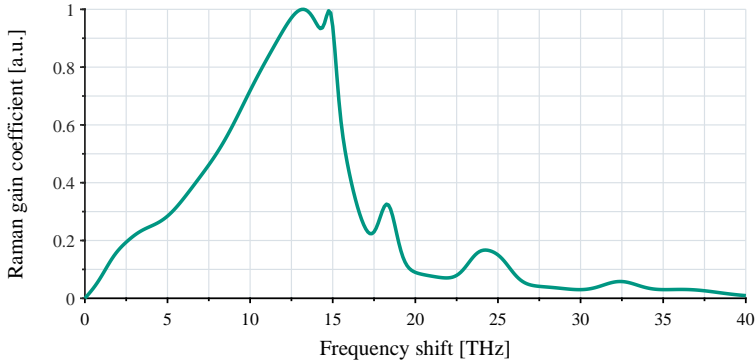


Figure 2.37: Normalized Raman gain coefficient  $g_{\text{SRS}}/g_{\text{p}}$  versus the frequency shift  $\Omega/(2\pi)$ . The spectrum is modeled according to [164]. At a pump wavelength of  $2\ \mu\text{m}$ , the SRS peak value is about  $0.5 \cdot 10^{-13}\ \text{m W}^{-1}$ .

In contrast to SBS, SRS involves the creation of optical phonons with much higher energy, corresponding to the resonant excitation of molecular vibrational modes in the material. Because these vibrational modes merge into a broad spectral continuum in amorphous glasses, the SRS gain spectrum in fused silica spans a wide range up to 40 THz [51, 162]. Figure 2.37 shows the spectrum of the normalized Raman gain coefficient. The peak of the gain coefficient  $g_{\text{SRS}}(\Omega)$  occurs at a frequency shift of approximately 13 THz [163]. The SRS gain scales inversely with the pump wavelength, and has a peak value of about  $g_{\text{p}} \sim 0.5 \cdot 10^{-13}\ \text{m W}^{-1}$  at a pump wavelength of  $2\ \mu\text{m}$  [51]. Moreover, SRS can cause a significant Stokes signal in co- as well as in counter-propagating direction of the pump [51]. In forward direction, the SRS small-signal gain can be expressed as

$$G_{\text{SRS}} = \frac{I_{\text{Stokes}}(L)}{I_{\text{Stokes}}(0)} = \exp\left(g_{\text{SRS}} \frac{P_0 L_{\text{eff}}}{A_{\text{eff}}} - \alpha L\right) \quad (2.242)$$

where the frequency-downshifted Stokes signal is assumed to be outside of the laser gain spectrum, but to experience the same background losses  $\alpha$  in the fiber [163].

The pump power threshold for significant SRS build-up from noise can be estimated analogous to SBS. For forward-SRS in a passive fiber this yields [159]

$$P_{\text{th}}^{\text{SRS}} \approx 16 \frac{A_{\text{eff}}}{g_{\text{p}}^{\text{eff}} L_{\text{eff}}}. \quad (2.243)$$

For pulse propagation in optical fibers, SBS and SRS can generate frequency-shifted Stokes pulses that subsequently interact with the pump pulse via XPM [51]. Although the SBS gain coefficient is intrinsically higher than that of SRS, its effective gain is highly sensitive to the pump linewidth. Consequently, SBS typically dominates only for narrow pump spectra up to  $\Delta f_{\text{pump}} \approx 3\text{--}5$  GHz ( $\Delta\lambda_{\text{pump}} < 40\text{--}70$  pm). For pulses with broader spectra, for instance, as a result of short pulse durations or spectral broadening by SPM, the Brillouin gain diminishes. Specifically, for pulse durations comparable to the acoustic phonon lifetime ( $\sim 10$  ns), SBS enters the transient regime. In this, the acoustic wave cannot reach its steady-state amplitude during the pulse, resulting in a significantly higher SBS threshold and allowing SRS to become the dominant process [51].

The propagation equation (2.213) must be adapted by adding a Raman response function  $R(t)$ , if the pulse spectrum expands over  $\sim 100$  GHz with a significant fraction of power [51]. For such wide pulse spectra, a phenomenon called intrapulse Raman scattering can occur, in which SRS amplifies the lower-frequency components of a pulse by transferring energy from the higher-frequency components [51]. This results in a Raman-induced red shift of the pulse; in the context of solitons also known as soliton self-frequency shift [165]. Solitons created by MI in the anomalous dispersion regime therefore expand their spectra to longer wavelengths while propagating along the fiber, which can be used for supercontinuum generation in the mid-IR [158].

### 2.3.4 Fiber Laser Architectures

The architecture of a fiber laser system is a critical factor in the development of reliable, high-power laser sources. Modern fiber laser designs integrate oscillators, amplifiers, and pump sources into a monolithic all-in-fiber system. The term "all-in-fiber" means that the laser signal is guided entirely within an optical fiber from its generation to the output. Such a design is enabled by specialized fiber-integrated laser components, such as FBGs and pump combiners. While high-performance fiber components are readily available in the  $1\ \mu\text{m}$  regime, their availability and performance at  $2\ \mu\text{m}$  are still limited, although the market is continuously growing. Consequently, the in-house manufacturing of these fiber components remains a key competence for realizing reliable high-power  $\text{Tm}^{3+}$ -doped fiber lasers at  $2\ \mu\text{m}$ . All-in-fiber integration provides compact and robust laser systems, ideally suited for a wide range of applications.

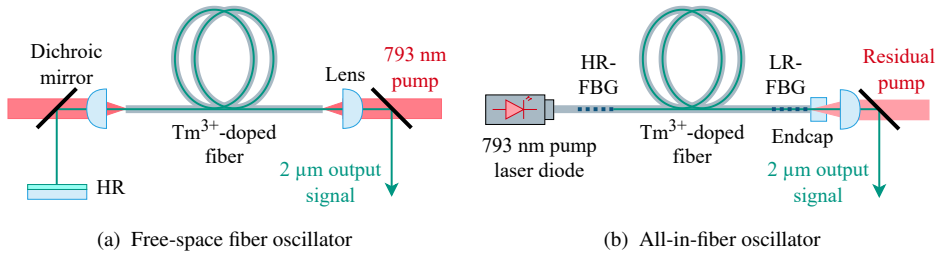


Figure 2.38: Linear fiber laser oscillator. Alignment sensitive free-space components can be replaced by fusion-spliced FBGs on both ends of the fiber resonator.

The basis of every laser system is an optical oscillator, which initially generates the coherent light, as discussed in sec. 2.2. A fiber laser oscillator consists of an actively doped fiber placed within an optical resonator. Figure 2.38a shows a schematic of a typical linear  $\text{Tm}^{3+}$ -doped fiber oscillator built with optical free-space components. The  $\text{Tm}^{3+}$ -doped fiber is pumped from both sides by laser diodes emitting at a wavelength of 793 nm. On each side, the pump light is collimated and then focused by an aspherical lens into the pump cladding of the active double-clad fiber. This bidirectional pump configuration provides a more uniform population inversion along the fiber compared to single-sided pumping. This avoids detrimental effects at high inversion levels, such as a lower CR1 rate (see sec. 2.3.1), and reduces the heat load per fiber end, thus reducing the risk of damage.

The laser cavity is formed between an HR mirror on one end and the straight-cleaved fiber facet on the other, which typically serves as the OC. At the HR end, the signal must be coupled into free space to get feedback from the external mirror—usually a broadband dielectric mirror or a wavelength-selective Bragg grating. In this free-space path, the signal is collimated, reflected by the HR, and then re-focused into the fiber core using the same lens as for the pump coupling. At the opposing output end, the Fresnel reflection of approximately 4% from the straight fiber endface provides sufficient feedback for efficient laser operation, because of the high single-pass gain of the active fiber. Dichroic mirrors with a dielectric coating that is highly reflective at  $2\ \mu\text{m}$  and highly transmissive for the 793 nm pump light are used to separate pump and laser radiation on both ends of the laser.

Free-space fiber oscillators are widely used in experimental setups for research and development because they allow for easy exchange of components and the active fiber. They have been shown to produce output powers up to 300 W with nearly diffraction-limited beam quality at wavelengths around 2  $\mu\text{m}$  [108, 166]. However, free-space coupling of the pump and especially of the signal into the small waveguide structures makes this approach very sensitive to misalignment of the optical components. Handling of high optical powers is particularly challenging in such a configuration, because heating of the components can cause their misalignment and can also induce refractive index changes leading to thermal lensing effects that degrade the coupling efficiency.

The sensitive free-space coupling can be omitted by replacing the free-space cavity with a pair of FBGs, which are fusion-spliced to both ends of the active fiber. Figure 2.38b shows an all-in-fiber design of a  $\text{Tm}^{3+}$ -doped fiber oscillator. A highly-reflective FBG (HR-FBG) and a low-reflective FBG (LR-FBG), act as the HR and OC mirrors of the linear cavity, respectively. This monolithic resonator eliminates the need for mechanical alignment of mirrors and lenses and provides stable laser operation that is largely insensitive to environmental conditions or power level. Pump light from a fiber-coupled laser diode can be delivered via a direct splice to the HR end of the fiber oscillator. Alternatively, a pump combiner can be used, which will be discussed below. For improved power handling, the output end is terminated with an endcap—a short segment of silica glass spliced to the fiber end for its protection. When the laser beam exits the fiber core, it expands during propagation through the endcap, resulting in a lower intensity at the vulnerable glass-to-air interface. This reduces the risk of damage at high power levels due to absorption and scattering by dust particles or irregularities on the output surface. Furthermore, any reflection from the output surface of the endcap is highly divergent, which minimizes its recoupling into the core and suppresses parasitic feedback.

Monolithic  $\text{Tm}^{3+}$ -doped fiber oscillators have been demonstrated to achieve output powers up to 680 W [167]. However, this approach also comes with significant challenges. Intra-cavity splice connections are exposed to high optical powers. Even small coupling losses can cause localized heating and eventual damage. Moreover, splice imperfections can also distort the beam profile by scattering light into cladding or pedestal modes. This issue can be remedied by inscribing the FBGs directly into the active fiber [168]. Another challenge arises when high pump or signal power propagates through the FBGs, thermally inducing a change in the grating period. Asymmetric heating between the HR- and LR-FBG can reduce their spectral overlap, causing destabilization of the laser oscillation or even self-pulsing [169].

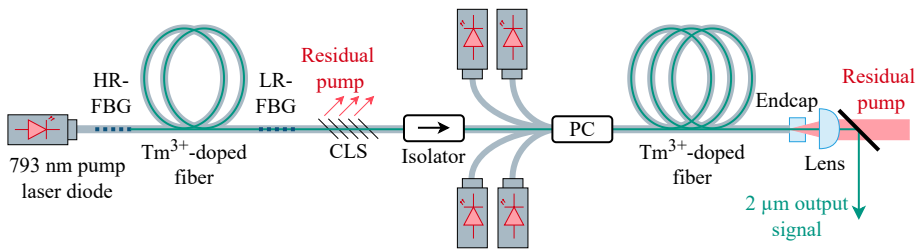


Figure 2.39: Fiber laser master oscillator power amplifier (MOPA). A monolithic design is enabled by fiber-integrated components, such as cladding light strippers (CLS), fiber-coupled optical isolators, and pump combiners (PC).

The most widely adopted solution to these issues is to separate signal generation and power amplification, by using a master oscillator power amplifier (MOPA) architecture. Figure 2.39 shows a two-stage  $\text{Tm}^{3+}$ -doped fiber MOPA configuration. The MOPA comprises a fiber oscillator that generates a stable seed signal with low to moderate power—the master oscillator—followed by one or more amplifier stages to scale the output power. The master oscillator is often a compact all-in-fiber laser built with FBGs, similar to the design in fig. 2.38b. Because it operates in a lower power regime, single-mode fibers can be used to ensure excellent beam quality, while the thermal issues discussed previously are less of a concern. Fiber lasers are particularly well-suited for the MOPA approach, as the long and easily saturated active fibers enable efficient power amplification with high gain. Despite the increase in system complexity, all-in-fiber integration of the MOPA allows for compact and robust laser designs. A monolithic MOPA chain is enabled by the implementation of several fiber-integrated components such as cladding light strippers (CLS), fiber-coupled isolators, and pump combiners.

Non-absorbed residual pump power at the end of a MOPA stage often needs to be removed from the cladding to avoid potential damage of subsequent components. This is accomplished with a CLS that releases light from being guided in the cladding. A CLS also serves to clean the beam profile by removing undesired signal light that has leaked from the core at splice connections. There are several methods to create a CLS by modifying the NA of the cladding, including recoating a fiber segment with a high-index polymer or cutting microstructures into the cladding by means of a  $\text{CO}_2$  laser [170, 171]. The challenge in designing a CLS is to achieve high cladding light attenuation over a sufficient length to avoid local heating.

In between the stages of a MOPA system, optical isolators prevent backscattered light and ASE from entering and destabilizing the previous stage. Optical isolators are usually based on

the Faraday effect, where a magnetic field rotates the polarization of forward and backward-propagating light in the same direction [40]. When combined with polarizers at the input and output, this non-reciprocal rotation ensures that light can only pass in the forward direction. Although there are approaches for all-in-fiber isolators [172], the devices typically contain free-space optics, but can be packaged and equipped with fiber connectors for compact integration in a fiber laser. Due to coupling losses and thermal management, these fiber-coupled isolators are currently limited to power levels of a few tens of watts in the 2  $\mu\text{m}$  wavelength range. Fiber circulators are related devices based on the same principle, which govern light sequentially between three or more fiber ports [173].

Pump combiners are used to couple several pump delivery fibers to the cladding of a double-clad fiber. Two general architectures of pump combiners are available: tapered fused-fiber bundles (TFBs) and side combiners. TFBs combine several pump delivery fibers in a capillary, which is tapered down to match the diameter of a subsequent double-clad fiber [174]. They are commonly used in co-pumping configurations, because it is difficult to isolate the pump fibers from a high-power output signal in a counter-pumping configuration [15]. TFBs often also incorporate a mode-field adapter that matches an input signal fiber with a smaller core diameter to the larger core diameter of the output fiber [175]. Side combiners can be applied in co- and counter-pumping configurations, but generally have lower pump coupling efficiencies [176, 177]. They are made by fusing a tapered pump fiber to the side of the double-clad fiber, which results in pump coupling depending on the NA of the multimode pump light.

The final power amplifier in the MOPA chain is usually based on a few-moded LMA fiber to reduce the intensity and mitigate nonlinear effects. Because the power amplifier consists of a single active fiber, splice connections that experience high optical powers are omitted, with the exception of the endcap splice terminating the output end. However, this splice is less critical, because it does not require the precise alignment of guiding microstructures. All-in-fiber MOPA systems have demonstrated output powers up to 1 kW with nearly diffraction-limited beam quality at wavelengths around 2  $\mu\text{m}$  [18–21].

## 2.4 Pulse Generation in Fiber Lasers

Pulsed fiber lasers emit their output power not continuously, but in short optical pulses. The peak power of these high-energy pulses can exceed the power in CW operation by several orders of magnitude. They are used whenever short-term intensity or fluence is crucial, rather than the average power delivered over time, for instance, in precise material processing, minimally invasive surgery, and for exploiting intensity-dependent nonlinear effects. Pulsed fiber lasers are categorized according to the pulse durations they deliver: Quasi-CW fiber lasers produce typical pulse durations as short as microseconds, which are generated by modulating the supplied pump power; nanosecond-pulsed fiber lasers rely on the mutual dynamics between population inversion and laser power and are realized by the methods of Q-switching, gain-switching, or by amplifying seed-pulses from a laser diode; finally, ultrafast fiber lasers generate pulse durations in the pico- to femtosecond regime, achieved through mode-locking techniques [15, 52].

In this work, nanosecond-pulsed fiber lasers are studied, as they are particularly well-suited to pump nonlinear converters efficiently. In contrast to the other pulsed fiber laser classes, they have the advantage of combining several crucial requirements, including high pulse energies in the range of hundreds of microjoules to millijoules, tens of kilowatt peak power, high average output powers greater than 100 W with nearly diffraction-limited beam quality, and a narrow spectral linewidth.

The mutual dynamics of population inversion and laser power are governed by the laser rate equations eqs. (2.180) and (2.181). A pulsed laser behavior based on these dynamics has already been discussed in sec. 2.2.2, in the context of spiking, caused by a substantial perturbation from the steady state. In contrast to spiking, where the pulses become smaller and smaller, it is generally desirable for pulsed lasers to deliver repeated pulses with the same characteristics, i.e. pulse energy, peak power, and duration. Consequently, the perturbation is replaced by a controlled modulation of the operation state. While Q-switching relies on modulating the Q-factor of a laser resonator (see eq. (2.154)), gain-switched lasers are repeatedly pumped by short pulses to achieve controlled pulse generation. In a diode-seeded fiber MOPA, seed pulses are injected at a repetition frequency that allows the gain to recover to a consistent level between the pulses.

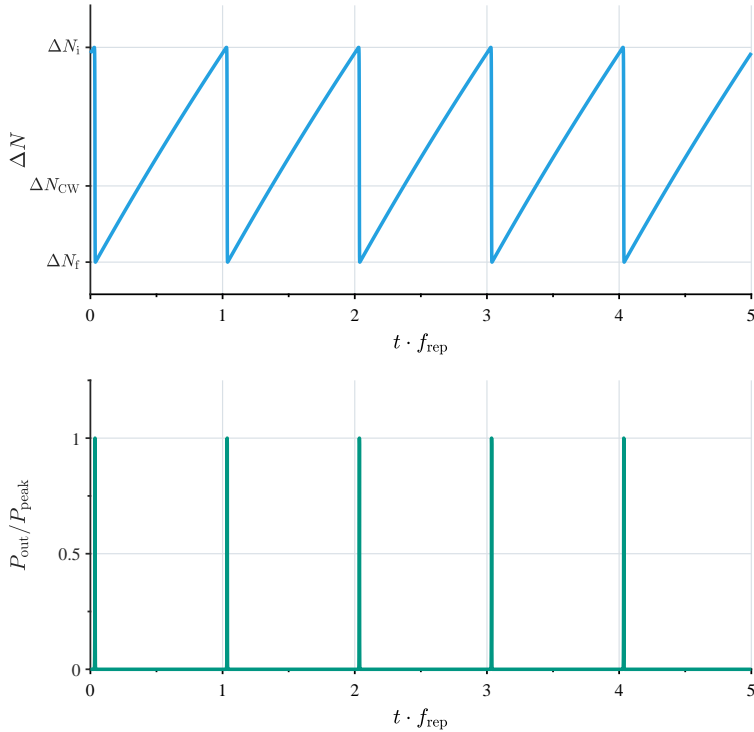


Figure 2.40: Dynamics in population inversion (top) and output power (bottom) for repetitive pulse extraction. The inversion charges in between the pulses and discharges by extracting energy in the pulse.

Figure 2.40 shows the dynamics in population inversion  $\Delta N$  and output power  $P_{\text{out}}$  of a laser gain medium for the repetitive extraction of nanosecond pulses. The output pulses are generated with a pulse repetition frequency  $f_{\text{rep}}$ , which is typically in the range of  $\sim 5\text{--}100$  kHz for pulsed  $\text{Tm}^{3+}$ -doped fiber lasers. A corresponding pulse repetition period  $T_{\text{rep}}$  comprises two intervals: a period  $T_{\text{charge}}$  in which the inversion is charged, and a period  $T_{\text{ext}}$  in which the energy is extracted. Similarly to spiking, the extraction process is significantly faster than the charging process (see fig. 2.20b), which is associated with the different time constants of the inversion  $\tau$  and of the photon field  $\tau_c$  in the rate eqs. (2.180) and (2.181).

The population inversion  $\Delta N$  oscillates between the levels  $\Delta N_i$  and  $\Delta N_f$ , defined as the initial inversion right before the pulse extraction, and the final inversion after the pulse is extracted. During the charging period  $T_{\text{charge}}$ , there is no significant photon field in the active fiber that

would deplete the inversion. Thus, the inversion builds up by absorbing the supplied pump power, until it reaches the level  $\Delta N_i$ . Subsequently, the inversion is discharged, dropping to the final level  $\Delta N_f$ , and the corresponding energy difference is extracted into the laser pulse.

The extracted energy is given by

$$E_{\text{ext}} = \frac{1}{2} \frac{hc_0}{\lambda_s} V (\Delta N_i - \Delta N_f) , \quad (2.244)$$

where  $V = A_{\text{core}}L$  is the volume of the doped fiber core and the factor  $1/2$  accounts for the fact that each excitation of  $\Delta N = N_2 - N_1$  is counted twice [42]. This expression can be written in terms of optical gain in the fiber, using eq. (2.163), resulting in

$$E_{\text{ext}} = E_{\text{sat}} \ln \left( \frac{G_i}{G_f} \right) , \quad (2.245)$$

where

$$E_{\text{sat}} = \frac{hc_0}{\lambda_s} \frac{A_{\text{core}}}{\Gamma_s [\sigma_a(\lambda_s) + \sigma_e(\lambda_s)]} \quad (2.246)$$

is the saturation energy containing the overlap factor  $\Gamma_s$  of the signal mode with the doped core area  $A_{\text{core}}$ . The saturation energy connects the energy extracted by a pulse, with the initial and final gain levels  $G_i$  and  $G_f$  before and after the pulse is extracted [41]. In accordance to eq. (2.245), the saturation energy is defined as the extracted energy that leads to a decay of the gain to  $1/e$  of its initial value.

The output pulse energy  $E_{\text{pulse}}$  of a laser oscillator corresponds to the extracted energy that is coupled out at the OC, i.e.

$$E_{\text{pulse}}^{\text{osc}} = \eta_R E_{\text{ext}} , \quad (2.247)$$

with the resonator efficiency given by eq. (2.159). For an amplifier, the output pulse energy results from the sum of input energy and extracted energy, if propagation losses can be neglected:

$$E_{\text{pulse}}^{\text{amp}} = E_{\text{in}} + E_{\text{ext}} . \quad (2.248)$$

The expression for the saturation energy, eq. (2.246), highlights a fundamental challenge in scaling the pulse energy from fiber lasers. Due to its direct proportionality to the core area ( $E_{\text{sat}} \propto A_{\text{core}}$ ), the small cores in optical fibers result in a low saturation energy compared to

bulk solid-state lasers. The lower saturation energy demands substantially higher initial gain levels to achieve the same pulse energy. However, a high gain causes strong ASE or parasitic lasing which relies on feedback from minor parasitic reflections [178]. Both effects limit the maximum gain in a fiber laser.

To increase the gain, the energy  $E = E_{\text{sat}} \ln G$  is stored in the form of population inversion  $\Delta N$  in the fiber. As shown in fig. 2.40, the inversion can significantly exceed the level  $\Delta N_{\text{CW}}$ , at which a CW laser would operate to produce the same average power in steady state. An ideal linear charging slope of the inversion proportional to the supplied pump power would mean that the pulsed laser operates as efficiently as in CW operation. However, in reality, the inversion charges with a curved characteristic, due to a progressively reduced pump absorption efficiency, spontaneous decay, and inversion-dependent energy transfer processes (see eq. (2.166)). In a fiber laser, the inversion is further depleted during the charging period by ASE proportional to the gain along the fiber (see eq. (2.174)). This flattens the inversion build-up at high gain levels, making further energy storage increasingly inefficient until it eventually saturates [178]. Furthermore, the occurrence of parasitic oscillations clamps the gain when it becomes high enough that the feedback condition (see eq. (2.176)) is fulfilled via parasitic reflections, which prevents any further storage of energy in the fiber.

In the absence of significant ASE or parasitic lasing between the output pulses, the pulse energy can be determined by dividing the average output power  $P_{\text{avg}}$  by the pulse repetition frequency  $f_{\text{rep}}$ :

$$E_{\text{pulse}} \approx \frac{P_{\text{avg}}}{f_{\text{rep}}}. \quad (2.249)$$

Although the maximum pulse energy from fiber lasers is limited, they remain superior in scaling of the average output power compared to bulk-solid state lasers, due to the beneficial fiber geometry (see sec. 2.3). When operated at high pulse repetition frequencies, nanosecond-pulsed fiber lasers have the potential to achieve high-average output powers, with excellent beam quality and a narrow linewidth in a compact and robust all-in-fiber configuration.

To characterize pulsed outputs more precisely, it is useful to introduce a metric that accounts for the temporal pulse shape. While the average power describes the temporal average of the laser output power and the pulse energy is the integral of the power over time, both metrics lose the information about the temporal profile of the output power. To account for the power distribution versus time, the effective power is defined [179]:

$$P_{\text{eff}} = \frac{\int_0^{T_{\text{rep}}} P^2(t) dt}{\int_0^{T_{\text{rep}}} P(t) dt}. \quad (2.250)$$

The effective power  $P_{\text{eff}}$  is the energy-weighted mean of the instantaneous power. Thus, it represents the mean power level at which the energy is concentrated. The effective power can be interpreted as the temporal equivalent to the effective intensity  $I_{\text{eff}} = P/A_{\text{eff}}$  defined by the effective mode area  $A_{\text{eff}}$  in the spatial domain (see eq. (2.215)). These spatial quantities are commonly used in nonlinear optics or to characterize damage thresholds. Analogously to the effective area  $A_{\text{eff}}$ , an effective duration can be defined in the temporal domain

$$T_{\text{eff}} = \frac{\left(\int_0^{T_{\text{rep}}} P(t) dt\right)^2}{\int_0^{T_{\text{rep}}} P^2(t) dt} \quad (2.251)$$

leading to the relation  $P_{\text{eff}} = E_{\text{pulse}}/T_{\text{eff}}$ . The effective power  $P_{\text{eff}}$  is a suitable metric for comparing the temporal power density of pulsed laser sources, as it directly incorporates the pulse shape.

Figure 2.41 illustrates the meaning of the introduced quantities  $P_{\text{eff}}$  and  $T_{\text{eff}}$  by comparing three examples for different pulse shapes. The  $y$ -axis describes the instantaneous power  $P(t)$  normalized by  $P_{\text{eff}}$  and the  $x$ -axis describes the time  $t$  normalized by  $T_{\text{eff}}$ . The three pulses with Gaussian, rectangular and exponential shapes exhibit the same pulse energy  $E_{\text{pulse}}$ , as well as the same effective power  $P_{\text{eff}}$  and effective pulse duration  $T_{\text{eff}}$ . However, their peak powers and full width at half maximum (FWHM) pulse durations differ significantly. For the rectangular pulse, the peak power corresponds to the effective power  $P_{\text{eff}}$  and the FWHM pulse duration to the effective pulse duration  $T_{\text{eff}}$ . The Gaussian pulse has a peak power of  $\sqrt{2} \cdot P_{\text{eff}} \approx 1.41 \cdot P_{\text{eff}}$  and an FWHM pulse duration of  $\sqrt{2 \ln 2 / \pi} \cdot T_{\text{eff}} \approx 0.66 \cdot T_{\text{eff}}$ , while the exponential pulse exhibits a peak power of  $2 \cdot P_{\text{eff}}$  and an FWHM pulse duration of  $\ln 2 / 2 \cdot T_{\text{eff}} \approx 0.34 \cdot T_{\text{eff}}$ . From this comparison, it is evident that while the Gaussian and, more prominently, the exponential pulses have significantly higher peak powers and narrower FWHM durations, a substantial portion of their energy is distributed in the pulse tails. This means that, compared to the rectangular pulse, more of their energy resides at instantaneous power levels below their respective peaks. This illustrates that relying solely on peak power and FWHM can be misleading, as these metrics tend to overstate the temporal power density for

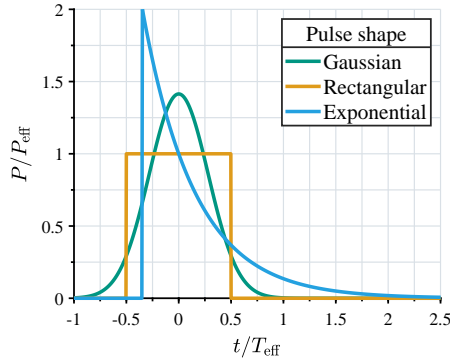


Figure 2.41: Comparison of different temporal pulse shapes that exhibit the same pulse energy  $E_{\text{pulse}}$  and the same effective power  $P_{\text{eff}}$ .

pulses with long tails. In contrast, the effective power  $P_{\text{eff}}$  accounts for the entire pulse profile and therefore provides a characteristic scalar metric for comparing the actual temporal power density of different pulsed laser sources.

In the following, concepts for pulsed-fiber lasers are discussed and the state of the art of these systems is reviewed, with special focus on  $\text{Tm}^{3+}$ -doped fiber lasers at wavelengths around  $2\ \mu\text{m}$ . First, the method of active Q-switching is introduced, followed by a discussion of pulse amplification in fiber lasers. Finally, concepts and analyses for pulse energy scaling are considered, and reported high-pulse-energy fiber laser systems at  $2\ \mu\text{m}$  are reviewed.

### 2.4.1 Active Q-switching

In Q-switching, the damping of a laser oscillator is modulated in order to generate pulses with durations in the nanosecond regime. The Q-factor was introduced by eq (2.154) as a measure of damping in a resonator. A laser with a high Q-factor is weakly damped, resulting in an inertial resonator field characterized by a long photon lifetime  $\tau_c$  (see eq. (2.153)), and a low laser threshold  $G_{\text{th}}$  given by eq. (2.176) for a linear cavity. By modulating the losses  $\Lambda$  in the laser cavity, its Q-factor is switched between a high and a low Q-state. At the low Q-state, the introduced losses suppress the oscillation of the laser, thus, pumping of the active medium leads to an accumulation of population inversion, exceeding the threshold level  $\Delta N_{\text{th}}$  of the high-Q cavity. Switching to the high Q-factor by removing the additional losses results in a rapid

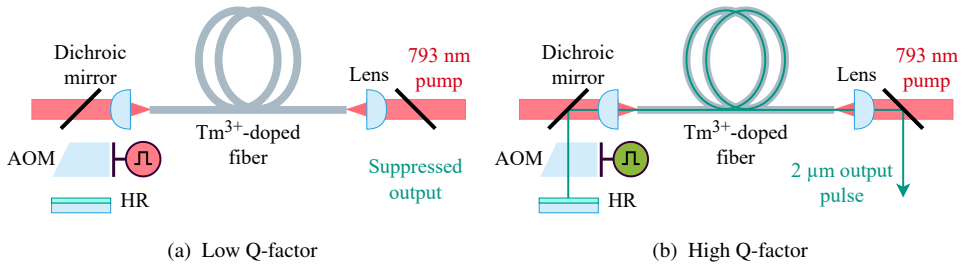


Figure 2.42: Q-switched  $\text{Tm}^{3+}$ -doped fiber oscillator using an acousto-optical modulator (AOM). The cavity is blocked by the AOM at the low Q-state and unblocked at the high Q-state enabling the generation of a pulse.

extraction of the stored energy in a short optical pulse, as a result of the transient oscillation process of the laser towards the threshold gain  $G_{\text{th}}$  of the unblocked cavity. After the pulse generation, the resonator is blocked again. This suppresses the formation of further pulses due to spiking and restarts the population inversion charging process.

There are several methods to implement Q-switching in a laser, generally distinguished between active and passive Q-switching techniques. While passive Q-switching based on saturable absorbers allows for shorter pulse durations, active Q-switching is generally preferred to generate high-energy pulses with minor variations in magnitude and jitter. A common method for repetitive active Q-switching of a fiber oscillator is the insertion of an AOM in the resonator between the active fiber and the HR, as shown in fig. 2.42. The fiber oscillator corresponds to the free-space design from fig. 2.38a. A monolithic setup can be realized using a fiber-coupled AOM, however, these devices are typically limited to lower average output powers due to a critical thermal management in the packaged design. The working principle of an AOM was discussed in sec. 2.1.4. In a Q-switched fiber oscillator, it acts as an optical switch that repeatedly suppresses and restores the feedback from the HR mirror by deflecting the beam when an RF signal is applied to the piezoelectric transducer. The RF signal and hence the acoustic wave in the AOM are turned on and off with a rectangular waveform, which switches the Q-factor of the laser with a typical frequency in the kHz range. This frequency corresponds to the pulse repetition rate. The pump power is usually supplied continuously during both Q-states.

Figure 2.43 provides a schematic diagram of the Q-switching process, including the temporal evolution of the resonator losses  $\Lambda$ , the inversion  $\Delta N$ , and the output power  $P_{\text{out}}$  during one

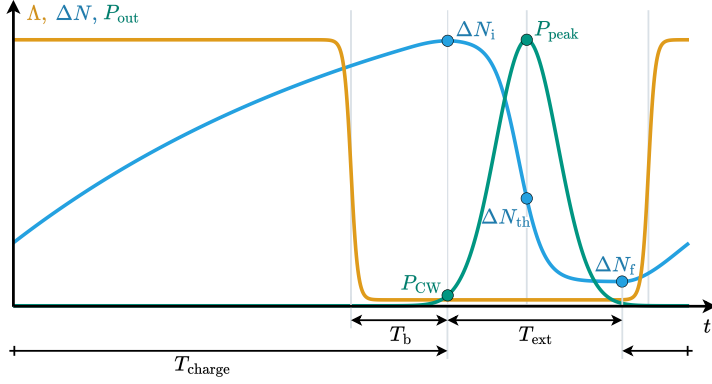


Figure 2.43: Schematic illustration of the active Q-switching process.

Q-switching period  $T_{\text{rep}} = 1/f_{\text{rep}}$ . The resonator losses  $\Lambda$  are modulated between a high level (low Q-state) when the AOM blocks the cavity, and a low level (high Q-state) when the cavity is unblocked. Pulse extraction occurs during a short time interval  $T_{\text{ext}}$  within the low loss period, in which the inversion discharges from its initial level  $\Delta N_i$  to the final level  $\Delta N_f$  by generating an output pulse. For the remainder of the period,  $T_{\text{charge}} = T_{\text{rep}} - T_{\text{ext}}$ , the inversion recovers by absorbing the supplied pump power. The charging period  $T_{\text{charge}}$  includes the time of the blocked resonator and the pulse build-up time  $T_b$  that is required to generate a pulse from vacuum noise after switching to the high Q-state. Note that the time relations in fig. 2.43 are purely schematic. In practice, the pulse extraction time ( $T_{\text{ext}} \sim 50$  ns) is typically much shorter than the charging time ( $T_{\text{charge}} \sim 50$   $\mu$ s), as illustrated in fig. 2.40.

### Pumping at the low Q-state

During the charging period, the laser intensity in the cavity is negligible  $\langle I_s \rangle \approx 0$  and the small-signal rate equation (2.166) can be applied. The inversion builds up as absorbed pump power populates the upper laser level, which is counteracted by spontaneous decay and other detrimental energy transfer processes. Assuming a constant pump power and absorption efficiency, the small-signal rate equation yields the approximate solution [42]

$$\langle \Delta N \rangle(t) = 2 \frac{\lambda_{\text{pump}} P_{\text{pump}}}{hc_0 V} \eta_{\text{abs}} \eta_q \tau \left( 1 - e^{-\frac{t}{\tau}} \right) - \langle N \rangle, \quad (2.252)$$

which results in a charging efficiency of the pump process given by [42]

$$\eta_{\text{charge}} = \frac{\tau}{T_{\text{charge}}} \left( 1 - e^{-\frac{T_{\text{charge}}}{\tau}} \right). \quad (2.253)$$

The equation highlights that a short charging time  $T_{\text{charge}} \ll \tau$  reduces the effect of spontaneous decay, leading to a higher efficiency of the pump process. For  $\text{Tm}^{3+}$ -doped fiber lasers with a typical lifetime of  $\tau = 200\text{--}650 \mu\text{s}$  of the  ${}^3\text{F}_4$  laser level, this means that pulse repetition frequencies  $f_{\text{rep}} > 10 \text{ kHz}$  are required to achieve charging efficiencies  $\eta_{\text{charge}} > 75\%$ . For high pulse repetition frequencies, the pulsed fiber laser acts effectively as a high-pass filter, suppressing slow detrimental effects that would otherwise quench the upper laser level.

If high gain levels are reached during the charging period, significant ASE can occur along the fiber, causing the small-signal rate equation (2.166) to lose validity. The local inversion  $\Delta N(z)$  is then depleted by the total ASE in both the forward and backward directions at this position, integrated over the entire gain spectrum [53]. This reduces the charging efficiency, especially for low pulse repetition frequencies [178]. In the limit of a long charging time ( $T_{\text{charge}} \rightarrow \infty$ ), the system reaches a steady state, in which ASE clamps the population inversion at the level

$$\Delta N(z) = \left( 1 + 2 \frac{\frac{\lambda_{\text{pump}}}{hc_0} \frac{\tau \Gamma_{\text{pump}} \sigma_a(\lambda_{\text{pump}})}{A_{\text{core}}} P_{\text{pump}}(z) + \int_0^\infty \frac{\lambda}{hc_0} \frac{\tau \Gamma_s \sigma_a(\lambda)}{A_{\text{core}}} P_{\text{ASE}}^{\text{tot}}(z, \lambda) d\lambda}{1 + \frac{P_{\text{pump}}(z)}{P_{\text{sat}}(\lambda_{\text{pump}})} + \int_0^\infty \frac{P_{\text{ASE}}^{\text{tot}}(z, \lambda)}{P_{\text{sat}}(\lambda)} d\lambda} \right) N \quad (2.254)$$

where  $P_{\text{sat}}$  is the saturation power given by eq. (2.169) and  $P_{\text{ASE}}^{\text{tot}}(z)$  is the total ASE power in both the forward and backward directions at position  $z$  in the fiber (see eq. (2.174)) [53, 178]. At this inversion level, the inversion depletion by ASE perfectly balances the excitations from the pump power. Consequently, for a given pump power  $P_{\text{pump}}(z)$ , eq. (2.254) yields the maximum inversion that can be stored in the fiber when limited by ASE.

In addition to ASE, the maximum inversion that can be stored in the active fiber is limited by the onset of parasitic lasing. Because the feedback from the HR mirror is suppressed by the AOM during the charging time, parasitic lasing occurs if the single-pass gain in the fiber reaches the threshold

$$G_{\text{th,paras}} = \frac{1}{\sqrt{R_{\text{OC}} R_{\text{paras}} (1 - \Lambda)}} \quad (2.255)$$

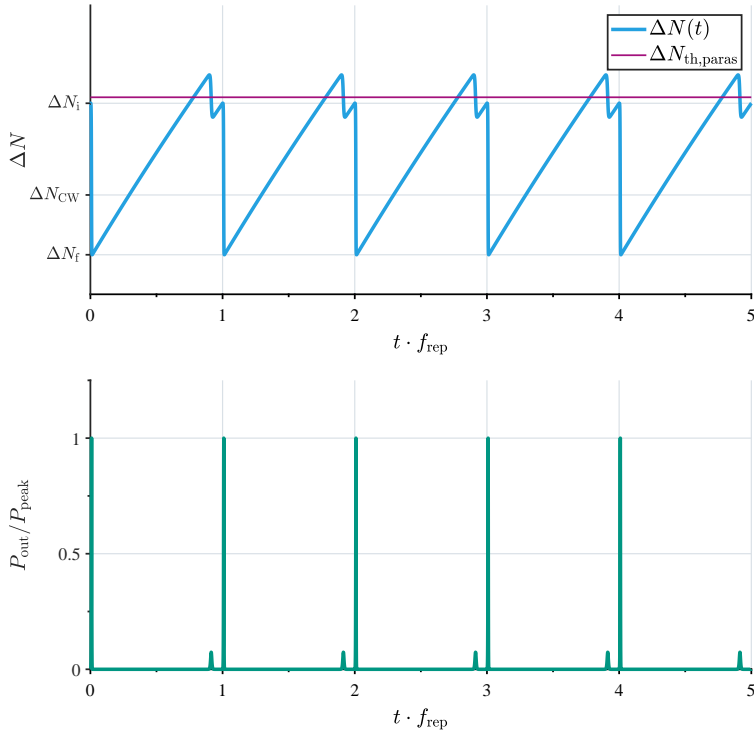


Figure 2.44: Pulsed fiber laser operation above the parasitic lasing threshold. When exceeding the parasitic threshold level  $\Delta N_{\text{th,paras}}$ , the inversion is partially discharged in a parasitic pulse preceding the desired pulse.

which is determined by the background losses  $\Lambda$  in the fiber, the OC reflectivity  $R_{\text{OC}}$  and the parasitic reflectivity  $R_{\text{paras}}$  on the HR side.

The parasitic reflectivity  $R_{\text{paras}}$  can be caused, for example, by the fiber endface on the HR side. Consequently, the fiber end facing the HR is commonly cleaved at an angle of  $\sim 8^\circ$  to prevent the coupling of endface reflections in the low-NA core. Even if all obvious sources of parasitic reflections are eliminated, there will always remain a residual amount of parasitic feedback from surface imperfections and distributed Rayleigh backscattering in the fiber. These minor reflections can cause parasitic lasing if the peak gain reaches high values of more than 30–40 dB.

Figure 2.44 illustrates the limitation of the maximum achievable inversion by parasitic lasing. The parasitic gain threshold  $G_{\text{th,paras}}$  corresponds to a population inversion level  $\langle \Delta N \rangle_{\text{th,paras}}$ .

When the population inversion in the fiber exceeds this threshold level, parasitic lasing builds up in a transient spiking process. After a build-up time  $T_{b,paras}$ , a parasitic pulse is formed that partially depletes the inversion. This ultimately limits the maximum initial inversion  $\Delta N_i$  that can be accumulated during the charging period.

### Pulse generation at the high Q-state

Switching to the high Q-state restores the feedback via the HR mirror. At this point, the population inversion has accumulated to a level  $\langle \Delta N \rangle > \langle \Delta N \rangle_{th}$ , resulting in the rapid build-up of a laser pulse in the cavity. The pulse build-up time  $T_b$  is defined as the time the laser intensity  $\langle I_s \rangle$  in the cavity requires to reach the CW level  $\langle I_s \rangle_{CW}$  corresponding to an output power  $P_{CW}$  (see fig. 2.43) [41].

During this build-up phase, two approximations can be made: First, because the intracavity laser signal is still very weak, its depleting effect on the population inversion is considered negligible. Second, as the build-up time is generally much shorter than the upper-state lifetime  $\tau$ , the effects of pumping and spontaneous decay can also be ignored. Therefore, the inversion is assumed to remain constant at its initial level,  $\Delta N = \Delta N_i$ , leading to a simplified rate equation (2.181) throughout this period:

$$\frac{d \langle I_s \rangle}{dt} \approx \frac{g_i}{g_{th}} - 1 \langle I_s \rangle, \quad (2.256)$$

where  $g_i$  and  $g_{th}$  are the gain coefficients at the initial inversion  $\langle \Delta N \rangle_i$  and the threshold inversion  $\langle \Delta N \rangle_{th}$ , respectively [41]. With the solution

$$\langle I_s \rangle (t) = \langle I_s \rangle_{noise} \exp \left( \frac{\left( \frac{g_i}{g_{th}} - 1 \right) t}{\tau_c} \right), \quad (2.257)$$

the pulse build-up time  $T_b$  is derived to be [41]

$$T_b = \frac{\tau_c}{\frac{g_i}{g_{th}} - 1} \ln \left( \frac{\langle I_s \rangle_{CW}}{\langle I_s \rangle_{noise}} \right). \quad (2.258)$$

After the build-up time, the laser intensity has reached a significant level, resulting in the depletion of the initial population inversion  $\langle \Delta N \rangle_i$ . The intensity grows until the inversion has

dropped to the threshold level  $\langle \Delta N \rangle_{\text{th}}$ . At this point, the output pulse reaches its peak power (see fig. 2.43) [41]. As the inversion and hence the gain falls below the threshold level, the laser intensity in the cavity starts to decay. The stored photons leave the resonator with the time constant  $\tau_c$ , while continuing to deplete the inversion via stimulated emission until the final level  $\langle \Delta N \rangle_f$  is reached.

During the extraction time  $T_{\text{ext}}$ , pump absorption and spontaneous decay can be neglected, because it is typically much shorter than the upper-state lifetime  $\tau$ . Using this approximation, dividing the rate eqs. (2.180) and (2.181) by each other and integrating over the inversion yields the following relationship between intensity and inversion [42]:

$$2 \frac{hc_0}{\lambda_s} \langle I_s \rangle \approx \langle \Delta N \rangle_i - \langle \Delta N \rangle_f + \left( \frac{\sigma_a(\lambda_s) - \sigma_e(\lambda_s)}{\sigma_a(\lambda_s) + \sigma_e(\lambda_s)} \langle N \rangle - \langle \Delta N \rangle_{\text{th}} \right) \ln \left( \frac{\langle \Delta N \rangle_i - \frac{\sigma_a(\lambda_s) - \sigma_e(\lambda_s)}{\sigma_a(\lambda_s) + \sigma_e(\lambda_s)} \langle N \rangle}{\langle \Delta N \rangle_f - \frac{\sigma_a(\lambda_s) - \sigma_e(\lambda_s)}{\sigma_a(\lambda_s) + \sigma_e(\lambda_s)} \langle N \rangle} \right). \quad (2.259)$$

At the end of the extraction period, i.e.  $\langle \Delta N \rangle = \langle \Delta N \rangle_f$ ,  $\langle I_s \rangle = 0$ , this results in the fundamental Q-switching equation [41, 42]

$$\langle \Delta N \rangle_i - \langle \Delta N \rangle_f = \left( \frac{\sigma_a(\lambda_s) - \sigma_e(\lambda_s)}{\sigma_a(\lambda_s) + \sigma_e(\lambda_s)} \langle N \rangle - \langle \Delta N \rangle_{\text{th}} \right) \ln \left( \frac{\langle \Delta N \rangle_i - \frac{\sigma_a(\lambda_s) - \sigma_e(\lambda_s)}{\sigma_a(\lambda_s) + \sigma_e(\lambda_s)} \langle N \rangle}{\langle \Delta N \rangle_f - \frac{\sigma_a(\lambda_s) - \sigma_e(\lambda_s)}{\sigma_a(\lambda_s) + \sigma_e(\lambda_s)} \langle N \rangle} \right). \quad (2.260)$$

The equation can be rewritten in terms of gain to obtain the simple form

$$\ln \left( \frac{G_i}{G_f} \right) = \ln G_{\text{th}} \ln \left( \frac{g_i}{g_f} \right) \quad (2.261)$$

which provides the implicit relationship between the initial and final gain in the Q-switching process, solely dependent on the parameters of the resonator included in  $G_{\text{th}}$  (see eq. (2.176)). For a given initial gain  $G_i$  and known resonator parameters, eq. (2.261) can be used to determine the final gain numerically, which yields the extractable energy  $E_{\text{ext}}$  according to eq. (2.245).

The peak intensity  $\langle I_s \rangle_{\text{peak}}$  can be derived from eq. (2.259) by setting  $\langle \Delta N \rangle = \langle \Delta N \rangle_{\text{th}}$  [42]. This results in the peak output power in terms of gain

$$P_{\text{peak}} = \eta_{\text{R}} \frac{E_{\text{sat}}}{\tau_{\text{c}}} \left( \ln \left( \frac{G_{\text{i}}}{G_{\text{th}}} \right) - \ln G_{\text{th}} \ln \left( \frac{g_{\text{i}}}{g_{\text{th}}} \right) \right) \quad (2.262)$$

where the factor  $\eta_{\text{R}}$  denotes the resonator efficiency to obtain the output power from the power within the resonator (see eq. (2.159)).

The temporal dynamics of a Q-switched pulse is determined by the initial gain  $G_{\text{i}}$ , the threshold gain of the high Q-state cavity  $G_{\text{th}}$ , and the response time of the resonator  $\tau_{\text{c}}$ . A higher initial gain compared to the threshold gain increases the rate of energy extraction per cavity round-trip and therefore leads to a shorter pulse width. An energy extraction faster than the cavity photon lifetime  $\tau_{\text{c}}$  results in an asymmetric pulse shape with a fast rising edge determined by the energy extraction and a slower falling edge characterized by the exponential decay of the photons that leave the cavity with the time constant  $\tau_{\text{c}}$  [41]. The cavity lifetime  $\tau_{\text{c}}$  therefore provides a lower limit for the minimum pulse duration. Another lower limit is given by the round-trip time  $\tau_{\text{rt}} = 2nL/c_0$ , because the laser signal must propagate at least once through the cavity to extract the energy stored in population inversion. If the round-trip time is longer than the cavity lifetime ( $\tau_{\text{rt}} > \tau_{\text{c}}$ ), the energy extraction is always slower than the response of the resonator field, resulting in pulse shapes that remain largely symmetric. This corresponds to an overdamped cavity with  $R_{\text{OC}}R_{\text{HR}}(1 - \Lambda) < e^{-1} \approx 0.37$ , which is the case for fiber lasers with low OC reflectivities. Thus, the pulses of Q-switched fiber lasers with  $R_{\text{OC}} < 0.37$  can generally be well approximated by Gaussian pulse shapes. The FWHM pulse width  $t_{\text{pulse}}$  then results from the pulse energy  $E_{\text{pulse}}$  and the peak power  $P_{\text{pulse}}$  by the relation

$$t_{\text{pulse}} \approx 2\sqrt{\frac{\ln 2}{\pi}} \frac{E_{\text{pulse}}}{P_{\text{peak}}} \approx 0.94 \frac{E_{\text{pulse}}}{P_{\text{peak}}}. \quad (2.263)$$

## 2.4.2 Pulse Amplification in Fiber Amplifiers

Pulses generated by a Q-switched laser or a seed laser diode can be amplified in pulse energy and average output power via a fiber amplifier. The separation of pulse generation and amplification in a MOPA system offers several advantages compared to the direct generation of high-energy pulses in a Q-switched oscillator. First, a pulsed MOPA enables a more flexible choice of pulse width and pulse shape. While the pulse characteristics in a Q-switched oscillator are linked to

the gain, in a MOPA, they can be specified by adapting the input pulse of the power amplifier. Second, a fiber amplifier can typically store more energy than an oscillator. Because it does not require an OC reflector, the threshold for parasitic lasing is generally higher. Finally, a MOPA system enables an all-in-fiber integration, making the pulsed laser more robust and reliable for practical purposes. Because the master oscillator can operate at a low power level, it can be realized by a monolithic Q-switched fiber oscillator using a fiber-coupled AOM or by a fiber-coupled seed laser diode, with the amplifier stages spliced sequentially. Proper isolation and ASE filtering in between the amplifier stages is essential for pulsed MOPAs, as amplification to high pulse energies requires high gain.

In repetitive pulse amplification, the input pulses are injected with a fixed pulse repetition frequency  $f_{\text{rep}}$  into the fiber amplifier. The injected pulses extract stored energy from the active fiber by stimulated emission and are therefore amplified in pulse energy. The fiber amplifier is usually continuously pumped to recover the population inversion and hence gain to a consistent initial level between the pulses. The charging process works analogously to that of the Q-switched laser described in the previous section. Similarly, the maximum storable energy is limited by ASE and parasitic lasing. The parasitic lasing threshold in a fiber amplifier is generally higher than in an oscillator because, as there is no OC mirror, feedback arises from parasitic reflections from both sides, resulting in a threshold gain of

$$G_{\text{th,paras}} = \frac{1}{\sqrt{R_{\text{paras},1} R_{\text{paras},2} (1 - \Lambda)}}. \quad (2.264)$$

An additional limiting factor can be the injected noise from a previous stage, which can saturate the inversion build-up when being amplified.

In the pulse amplification process, the leading edge of the injected pulse begins to deplete the inversion. Thus, the subsequent part of the pulse experiences a lower gain, resulting in an inhomogeneous amplification along the pulse duration and consequently a distortion of the pulse shape. To describe this gain saturation effect, it is convenient to use a retarded time frame  $T = t - z/v_g$ , as for the nonlinear propagation equation (2.213). The time  $T$  refers to a temporal point in the pulse profile, independent of the propagation distance  $z$ . Within this time frame, the accumulated input and output pulse energies are expressed as [41]

$$E_{\text{in}}(T) = \int P_{\text{in}}(T) dT, \quad E_{\text{out}}(T) = \int P_{\text{out}}(T) dT, \quad (2.265)$$

where  $P_{\text{in}}(T)$  and  $P_{\text{out}}(T)$  are the power profiles of the input and output pulse, respectively. As the gain in the amplifier is continuously depleted by the pulse, each part of the pulse generally experiences a different gain  $G(T)$ , leading to the relation [41]

$$P_{\text{out}}(T) = G(T)P_{\text{in}}(T) . \quad (2.266)$$

By neglecting pump excitation, spontaneous decay, and propagation losses during pulse amplification, the power difference between the input and output signals corresponds to the depleted population inversion, resulting in the rate equation [41]

$$\frac{d \langle \Delta N \rangle}{dT} = - \frac{\lambda_s}{hc_0} \frac{\Gamma_s}{V} [P_{\text{out}}(T) - P_{\text{in}}(T)] . \quad (2.267)$$

Substituting eq. (2.266) into eq. (2.267) and integrating leads to

$$\frac{hc_0}{\lambda_s} V \int_{\langle \Delta N \rangle_i}^{\langle \Delta N \rangle(T)} \frac{1}{G(T) - 1} d \langle \Delta N \rangle = \int P_{\text{in}}(T) dT = E_{\text{in}}(T) . \quad (2.268)$$

Conducting the integral on the left-hand side and solving for  $G(T)$  yields

$$G(T) = \frac{G_i}{G_i - (G_i - 1) \exp\left(-\frac{E_{\text{in}}(T)}{E_{\text{sat}}}\right)} . \quad (2.269)$$

This equation determines the saturated gain  $G(T)$  for a given input pulse  $P_{\text{in}}(T)$  and initial gain  $G_i$ , which can be used to calculate the output pulse profile  $P_{\text{out}}(T)$  using eq. (2.266). By inserting the total input pulse energy  $E_{\text{in}}$  into eq. (2.269) the final gain  $G_f$  after the pulse amplification is obtained. Using the eqs. (2.245) and (2.248) the output pulse energy can be expressed as

$$E_{\text{pulse}} = E_{\text{in}} + E_{\text{sat}} \ln \left[ G_i - (G_i - 1) \exp\left(-\frac{E_{\text{in}}}{E_{\text{sat}}}\right) \right] . \quad (2.270)$$

These relations are known as the Frantz-Nodvik equations and can be used to model gain saturation, pulse distortion, and energy extraction from a fiber amplifier [180]. Figure 2.45 illustrates the pulse amplification for a Gaussian input pulse (fig. 2.45a) and a rectangular input pulse (fig. 2.45b). Both input pulses have a pulse energy of  $E_{\text{in}} = 0.4 \cdot E_{\text{sat}}$ . The population inversion in the fiber is significantly depleted during pulse amplification if the extracted energy is on the order of the saturation energy  $E_{\text{sat}}$ . Consequently, strong gain saturation effects can be

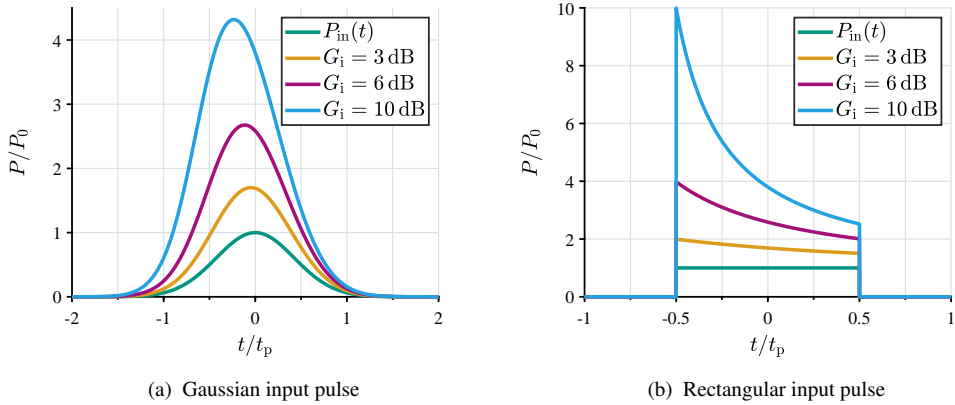


Figure 2.45: Pulse amplification in a fiber amplifier. Both, the Gaussian and the rectangular input pulse have an input pulse energy  $E_{\text{in}} = 0.4 \cdot E_{\text{sat}}$ . For  $E_{\text{in}}G_i > E_{\text{sat}}$  the pulse amplification leads to significant pulse shape distortion because of gain saturation throughout the pulse.

expected for  $E_{\text{in}}G_i > E_{\text{sat}}$ , leading to a pulse shape distortion. For a Gaussian input pulse, gain saturation causes the leading edge to become steeper than the trailing edge of the pulse. Thus, for higher initial gain values, the pulse peak shifts forward in time. For an ideal rectangular pulse, the leading edge of the pulse is strongly amplified, causing rapid gain saturation that forms a sharp spike at the beginning of the pulse.

To counteract this pulse distortion by gain saturation, active pulse-shaping techniques can be applied [181, 182]. In this technique, a diode laser seeds a fiber MOPA with an arbitrarily pre-shaped pulse designed to compensate for the anticipated gain saturation effects. The output signal of the low-power diode laser can be controlled by a fast modulation of its driving current. To amplify this low-energy input signal, several amplifier stages are typically required. Additional pulse-shaping and ASE filtering can be achieved using an electro-optical modulator (EOM) or an AOM between the stages. By implementing this active pulse shaping method, close to rectangular-shaped output pulses with a pulse energy of 1 mJ, a pulse duration of 100 ns, and a peak power of 13 kW have been demonstrated from a  $\text{Tm}^{3+}$ -doped fiber MOPA at 1950 nm [182].

### 2.4.3 Pulse Energy Scaling and State of the Art

To scale the pulse energy of a fiber laser, both the charging and the extraction process need to be considered. During the charging period, the supplied pump power is absorbed to build up the inversion, and hence the gain in the fiber. The stored energy can be increased either by increasing the pump power or by pumping over a longer time period. A longer charging period is typically achieved by decreasing the pulse repetition rate. Pulse energy extraction is associated with a drop in population inversion and gain to their final levels  $\Delta N_f$  and  $G_f$ . In a Q-switched laser, efficient energy extraction requires a low threshold gain  $G_{th}$  according to eq. (2.261), meaning low resonator losses in the high Q-state. In an amplifier, a sufficiently high input pulse energy on the order of the saturation energy ( $E_{in} \sim E_{sat}$ ) is required to efficiently extract the stored energy. The maximum extractable pulse energy is therefore determined by the difference between the highest achievable initial gain  $G_i$  and the lowest possible final gain  $G_f$ , as described in eq. (2.245). These gain limits are in turn set by various limiting mechanisms depending on the laser design and its operating point.

There are several limitations for the maximum achievable pulse energy from a fiber laser. Most fundamentally, the storable energy in an active laser medium is limited by pump bleaching at a population inversion level  $\Delta N_{bleach}$  (see eq. (2.173)), depending on the pump wavelength  $\lambda_{pump}$ . Spontaneous decay can lower this inversion limit to the steady-state small-signal inversion  $\Delta N_{ss}$  (see eq. (2.166)) for long charging periods  $T_{charge}$  on the order of the upper laser level lifetime  $\tau$ . In fiber lasers, the inversion is distributed over a long length, leading to a lower local inversion but a rapidly growing gain. Thus, the storable energy in a fiber laser is generally limited well before reaching the bleaching level by the gain-related effects of ASE and parasitic lasing. ASE depletes the population inversion at a rate proportional to the gain (see eq. (2.174)). It reduces the efficiency of the charging process and can completely cap the inversion build-up if its depletion rate balances the pump excitation rate (see eq. (2.254)). Therefore, the pulse energy limit caused by ASE depends on the pump power. In contrast, the threshold gain  $G_{th,paras}$  of parasitic lasing depends only on the feedback condition of the parasitic cavity (see eqs. (2.255) and (2.264)). However, the pulse energy limit caused by parasitic lasing is not completely independent of the pump power, because after reaching the parasitic threshold gain, the parasitic oscillation requires a build-up time  $T_{b,paras}$  to saturate the population inversion. During this delay, it is still possible to charge more energy in the fiber. The charged energy must be extracted in a laser pulse before the parasitic spike can deplete it (see fig. 2.44).

Another limitation for pulsed fiber lasers is the onset of nonlinear effects caused by the high peak intensities propagating along the fiber. The fiber nonlinearities discussed in sec. 2.3.3 lead to the emergence of undesired spectral components that distort the output spectrum and the temporal pulse profile. For high pulse peak powers, these spectral features can contain a significant fraction of the total output power limiting the power and pulse energy within the desired laser linewidth. Because the impact of these effects scales with intensity and propagation length, pulsed fiber lasers typically utilize fibers with large mode field areas and short lengths.

### Studies and analyses on pulse energy extraction from fiber lasers

Several studies have investigated the pulse energy limits in fiber lasers. One of the most influential works was published in 2001 by Renaud et al. with a focus on Q-switched  $\text{Yb}^{3+}$ -doped fiber lasers [178]. The paper points out the importance of the saturation energy  $E_{\text{sat}}$  and outlines general strategies for pulse energy scaling in fiber lasers. A low saturation energy causes the gain to increase rapidly when energy is stored in the fiber, triggering ASE and parasitic lasing. Consequently, increasing the saturation energy enables the generation of higher pulse energies before these limitations set in. An effective approach for increasing the extractable pulse energy from a fiber laser is to employ a fiber with a large core area, as this increases the saturation energy and decreases the intensity, mitigating nonlinear effects. However, this method is only applicable to a limited extent if single-mode operation is desired. Special fiber designs that allow single-mode operation with large core diameters, such as LMA fibers, PCFs, or LPFs are commonly used to push the maximum achievable pulse energies with nearly diffraction-limited beam quality [129, 147, 183]. Other approaches, including a tapered section of a multimode fiber for suppressing higher-order modes or a ring-doped core design for increasing the saturation energy by reducing the overlap factor  $\Gamma_s$ , have been investigated but are typically more complicated and less effective [184, 185].

Although parasitic lasing and nonlinear effects were mentioned as possible limitations for pulse energy scaling in fiber lasers, the analysis by Renaud et al. primarily focuses on the effect of ASE [178]. The ASE limit is determined by a simplified model considering a time-independent steady state where ASE at a single wavelength balances the pump excitation. Subsequent work refined the modeling of the ASE limit using numerical and analytical approaches [186, 187]. Parasitic lasing and nonlinear effects were also neglected in these analyses. It should be noted

that pulsed fiber lasers were typically operated at output powers below 10 W and pulse repetition frequencies of a few kilohertz at this time, due to less mature components and fiber endface terminations [178, 183–185, 188]. Thus, ASE was possibly the main limiting factor in these early works. In the numerical analysis by Wang et al. it is shown that higher average power levels at higher pulse repetition frequencies can effectively mitigate the pulse energy limitation from ASE, as the relative contribution of ASE to the total output power diminishes [186]. Gain clamping by parasitic lasing was investigated by Canat et al. in 2005 using a numerical model for erbium-ytterbium fiber amplifiers [189]. The assumption of parasitic reflectivities on the order of  $-40$  dB to  $-50$  dB yielded a good agreement with experimental data. Furthermore, the dynamic build-up of parasitic lasing between the pulses is also discussed in this paper. A more recent study by L. Dong from 2020 considers the nonlinear pulse propagation in fiber amplifiers [190]. The model solves the nonlinear propagation equation numerically, taking higher order dispersion, Kerr nonlinearity and Raman response into account, as well as gain saturation, gain dispersion and ASE in the amplifier. However, this model neglects parasitic reflections.

These previous analyses of the pulse energy limitations in fiber lasers have focused primarily on  $\text{Yb}^{3+}$ - or  $\text{Er}^{3+}$ -doped fiber laser systems. In 2007, Eichhorn et al. experimentally investigated the pulse energy limits of Q-switched  $\text{Tm}^{3+}$ -doped silica fiber lasers at  $2\ \mu\text{m}$ . In this study, the pulsed fiber laser was operated at different pulse repetition frequencies, and the pump power was gradually increased until the pulse energy limit was reached. When reaching this limit, a kink in the output power characteristic was observed, beyond which the slope efficiency dropped to approximately half its previous value. This behavior was explained by the argument that the parasitic signal between the pulses does not experience feedback via the HR, leading to its output at both ends of the active fiber. The maximum pulse energy was measured to be  $270\ \mu\text{J}$  in this experiment and, critically, was found to be largely independent of the pulse repetition frequency and the average power level. This latter observation is a typical signature of parasitic lasing as the limiting factor, which clamps the gain at a fixed threshold. In contrast, a limit imposed by ASE would be expected to increase with higher pump power.

Pulsed  $2\ \mu\text{m}$   $\text{Tm}^{3+}$ -doped fiber lasers present a distinct set of considerations compared to other rare-earth-doped fiber lasers. First, there is the CR1 process that enhances the quantum yield for diode pumping at  $790\ \text{nm}$  (see sec. 2.3.1). However, this process relies on the local population inversion, as it requires ions in the  $^3\text{H}_4$  pump level and the  $^3\text{H}_6$  ground level to be in close proximity. Conversely, high local inversions enhance the reverse ETU processes that

quench the  ${}^3F_4$  laser level (see fig. 2.25). Reaching high inversions during the charging process can therefore lead to a decrease in efficiency. Second, the emission wavelength around  $2\ \mu\text{m}$  changes the impact of certain nonlinear effects. While the Raman gain is reduced compared to  $1\ \mu\text{m}$  fiber lasers, the anomalous GVD at  $2\ \mu\text{m}$  facilitates modulation instability (see sec. 2.3.3). Another special characteristic of  $\text{Tm}^{3+}$ -doped silica is the particularly broad spectroscopic cross-sections of the  $2\ \mu\text{m}$  laser transition, resulting in a wide gain spectrum that is strongly influenced by reabsorption effects (see fig. 2.27). Because ASE arises from this gain spectrum and parasitic lasing occurs at the gain maximum, both limitations are affected by reabsorption. A comprehensive analysis of the extractable pulse energy in  $\text{Tm}^{3+}$ -doped fiber laser must therefore consider the saturation energy, nonlinear effects, and the spectral gain that determines the threshold for parasitic lasing and strong ASE. An optimal design involves a large number of parameters, including the core and mode field area, the overlap factor, the emission and pump wavelengths, the fiber length, and the doping concentration. There is no comprehensive model that would enable an optimized selection of these parameters or a full understanding of the underlying limiting mechanisms and their mutual dependencies in an optimized fiber laser design.

### State of the Art in High-Pulse-Energy $\text{Tm}^{3+}$ -doped Fiber Lasers

Due to the lack of more detailed design strategies, most work on pulsed  $2\ \mu\text{m}$  fiber lasers follows the effective approach of employing fibers with large core areas. An overview of high-energy nanosecond-pulsed  $\text{Tm}^{3+}$ -doped fiber lasers with close to diffraction-limited beam quality is given in Table 2.2. The table lists publications that were published prior to the start of this work in 2021. Another table containing publications to date is provided at the end of this thesis in sec. 6.4 to evaluate the results of this work. The pulsed fiber lasers listed in table 2.2 are compared based on their central emission wavelength ( $\lambda_c$ ), architecture, polarization, 10-dB-linewidth ( $\Delta\lambda_{10\text{-dB}}$ ), pulse energy ( $E_{\text{pulse}}$ ), effective power ( $P_{\text{eff}}$ ), average output power ( $P_{\text{avg}}$ ), and slope efficiency ( $\eta_s$ ) with respect to the launched  $793\ \text{nm}$  pump if not stated otherwise. The table is structured by three different fiber types used in the oscillators or final amplifier stages:  $\text{Tm}^{3+}$ -doped LMA fibers with a  $25\ \mu\text{m}$  core diameter, bendable  $\text{Tm}^{3+}$ -doped PCFs with a  $50\ \mu\text{m}$  core diameter, and non-bendable LPFs with an  $80\ \mu\text{m}$  core diameter.

As can be seen from table 2.2, pulse energies up to  $1\ \text{mJ}$  have been reported using  $25\ \mu\text{m}$   $\text{Tm}^{3+}$ -doped LMA fibers [182, 191]. The highest effective power of  $9.2\ \text{kW}$  for this fiber type

Table 2.2: Overview of high-energy nanosecond-pulsed  $\text{Tm}^{3+}$ -doped fiber lasers with close to diffraction-limited beam quality published before 2021.

$\lambda_c$	Architecture <sup>1</sup>	Lin. polarization	$\Delta\lambda_{10\text{-dB}}$	$E_{\text{pulse}}$	$P_{\text{eff}}$	$P_{\text{avg}}$	$\eta_s$	Year
25 $\mu\text{m}$ $\text{Tm}^{3+}$ -doped LMA fiber								
1950 nm	AF - DS MOPA	Seed lin. polarized	1 nm	1 mJ	9.2 kW	13 W	30 %	2014 [182]
1970 nm	AF - CM MOPA	No	1 nm	750 $\mu\text{J}$	8.5 kW	150 W	37 %	2016 [193]
1977 nm	FS - QS MOPA	Seed PER > 14 dB	4 nm	700 $\mu\text{J}$	3.7 kW	14 W	47 % <sup>2</sup>	2018 [192]
2024 nm	QS Oscil.	PER $\sim$ 16 dB	0.5 nm	575 $\mu\text{J}$	5.9 kW	23 W	33 %	2015 [194]
2050 nm	AF - GS MOPA	Seed PER > 16 dB	0.4 nm	1 mJ	6.8 kW	41 W	42 %	2015 [191]
50 $\mu\text{m}$ $\text{Tm}^{3+}$ -doped PCF								
1950 nm	FS - QS Oscil.	PER > 18 dB	-	435 $\mu\text{J}$	6.3 kW	4.4 W	26 %	2012 [38]
1980 nm	FS - QS MOPA	Yes	1.8 nm	840 $\mu\text{J}$	78 kW	3.4 W	7 %	2014 [39]
80 $\mu\text{m}$ $\text{Tm}^{3+}$ -doped rod-type LPF								
1900 nm	FS - QS Oscil.	No	50 nm	2.4 mJ	69 kW	33 W	21 %	2013 [195]
1965 nm	FS - QS MOPA	No	2.6 nm	6.4 mJ	660 kW	6.4 W	9 %	2013 [196]

<sup>1</sup> AF: All-in-fiber, FS: Free-space, DS: Diode-seeded, CM: CW-modulated, QS: Q-switched, GS: Gain-switched.

<sup>2</sup> with respect to absorbed pump power

was enabled by an active pulse shaping approach that allowed for the generation of nearly rectangular-shaped pulses with a duration of 100 ns [182]. Parasitic lasing is reported as the pulse energy limitation in [192, 193] and significant modulation instability is observed in [191, 193]. The fiber MOPAs reported in [182, 191, 192] use a linearly polarized seed source, but the publications do not provide the polarization extinction ratio (PER) of the output signal. Linear polarization generally causes stronger fiber nonlinearities but is required for some applications, such as pumping of optical parametric oscillators using birefringent phase matching [194].

To increase the saturation energy and mitigate intensity-dependent nonlinear effects,  $\text{Tm}^{3+}$ -doped PCFs and LPFs with larger core diameters of 50–80  $\mu\text{m}$  have been applied in several nanosecond-pulsed fiber laser systems [38, 39, 195, 196]. However, all systems published before 2021 suffer from low efficiency, restricting their average output power to low to moderate levels. A nanosecond-pulsed  $\text{Tm}^{3+}$ -doped fiber laser based on a 2.7 m long flexible PCF was first demonstrated by Kadwani et al. in 2012 and provided pulse energies up to 435  $\mu\text{J}$  by active Q-switching [38]. The same fiber was subsequently used in a MOPA system to generate pulse energies of 840  $\mu\text{J}$  with a short pulse duration of 7 ns, resulting in a high effective power of 78 kW [39]. However, the poor slope efficiency of 7 % limited the average output power of the MOPA to 3.4 W. Despite their larger core diameter, these early works on flexible PCFs did not achieve pulse energies higher than those with LMA fibers. The highest pulse energies of 2.4 mJ

and 6.4 mJ were reported using 80  $\mu\text{m}$  rod-type LPFs [195, 196]. However, the non-coilable LPFs are practically restricted to short fiber lengths of about 1 m. This leads to a lower pump absorption efficiency and high population inversion levels, reducing the CR1 rate and hence the overall efficiency of the fiber laser system. The LPF MOPA reported in [196] has a slope efficiency of only 9 %, limiting the average output power to 6.4 W. Although the Q-switched LPF oscillator from [195] demonstrated a higher slope efficiency of 21 % and reached an average output power of 31 W, it exhibited an enormous threshold of 190 W. The high inversion also leads to a blue shift of the gain spectrum, restricting the nanosecond-pulsed LPFs to short emission wavelengths.

In this work, the pulse energy limits in  $\text{Tm}^{3+}$ -doped fiber lasers are investigated experimentally in chapter 3. Based on these experimental results, a detailed analysis of pulse energy extraction in  $\text{Tm}^{3+}$ -doped fiber lasers is presented in chapter 4. This analysis aims to provide a comprehensive framework for refining the understanding and for enabling an easy optimization of nanosecond-pulsed fiber lasers. Optimization strategies are developed, followed by their experimental verification and evaluation. Finally, an optimized high-energy nanosecond-pulsed  $\text{Tm}^{3+}$ -doped fiber laser is reported in chapter. 5.

## 2.5 Mid-Infrared Generation via Optical Parametric Oscillators

High-power laser radiation in the mid-infrared range between 3–5  $\mu\text{m}$  is in demand for various applications in the fields of medicine, chemical sensing, defense, and research. However, there is a lack of suitable laser sources that can directly address this spectral region with high pulse energies and average output power. Nonlinear frequency down-conversion offers an attractive solution as it enables the efficient conversion of short-wave infrared radiation from available high-power laser sources into the targeted mid-infrared range.

Mid-IR generation via OPOs has been shown to enable conversion efficiencies of more than 60 %—and even up to 75.7 %—while providing widely tunable signal and idler outputs in the 3–5  $\mu\text{m}$  spectral range [197, 198]. Birefringent ZGP crystals represent an ideal nonlinear medium for high-power mid-IR OPOs, as they exhibit high nonlinearity, excellent thermal conductivity, and a wide transparency range from 2–8  $\mu\text{m}$  that accommodates the pump, signal, and idler wavelengths [199]. This allows for generating both signal and idler in the targeted 3–5  $\mu\text{m}$  range using a doubly-resonant cavity design pumped by a 2  $\mu\text{m}$  laser.

The characteristics of the pump beam crucially determine the output characteristics and efficiency of the parametric conversion process, as discussed in sec. 2.2.3. Commonly used solid-state laser systems based on  $\text{Ho}^{3+}$ -doped  $\text{Y}_3\text{Al}_5\text{O}_{12}$  (YAG) have been shown to provide several millijoules of pulse energy and hundreds of kilowatt peak power with an average output power of up to 450 W [200]. By applying high-power  $\text{Ho}^{3+}$ :YAG systems as pump sources for nonlinear frequency conversion, mid-IR output powers of 150 W have been demonstrated from a ZGP OPO, and 161 W from a ZGP optical parametric amplifier (OPA) system [36, 37]. However, reaching such power levels with  $\text{Ho}^{3+}$ :YAG crystals demands a MOPA approach with high complexity: to achieve the necessary gain, multiple  $\text{Ho}^{3+}$ :YAG amplifier stages are required, and each of them needs to be pumped with another high-brightness laser at 1.9  $\mu\text{m}$ , making the overall system inefficient, difficult to integrate, and less robust. Replacing these bulk solid-state lasers with compact and robust 2  $\mu\text{m}$  fiber laser systems is therefore a highly appealing approach.

As discussed in sec. 2.3,  $\text{Tm}^{3+}$ -doped fiber lasers are well-suited to efficiently generate high output powers with ideal beam quality. In contrast to bulk solid-state lasers, the active fiber as a gain medium provides high gain, excellent heat dissipation, and the possibility of pumping

with high-power laser diodes. Furthermore, even multi-stage MOPA systems are considered feasible for compact and robust all-in-fiber integration. However, these advantages come at the cost of a more challenging generation of high pulse energies, due to limitations imposed by ASE, parasitic lasing, and fiber nonlinearities (see sec. 2.4). The limited pulse energy of fiber lasers leads to specific design constraints and typically lower conversion efficiencies when using them as pump sources for ZGP OPOs [22, 201]. Nevertheless, fiber-laser-pumped ZGP OPOs remain promising, as the rapidly evolving fiber laser technology and novel strategies for pulse energy scaling open up new perspectives for this topic. This thesis presents new approaches to overcome these challenges, demonstrating the enormous potential of high-power, fiber-pumped mid-IR sources.

The following section discusses the technology and concepts of mid-IR ZGP OPOs with a focus on fiber-pumped systems. First, the characteristics of the nonlinear crystal ZGP are presented. Subsequently, the requirements for the pump sources are studied, paying special attention to the specific design considerations for fiber laser pump sources. Finally, the state of the art in fiber-laser-pumped ZGP OPOs is reviewed.

### 2.5.1 The Nonlinear Crystal $\text{ZnGeP}_2$

There are several requirements for the nonlinear crystal in an OPO to generate high-power mid-IR radiation in the 3–5  $\mu\text{m}$  range. First, the material must be highly transparent for the pump, signal and idler wavelengths to mitigate heating by background absorption. Second, it must allow for phase matching either by birefringence or periodic poling. To achieve a high nonlinear conversion efficiency, a low pump threshold and the suppression of backconversion are essential, as discussed in sec. 2.2.3. Both factors impose further demands on the nonlinear crystal. According to eq. (2.183), a low pump threshold requires a large effective nonlinear coefficient  $d_{\text{eff}}$  of the material, which quantifies its nonlinear response to the incident laser beam (see sec. 2.1.4). Backconversion is effectively suppressed by a large GVM between the pump and the signal and idler in the nonlinear crystal. In a birefringent crystal, type I phase matching can be applied to ensure sufficient GVM as it generally leads to a larger spectral separation of the pump and the output wavelengths. As a result of the Kramers-Kronig relations eqs. (2.64) and (2.65), the group velocity increases for wavelengths in the vicinity of an absorption line. Consequently, a large GVM requires the pump or the signal and idler to be spectrally close to the edge of the transparency range. To achieve low absorption losses in these critical spectral

regions, a high purity of the nonlinear crystal is essential to prevent broadening of the short-wavelength band edge due to defect states. Finally, there are some practical considerations such as availability of the crystal itself and of optical coatings having a sufficiently high damage threshold.

Zinc Germanium Phosphide (ZGP) represents a nearly ideal material for high-power mid-IR OPOs. It is a positive uniaxial crystal and belongs to the group of ternary chalcopyrites (point group  $\bar{4}2m$ ) [202]. Its highly covalent bonds and dense packing result in a high effective nonlinear coefficient of  $d_{\text{eff}} = 75 \text{ pm V}^{-1}$  (see eq. (2.112) for type I phase matching) [199]. With a birefringence of around 0.04, ZGP is sufficiently anisotropic to achieve phase matching (see fig. 2.12) but not so much to cause severe spatial walk-off [199]. Furthermore, the high thermal conductivity of  $35 \text{ W m}^{-1} \text{ K}^{-1}$  facilitates efficient cooling.

The absorption coefficient of ZGP versus the wavelength is depicted in fig. 2.46. The wide transparency range that spans from  $2 \mu\text{m}$  up to  $8.5 \mu\text{m}$  is a crucial advantage for mid-IR generation compared to other commonly used nonlinear crystals such as  $\text{LiNbO}_3$  (including PPLN) and KTP which show significant absorption beyond  $4 \mu\text{m}$  [203–205]. However, the absorption coefficient of typical ZGP crystals grows rapidly for wavelengths shorter than  $2 \mu\text{m}$ . The high absorption between the theoretical band edge at  $0.72 \mu\text{m}$  and  $2 \mu\text{m}$  is mainly caused by singly ionized zinc vacancies [206]. To achieve low losses at wavelengths around  $2 \mu\text{m}$  a careful control of the growth process is required, which can be supplemented by a post-treatment with electron-beam irradiation to create compensating defects [199]. However, the latter strategy complicates the deposition of optical coatings with high-damage thresholds because the inserted defects become unstable at temperatures above  $200 \text{ }^\circ\text{C}$  [199]. The damage threshold of ZGP is typically around  $2 \text{ J cm}^{-2}$  and is highly dependent on surface preparation [207].

There are some alternative nonlinear crystals for high-power OPOs addressing the  $3\text{--}5 \mu\text{m}$  range. Among the most promising are orientation-patterned GaAs (OP-GaAs) and Cadmium Silicon Phosphide (CSP). OP-GaAs has a higher nonlinear coefficient ( $94 \text{ pm V}^{-1}$ ), a better thermal conductivity ( $46 \text{ W m}^{-1} \text{ K}^{-1}$ ), and a wider transparency range from  $1.9 \mu\text{m}$  to  $12 \mu\text{m}$ , compared to ZGP [199]. It utilizes quasi-phase-matching, which practically results in a comparable effective parametric gain to ZGP, but has the advantage of eliminating spatial walk-off. The main drawback of OP-GaAs is its limited aperture size, as a result of the growth process of the periodically poled layer structure on a substrate [199]. This limits the pump spot size and hence the pump pulse energy to remain below the typical damage threshold of around  $2 \text{ J cm}^{-2}$  [208]. CSP is a birefringent nonlinear crystal largely analogous to ZGP but exhibits

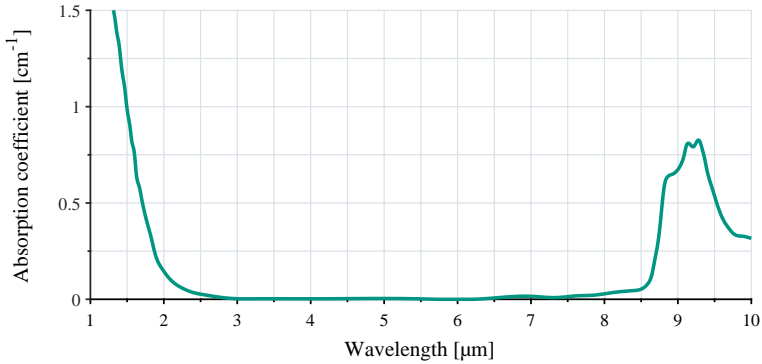


Figure 2.46: Absorption coefficient of ZnGeP<sub>2</sub> (ZGP) versus the wavelength. Data from [199].

a higher nonlinear coefficient of  $84.5 \text{ pm V}^{-1}$  and low absorption losses in the spectral range from  $1 \text{ }\mu\text{m}$  to  $6.5 \text{ }\mu\text{m}$ , allowing pumping at shorter wavelengths [209, 210]. Although CSP and OP-GaAs have high potential for the generation of coherent high-power mid-IR radiation, their availability is currently still limited, making ZGP the most widely used crystal in this field.

## 2.5.2 Pump Source Requirements

The characteristics of the pump beam crucially determine the output characteristics and efficiency of the nonlinear conversion process in an OPO. Generating coherent mid-IR radiation with high output power, high pulse energy and excellent beam quality requires maximizing the pump intensity across the spatial, spectral, and temporal domain, as illustrated in fig. 2.47. This ensures that as much pump power as possible exceeds the nonlinear threshold of the OPO, resulting in a high conversion efficiency. However, the optimization of a fiber laser within this requirement space involves managing various competing design criteria. An optimal design must balance the needs for a high intensity above threshold and a rapid mid-IR pulse build-up against the mitigation of spatial walk-off, thermal lensing, and optical damage.

In the spatial domain, a high average power and a nearly diffraction-limited beam quality are required from the pump to generate a mid-IR output with comparable characteristics. As discussed in sec. 2.3, fiber lasers are ideally suited to fulfill these requirements due to their waveguide geometry and excellent heat dissipation. However, the OPO conversion process

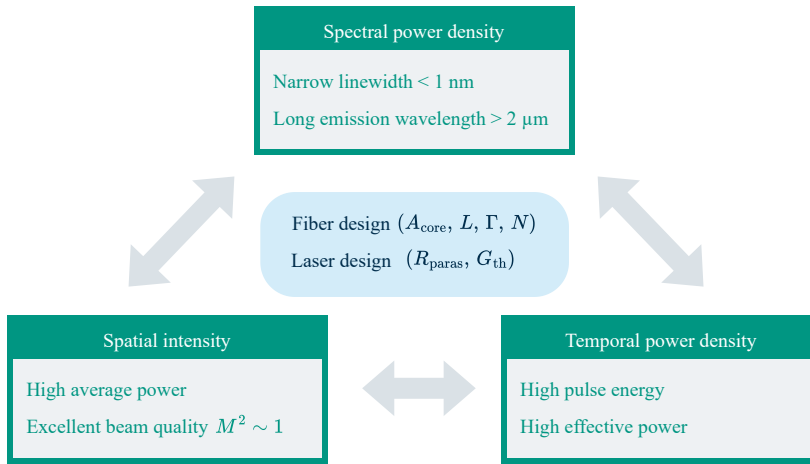


Figure 2.47: Pump source requirements and parameter optimization for a fiber laser to pump a ZGP OPO. The choice of the design parameters of the laser and active fiber has different, partly competing effects in the spatial, spectral, and temporal domain. An optimized pump source must provide a high intensity in all of three domains.

generally affects the beam quality by several spatial effects. For an approximately Gaussian beam typical for a single-mode fiber, the nonlinear conversion is restricted to the central part of the beam profile where the intensity is above the nonlinear threshold, leading to a dynamic gain-guiding effect for signal and idler that must be considered when designing the OPO cavity. The power in the wings of the Gaussian intensity profile that falls below the OPO threshold does not contribute to the conversion, thus reducing the efficiency. Furthermore, because the pump beam converts into two distinct mode fields of signal and idler in the DRO, perfect spatial coupling between the three fundamental modes is impossible. This imperfect coupling results in a degradation of the signal and idler beam quality or a reduction in conversion efficiency [211, 212]. In addition to these gain-related spatial effects, a high pump power can also induce thermal lensing in the nonlinear crystal or the resonator optics, which can degrade the beam quality. Mitigating thermal effects requires materials and coatings with low background absorption.

In the spectral domain, the absorption spectrum of ZGP (see fig. 2.46) demands pump wavelengths longer than  $2 \mu\text{m}$  to minimize thermal effects at high pump power levels. The exact pump wavelength is also a critical design choice for generating specific signal and idler output spectra that align with atmospheric transmission windows or to target specific molecular absorption lines.

Furthermore, a high spectral power density ensured by a narrow pump linewidth is essential for achieving a high conversion efficiency. Pump power distributed over a broad spectrum cannot effectively exceed the nonlinear threshold and does not contribute to the conversion [64].  $\text{Tm}^{3+}$ -doped fiber lasers are generally well suited to achieve a narrow output spectrum at wavelengths longer than  $2\ \mu\text{m}$ . Reabsorption in the long gain medium suppresses gain at short wavelengths and therefore shifts the gain spectrum to longer wavelengths.

The primary challenge for a fiber laser pump source concerns the temporal domain: fiber lasers are limited in their temporal power density because of parasitic lasing or strong ASE that limits the maximum achievable pulse energy (see sec. 2.4) and fiber nonlinearities that occur at high peak powers (see sec. 2.3.3). To characterize the temporal power density of arbitrary pulse shapes, the effective power  $P_{\text{eff}}$  given by eq. (2.250) serves as a useful metric. In contrast to the peak power, this metric evaluates how much of the pulse energy is available at high instantaneous power levels above the nonlinear threshold and can thus contribute to the conversion process. A favorable pulse shape, such as a rectangular pulse, maximizes the energy above the nonlinear threshold and exhibits a fast rise time, thus facilitating a rapid build-up of signal and idler in the OPO cavity (see eq. (2.185)). As discussed in sec. 2.4.2, fiber lasers are particularly advantageous for generating such pulses, as they allow for active pulse shaping in a diode-seeded MOPA configuration [181, 182].

The limitations of fiber lasers for achieving a high temporal power density lead to conflicts with the spatial and spectral requirements. First, intensity-dependent fiber nonlinearities such as SPM, MI, and SRS can cause severe spectral broadening, the emergence of undesired side peaks in the spectrum, or even supercontinuum generation that can cover a significant amount of the total output power (see sec. 2.3.3). This contradicts the requirement of a narrow linewidth. Second, due to the limited temporal power density, the pump beam must be focused to a small spot size to exceed the nonlinear intensity threshold. The pump spot size is chosen to reach intensities that are high enough for an efficient conversion but that also remain below the damage threshold of the nonlinear crystal. However, a small pump spot size has two detrimental consequences: it exacerbates thermal lensing at high average powers and it increases the impact of spatial walk-off.

For birefringent type I phase matching, spatial walk-off causes an angular mismatch between the collinear wave vectors of pump, signal, and idler and the Poynting vectors of the extraordinary signal and idler modes (see fig. 2.2b). This reduces the nonlinear coupling between

the mode fields along the propagation direction  $z$  according to the walk-off coupling coefficient [212]

$$C_{\text{wo}} = \exp\left(-\frac{\pi}{4} \left(\frac{z}{l_{\text{wo}}}\right)^2\right), \quad (2.271)$$

where

$$l_{\text{wo}} = \frac{\sqrt{\pi} w_{\text{pump}}}{2 \rho} \sqrt{\frac{w_{\text{id1}}^2 w_{\text{sig}}^2}{w_{\text{sig}}^2 + w_{\text{pump}}^2} \left(\frac{1}{w_{\text{sig}}^2} + \frac{1}{w_{\text{id1}}^2} + \frac{1}{w_{\text{pump}}^2}\right)} \quad (2.272)$$

is the walk-off length dependent on the mode field radii  $w_{\text{pump}}$ ,  $w_{\text{sig}}$ , and  $w_{\text{id1}}$  of the pump, signal, and idler, and  $\rho$  is the walk-off angle given by eq. (2.43) [212]. The walk-off coupling coefficient  $C_{\text{wo}}$  must be considered as an additional factor in the coupled mode eqs. (2.113) to (2.115) reducing the parametric gain along the nonlinear crystal. This reduction in parametric gain can be quantified by an effective interaction length

$$L_{\text{eff}}^{\text{wo}} = l_{\text{wo}} \text{erf}\left(\frac{\sqrt{\pi} L}{2 l_{\text{wo}}}\right), \quad (2.273)$$

where  $\text{erf}(\cdot)$  is the error function, and  $L$  the crystal length [211, 212].

Figure 2.48 illustrates the dependencies of these parameters on the propagation distance and the pump beam radius. In this simplified illustration, the pump, signal, and idler beams are assumed to have the same size ( $w_{\text{pump}} = w_{\text{sig}} = w_{\text{id1}}$ ). As shown in the plots, a smaller pump spot size leads to a more rapid decrease in the coupling coefficient and thus a significantly reduced effective gain length. This analysis implies that for a 20 mm crystal, a pump spot radius of at least  $w_{\text{pump}} \approx 0.5$  mm is required to efficiently utilize the crystal length. The reduced parametric gain due to spatial walk-off leads to an increase in pump threshold by a factor of  $(L/L_{\text{eff}})^2$  and hence to a decrease in conversion efficiency.

Taking these conflicts into account, an optimal design for a fiber laser pump source must find a trade-off between these requirements to achieve a high intensity in all of the three domains. This involves an appropriate selection of the active fiber and of the fiber laser architecture.

The choice of a suitable active fiber requires consideration of several parameters concerning the waveguide geometry and the doping composition, each having competing effects on the overall output performance of the pulsed fiber laser:

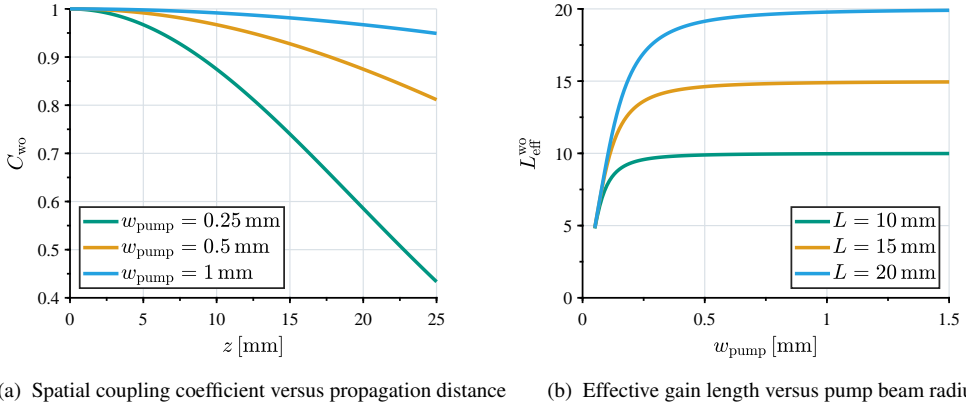


Figure 2.48: Effects of spatial walk-off on parametric coupling in a ZGP OPO. A small pump spot radius  $w_{\text{pump}}$  causes a more severe effect of spatial walk-off, reducing the parametric coupling and the effective parametric gain length along the nonlinear crystal.

- Doped core area ( $A_{\text{core}}$ ): A larger core mitigates intensity-dependent nonlinear effects and increases the saturation energy to achieve higher pulse energies (see eq. (2.246)). However, to maintain single-mode operation, an increase in core diameter requires a decrease in numerical aperture (see eq.(2.197)), making the guiding more sensitive to bending losses. For example, rod-type LPFs exhibit very large core diameters but cannot be coiled and are therefore practically restricted to short fiber lengths.
- Fiber length ( $L$ ): Long fibers are beneficial for laser operation at long wavelengths  $> 2 \mu\text{m}$ , because they lead to a lower local population inversion causing a red shift of the gain spectrum by reabsorption (see fig. 2.27). However, a long fiber length also increases the gain for nonlinear effects.
- Overlap factors ( $\Gamma$ ): A lower overlap factor  $\Gamma_{\text{s}}$  of the signal mode with the core increases the saturation energy but also reduces reabsorption, hindering long-wavelength operation. The pump overlap  $\Gamma_{\text{pump}}$  dictates the absorption efficiency and the longitudinal inversion distribution, which in turn affects the nonlinear gain (see fig. 2.35).
- Doping concentration  $N$ : Higher doping improves the efficiency in  $\text{Tm}^{3+}$ -doped fibers (see sec. 2.3.1) and enhances reabsorption, but also increases the refractive index in the core. This complicates the design of fibers with large-mode-field area and low NA.

The fiber laser architecture plays an equally important role for designing a suitable pump source. In a Q-switched fiber laser, a low-loss cavity design with a low threshold gain  $G_{\text{th}}$  allows for an efficient pulse energy extraction (see sec. 2.4.1). A higher reflectivity  $R_{\text{OC}}$  of the OC decreases the inversion for operation at long wavelengths and leads to a lower threshold gain  $G_{\text{th}}$  but also reduces the resonator efficiency (see eq. (2.159)). In contrast, efficient pulse energy extraction from a fiber amplifier demands input pulses with sufficient energy and suitable pulse shape (see sec. 2.4.2). This requires an elaborate design of several amplifier stages in a pulsed fiber MOPA. Despite this additional complexity, the MOPA approach generally allows for improved output power scalability and easier all-in-fiber integration (see sec. 2.3.4). Moreover, fiber MOPAs enable the implementation of active pulse shaping to optimize the temporal power density for nonlinear conversion. In both architectures, fiber oscillators and MOPAs, it is essential to suppress parasitic reflections at interfaces and splices to enable high pulse energy extraction.

### 2.5.3 State of the Art in Fiber-Laser-Pumped ZGP OPOs

There are several demonstrations of mid-IR ZGP OPOs pumped by 2  $\mu\text{m}$  fiber lasers in the literature. Table 2.3 summarizes publications prior to the work in this thesis, comparing the pump characteristics and the generated mid-IR output. Since the first demonstration by Creeden et al. in 2008, the performance of these systems has advanced through subsequent publications, reaching a maximum mid-IR output power of 8.1 W reported by Dalloz et al. in 2019 [22, 213]. However, the limited pulse energies of the fiber laser pumps and the consequently small pump spot diameters of 140–350  $\mu\text{m}$  caused substantial challenges in each of the listed publications. Severe spatial walk-off and thermal lensing limited the optical-to-optical conversion efficiency  $\eta_{\text{oo}}$  to 16–33 %, which is significantly lower than the typical 50–60 % achieved with bulk solid-state lasers [36, 197, 214]. Despite the potentially high average output powers from fiber lasers, these low conversion efficiencies have hindered the scaling of mid-IR output powers beyond the 10 W level.

The first fiber-laser-pumped ZGP OPO demonstrated by Creeden et al. in 2008 utilized a  $\text{Tm}^{3+}$ -doped fiber amplifier that was gain-switched by a 1.5  $\mu\text{m}$   $\text{Er}^{3+}$ :fiber MOPA [22]. As  $\text{Tm}^{3+}$ -doped fiber technology was still in its early stages at the time, the MOPA did not employ a PM fiber in the final amplifier stage. This resulted in additional losses in the polarization-sensitive

Table 2.3: Overview of fiber laser pumped ZGP OPOs published before 2021.

Architecture*	Pump Laser				Mid-IR Output				
	$E_{\text{pulse}}$	$P_{\text{eff}}$	$\lambda_c$	$d_{\text{pump}}$	$P_{\text{out}}$	$E_{\text{pulse}}$	$\eta_{\infty}$	$M^2$ (S/I)	Year
AF - GS MOPA	96 $\mu\text{J}$	2.1 kW	1995 nm	140 $\mu\text{m}$	0.66 W	22 $\mu\text{J}$	22 %	1.3/2.9	2008 [22]
AF - GS MOPA	127 $\mu\text{J}$	-	2000 nm	170 $\mu\text{m}$	2 W	50 $\mu\text{J}$	15.7 %	-	2008 [215]
AF - GS MOPA	160 $\mu\text{J}$	-	2044 nm	140 $\mu\text{m}$	3 W	50 $\mu\text{J}$	25 %	-/2.1	2012 [201]
FS - QS MOPA	840 $\mu\text{J}$	78 kW	1980 nm	335 $\mu\text{m}$	1.1 W	284 $\mu\text{J}$	28 %	-	2014 [39]
FS - QS Oscil.	500 $\mu\text{J}$	5.1 kW	2024 nm	350 $\mu\text{m}$	6.5 W	163 $\mu\text{J}$	32.5 %	-	2015 [194]
FS - QS Oscil.	340 $\mu\text{J}$	2.5 kW	2090 nm	300 $\mu\text{m}$	8.1 W	81 $\mu\text{J}$	24 %	-	2019 [213]

\* AF: All-in-fiber, FS: Free-space, GS: Gain-switched, QS: Q-switched

optical isolator between the fiber laser and the ZGP OPO. After the isolator, the pump pulses with a pulse energy of 96  $\mu\text{J}$  and an effective power of 2.1 kW at a central emission wavelength of 1995 nm were launched into the linear ZGP OPO. A total mid-IR power of 0.66 W combined signal and idler output was generated with a conversion efficiency of 22 %. The beam quality was characterized by  $M^2$  factors of 1.3 and 2.9 for signal and idler, respectively. The low conversion efficiency was attributed to the small pump spot diameter of 140  $\mu\text{m}$  which caused substantial walk-off and thermal lensing within the 15 mm ZGP crystal.

Shortly thereafter, the same authors investigated power scaling of this approach in a follow-up publication [215]. By implementing an additional  $\text{Tm}^{3+}$ -doped fiber amplifier stage, they increased the available pump power to 12.7 W. However, the still-small 170  $\mu\text{m}$  pump spot diameter led to a roll-off in the mid-IR output power due to thermal lensing and walk-off. Thus, for pump powers exceeding 10 W, the maximum output power was limited to 2 W, corresponding to a conversion efficiency of only 15.7 %.

A 2012 publication by Simakov et al. built upon the initial results by addressing some of the described issues. The work employed a similar gain-switched MOPA architecture but incorporated  $\text{Tm}^{3+}$ -doped PM fibers. Due to the limited pump pulse energy of 160  $\mu\text{J}$ , the pump still had to be focused to a small spot size of 140  $\mu\text{m}$ . However, the authors employed two strategies to mitigate thermal lensing and spatial walk-off. First, a long emission wavelength of 2044 nm was achieved in the fiber laser to reduce background absorption in the ZGP crystal. Second, two 16 mm ZGP crystals were placed in a walk-off compensating orientation within the OPO cavity. Despite these strategies, the mid-IR output power still exhibited a thermal roll-off for pump powers exceeding  $\sim 8$  W, accompanied by a degradation in mid-IR beam quality.

The output power was ultimately limited to a maximum of 3 W with a conversion efficiency of 25 %.

In 2014, Gebhardt et al. targeted the generation of higher pump pulse energies from a fiber laser [39]. Their fiber MOPA was entirely based on  $\text{Tm}^{3+}$ -doped fibers but implemented in a free-space configuration. A Q-switched fiber oscillator was used to generate the seed pulses, which were subsequently amplified within two amplifier stages based on  $\text{Tm}^{3+}$ -doped PCFs. The large 50  $\mu\text{m}$  core diameters of the PCFs enabled the generation of high pulse energies of 840  $\mu\text{J}$  with an effective power of 78 kW. However, the final PCF amplifier stage suffered from a poor slope efficiency of only 9 % (see tab. 2.2), limiting the pump power to 3.4 W at a wavelength of 1980 nm. Although this enabled a larger pump spot diameter of 335  $\mu\text{m}$  to pump the 12 mm ZGP crystal, the conversion efficiency was only 28 % in the linear OPO. A maximum output power of 1.1 W and a high pulse energy of 284  $\mu\text{J}$  were generated in the mid-IR. The authors identified the power limitations and unreliability of their complex free-space setup as the primary obstacles, reporting parasitic lasing and, ultimately, damage to a fiber end-face due to contamination.

To reduce the complexity of the pump laser system, Kieleck et al. demonstrated a ZGP OPO directly pumped by a single fiber oscillator in 2015 [194]. The free-space fiber oscillator was based on a 25  $\mu\text{m}$   $\text{Tm}^{3+}$ -doped PM fiber. Using an AOM for active Q-switching, the oscillator provided pump pulses with 500  $\mu\text{J}$  pulse energy and 5.1 kW of effective power at a wavelength of 2024 nm to pump a linear ZGP OPO. The higher effective power allowed for a larger pump spot diameter of 350  $\mu\text{m}$ , leading to an improved conversion efficiency of 32.5 % and thus a maximum mid-IR output power of 6.5 W. The beam quality of signal and idler was reported as  $M_{\text{sig}}^2 < 2.1$  and  $M_{\text{idl}}^2 < 2.4$  at a total mid-IR output power of 2 W, though these values were not provided at maximum output power.

The concept of the Q-switched fiber oscillator was adapted in 2019 by Dalloz et al., who used a  $\text{Tm}^{3+}:\text{Ho}^{3+}$ -co-doped LMA fiber to achieve a longer pump wavelength of 2090 nm [213]. The lower background absorption in ZGP at this pump wavelength enabled them to scale the mid-IR output power to 8.1 W—the highest reported for a fiber-pumped ZGP at the time. However, the low pulse energy of 340  $\mu\text{J}$  and effective power of 2.5 kW required a smaller pump spot size with a diameter of 300  $\mu\text{m}$ . This led to a low conversion efficiency of 24 %.

Beyond the work on ZGP, the literature also contains a few demonstrations of OP-GaAs OPOs pumped by  $\text{Tm}^{3+}$ -doped fiber lasers. These include a 2.2 W system pumped by a Q-switched

fiber oscillator and a brief report of an 18 W mid-IR system for which no further details are available [199, 216].

These previous publications on fiber-laser-pumped mid-IR OPOs reveal a clear pathway for future developments. To become serious competitors to pump sources based on bulk solid-state lasers such as  $\text{Ho}^{3+}$ :YAG, the conversion efficiencies in fiber-laser-pumped ZGP OPOs must be significantly improved. The low conversion efficiencies in previous systems are a direct consequence of the small pump spot diameters of 140–350  $\mu\text{m}$ , required by the limited pump pulse energies, which cause detrimental thermal lensing and spatial walk-off. As illustrated in fig. 2.48, significantly larger pump spot diameters on the order of 1 mm are necessary to efficiently utilize the length of a 10–20 mm ZGP crystal ( $d_{\text{pump}} = 2w_{\text{pump}}$ ). Such large spot sizes, however, demand a substantial improvement in the temporal power density,  $P_{\text{eff}}$ , to sufficiently exceed the OPO threshold. Improving the effective power involves maximizing the pulse energy and optimizing the temporal shape of the pulses generated from the fiber laser. Furthermore, the motivation for using a fiber laser pump source extends beyond the demand of mere performance; it includes the promise of a more robust, reliable, and integrable laser system compared to bulk solid-state lasers. Consequently, a fiber laser design must not only convince through its performance, but must also feature an architecture suitable for monolithic, all-in-fiber integration.

This thesis presents a detailed study and analysis of the pulse energy limitations in fiber lasers. This analysis provides the foundation for improving the temporal power density while maintaining spectral purity in fiber laser pump sources for highly-efficient nonlinear frequency conversion into the mid-IR.



### 3 Investigation of Pulse Energy Limits and Nonlinear Conversion

This chapter presents an experimental investigation into the pulse energy limitations of  $\text{Tm}^{3+}$ -doped fiber lasers and initial results for mid-IR generation via fiber-pumped  $\text{ZnGeP}_2$  (ZGP) optical parametric oscillators (OPOs). Parts of the work described herein have been published in two journal articles and three conference proceedings [217–221].

To investigate the mechanisms that limit the pulse energy in fiber lasers, a Q-switched fiber oscillator with a linear free-space design is developed and examined in section 3.1. This architecture offers high transparency and flexibility, facilitating a clear analysis of the fundamental limiting effects. The section details the experimental setup and the measurement procedure, followed by a presentation and discussion of the experimental results. This discussion provides a qualitative comparison between the observed limitations in pulse energy scaling and the theoretical limiting mechanisms described in sec. 2.4. A comprehensive quantitative analysis and refinement of the theory is presented in chapter 4.

Section 3.2 subsequently demonstrates the application of the developed fiber lasers as a pump source for a ZGP OPO. An evaluation of the mid-IR output and conversion efficiency serves to experimentally validate and quantify the impact of the pump characteristics. This provides a practical basis for the fiber laser optimization detailed in the subsequent chapters.

## 3.1 Q-switched Fiber Oscillator

### 3.1.1 Experimental Setup and Procedure

The pulse energy limits in  $\text{Tm}^{3+}$ -doped fiber lasers were investigated using a free-space oscillator configuration depicted in fig. 3.1a. The general architecture of fiber oscillators is discussed in sec. 2.3.4, the physical principles of the optical components are detailed in sec. 2.1, and a description of the Q-switching process is provided in sec. 2.4.1.

Two different  $\text{Tm}^{3+}$ -doped large-mode-area (LMA) fibers were examined; their geometry parameters are summarized in table 3.1. The first fiber, designated Tm-20-300, has a core diameter of  $20\ \mu\text{m}$ , a cladding diameter of  $300\ \mu\text{m}$ , and a length of 3.7 m. The second, designated Tm-25-400, has a core diameter of  $25\ \mu\text{m}$ , a cladding diameter of  $400\ \mu\text{m}$ , and a length of 5 m. Both are polarization-maintaining (PM) fibers of the PANDA type, employing circular, boron-doped stress rods along the slow-axis. A micrograph of the Tm-20-300 fiber cross-section is shown in fig. 3.1b. During operation, the fibers were coiled to a bending radius of approximately 10 cm and actively water-cooled. The active fibers were pumped bidirectionally by two 793 nm laser diodes, with dichroic mirrors used to combine or separate the pump and laser beams.

The laser cavity is formed by a volume Bragg grating (VBG) and the straight-cleaved opposing fiber end facet. The VBG acts as the high reflector (HR), defining the laser wavelength, while the fiber end facet serves as the output coupler (OC) with approximately 4 % Fresnel reflectivity. To suppress parasitic feedback, the fiber end facing the VBG was angle-cleaved. Two different VBGs, centered at 2044 nm and 2050 nm, were utilized in the experiments. The 2044 nm VBG has a FWHM reflectance bandwidth of 0.77 nm, and the 2050 nm VBG has a bandwidth of 0.37 nm. Both VBGs have a peak reflectance  $>99\%$ . Consequently, both VBGs resulted in similar laser performance, except for the distinct central emission wavelength.

To enforce linearly polarized operation of the fiber laser, a Brewster-cut thin-film polarizer (TFP) was inserted into the cavity between the VBG and the active fiber. The dichroic coating of the TFP is highly reflective for s-polarized light and highly transmissive for p-polarized light from  $\sim 2030\ \text{nm}$  to  $\sim 2070\ \text{nm}$ , thus causing the laser to oscillate with linear polarization. For wavelengths shorter than 1970 nm the TFP acts as a long-pass filter, highly reflective for both

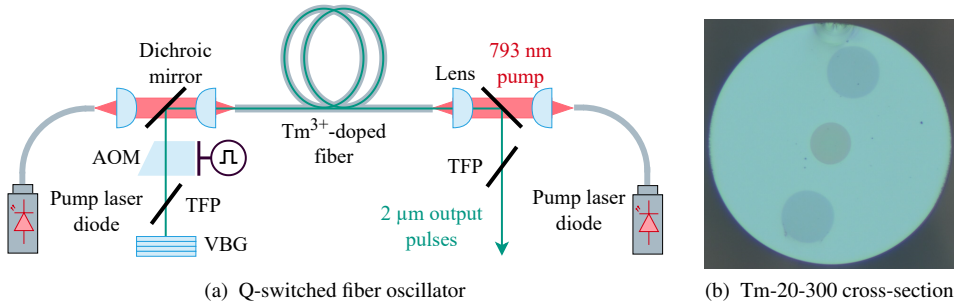


Figure 3.1: Schematic of the experimental setup of the Q-switched fiber oscillator and fiber cross-section of the Tm-20-300 fiber.

Table 3.1: Geometry parameters of the two investigated Tm<sup>3+</sup>-doped LMA fibers.

Designation	PM-type	$d_{\text{core}}$	$d_{\text{clad}}$	$\text{NA}_{\text{core}}$	$\text{NA}_{\text{clad}}$	$V$ at 2050 nm	$w_0$	$L$
Tm-20-300	PANDA	20 $\mu\text{m}$	300 $\mu\text{m}$	0.08	0.46	2.45	10.9 $\mu\text{m}$	3.7 m
Tm-25-400	PANDA	25 $\mu\text{m}$	400 $\mu\text{m}$	0.07	0.46	2.68	12.8 $\mu\text{m}$	5 m

polarization states. An additional TFP at the laser output ensures high polarization purity for measurement and application. For comparison, the laser was also operated without the TFPs, which resulted in a randomly polarized output; both polarized and unpolarized configurations were investigated.

Active Q-switching was achieved using an acousto-optical modulator (AOM) placed in the cavity between the VBG and the active fiber. To scale the pulse energy, the fiber laser was operated at a constant pump power while the pulse repetition frequency (PRF) was gradually decreased. Lowering the PRF extends the charging period between pulses to accumulate a higher initial inversion and gain, resulting in a higher extracted pulse energy. This scaling method was chosen because it maintains a nearly constant thermal load on the system, minimizing the need for cavity re-alignment during the measurements.

The free-space oscillator configuration provides high flexibility for easy exchange of components and of the active fiber to investigate their impact. A drawback, however, is its sensitivity to thermal misalignment. The VBG needs to be frequently re-aligned, in particular when changing the pump power, to optimize the feedback and maximize the output power. At high pump power, a reduced coupling efficiency can easily cause damage to the fiber end facets. To reduce thermal

effects and the risk of damage, the fiber laser was operated at moderate pump power levels, limited to a maximum of  $\sim 60$  W for these experiments.

The pulsed fiber laser was characterized by measuring its average output power, temporal pulse signal, output spectrum, and spatial beam profile, following the methods described in sec. 2.1.1. The average output power was measured with a thermopile sensor; the temporal signal was recorded using a photoelectromagnetic (PEM) detector with a time constant  $< 1$  ns; the output spectrum was captured by an optical spectrum analyzer (OSA); and the beam profile was acquired using a pyroelectric camera with a pixel size of  $80\ \mu\text{m} \times 80\ \mu\text{m}$ . The pulse energy was determined by dividing the measured average output power by the pulse repetition frequency (see eq. (2.249)), as long as there is no parasitic lasing and negligible amplified spontaneous emission (ASE) between the pulses. To detect the onset of parasitic lasing or significant ASE, the spectral and temporal laser characteristics of the output signal, the reflected signals from the TFPs, and the transmitted signal behind the VBG were continuously monitored. These characteristics were recorded throughout multiple measurement series at different power levels and in various laser configurations to systematically identify and investigate the pulse energy limits.

### 3.1.2 Experimental Results and Discussion

The experimental results are presented in three parts—temporal, spectral, and spatial characteristics—aligning with the OPO pump source requirements detailed in sec. 2.5. Within each part, it is emphasized how the laser characteristics change during pulse energy scaling, and how limitations manifest in the measurements across the respective domains.

#### Pulse characteristics

Figure 3.2 shows the results for pulse energy scaling of the unpolarized Tm-20-300 fiber laser, operated at a wavelength of 2044 nm. At constant pump powers of 43 W and 54 W, decreasing the PRF resulted in the expected trends: the pulse energy increased approximately as  $E_{\text{pulse}} \propto 1/f_{\text{rep}}$  (fig. 3.2a), while the pulse duration decreased linearly (fig. 3.2b). The pulse durations are specified in terms of the FWHM of a Gaussian profile fitted to the measured pulse shape (see fig. 3.3). For both pump power levels, a maximum pulse energy of  $\sim 800\ \mu\text{J}$  was achieved at PRFs of 16 kHz and 21 kHz, respectively, corresponding to minimum pulse

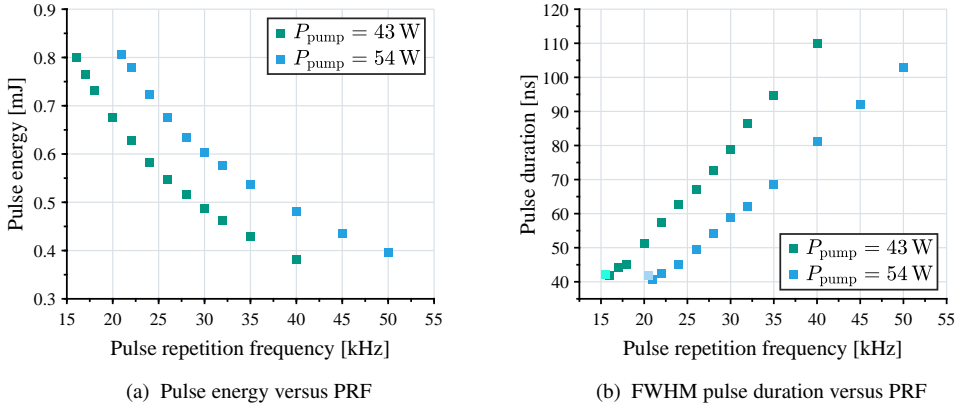


Figure 3.2: Measured pulse characteristics for the unpolarized Tm-20-300 fiber during pulse energy scaling at 2044 nm. The pulse energy was scaled at two constant pump powers of 43 W and 54 W by gradually decreasing the PRF. In (b), the points at the lowest PRFs differing in color deviate from the linear decrease in pulse duration with lower PRF, indicating that the pulse energy limit was exceeded.

durations of  $\sim 41\text{--}42$  ns. When further decreasing the PRF, parasitic lasing was observed in between the pulses, which limited a further increase in pulse energy. Consequently, the measured pulse duration stagnated or even increased beyond the pulse energy limit. This behavior is clearly evidenced in fig. 3.2b, where the final highlighted data points deviate from the linear trend.

The same measurements were conducted for the polarized Tm-20-300 fiber laser. This configuration reached a lower maximum pulse energy of  $\sim 625 \mu\text{J}$  with a minimum pulse duration of 43 ns, a limit also imposed by parasitic lasing. This lower pulse energy limit is attributed to the lower efficiency of the polarized fiber laser, a factor that will be analyzed in the context of average power characteristics.

The temporal pulse profiles at maximum pulse energy of both the unpolarized and polarized Tm-20-300 fiber laser are shown in fig. 3.3. Both measured pulse shapes exhibit good agreement with the fitted Gaussian profiles. Based on this shape, the effective power  $P_{\text{eff}}$  was calculated from the Gaussian peak power (see eq. (2.262)) using the relation  $P_{\text{eff}} = P_{\text{peak}}/\sqrt{2}$ . For the unpolarized pulse, a peak power of  $P_{\text{peak}} \approx 18.5 \text{ kW}$  yields an effective power of  $P_{\text{eff}} \approx 13.1 \text{ kW}$ , while the polarized pulse had a peak power of  $P_{\text{peak}} \approx 13.7 \text{ kW}$  and an effective power of  $P_{\text{eff}} \approx 9.7 \text{ kW}$ , indicated by the dashed lines in fig. 3.3.

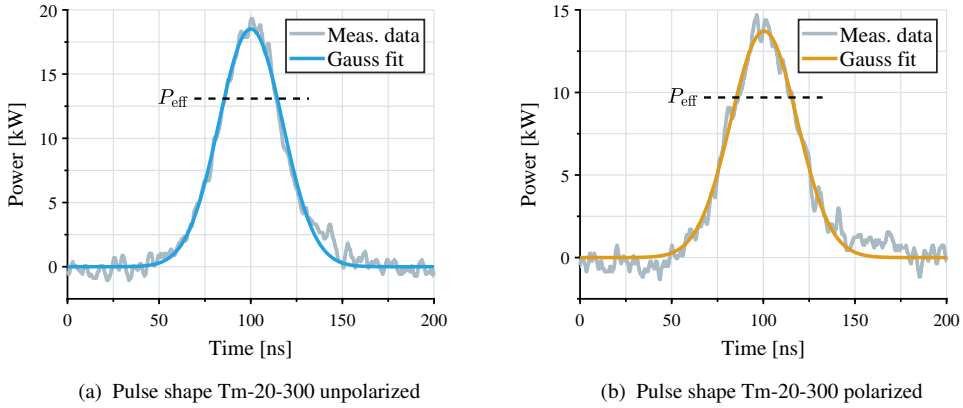


Figure 3.3: Measured temporal pulse profiles at maximum pulse energy for the Tm-20-300 fiber in unpolarized (a) and polarized (b) configuration. The FWHM pulse durations are 40.9 ns and 43.0 ns, respectively. The dashed lines indicate the effective power  $P_{\text{eff}}$  of the pulses. The length of the dashed lines correspond to the effective duration  $T_{\text{eff}}$ .

Parasitic lasing occurs in a transient spiking process when the gain exceeds the parasitic threshold  $G_{\text{paras}}$  during the charging period  $T_{\text{charge}}$ , as described in sec. 2.4.1. After a build-up time  $T_{\text{b,paras}}$ , the parasitic spikes partially deplete the accumulated population inversion and therefore limit a further increase in gain. The parasitic cavity is typically formed by  $\sim 4\%$  reflection from the OC and a much weaker parasitic reflection  $R_{\text{paras}}$  from the opposing fiber end (see eq. (2.255)). Consequently, the majority of the parasitic lasing signal is emitted from the HR side of the fiber laser. Parasitic lasing occurs at the gain maximum, generally at shorter wavelengths than the 2044 nm operation wavelength. In the unpolarized laser without intracavity TFP, this parasitic signal was transmitted through the VBG and measured behind it. In the polarized laser, it was detected in the reflection from the TFP, which acts as a long-pass filter.

The transient build-up of parasitic lasing measured at different operation points for the unpolarized Tm-20-300 fiber is depicted in fig. 3.4. The rectangular AOM driving voltage, designated as  $\Lambda$ , corresponds to the loss modulation of the Q-switching process (see fig. 2.43 for comparison). The signal S1 represents the generated output pulse measured right at the pulse energy limit, which formed  $\sim 1.5 \mu\text{s}$  after switching to the high Q-factor. At the same operation point, the signal S2 was measured behind the VBG. Normalized to the same peak intensity, the pulse in S2 coincides well with the output pulse S1, but has a slightly longer pulse tail at the rising

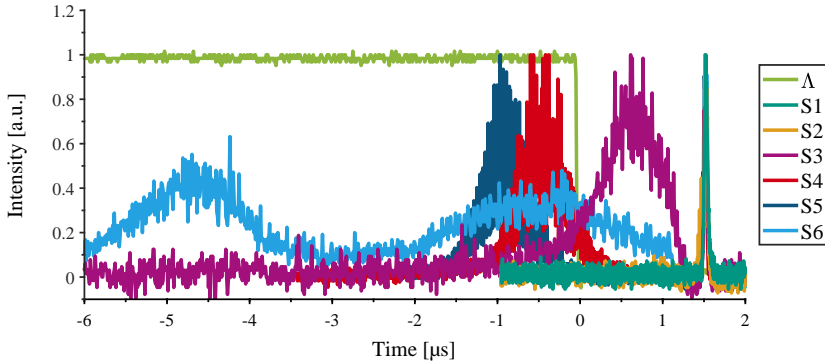


Figure 3.4: Transient parasitic lasing at different operation points for the unpolarized Tm-20-300 fiber laser.  $\Lambda$  is the AOM loss modulation. S1 and S2 are the output signal and the signal measured behind the VBG, respectively, recorded right at the pulse energy limit. The other signals S3-S6 are measured behind the VBG at different operation points beyond the pulse energy limit, showing parasitic pulses that arise before the desired pulse.

edge. This detail reveals an initial build-up of parasitic lasing which is interrupted by the much faster build-up of the desired pulse. The signals S3-S6 are all measured behind the VBG and show the parasitic spiking that occurred at different operation points beyond the pulse energy limit. Note that the intensities of the parasitic signals (S2-S6) have been exaggerated for visibility; their actual magnitude is significantly lower than that of the desired output pulse (S1).

Signal S3, measured at a pump power of 35.7 W and a PRF of 11 kHz, shows a parasitic spike that forms immediately before the desired output pulse. The falling edge of this parasitic pulse is truncated by the much faster build-up of the desired pulse. By this point, however, the parasitic pulse has already peaked; thus, it has had sufficient time to deplete the population inversion below the parasitic threshold.

When further decreasing the PRF or increasing the pump power the parasitic threshold is reached earlier, resulting in an earlier formation of the parasitic pulse. This effect is demonstrated by the signals S4 and S5, measured at PRFs of 15.5 kHz and 15.4 kHz, respectively, at a pump power of 43.2 W. The slight reduction of the PRF from S4 to S5 shifts the parasitic spike to an earlier time. Compared to the parasitic pulse in S3, these pulses are also shorter in duration, indicating a higher maximum gain. The higher pump power allows the gain to accumulate more rapidly.

Thus, the gain can further exceed the parasitic threshold  $G_{\text{th,paras}}$  during the parasitic build-up time  $T_{\text{b,paras}}$ , before the parasitic emission eventually quenches it.

At even lower PRFs, a second parasitic spike can form, as shown in signal S6. The signal was recorded at a pump power of 28.2 W and a PRF of 9 kHz. As a consequence of the lower pump power, these parasitic spikes have a longer duration compared to S3-S5. The temporal separation between the end of the first and the beginning of the second spike is approximately 2  $\mu\text{s}$ . This inter-spike period provides an estimate for the parasitic build-up time  $T_{\text{b,paras}}$ . As shown in fig. 2.20b, the temporal separation between the spikes gradually decreases compared to the initial build-up time. The exact parasitic build-time  $T_{\text{b,paras}}$  depends on the initial gain, the photon lifetime of the parasitic cavity, and the initial noise intensity. However, the measurement indicates that  $T_{\text{b,paras}}$  is on the order of a few microseconds for this system.

The analysis of the transient parasitic lasing leads to an important conclusion: the pulse energy limit set by parasitic lasing is not fixed but increases with pump power. The shorter duration of the parasitic pulses at higher pump powers confirms that a higher pump rate results in a higher maximum initial gain  $G_{\text{i,max}}$  before the first parasitic spike can form. Consequently, more energy is temporarily stored in the fiber, allowing for a higher maximum pulse energy if the pulse is extracted within the parasitic build-up time  $T_{\text{b,paras}}$ .

In the low-PRF regime of  $\sim 10\text{--}25$  kHz investigated in this experiment, this effect was minor, because the parasitic build-up time was much shorter than the total charging time ( $T_{\text{b,paras}} \ll T_{\text{charge}} \approx 1/f_{\text{rep}}$ ). Nevertheless, fig. 3.2a already shows a subtle trend toward a higher pulse energy limit at higher pump power. This effect is expected to become more significant at higher PRFs of  $\sim 100$  kHz where the charging time of  $T_{\text{charge}} < 10 \mu\text{s}$  becomes comparable to  $T_{\text{b,paras}}$ . In this regime, a parasitic build-up time of a few microseconds significantly extends the maximum charging time, in which a higher pump power can accumulate additional population inversion exceeding the parasitic threshold. This makes operation at high pump powers and high PRFs highly advantageous.

Beyond increasing gain, the maximum extractable energy can also be enhanced by a higher saturation energy  $E_{\text{sat}}$  of the gain medium (see eqs. (2.245) and (2.246)), which is typically achieved by employing a fiber with a larger core area  $A_{\text{core}}$ . Following this principle, the Tm-25-400 fiber was investigated; the results are shown in figure 3.5. At a pump power of 51 W and a PRF of 16 kHz in a randomly polarized configuration, a maximum pulse energy of 950  $\mu\text{J}$  was

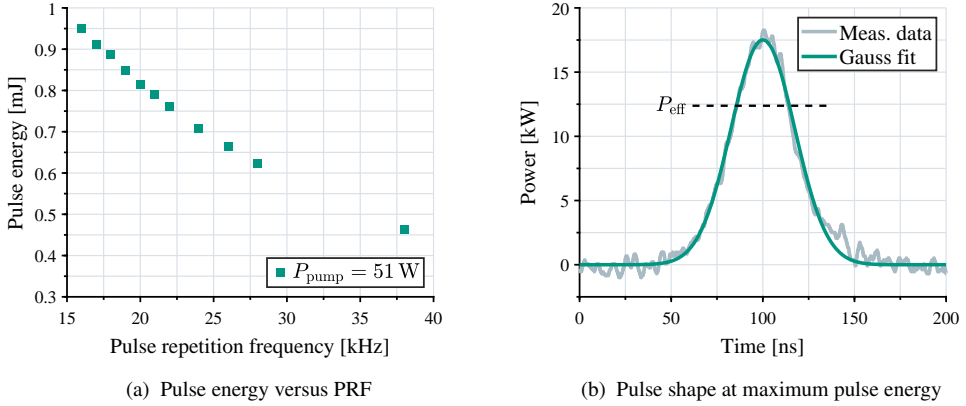


Figure 3.5: Pulse energy scaling of the unpolarized Tm-25-400 fiber laser at 2050 nm. A maximum pulse energy of 950  $\mu\text{J}$  was reached at a pump power of 51 W and a PRF of 16 kHz. At the maximum pulse energy, the FWHM pulse duration was 51 ns.

achieved, again limited by the onset of parasitic lasing. Assuming uniformly-doped step-index profiles and using  $\sigma_e(2044 \text{ nm}) \approx 1.89 \cdot 10^{-25} \text{ m}^{-2}$  and  $\sigma_e(2050 \text{ nm}) \approx 1.78 \cdot 10^{-25} \text{ m}^{-2}$ , the parameters from table 3.1 yield saturation energies of  $\sim 198 \mu\text{J}$  for the Tm-20-300 fiber, and  $\sim 312 \mu\text{J}$  for the Tm-25-400 fiber. This reveals a discrepancy: while the Tm-25-400 fiber has an approximately 58 % higher saturation energy, its maximum pulse energy was only 19 % higher.

Theoretically, this discrepancy can be explained by two possible reasons, according to the eqs. (2.245) and (2.247): a lower initial gain  $G_i$  or higher cavity losses that result in a higher threshold gain  $G_{\text{th}}$ . The latter leads to less efficient energy extraction (higher  $G_f$ ) and a lower outcoupling efficiency  $\eta_R$ . At its pulse energy limit, the Tm-25-400 fiber laser produces pulses with a minimum duration of  $\sim 51 \text{ ns}$  (see fig. 3.5b), which is  $\sim 21 \%$  longer than the  $\sim 42 \text{ ns}$  pulses from the Tm-20-300 fiber laser. According to the eqs. (2.262) and (2.263), the pulse duration is directly proportional to the fiber length  $L$  included in the resonator lifetime  $\tau_c$  (see (2.153)). Because the Tm-25-400 fiber is  $\sim 35 \%$  longer than the Tm-20-300 fiber, this should have resulted in a proportionally longer pulse. The fact that the duration increased by only 21 % implies that the maximum initial gain of the Tm-25-400 fiber laser must have been higher, not lower, to compensate and produce the measured pulse width. This leads to the conclusion that the Tm-25-400 fiber laser suffers from substantially higher cavity losses, preventing the

laser from generating higher pulse energies. This hypothesis will be investigated further in the analysis of the average power characteristics.

### Spectral characteristics

Scaling of the pulse energy and peak power changes the output spectrum of a fiber laser because of intensity-dependent nonlinear effects in the fiber, as established in sec. 2.3.3. The measured output spectra of the polarized Tm-20-300 fiber laser at different pulse peak powers are plotted in fig. 3.6a. Evidently, a higher peak power led to a broader output spectrum. Figure 3.6b shows the measured 3-dB, 10-dB, and 20-dB linewidth of the output spectrum versus the peak power. While the 3-dB linewidth grew modestly, the 10-dB and 20-dB linewidths exhibited a steeper, nearly linear increase with peak power. At the maximum peak power of 13.5 kW, the 3-dB, 10-dB, and 20-dB linewidths reached 0.85 nm, 3.33 nm, and 7.27 nm, respectively. The spectral characteristics depicted in fig. 3.6 agree qualitatively well with the behavior illustrated in fig. 2.34, indicating ASE as the reason for the spectral broadening. The parameter  $Z = L_{\text{eff}}/L_{\text{NL}}$  used in fig. 2.34 is proportional to the peak power but also depends on the gain along the fiber. A quantitative comparison therefore requires an analysis of the gain, which will be considered in chapter 4.

When reaching the pulse energy limit set by parasitic lasing, the peak power is clamped and the spectral broadening by SPM ceases. Therefore, the stagnation of the spectral linewidth serves as another indicator for reaching the pulse energy limit in a fiber laser.

The output spectrum of the unpolarized Tm-25-400 fiber laser at its maximum pulse energy of 950  $\mu\text{J}$  and peak power of 17.5 kW is shown in fig. 3.7. A high-resolution scan of the central laser line at  $\sim 2050$  nm in fig. 3.7a reveals a 3-dB linewidth of 0.35 nm, a 10-dB linewidth of 1.19 nm, and a 20-dB linewidth of 3.44 nm. Figure 3.7b shows the output spectrum measured with a resolution of 2 nm over a wider spectral range of 1800–2400 nm. On both sides of the central laser line, side peaks are visible at  $\sim 25$  dB below the central peak. This is a typical characteristic of modulation instability (MI) equivalent to degenerate four-wave mixing (DFWM) (see fig. 2.35b). However, in contrast to the symmetric gain spectrum of MI, the measured output spectrum is highly asymmetric. On the longer-wavelength side, the side peaks are higher and the spectrum exhibits a long tail that extends beyond 2.3  $\mu\text{m}$ .

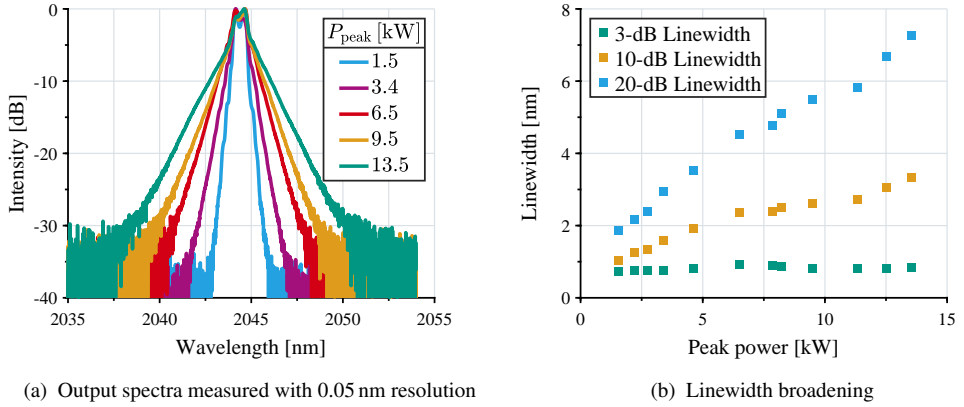


Figure 3.6: Output spectra and spectral broadening of the the 3-dB, 10-dB, and 20-dB linewidth for different peak powers of the Tm-20-300 fiber laser at 2044 nm. The linewidth broadens approximately linearly with the peak power.

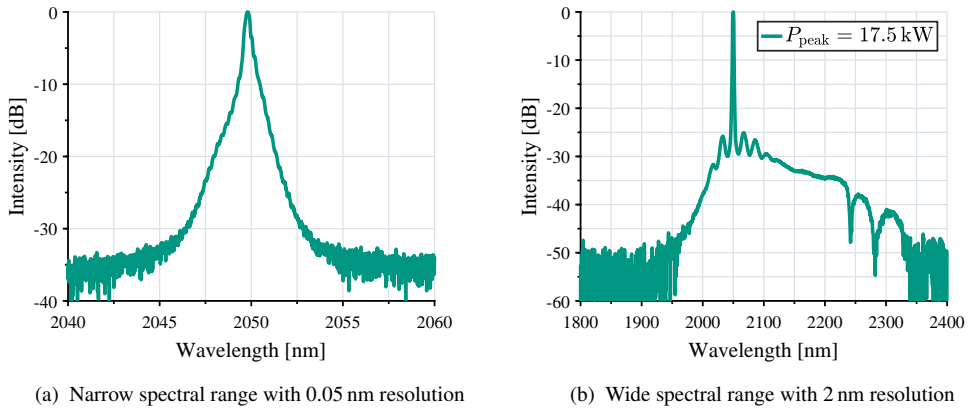


Figure 3.7: Output spectra of the unpolarized Tm-25-400 fiber laser measured at maximum pulse energy and peak power. The 10-dB linewidth is 1.19 nm. The spectrum measured over a wider range, exhibits significant side peaks typical for modulation instability (MI) and a supercontinuum extending beyond 2.3  $\mu\text{m}$ . Due to these nonlinearities, the spectral band  $\pm 2$  nm around the central laser line contains only 92 % of the total power.

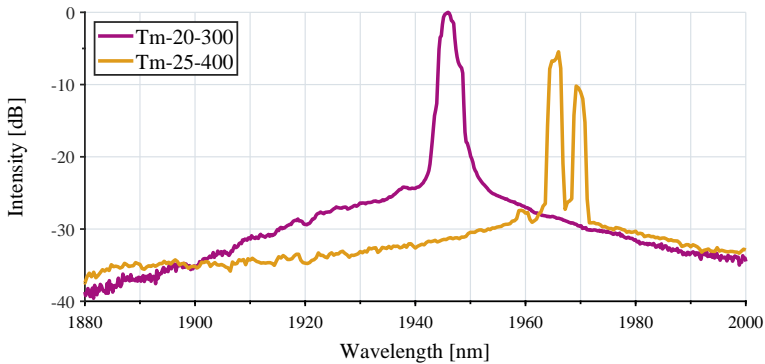


Figure 3.8: Parasitic lasing spectra for the 3.7 m Tm-20-300 and the 5 m Tm-25-400 fibers measured with a resolution of 2 nm. Stronger reabsorption in the Tm-25-400 red-shifts the parasitic lasing spectrum.

As discussed in sec. 2.3.3, growing MI breaks the pulse into ultra-short sub-pulses which undergo a Raman-induced self-frequency shift. This interplay between different nonlinear effects leads to the formation of a supercontinuum that extends primarily to the long wavelength side. Integrating the spectral power density reveals that the measured supercontinuum contains a significant amount of the spectral power; only 92 % of the total output power is maintained within the the spectral band  $\pm 2$  nm around the central laser line at 2050 nm. Moreover, the supercontinuum not only degrades the spectral purity, it also causes higher losses in the fiber laser. The broad spectrum exceeded the VBG bandwidth, causing higher losses at the HR, and the dips in the supercontinuum at 2242 nm and 2282 nm are due to transmission resonances of the dichroic mirrors. Furthermore, background absorption in the silica fiber increases substantially for wavelengths beyond 2180 nm (see fig. 2.6), which contributes to the heat load in the active fiber.

For both of the investigated fibers, the maximum extractable pulse energy was ultimately limited by the onset of parasitic lasing occurring at wavelengths shorter than the operation wavelengths. The parasitic lasing spectra measured behind the VBGs for both the Tm-20-300 and the Tm-25-400 fiber laser configuration are shown in fig. 3.8. For the Tm-20-300 fiber, parasitic lasing appeared at a wavelength of  $\sim 1946$  nm, and for the Tm-25-400 fiber, the parasitic lasing peak was around 1966 nm. If external feedback sources are eliminated, the parasitic cavity is generally formed by the reflections from the fiber ends, which means  $\sim 4$  % feedback from the straight cleave and minor feedback from the angle-cleave. Because both of these parasitic

reflectors are not wavelength-selective, parasitic lasing arises at the gain maximum once the threshold gain  $G_{\text{th,paras}}$  is reached.

While the parasitic threshold gain  $G_{\text{th,paras}}$  represents a fixed level given by the parasitic feedback condition (see eq. (2.255)), the wavelength at which it is reached first depends on the exact shape of the gain spectrum  $G(\lambda)$ . According to eq. (2.163), the gain spectrum is influenced by the spectroscopic cross-sections  $\sigma_e$  and  $\sigma_a$ , the fiber length  $L$ , the overlap factor  $\Gamma_s$ , the doping concentration  $N$ , and the accumulated population inversion  $\Delta N$ . Because of the longer fiber length and a potentially different doping concentration of the Tm-25-400 fiber, the parasitic threshold gain is reached at a lower axial population inversion  $\langle \Delta N \rangle$ . Stronger reabsorption therefore shifts the gain maximum and thus the parasitic lasing wavelength to longer wavelength, as illustrated in fig. 2.27. This effect not only influences the parasitic lasing spectrum, but also the capability of energy storage in the fiber. Because reabsorption suppresses parasitic lasing at short wavelengths, more energy can be stored in the fiber until the parasitic threshold is reached at longer wavelengths. This behavior is investigated in more detail in chapter 4.

### Average Power, Efficiency, and Beam Quality

Pulse energy scaling is typically accompanied by a reduction in efficiency due to various loss mechanisms that work against the build-up of population inversion during the charging period. Figure 3.9a compares the output power characteristic of the polarized Tm-20-300 fiber laser in continuous-wave (CW) operation, with the pulsed operation at constant PRFs of 30 kHz and 20 kHz. In CW operation, a linear fit to the measured data reveals a slope efficiency of 41.4%. Compared to this, the slope efficiency in pulsed operation gradually decreased with pump power. At the pump power of 54 W, the laser operated at a PRF of 30 kHz delivered an average output power of 16.9 W corresponding to a pulse energy of 563  $\mu\text{J}$ , compared to 19.8 W achieved in CW operation. The slope efficiency of the pulsed laser has dropped to approximately 29.9% at this point.

In addition to this continuous decrease, the slope efficiency of the 20 kHz data exhibits an abrupt kink when exceeding a pump power of 46.7 W. While the slope efficiency was 26.4% before this kink, it dropped to approximately 4.2% after it. A similar behavior has been observed in [222] and was identified as a sign for reaching the pulse energy limit. Indeed, the output power of 13.1 W at this point is consistent with the previously determined pulse energy limit

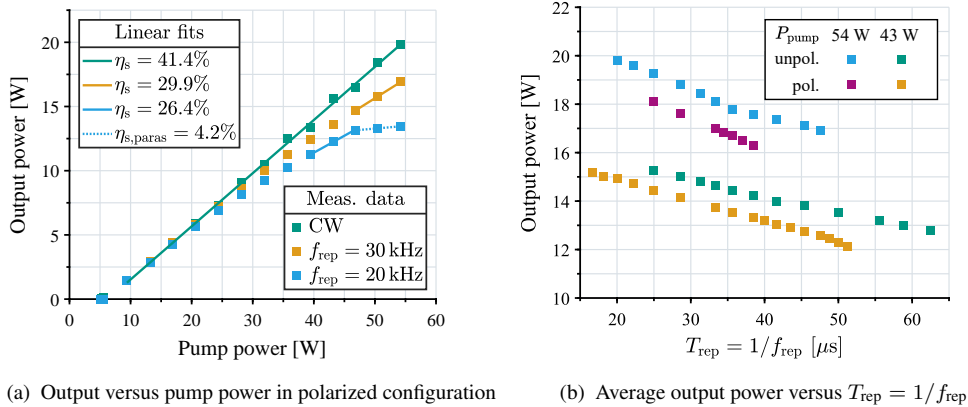


Figure 3.9: Average output power characteristics of the Tm-20-300 fiber laser. Scaling of the pulse energy leads to a reduced efficiency depending on the PRF. The onset of parasitic lasing causes an abrupt drop in slope efficiency at the laser output, because it is mainly emitted from the opposing fiber end.

of  $\sim 625 \mu\text{J}$  for the polarized Tm-20-300 fiber laser. Beyond this threshold, the population inversion is clamped and additional pump power is converted into parasitic lasing. Because the OC has a much higher reflectivity than the parasitic reflector on the opposing side, the parasitic lasing power is primarily emitted from the HR side through the VBG. Consequently, the slope efficiency measured at the laser output becomes almost horizontal.

At a constant pump power, the average output power decreased as the PRF was reduced. This reduction in efficiency is expected, as a lower PRF is associated with a longer charging time, in which the accumulated population inversion suffers spontaneous decay. Figure 3.9b illustrates this trend for the polarized and unpolarized configurations of the Tm-20-300 fiber laser, plotting average output power against the pulse repetition period  $T_{\text{rep}} = 1/f_{\text{rep}}$ . Each configuration was operated with constant pump powers of 43 W and 54 W. An increase in the pulse repetition period  $T_{\text{rep}}$  is equivalent to a decrease in PRF, leading to a higher pulse energy as shown in fig. 3.2a. In all datasets, the output power decreased approximately linearly as  $T_{\text{rep}}$  increases, clearly demonstrating the reduction in efficiency during pulse energy scaling.

The data also reveal that the polarized fiber laser delivered a lower average output power when operated at the same pump power and PRF. The insertion of the TFP introduces additional losses in the cavity, as it rejects light that is not in the desired polarization state. Although the fiber is

PM, a small degree of polarization degradation is unavoidable in the cavity, due to imperfect alignment of the free-space optics with respect to the polarization axes. These additional losses not only decrease the efficiency of the polarized fiber laser but also the maximum extractable pulse energy. Higher losses increase the threshold gain  $G_{\text{th}}$  of the laser resonator. This leads to a higher final gain  $G_f$  according to eq. (2.261), meaning a smaller fraction of the total stored energy is extracted.

Several mechanisms contribute to the reduction in efficiency during pulse energy scaling. First, spontaneous decay of the  ${}^3\text{F}_4$  laser level reduces the charging efficiency according to eq. (2.253). This process only depends on the  ${}^3\text{F}_4$  lifetime of typically  $\tau \approx 200\text{--}650\ \mu\text{s}$  and the charging time  $T_{\text{charge}}$ . Second, ASE further depletes the population inversion during the charging period. The energy lost in ASE depends on the instantaneous gain integrated over the charging time. Third, the rate of the cross-relaxation process CR1 decreases with high population inversion densities (see fig. 2.24b), resulting in a lower quantum yield for pumping the  ${}^3\text{F}_4$  laser level. Finally, the spectral broadening by intensity-dependent nonlinear effects can cause additional losses at bandwidth-limited components like the VBG.

To quantify the combined impact of these effects, the relative efficiency reduction per unit of charging time was calculated from the data:

$$\Delta\eta_{\text{charge}} = \frac{P_{\text{max}} - P_{\text{min}}}{(T_{\text{min}} - T_{\text{max}})P_{\text{max}}} . \quad (3.1)$$

For the unpolarized configuration, this yields  $\Delta\eta_{\text{charge}} \approx -5.3 \cdot 10^{-3}\ \mu\text{s}^{-1}$  at a pump power of 54 W, and  $\Delta\eta_{\text{charge}} \approx -4.3 \cdot 10^{-3}\ \mu\text{s}^{-1}$  at a pump power of 43 W. For the polarized configuration, the efficiency reduction is slightly steeper, resulting in  $\Delta\eta_{\text{charge}} \approx -8.1 \cdot 10^{-3}\ \mu\text{s}^{-1}$  at a pump power of 54 W, and  $\Delta\eta_{\text{charge}} \approx -5.9 \cdot 10^{-3}\ \mu\text{s}^{-1}$  at a pump power of 43 W. For comparison, the contribution from spontaneous decay was estimated using eq. (2.253); assuming a lifetime of  $\tau = 350\ \mu\text{s}$  for charging periods in the range of  $T_{\text{charge}} = 10\text{--}70\ \mu\text{s}$  yields a relative efficiency reduction of  $\Delta\eta_{\text{charge}} \approx -1.5 \cdot 10^{-3}\ \mu\text{s}^{-1}$  from spontaneous decay alone. This calculated value is 3 to 5 times lower than the measured rates, confirming that gain- and intensity-dependent mechanisms, such as ASE and reduced pump efficiency, play a dominant role in reducing the laser efficiency during pulse energy scaling.

The reduction in average output power for the unpolarized Tm-25-400 fiber laser is depicted in fig. 3.10a. The relative reduction in efficiency of  $\Delta\eta_{\text{charge}} \approx -4.9 \cdot 10^{-3}\ \mu\text{s}^{-1}$  is similar to the Tm-20-300 fiber. However, the output spectrum of the Tm-25-400 fiber laser exhibits a supercon-

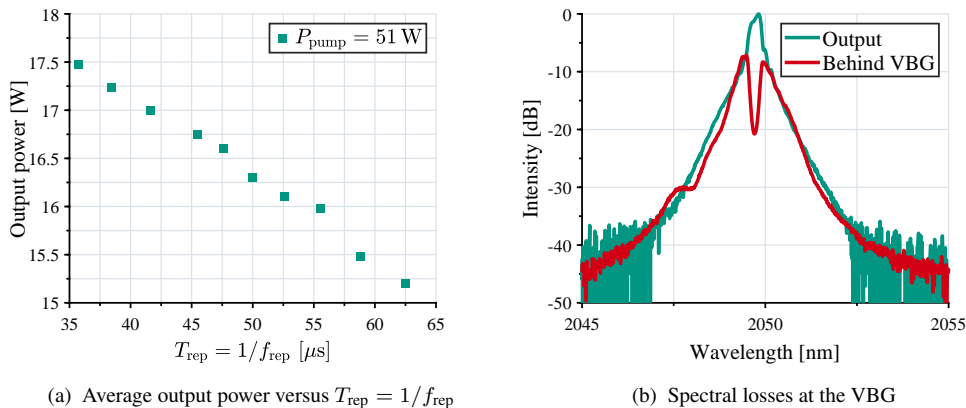


Figure 3.10: Average output power characteristics of the Tm-25-400 fiber laser. Spectral broadening caused by nonlinear effects leads to additional losses at the VBG. Although these losses showed no significant impact to the output power characteristic, they reduce the Q-factor of the cavity and therefore result in a lower extractable pulse energy.

tinuum that contains a significant portion of around 8 % of the total power. This broad spectrum lies outside of the VBG bandwidth of  $\sim 0.37 \text{ nm}$  centered at 2050 nm. Figure 3.10b provides direct evidence of the resulting losses, comparing the output spectrum and the spectrum transmitted through the VBG. The spectra were recorded at a peak power of 15.7 kW. The narrow reflection characteristic of the VBG carves a clear dip into the transmitted spectrum, confirming that the spectrally broadened wings are rejected by the reflector.

Except for this dip, the spectra in fig. 3.10b agree remarkably well with each other. To build up in the oscillator, the laser field must have a self-consistent phase relationship and hence spectrum along the entire cavity, even in the presence of nonlinear effects such as SPM. This explains why the spectrum at the HR end matches that at the output end, although the intensity varies strongly within the cavity. Because the power at the HR end is much lower than at the output, the losses at the VBG do not lead to a substantial decrease in the total output power, as shown in fig. 3.10a. However, the nonlinear spectral broadening imposes another effect on the laser performance: the higher losses at the HR reduce the Q-factor of the fiber oscillator, resulting in a higher threshold gain  $G_{\text{th}}$ , which in turn leads to a higher final gain  $G_{\text{f}}$  remaining after pulse extraction (see eq. (2.261)). Therefore, although the supercontinuum does not cause a major drop in average power, it leads to a less efficient energy extraction, imposing a penalty on the maximum extractable pulse energy.

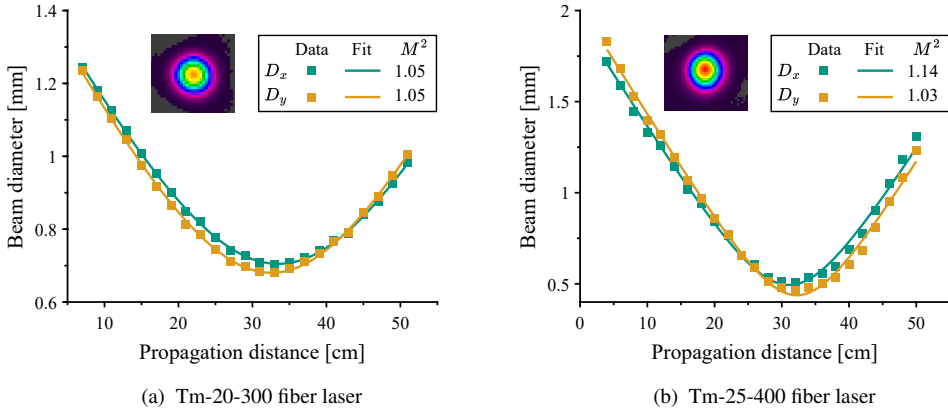


Figure 3.11: Measured beam caustic versus the propagation distance. Fit to the data yields the  $M^2$  factors.

The beam quality of the Q-switched fiber laser was characterized by measuring the beam caustic after a focusing lens with a pyroelectric camera. Figure 3.11 shows the measured beam diameters in two transverse axes  $x$ , and  $y$  along the propagation distance for the Tm-20-300 fiber (a) and the Tm-25-400 fiber (b). For the Tm-20-300 fiber, the measurement was performed in the polarized laser configuration at a pump power of 43 W and a PRF of 20 kHz. The measurement for the unpolarized Tm-25-400 fiber laser was conducted at a pump power of 51 W and a PRF of 19 kHz. Fitting the caustic data with eq. (2.25) yielded  $M^2$  factors of  $\sim 1.05$  for the Tm-20-300 fiber, and  $\sim 1.14$  for the Tm-25-400 fiber. These  $M^2$  values confirm a nearly diffraction-limited beam quality typical for single-mode operation in a fiber laser. The measured beam profiles are depicted as insets in the two graphs.

## Summary

The pulse energy limits in Tm<sup>3+</sup>-doped fiber lasers were investigated by examining a Q-switched fiber oscillator operated with two different active LMA fibers, randomly and linearly polarized configurations, and at different pump power levels. In randomly polarized operation, the Q-switched fiber oscillator generated maximum pulse energies of 800  $\mu\text{J}$  for the Tm-20-300 fiber and 950  $\mu\text{J}$  for the Tm-25-400 fiber. The higher pulse energy from the Tm-25-400 fiber was enabled by a larger Tm<sup>3+</sup>-doped core area, resulting in a higher saturation energy.

Inserting TFPs into the cavity resulted in a linearly polarized output but reduced the cavity Q-factor, which led to a lower maximum pulse energy of 625  $\mu\text{J}$ . In all configurations, the maximum extractable pulse energy was limited by the onset of parasitic lasing. For the investigated pump power levels between 40–60 W and PRFs of 15–25 kHz, the pulse energy limit set by parasitic lasing was largely independent of the pump power. This behavior may differ at higher pump powers and PRFs on the order of 100 kHz, for which the build-up time of parasitic lasing is no longer negligible compared to the inversion charging time.

The Q-switched Tm-20-300 fiber laser generated Gaussian-shaped pulses with FWHM pulse durations of approximately 40 ns, and effective powers of 13.1 kW and 9.7 kW for unpolarized and polarized operation, respectively. For the Tm-25-400 fiber laser, the longer fiber length led to longer pulse durations of around 50 ns and an effective power of 12.4 kW. The output spectra of the pulsed fiber lasers were broadened proportionally to the pulse peak power due to the effect of SPM. Furthermore, the Tm-25-400 fiber laser exhibited substantial spectral distortion due to MI, which resulted in the formation of a supercontinuum that contained  $\sim 8\%$  of the total power at the highest pulse energies. This spectral broadening also led to a reduction of the cavity Q-factor, resulting in a reduced extractable pulse energy. At high gain and population inversion levels, ASE and a reduced CR1 rate were found to have an impact on the laser efficiency. Both Tm<sup>3+</sup>-doped LMA fibers enabled a nearly diffraction-limited beam quality.

## 3.2 Pumping of a ZGP OPO

### 3.2.1 Experimental Setup

The Q-switched  $\text{Tm}^{3+}$ -doped fiber oscillator developed in the previous section served as the pump source for a ZGP OPO. A schematic of the experimental setup is depicted in fig. 3.12. The OPO consisted of a 2 cm long, water-cooled ZGP crystal in a doubly-resonant linear cavity. This cavity was formed by an HR ( $R_{\text{HR}} > 99.9\%$ ) and an OC ( $R_{\text{OC}} \approx 50\%$ ), both specified for the 3–5  $\mu\text{m}$  mid-IR range and highly transmissive ( $T > 95\%$ ) for the  $\sim 2\ \mu\text{m}$  pump light. An optical isolator between the pump source and the OPO prevented backscattered pump light from coupling back into the fiber laser. To control the pump power delivered to the OPO, a variable attenuator was used. This allowed for adjusting the supplied pump power and pump pulse energy, while maintaining a constant pulse shape, as the fiber laser can be operated at a constant operation point. A half-wave plate defined the polarization direction of the pump beam for type I phase matching. The pump beam was focused by a lens into the ZGP crystal to achieve a pump fluence exceeding the nonlinear threshold while remaining below the damage threshold. At the OPO output, a dichroic mirror separated the signal and idler mid-IR beams from the residual pump.

Two distinct pump laser configurations were examined, based on the  $\text{Tm}^{3+}$ -doped fibers from the previous section. Table 3.2 provides the characteristics of the respective pump lasers. The listed characteristics were measured after the optical isolator, accounting for the 10–15% insertion loss. For this experiment, both pump lasers were linearly polarized and operated at an emission wavelength of 2050 nm.

The first configuration, based on the 3.7 m Tm-20-300 fiber, delivered pump pulse energies of 590  $\mu\text{J}$  with an effective power of 8.3 kW, and an average output power of 10 W. With the beam focused to a 300  $\mu\text{m}$  diameter, this resulted in a pump fluence of  $\sim 1.65\ \text{J cm}^{-2}$ . Compared to the previous experiments, the Tm-25-400 fiber was shortened to a length of  $\sim 3.5$  m to enable shorter pulse durations and to mitigate nonlinear effects. This fiber laser provided 36 ns pump pulses with a pulse energy of 770  $\mu\text{J}$ , an effective power of 9.2 kW, and an average output power of 11.5 W. The higher pulse energies and effective power allowed for a larger 500  $\mu\text{m}$  pump spot diameter, resulting in a peak fluence of  $\sim 0.78\ \text{J cm}^{-2}$ .

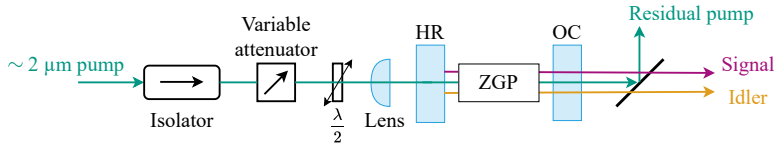


Figure 3.12: Experimental setup for pumping the ZGP OPO.

Table 3.2: Characteristics of the  $\text{Tm}^{3+}$ -doped fiber lasers for pumping the ZGP OPO.

Active Fiber	$E_{\text{pulse}}$	$P_{\text{eff}}$	$f_{\text{rep}}$	$\lambda_c$	$d_{\text{pump}}$	$P_{\text{avg}}$	$M^2$
Tm-20-300 ( $L = 3.7$ m)	590 $\mu\text{J}$	8.3 kW	17 kHz	2050 nm	300 $\mu\text{m}$	10.0 W	1.05
Tm-25-400 ( $L = 3.5$ m)	770 $\mu\text{J}$	9.2 kW	15 kHz	2050 nm	500 $\mu\text{m}$	11.5 W	1.14

## 3.2.2 Experimental Results and Discussion

### High-Efficiency Conversion with a Spectrally Pure Pump

The experimental results of the ZGP OPO pumped by the Tm-20-300 fiber laser are presented in fig. 3.13. Figure 3.13a shows the combined 3–5  $\mu\text{m}$  mid-IR output power and pulse energy from signal plus idler. By adjusting the variable attenuator the supplied pump power was gradually increased. The OPO reached threshold at a pump power of 1.7 W ( $E_{\text{pulse}} = 100 \mu\text{J}$ ). Above this point, the output power increased linearly with a slope efficiency of 49%. At the maximum available pump power of 10 W, the OPO generated 3.9 W mid-IR output power and 230  $\mu\text{J}$  of pulse energy, corresponding to an optical-to-optical conversion efficiency of 39%.

The temporal dynamics of the nonlinear conversion are illustrated in fig. 3.13b, which compares the incident pump pulse, the mid-IR pulse, and the depleted residual pump. Using eq. (2.185), the build-up time of signal and idler in the OPO was calculated to be  $\sim 10$  ns. Taking this delay into account, the nonlinear threshold was reached at an instantaneous pump power of  $\sim 2$ –3 kW. Thus, the peak of the pump pulse was roughly five times above the threshold. After the build-up time, significant pump depletion began as the mid-IR output pulse formed. The mid-IR pulse then grew and decayed according to the pump power above threshold. Finally, the conversion ceased when the pump power again fell below the threshold.

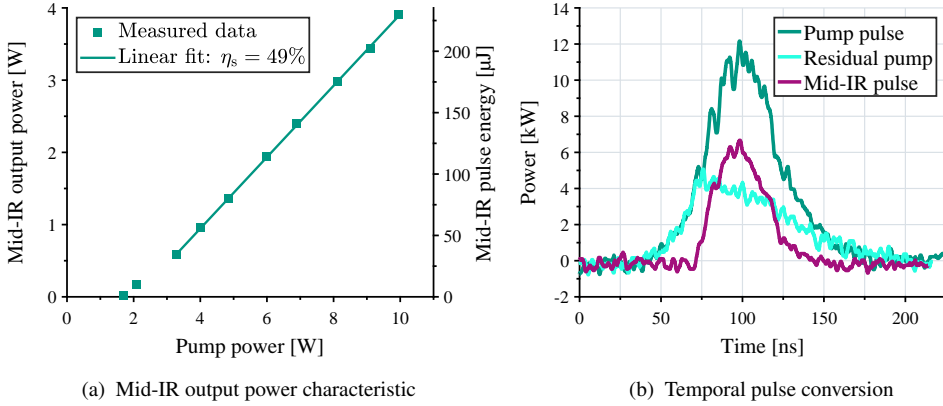


Figure 3.13: Characteristics of the nonlinear frequency conversion in the ZGP OPO pumped by the Q-switched Tm-20-300 fiber laser. An optical-to-optical conversion efficiency of 39% was achieved.

The beam quality of the mid-IR output was characterized by separating the signal and idler with optical filters and measuring their respective beam caustics. Figure 3.14 shows these measurements, which were performed at maximum output power. Fitting the caustic data yielded an  $M^2 < 2.00$  for the signal and  $M^2 < 2.15$  for the idler beam.

The 39% conversion efficiency achieved in this experiment represents an improvement over previously reported fiber-laser-pumped ZGP OPOs (see Table 2.3). This enhancement is not attributed to the OPO design itself; the 300  $\mu\text{m}$  pump spot was similar to that in prior work. This small spot size hindered the slightly longer 20 mm ZGP crystal from being beneficial, as spatial walk-off limited the effective interaction length (see fig. 2.48b). In this case, the longer crystal might even be detrimental, as the longer cavity lifetime causes a longer build-up time of signal and idler, if the walk-off prevents the nonlinear gain from increasing accordingly (see eq. (2.185)). Instead, the improved conversion efficiency is attributed to the higher effective power  $P_{\text{eff}}$  of the pump pulses in this experiment. This indicates that a larger fraction of the pulse energy was delivered at high instantaneous power levels above the OPO threshold, thus effectively contributing to the conversion.

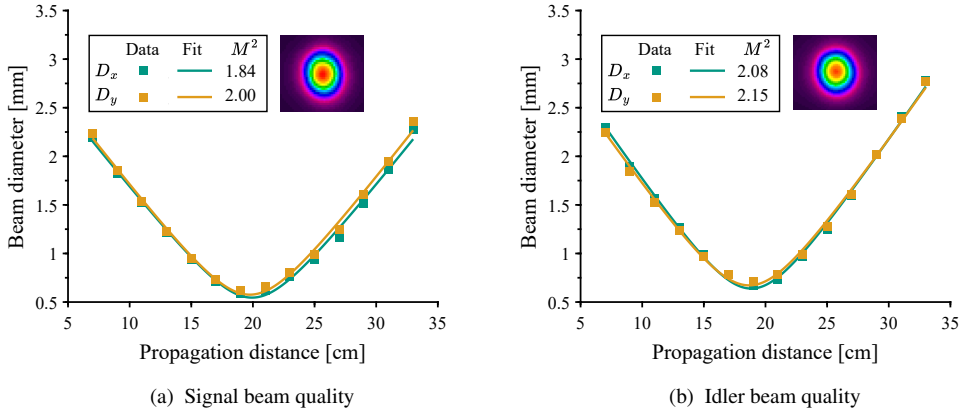


Figure 3.14: Measured beam caustic versus the propagation distance for signal and idler in the mid-IR. Fit to the data yields the  $M^2$  factors.

### Impact of Pump Spectral Broadening on Conversion Efficiency

The second experiment utilized the Tm-25-400 fiber laser, which produced pump pulses with a higher effective power of 9.2 kW. Furthermore, a larger pump spot diameter of  $\sim 500 \mu\text{m}$  was chosen to mitigate the effect of spatial walk-off. However, the performance of the ZGP OPO did not improve. As shown in fig. 3.15b, the OPO generated a similar mid-IR output power of 4 W, with a lower optical-to-optical conversion efficiency of only 35 %, compared to the experiment with the first pump laser. This reduction in conversion efficiency is attributed to the severe distortion of the pump spectrum, depicted in fig. 3.15a.

Although the length of the Tm-25-400 fiber was specifically shortened, the pump spectrum was substantially affected by fiber nonlinearities. Compared to the unpolarized configuration investigated in sec. 3.1, the linear polarization required for pumping the ZGP OPO increased the effective nonlinear gain. As shown in fig. 3.15a, the resulting spectrum measured after the optical isolator exhibited significant side peaks caused by MI, only  $\sim 21$  dB below the central laser line, and a broad supercontinuum extending to  $\sim 2.2 \mu\text{m}$ . Spectral power content beyond  $2.2 \mu\text{m}$  was cut off by the transmission characteristics of the TFPs and the isolator. Integrating the spectral power density reveals the severity of the issue: due to the nonlinear spectral broadening, only  $\sim 85$  % of the total pump power was contained within a  $\pm 2$  nm band around the central laser wavelength.

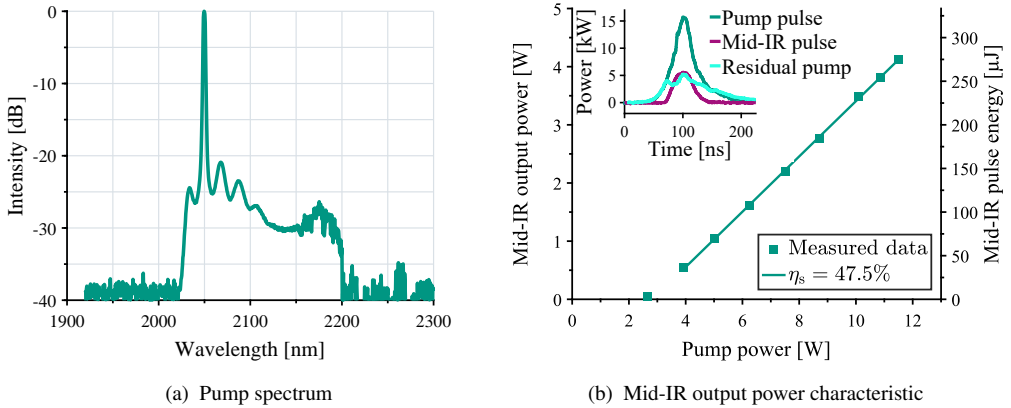


Figure 3.15: Characteristics of the nonlinear frequency conversion in the ZGP OPO pumped by the Q-switched Tm-25-300 fiber laser. An optical-to-optical conversion efficiency of 35 % was achieved. Because of the spectral distortion by nonlinear effects, only  $\sim 85\%$  of the total pump power are within  $\pm 2$  nm around the central peak. This reduces the conversion efficiency in the ZGP OPO, in particular at the peak of the pump pulse, as shown in the inset.

The temporal pulse shapes in the inset of fig. 3.15b clearly illustrate the impact of the broad pump spectrum. Taking into account the  $\sim 10$  ns signal and idler build-up time, the OPO power threshold was again estimated to be  $\sim 2\text{--}3$  kW. This confirms the benefit of the larger pump spot: despite the reduction in pump intensity, the threshold power remained as low as in the first experiment, because the reduced effect of spatial walk-off enabled a longer effective gain length (see fig. 2.48b).

Although the peak of the pump pulse was around six times above threshold, it was not converted efficiently. Since the nonlinear spectral broadening primarily concerns the most intense part of the pulse, much of the power at the peak was shifted into the unusable spectral wings and supercontinuum. This inefficiency is directly visible in the temporal traces: the residual, non-converted pump power increases at the center of the pulse, and the generated mid-IR pulse exhibits a flattened top. This resulted in a lower overall efficiency for the Tm-25-400 pump laser, emphasizing the critical importance of a spectrally pure pump source.

### 3.3 Conclusion

The experiments on pumping a ZGP OPO demonstrated how the temporal, spectral, and spatial characteristics of the developed Q-switched fiber laser influence the mid-IR conversion efficiency. Two different pump laser configurations based on  $\text{Tm}^{3+}$ -doped LMA fibers with 20  $\mu\text{m}$  and 25  $\mu\text{m}$  core diameters were tested. With the 20  $\mu\text{m}$  LMA fiber, a high effective pump power of 8.3 kW was achieved. This resulted in an improved conversion efficiency compared to previously reported fiber-laser-pumped ZGP OPOs, because more of the pulse energy was effectively contributing to the conversion above the OPO threshold. The second configuration, utilizing the 25  $\mu\text{m}$   $\text{Tm}^{3+}$ -doped LMA fiber, achieved a further enhancement in effective pump power to 9.2 kW. This allowed the use of a larger pump spot, which mitigated the effect of spatial walk-off and improved the effective interaction length. However, this increase in effective power also caused severe broadening in the pump laser induced by fiber nonlinearities. Despite the enhanced temporal power density and effective gain length, this spectral distortion ultimately reduced the conversion efficiency compared to that in the first experiment. This emphasizes the importance of finding an optimal design trade-off between the temporal, spectral, and spatial domains.

The investigation of the Q-switched fiber laser identified several mechanisms that can be leveraged for optimization of the pump source in these domains:

#### **Effects that improve the maximum pulse energy:**

- A larger core diameter of the  $\text{Tm}^{3+}$ -doped fiber increases the saturation energy.
- Higher pump power leads to a higher dynamic overshoot of population inversion above the parasitic lasing threshold, resulting in a higher maximum initial gain.
- Reabsorption suppresses parasitic lasing at short wavelengths, which is associated with a red shift of the gain peak and an effective increase in energy storage capacity.

#### **Effects that mitigate nonlinear spectral broadening:**

- A larger mode field area reduces the intensity in the fiber.
- A shorter fiber length reduces the interaction length for nonlinear effects.

**Effects that enable high average output power and beam quality:**

- The examined few-moded LMA fibers provide single-mode beam quality.
- Operation at high PRFs improves the efficiency by reducing the losses from ASE and spontaneous decay during the shorter charging period.

These effects can be exploited in the design of a pulsed fiber laser for pumping a ZGP OPO. As discussed in sec. 2.5.2, an optimal design must find a trade-off between competing effects. For example, a large core diameter is needed for high energy extraction but must still provide single-mode operation, and a fiber length must be long enough to benefit from reabsorption but also short enough to avoid severe nonlinearities. Navigating these trade-offs requires the quantitative analysis that will be presented in the following chapter.



## 4 Analysis and Optimization of Pulse Energy Extraction

Scaling the pulse energy from fiber lasers requires overcoming two competing classes of physical limitations: gain-related effects that cap the storable energy and intensity-dependent nonlinearities that degrade the spectral purity. As established in sec. 2.4.3, the potential gain-related limiting mechanisms are pump bleaching, amplified spontaneous emission (ASE), and, most importantly, parasitic lasing. In contrast, as described in sec. 2.3.3, nonlinear effects become significant at high peak powers and long interaction lengths, causing spectral distortion that is detrimental for applications requiring a narrow linewidth, such as pumping optical parametric oscillators (OPOs). Due to these different limitations, design choices often have conflicting effects on the spatial, temporal, and spectral output characteristics. Developing a high-pulse-energy  $\text{Tm}^{3+}$ -doped fiber laser for efficient nonlinear conversion therefore demands a quantitative framework that accounts for these trade-offs to find an optimal design. Previous studies on pulse energy limitations in fiber lasers have been reviewed in sec 2.4.3. However, most of these works focus on  $\text{Yb}^{3+}$ - or  $\text{Er}^{3+}$ -doped fiber laser systems, and primarily analyze a pulse energy limitation imposed by ASE [178, 186, 187, 189, 190]. There is no comprehensive model that considers the distinct characteristics of pulsed  $2\ \mu\text{m}$   $\text{Tm}^{3+}$ -doped fiber lasers and that would allow optimization of their design.

This chapter develops such a model to analyze and optimize the pulse energy extraction in  $\text{Tm}^{3+}$ -doped fiber lasers, considering gain limitations and nonlinear effects. The semi-analytical approach is built directly upon the experimental observations from chapter 3, which identified two dominant limiting mechanisms. First, parasitic lasing was found to be the ultimate limitation on the maximum achievable gain and hence the maximum extractable pulse energy. The spectral gain-shift induced by reabsorption was found to significantly influence the wavelength at which

this parasitic emission occurred, which consequently also impacts the energy storage capacity in the fiber. Although ASE potentially reduced the efficiency of the pulsed fiber laser, it did not set an ultimate limitation on the maximum pulse energy. Second, intensity-dependent nonlinear effects caused substantial broadening of the output spectrum. Because the 2  $\mu\text{m}$  emission wavelength is in the anomalous group velocity dispersion (GVD) regime of silica, this limitation was mainly due to modulation instability (MI), which eventually led to the formation of an incoherent supercontinuum. The nonlinear gain of MI depends on the intensity distribution along the fiber, as described in sec. 2.3.3. A comprehensive and practically useful model must therefore include a quantitative analysis of these two distinct phenomena: the spectral gain characteristics that determine the parasitic lasing threshold and the intensity-dependent nonlinear gain for MI.

Quantitative modeling of a pulsed fiber laser requires the treatment of numerous parameters of the active fiber and the setup, which fall into two distinct categories. First, there are the design parameters, which can be freely chosen, such as the fiber length, core size, and cavity mirror reflectivities. The primary goal of the model is to predict how these choices affect laser performance. On the other hand, there are several critical intrinsic parameters that are often unknown and difficult to measure directly. These include the doping concentration, which is rarely provided by the manufacturer, the magnitude of parasitic reflections that set the parasitic lasing threshold, and the spectroscopic cross-sections. As discussed in sec. 2.3.1, the spectroscopic cross-sections can vary significantly depending on the exact doping composition of the specific investigated fiber. As a result, the available cross-section data from the literature exhibit significant discrepancies (see fig. 2.26). Accurate quantitative modeling therefore requires a practical calibration procedure to determine these intrinsic parameters from simple and accessible experimental measurements.

In the following, a novel modeling approach is presented that enables the accurate performance analysis of nanosecond-pulsed  $\text{Tm}^{3+}$ -doped fiber lasers. Instead of a computationally intensive numerical simulation, the developed model distills the limiting mechanisms into a set of fundamental physical relationships, many of which are analytically solvable. Consequently, it is easy to implement and allows for rapid computation, which makes it ideally suited for optimizing the laser design by exploring a wide parameter space. Parts of this analysis approach have been published in a journal article [223].

Modeling and calibration are performed using the Tm-20-300 fiber from sec. 3.1 as a practical case study. First, the gain characteristics that govern the maximum extractable pulse energy

are analyzed in sec. 4.1. By calibrating intrinsic parameters against measured pulse data, the model provides a quantitative prediction of how design choices, such as fiber length, influence the maximum extractable pulse energy, peak power, and pulse duration. This analysis highlights the critical role of reabsorption in maximizing energy storage before the onset of parasitic lasing.

Subsequently, the analysis addresses the nonlinear effects that constrain peak power in sec. 4.2. Based on the previously identified gain saturation, the intensity distribution along the fiber is estimated to determine the parametric gain for MI. The evaluation of the measured output spectra reveals a critical distinction in the parametric gain spectra of laser amplifiers and oscillators, which must be considered for analyzing the impact of MI. From this analysis, the critical fiber length is determined, beyond which significant nonlinear spectral broadening is expected.

Finally, the analysis is concluded in sec. 4.3 summarizing the design trade-offs and highlighting optimization perspectives. These conclusions form the basis for the investigation of a  $\text{Tm}^{3+}$ -doped photonic crystal fiber (PCF) in chapter 5.

## 4.1 Analysis of Gain Limitations

To model and eventually optimize the pulse extraction in a fiber laser, the maximum initial gain and minimum final gain were analyzed considering the limitation by parasitic lasing. These gain levels define the boundaries of the pulse generation process, consisting of a charging period where energy is stored, followed by an extraction period where it is released.

In a Q-switched fiber laser (see sec. 2.4.1), this process is controlled by modulating the cavity Q-factor. During the low Q-state, the inversion and the gain can increase to maximum levels  $\Delta N_{i,\max}$  and  $G_{i,\max}$  before the onset of parasitic lasing clamps them. When switching to the high Q-state, the threshold gain  $G_{\text{th}} < G_i$  of the unblocked cavity is restored, initiating the pulse generation that discharges the inversion to a final level  $\Delta N_f < \Delta N_{\text{th}}$ , corresponding to the gain level  $G_f < G_{\text{th}}$ .

For the case of a fiber amplifier (see sec. 2.4.2), the charging period is the time between input pulses, during which the maximum initial gain is again limited by the parasitic las-

ing threshold. The extraction period is initiated by the arrival of the seed pulse, and the final gain  $G_f$  is determined by the gain saturation dynamics depending on the input pulse energy.

The following analysis uses the Tm-20-300 fiber oscillator as a detailed case study. However, the derived principles are broadly applicable, and differences for the analogous analysis of an amplifier configuration are mentioned.

### 4.1.1 Modeling of Gain Saturation and Parameter Calibration

The pulse generation process in a fiber laser is governed by the relationships established in sec. 2.4. In a Q-switched fiber oscillator, the output pulse energy  $E_{\text{pulse}}$  is directly proportional to the energy extracted from the gain medium  $E_{\text{ext}}$ , through the resonator efficiency  $\eta_R$  (see eq. (2.247)). The extracted energy, in turn, is given by the initial and final gain levels,  $G_i$  and  $G_f$ , and proportional to the saturation energy  $E_{\text{sat}}$  (see eq. (2.245)). Furthermore, the Q-switching master equation (2.261) links the initial and final gain through the threshold gain of the unblocked cavity  $G_{\text{th}}$ . Together, these gain levels also determine the resulting peak power  $P_{\text{peak}}$  by eq. (2.262), which completes this set of equations that fully describes the Q-switched pulse dynamic.

This system of equations provides a powerful framework for calibrating the gain saturation. The resonator-related parameters of the resonator efficiency  $\eta_R$ , threshold gain  $G_{\text{th}}$ , and photon lifetime  $\tau_c$  are given by known design choices, namely mirror reflectivities  $R_{\text{HR}}$  and  $R_{\text{OC}}$ , fiber length  $L$ , and estimated internal losses  $\Lambda$  (see eqs. (2.153), (2.159) and (2.176)). Thus, by experimentally measuring the output characteristics  $E_{\text{pulse}}$  and  $P_{\text{peak}}$ , the unknown intrinsic parameters  $G_i$ ,  $G_f$ , and  $E_{\text{sat}}$  at the operating wavelength can be determined by numerically solving this set of equations.

This calibration procedure was applied to the Q-switched Tm-20-300 fiber laser characterized in sec. 3.1. The measured maximum pulse energy of  $\sim 800 \mu\text{J}$  and peak power of  $\sim 18.4 \text{ kW}$  served as the primary inputs to the numerical calculation. The complete set of parameters is listed in table 4.1. The assumptions for the resonator include an output coupler (OC) reflectivity of 3.5 %, an effective high reflector (HR) feedback of 90 % to account for coupling losses from the volume Bragg grating (VBG) back into the fiber, and a standard background loss

Table 4.1: Parameters to model the Q-switched Tm-20-300 fiber laser at an operation wavelength of 2044 nm. The model used the inputs on the left to calculate the intrinsic gain characteristics on the right.

$E_{\text{pulse}}$	$P_{\text{peak}}$	$R_{\text{OC}}$	$R_{\text{HR}}$	$\alpha$	$L$	$G_{\text{th}}$	$\tau_c$	$E_{\text{sat}}$	$G_{\text{i,max}}$	$G_{\text{f,min}}$
805 $\mu\text{J}$	18.4 kW	3.5 %	90 %	0.13 dB/m	3.7 m	8 dB	10.5 ns	238 $\mu\text{J}$	18.6 dB	1.77 dB

of  $\alpha \approx 0.13$  dB/m for Tm<sup>3+</sup>-doped fibers [224]. The total cavity length was composed of the 3.7 m fiber length and a free-space section of  $\sim 40$  cm between the HR and the fiber end. Solving the system of equations with these inputs yielded the intrinsic gain parameters at the operating wavelengths of 2044 nm: a saturation energy of  $E_{\text{sat}} \approx 238$   $\mu\text{J}$ , a maximum initial gain of  $G_{\text{i,max}} \approx 18.6$  dB, and a minimum final gain of  $G_{\text{f}} \approx 1.77$  dB.

While the previous calculation yielded the gain saturation characteristics at the operating wavelength, a complete analysis of the spectrally dependent gain limitations requires modeling of the entire gain spectrum. For this, a simplified two-level system is considered, assuming that the majority of the Tm<sup>3+</sup>-ions are in the <sup>3</sup>F<sub>4</sub> laser level and in the <sup>3</sup>H<sub>6</sub> ground level. The gain spectrum is then given by eq. (2.163), which depends on several parameters: the population inversion  $\Delta N$ , the signal overlap factor  $\Gamma_s$ , the fiber length  $L$ , the doping concentration  $N$ , and the spectroscopic cross-sections  $\sigma_a(\lambda_0)$  and  $\sigma_e(\lambda_0)$ .

Among these, the fiber length and overlap factor are known design parameters. The crucial intrinsic parameters are the doping concentration  $N$  and the exact shape and magnitude of the spectroscopic cross-sections. As these properties vary significantly between fibers, they cannot be reliably taken from the literature. Therefore, to accurately model the gain spectrum of a specific fiber, these unknown parameters must be calibrated against the measured laser performance.

The spectroscopic cross-sections are directly linked to the saturation energy via eq. (2.246). At the long operation wavelength of 2044 nm, the absorption cross-section becomes negligible compared to the emission cross-section ( $\sigma_e(2044 \text{ nm}) \gg \sigma_a(2044 \text{ nm})$ ). This simplification allows determining the emission cross section at the operating wavelength from the corresponding saturation energy. For the case of the Tm-20-300 fiber, this yielded:

$$\sigma_e(2044 \text{ nm}) \approx \frac{hc_0}{2044 \text{ nm}} \frac{A_{\text{core}}}{\Gamma_s E_{\text{sat}}(2044 \text{ nm})} \approx 1.57 \cdot 10^{-25} \text{ m}^2 \quad (4.1)$$

where the values from table 3.1 were used for  $\Gamma_s$  and  $A_{\text{core}}$ . As illustrated in fig. 4.1a, this calculated point at 2044 nm (green marker) is notably lower than the literature data from [100] (dashed line). This discrepancy highlights the necessity of this calibration; published cross-section data vary significantly due to differences in the fiber material composition [100, 106, 112–115]. To construct the full emission spectrum, the determined value  $\sigma_e(2044 \text{ nm})$  was used as an anchor point to fit a Gaussian function, with a peak that was assumed to match the data from [100]. The resulting fitted emission cross-section is illustrated in fig. 4.1a by the solid green line.

The gain spectrum of the  $\sim 2 \mu\text{m}$  laser emission results from the rates of stimulated emission and reabsorption processes. For the reabsorption rate, the absorption cross-section at wavelengths longer than  $\sim 1.9 \mu\text{m}$  is the most relevant. Although the magnitude of  $\sigma_a$  is low in this spectral range, it crucially influences the shape of the gain spectrum. However, because of this low magnitude, the relative measurement error in the absorption cross-section increases in this spectral range. For modeling the reabsorption, the absorption cross-section was therefore calculated from the fitted emission cross-section using the McCumber relation, assuming  $\lambda_\mu = 1725 \text{ nm}$  (see eq. (2.86)). The result is illustrated by the solid red line in fig. 4.1a, and compared with the baseline corrected data from [100] (dashed red line).

With these calibrated spectroscopic cross-sections, the remaining unknown parameters—namely the doping concentration  $N$  and parasitic reflection  $R_{\text{paras}}$ —were determined. This was achieved by linking the known gain at the 2044 nm operating wavelength to the known parasitic lasing wavelength of 1946 nm. Using the calculated initial gain  $G_{i,\text{max}}(2044 \text{ nm})$  at the pulse energy limit, the axial mean of the initial inversion  $\langle \Delta N \rangle_{i,\text{max}}$  was expressed as a function of the doping concentration  $\langle N \rangle$  by rearranging eq. (2.163):

$$\langle \Delta N \rangle_{i,\text{max}} (\langle N \rangle) = \frac{2 \ln G_{i,\text{max}}(2044 \text{ nm})}{[\sigma_a(2044 \text{ nm}) + \sigma_e(2044 \text{ nm})]\Gamma_s L} + \frac{\sigma_a(2044 \text{ nm}) - \sigma_e(2044 \text{ nm})}{\sigma_a(2044 \text{ nm}) + \sigma_e(2044 \text{ nm})} \langle N \rangle. \quad (4.2)$$

This expression for  $\langle \Delta N \rangle_i$  was then substituted back into the wavelength-dependent gain equation (2.163), yielding the gain spectrum  $G_{i,\text{max}}(\lambda_0, \langle N \rangle)$  as a function of the doping concentration. Parasitic lasing occurs at the gain maximum when the parasitic threshold is exceeded, which was experimentally observed at a wavelength of 1946 nm for the Tm-20-300 fiber laser. Because the pump power was relatively low in the experiment (43 W), the dynamic overshoot above the parasitic threshold was neglected. This means that the maximum initial inversion corresponds approximately to the parasitic threshold inversion ( $\langle \Delta N \rangle_{\text{th,paras}} \approx \langle \Delta N \rangle_{i,\text{max}}$ ).

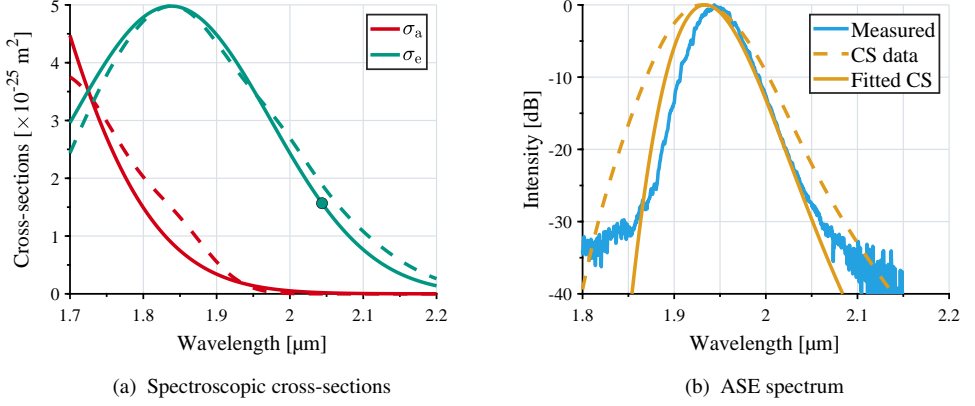


Figure 4.1: Calibration of the spectroscopic cross-sections (CS) and modeling of the ASE spectrum. In (a), the fitted CS are illustrated by the solid lines and compared with the measured CS data from [100]. In (b), the measured ASE spectrum (blue line) is compared with the calculated ASE spectra using the CS data from [100] (dashed orange line), and using the fitted CS (solid orange line). With the calibrated CS, the ASE spectrum is modeled significantly more accurately.

Consequently, the maximum of the gain function  $G_{i,\max}(\lambda_0, \langle N \rangle)$  corresponds to the parasitic threshold gain, and must be located at the parasitic lasing wavelength of  $\lambda_{\text{paras}} = 1946 \text{ nm}$ . Solving the resulting condition

$$G_{\text{th,paras}} \stackrel{!}{\approx} \max G_{i,\max}(\lambda_{\text{paras}}, \langle N \rangle) \quad (4.3)$$

yielded a doping concentration of  $\langle N \rangle \approx 8.6 \cdot 10^{25} \text{ m}^{-3}$  and a parasitic threshold gain of  $G_{\text{th,paras}} \approx 32.5 \text{ dB}$ . Using eq. (2.255) for a parasitic cavity between the OC and an opposing parasitic reflection results in a parasitic reflectance of  $R_{\text{paras}} \approx -49.4 \text{ dB}$ .

Note that these calibrated values of the spectroscopic cross-sections  $\sigma_a$  and  $\sigma_e$ , the doping concentration  $\langle N \rangle$ , and the parasitic reflection  $R_{\text{paras}}$  do not necessarily correspond to the exact physical values of the Q-switched Tm-20-300 fiber. Rather, they form a self-consistent model to accurately analyze the pulse extraction under the consideration of reabsorption effects. For instance, a different choice for  $\lambda_\mu$  in the McCumber relation would yield slightly different values. However, the shape of the resulting gain spectrum remains the same, leading to a consistent prediction of the effect of reabsorption on the output performance.

To verify that the model accurately predicts the spectral gain under different operating conditions of the fiber, a simple experiment was performed. The Tm-20-300 fiber was continuously pumped in three distinct configurations. In each case, the bidirectionally supplied pump power was increased until the laser threshold was reached, and the initial oscillation wavelength was recorded. In the first configuration, the 3.7 m Tm-20-300 fiber was pumped without an HR mirror, with a straight cleave on one fiber end and an angled cleave on the opposing end. This configuration corresponds to the situation during the low Q-state in the Q-switched fiber oscillator, when the acousto-optical modulator (AOM) blocks the feedback from the HR mirror. In the second configuration, a 4.5 m long piece of the fiber was used, with angled cleaves at both ends. Finally, the third configuration consisted of the 3.7 m fiber within a linear cavity between a broadband HR mirror with  $> 99\%$  reflection and the straight cleaved fiber end. The output spectrum from both ends was measured using an optical spectrum analyzer (OSA). The measured threshold oscillation wavelengths for the first, second, and third configurations were  $\sim 1946$  nm,  $\sim 1947$  nm, and  $\sim 1995$  nm, respectively. These experimental values provide benchmarks for validating the model.

Figure 4.1b shows the measured ASE spectrum for configuration 2. The spectrum was recorded at the operation point, where a parasitic oscillation peak appeared in the output spectrum at the opposing end, indicating that the gain was clamped. The ASE spectrum offers a powerful test of the model, as its shape is a direct result of the entire spectral gain profile. Using the calibrated values for  $\sigma_e$ ,  $\sigma_a$ ,  $\langle N \rangle$ , and  $R_{\text{paras}}$ , the ASE spectrum at the threshold gain was calculated by eq. (2.174), where equivalent parasitic reflections from both ends were assumed. The result shown by the solid orange line in fig. 4.1b demonstrates excellent agreement with the measured spectrum.

For comparison, the ASE spectrum was also calculated using the literature cross-section data from [100]. To ensure a fair comparison, the doping concentration and parasitic reflection were analogously re-calibrated for this dataset to match the parasitic lasing wavelength, resulting in values of  $\langle N \rangle \approx 3.1 \cdot 10^{25} \text{ m}^{-3}$  and  $R_{\text{paras}} \approx -47.4$  dB. The resulting ASE spectrum illustrated by the dashed orange line shows a significantly worse agreement with the measured spectrum, confirming that the fitted cross-sections indeed enable a more accurate modeling of the gain spectrum.

The calculation of the gain spectra for the three configurations is illustrated in fig. 4.2. First, the threshold gains  $G_{\text{th},1}$ ,  $G_{\text{th},2}$ , and  $G_{\text{th},3}$  for the respective configurations were calculated using  $R_{\text{HR}} \approx 0.9$  for the feedback from the broadband mirror,  $R_{\text{OC}} \approx 0.035$  for the straight cleave, and

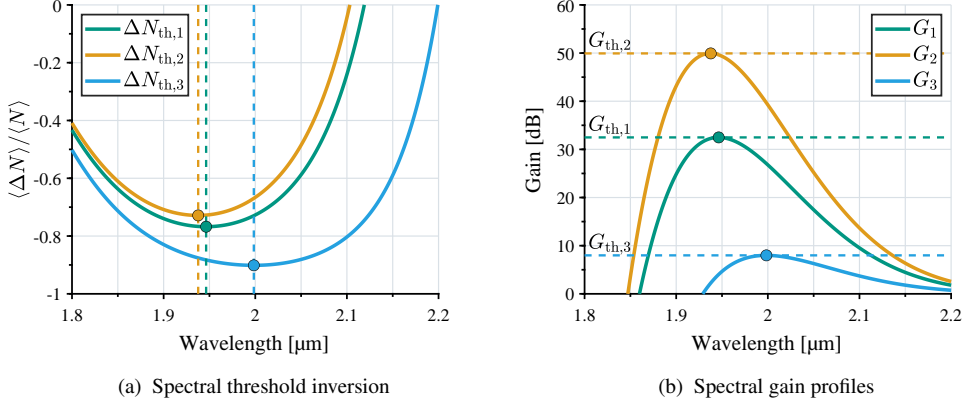


Figure 4.2: Calculated spectral gain shift for three different threshold gain levels  $G_{th,1}$ ,  $G_{th,2}$ , and  $G_{th,3}$ . The laser oscillation starts at the wavelengths at the respective minima of the threshold inversion curves and the maxima of the gain spectra. A higher threshold gain results in a shorter initial oscillation wavelength because of weaker reabsorption.

$R_{paras} \approx -49.4$  dB for the angled cleaves. Substituting these gain levels in eq. (2.177) yielded the wavelength-dependent threshold inversions  $\langle \Delta N \rangle_{th,1}$ ,  $\langle \Delta N \rangle_{th,2}$ , and  $\langle \Delta N \rangle_{th,3}$  plotted in fig. 4.2a. Laser oscillation begins at the wavelength corresponding to the minimum of this curve, as this inversion level is reached first when pumping the respective configuration. Substituting the minima of the three curves  $\min \langle \Delta N \rangle_{th}$  into eq. (2.163) yields the gain spectra at threshold, which are plotted in fig. 4.2b.

The minima of the threshold inversion curves and hence the maxima of the gain spectra match well with the oscillation wavelengths measured in the experiment. For configuration 1 the match is perfect, because it is identical to the calibration condition. The calculated oscillation wavelength in configuration 2 of 1938 nm is  $\sim 9$  nm shorter than in the measured spectrum. This small discrepancy is likely due to slight variations in the parasitic reflections from the angled cleaves. For configuration 3, the model shows a deviation of only  $\sim 3$  nm from the measured wavelength. These results verify that the calibrated parameters provide an accurate and predictive model for the spectral gain shift caused by reabsorption.

The validation experiment also provides a straightforward method to exclude ASE as the limitation for the extractable pulse energy. Configuration 1 is identical to the parasitic cavity in the low Q-state of the pulsed fiber laser. By continuously pumping this configuration

just below the laser threshold, it reaches a steady-state where pump absorption is perfectly balanced by ASE, resulting in a constant population inversion and gain. At this operation point, the total output power measured at both fiber ends represents the maximum possible ASE power that can be generated from the configuration before the gain is clamped by parasitic lasing.

This steady-state ASE power serves as a worst-case scenario. In pulsed operation, the laser only reaches this peak gain level for a brief period, meaning the time-averaged ASE power will be significantly lower. For all fiber lasers investigated in this work, this maximum ASE power was found to be negligible compared to the target average output power of the pulsed laser. Therefore, it can be confidently concluded that while ASE may slightly impact efficiency, it does not set an ultimate limit on the maximum extractable pulse energy in these nanosecond-pulsed  $\text{Tm}^{3+}$ -doped fiber laser systems.

## 4.1.2 Analysis of Pulse Extraction

With the model calibrated and validated, it can now be used to analyze the pulse extraction by calculating the initial and final gain spectra under various operation conditions. In the Q-switched fiber laser, the maximum initial gain  $G_{i,\max}$  is limited by the previously calculated parasitic threshold gain  $G_{\text{th,paras}}$ . This value is independent of the operating wavelength and slightly dependent on the fiber length due to the propagation losses  $\Lambda$ . The minimum final gain  $G_{f,\min}$  results from the maximum initial gain and the threshold gain of unblocked cavity  $G_{\text{th}}$  by eq. (2.261).

To visualize the energy storage in the fiber laser, it is instructive to consider the inversion levels at these gain boundaries. Inserting the threshold gains  $G_{\text{th,paras}}$  and  $G_{\text{th}}$  for parasitic lasing and signal pulse extraction into eq. (2.177) yields the wavelength-dependent threshold inversions  $\langle \Delta N \rangle_{\text{th,paras}}$  and  $\langle \Delta N \rangle_{\text{th}}$  that are required at a certain wavelength to provide these gain levels, respectively.

Figure 4.3a shows these inversion curves multiplied by the fiber length  $L$  versus the wavelength. The curves were calculated using the previously calibrated cross-sections and doping concentration of the Tm-20-300 fiber. When charging the inversion, the minimum of the curve  $\langle \Delta N \rangle_{\text{th,paras}}$  indicated by the pink marker is reached first and provides the gain  $G_{\text{th,paras}}$ , resulting in parasitic lasing at this specific wavelength. Therefore, the maximum population inversion that

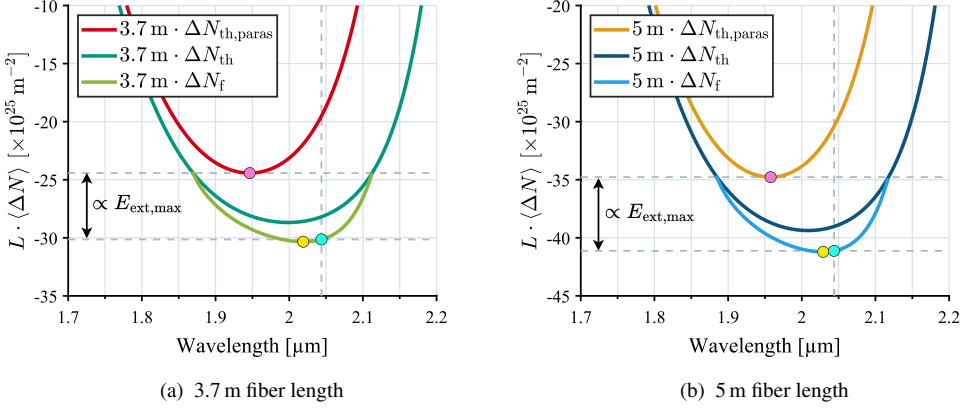


Figure 4.3: Maximum extractable energy from the population inversion in the Q-switched Tm-20-300 fiber laser for 3.7 m and 5 m fiber length. Pink marker: parasitic lasing wavelength. Turquoise marker: laser operating wavelength. Yellow marker: Optimal operating wavelength. A longer fiber length increases the maximum extractable pulse energy at long wavelengths because of stronger reabsorption at short wavelengths.

can be reached in the active fiber is directly related to the minimum of the parasitic threshold inversion:

$$\langle \Delta N \rangle_{i,\max} \sim \min \langle \Delta N \rangle_{\text{th,paras}} . \quad (4.4)$$

This relation is not an equality due to dynamic gain overshoot. Parasitic lasing needs the time  $T_{b,\text{paras}}$  to build up from fluorescence and eventually saturate any further inversion increase. During this build-up time the inversion can temporarily exceed the parasitic threshold. If the inversion is discharged within this time period, initial inversions higher than the parasitic threshold inversion can be extracted. This possible overshoot of the inversion and gain above the parasitic threshold increases with higher pump power and can be calculated numerically. For operation at low-to-moderate pump powers up to  $\sim 50$  W used for calibration, this effect is negligible, because the total charging time is much longer than the parasitic build up time ( $T_{\text{charge}} \gg T_{b,\text{paras}}$ ). However, for higher pump power, its impact on the maximum initial inversion and gain becomes significant, resulting in enhanced energy storage and extraction. This effect will be examined in detail later in this section.

The wavelength-independent potential  $L \cdot \langle \Delta N \rangle_{i,\max}$  can be used to determine the wavelength-dependent maximum initial gain  $G_{i,\max}$  using eq. (2.163). The operation wavelength of the Q-switched fiber laser was defined by the  $\sim 2044$  nm VBG in this experiment. Pulse extraction

is possible at operation wavelengths that meet the condition  $\langle \Delta N \rangle_{\text{th,paras}}(\lambda_{\text{paras}}) > \langle \Delta N \rangle_{\text{th}}(\lambda_s)$ , which determines the tuning range of the fiber laser. Within this wavelength range, the final gain  $G_f$  and the corresponding final inversion  $\langle \Delta N \rangle_f$ —both wavelength-dependent—can be calculated using the Q-switching master equation (2.261).

The curve  $L \cdot \langle \Delta N \rangle_f$  illustrates the discharge of inversion from the maximum initial inversion depending on the laser operating wavelength. For the operation wavelength of 2044 nm, the minimum final inversion  $\langle \Delta N \rangle_{f,\text{min}}(2044 \text{ nm})$  is indicated by the turquoise marker. If  $\langle \Delta N \rangle_{i,\text{max}} \approx \min \langle \Delta N \rangle_{\text{th,paras}}$  is assumed, the maximum extractable pulse energy results from the vertical distance between the turquoise and the pink marker, illustrated by the dashed lines (see eq. (2.244)). The metric  $L \cdot \langle \Delta N \rangle$  can therefore be interpreted as a wavelength-independent potential, for which the potential difference is directly proportional to the extractable pulse energy by multiplying it with the factor  $(1/2)(hc_0/\lambda_s)A_{\text{core}}$ .

Because the potential  $L \cdot \langle \Delta N \rangle_{i,\text{max}}$  is independent of the operating wavelength, the optimum operating wavelength is determined by the minimum of  $L \cdot \langle \Delta N \rangle_f$  at  $\sim 2019 \text{ nm}$ , indicated by the yellow marker. For the application of pumping a ZGP OPO, long wavelengths are required and the operation wavelength is not intended to be changed. Therefore, the inversion curves can be shifted to longer wavelengths by utilizing the effect of reabsorption to enhance the maximum extractable energy.

Figure 4.3b shows the calculated inversion curves for a longer fiber length of 5 m. The longer fiber reduces the population inversion that is required to reach the threshold gain levels  $G_{\text{th,paras}}$  and  $G_{\text{th}}$  and therefore increases the reabsorption, resulting in a red shift of the inversion curves. Thus, parasitic lasing occurs at a longer wavelength of  $\sim 1957 \text{ nm}$  (pink marker), and the optimal operation wavelength (yellow marker) shifts to 2028 nm closer to the fixed operating wavelength at 2044 nm (turquoise marker). This increases the difference between the initial and final potentials, enhancing the maximum extractable pulse energy at the operating wavelength.

This reabsorption effect is illustrated more intuitively in fig. 4.4 by considering the respective gain spectra for the fiber lengths of 3.7 m and 5 m. Figure 4.4a shows the gain spectra at the respective maximum initial inversions  $\langle \Delta N \rangle_{i,\text{max}}$  for the two fiber lengths calculated by eq. (2.163). Parasitic lasing limits the energy that can be stored in the fiber when the gain peak reaches the parasitic gain threshold  $G_{\text{th,paras}}$ . For the longer 5 m fiber, the stronger reabsorption suppresses the gain at short wavelengths. Therefore, more energy can be stored in the

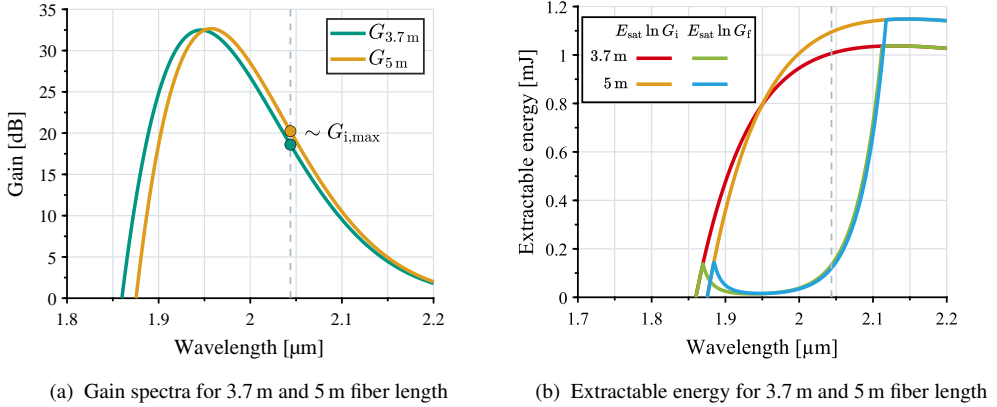


Figure 4.4: Gain spectra and extractable pulse energy of the Q-switched Tm-20-300 fiber laser for 3.7 m and 5 m fiber length. The red shift of the gain spectrum by reabsorption leads to higher initial gain for the longer fiber, resulting in a higher extractable energy.

fiber until the parasitic threshold is reached at a longer wavelength. This results in a higher maximum initial gain  $G_{i,\text{max}}$  at the operating wavelength of 2044 nm indicated by the dashed line.

Figure 4.4b illustrates how this increase in initial gain influences the extractable energy. The difference between the curves  $E_{\text{sat}} \ln G_i$  and  $E_{\text{sat}} \ln G_f$  spans the extractable energy for the respective fiber lengths, according to eq. (2.245). At short wavelengths, the energy extraction is limited by reabsorption that decreases the maximum initial gain, while at long wavelengths, the energy cannot be extracted due to a vanishing emission cross-section, resulting in an increase of the final gain. The plot clearly shows that the higher initial gain of the 5 m fiber at 2044 nm leads to a higher maximum extractable energy.

Not all of the extracted energy leaves the laser resonator as output power at the OC, but is dissipated into other loss sinks within the cavity. Consequently, the output pulse energy  $E_{\text{pulse}}$  results from the extracted energy  $E_{\text{ext}}$  by multiplication with the resonator efficiency  $\eta_R$  (see eqs. (2.159) and (2.247)). Furthermore, the peak power of the output pulses was calculated from the determined initial gain levels using eq. (2.262), and the FWHM pulse duration was calculated from eq. (2.263). These output pulse characteristics are plotted in fig. 4.5 versus the fiber length.

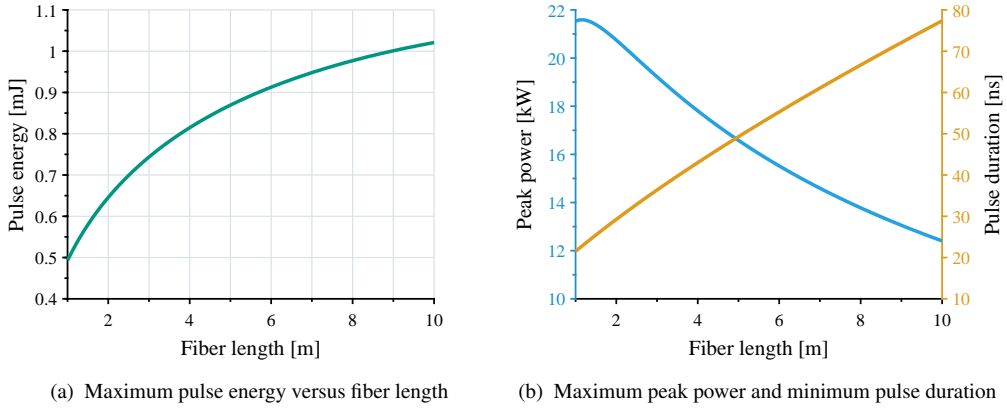


Figure 4.5: Calculated maximum output pulse energy and the corresponding maximum peak power and minimum FWHM pulse duration versus the fiber length at an operating wavelength of 2044 nm.

For the considered Q-switched Tm-20-300 fiber laser, a longer fiber length results in an increase of the maximum pulse energy, but a decrease in peak power and an increase in pulse duration. While the 3.7 m fiber provides a maximum pulse energy of  $\sim 800 \mu\text{J}$ , with a peak power of  $\sim 18.2 \text{ kW}$ , and a pulse duration of  $\sim 41 \text{ ns}$ , as it has been measured in sec. 3.1.2, a 5 m fiber is theoretically expected to deliver  $\sim 870 \mu\text{J}$  pulse energy,  $\sim 16.6 \text{ kW}$  peak power, and a  $\sim 49.3 \text{ ns}$  pulse duration. A further increase in the fiber length results in a progressively smaller enhancement in the maximum pulse energy.

To correctly interpret this result, it must be noted that this analysis is only valid in the absence of significant nonlinear effects. As it was experimentally observed in sec. 3.1, a longer fiber leads to a higher nonlinear interaction length, which can result in severe spectral broadening and a degradation of the cavity Q-factor due to higher losses at the VBG. Therefore, the selection of the optimal fiber length is a trade-off between potentially higher energy extraction by increasing the reabsorption, and remaining below the critical fiber length where fiber nonlinearities become significant. Determining this critical fiber length by analyzing the parametric gain of modulation instability is the focus of the following section 4.2.

So far, the analysis has neglected the effect of pump power by assuming a steady-state parasitic lasing limit ( $G_{i,\text{max}} \approx G_{\text{th,paras}}$  and  $\langle \Delta N \rangle_{i,\text{max}} \approx \langle \Delta N \rangle_{\text{th,paras}}$ ). To analyze the dynamic overshoot of the inversion and gain above the parasitic threshold level, the laser rate eqs. (2.180) and (2.181) of a simplified two-level system were numerically solved to model the build-up

process of parasitic lasing. For this, it is not necessary to fully resolve the temporal, spatial, and spectral domains.

Based on the experimental findings and prior steady-state analysis, two crucial simplifications were made: In the spectral domain, the parasitic lasing wavelength  $\lambda_{\text{paras}}$  at the minimum of  $\langle \Delta N \rangle_{\text{th,paras}}$  is already known from the steady-state analysis. Therefore, for each design parameter set, only this single wavelength needs to be modeled. For the spatio-temporal domain, the experiment showed that the parasitic lasing build-up process occurs on a microsecond time scale (see fig. 3.4). This is orders of magnitude slower than the round-trip time in the parasitic cavity on the nanosecond-scale, which allows to linearize the rate equations within these time steps ( $\Delta t = 2nL/c_0$ ). Consequently, it is also not required to spatially resolve the fiber, enabling the use of axial-averaged values  $\Delta \langle \Delta N \rangle / \Delta t$  and  $\Delta \langle I_s \rangle / \Delta t$  for the changing rates. These simplifications maintain the fast computation time of the model.

The model used a constant quantum yield of  $\eta_q = 1.4$ , as a result of the CR1 cross-relaxation process, an upper-state lifetime of  $\tau = 350 \mu\text{s}$ , and a parasitic cavity photon lifetime given by

$$\tau_{\text{c,paras}} = \frac{nL}{\ln G_{\text{th,paras}}} . \quad (4.5)$$

The simulation was initialized at  $t = 0$  with the inversion at the steady-state parasitic threshold ( $\langle \Delta N \rangle_0 = \langle \Delta N \rangle_{\text{th,paras}}$ ), and the parasitic intensity at the fluorescence noise level. The computation was performed until the growing parasitic lasing intensity caused a decrease in population inversion. The inversion value from the previous time step was then used as the maximum initial inversion  $\langle \Delta N \rangle_{\text{i,max}}$ .

Figure 4.6 shows the calculated maximum output pulse characteristics as a function of pump power for the 3.7 m long Q-switched Tm-20-300 fiber at an operating wavelength of 2044 nm. At high pump powers, the higher achievable initial gain results in a significant increase in pulse energy and peak power and a reduction in pulse duration. At a low pump power of 30 W, the calculated parasitic build-up time was  $\sim 3.15 \mu\text{s}$ , which is in excellent agreement with the intra-spike period recorded in fig. 3.4 and validates the dynamic model. The enhancement in pulse energy for pump powers  $< 50 \text{ W}$  is less than 4%. For higher pump powers, the calculated parasitic build-up time decreases reaching  $0.9 \mu\text{s}$  at 500 W. At this power level, the theoretical enhancement is  $\sim 19.0\%$  in pulse energy and  $40\%$  in peak power.

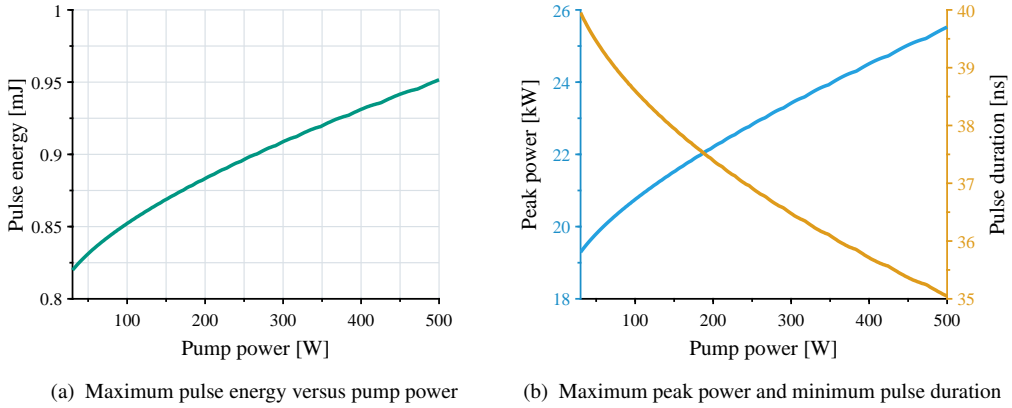


Figure 4.6: Calculated maximum output pulse energy and the corresponding maximum peak power and minimum FWHM pulse duration versus the pump power at an operating wavelength of 2044 nm for a fiber length of 3.7 m.

In practice, it must be noted that an increase in pump power can also have detrimental effects that were not considered here. The thermal load associated with higher pump powers reduces the cross-relaxation rate and hence the efficiency of the pump process [225]. This decreases the potential overshoot of the initial gain during the parasitic build-up time. Especially in an oscillator, thermal effects can destabilize the resonator. In a free-space setup, the cavity Q-factor can be reduced by thermal misalignment, resulting in a degradation of pulse extraction. These effects counteract the improvement in pulse extraction at higher pump powers, suggesting that the theoretical improvements at high pump powers represent an upper bound.

In addition to a gain limitation by parasitic lasing, high inversion levels can also cause pump bleaching that would limit the energy storage. However, within the entire space of examined parameters, the maximum initial inversion was well below the bleaching level for  $\sim 793$  nm pumping. Using  $\sigma_a(790 \text{ nm}) = 10.0 \cdot 10^{-25} \text{ m}^{-2}$  and  $\sigma_e(790 \text{ nm}) = 13.5 \cdot 10^{-25} \text{ m}^{-2}$  results in a bleaching level of  $\Delta N/N \approx -0.15$ . Considering the limitation by parasitic lasing, the highest inversion level of  $\Delta N/N \approx -0.41$  was determined for a 1 m fiber length and a pump power of 500 W. Therefore, even in this extreme case, the parasitic lasing limit is much more restrictive than pump bleaching. This shows that for 790 nm pumping, pump bleaching does not set an ultimate limit to the extractable pulse energy. However, for short fiber lengths, a significant decrease in pump absorption efficiency is expected.

The model presented for this Q-switched fiber oscillator is also directly applicable to fiber amplifiers. In this case, the parasitic threshold gain is defined by two parasitic reflectivities (see eq. (2.264)), leading to a generally higher maximum initial gain than for a Q-switched laser. The final gain and inversion result from eq. (2.269) depending on the input pulse energy.

## 4.2 Analysis of Fiber Nonlinearities

The experiments in chapter 3 demonstrated that fiber nonlinearities led to a distortion of the output spectrum at high peak powers, which reduced the conversion efficiency for pumping a ZGP OPO. Furthermore, the nonlinear spectral broadening was found to decrease the cavity Q-factor due to additional losses at the VBG, which in turn reduced the maximum extractable pulse energy. From the characteristic side peaks in the output spectrum, MI was identified as the primary effect that initiated the spectral broadening. This effect was introduced in sec. 2.3.3 and is a specific challenge for  $2\ \mu\text{m}$   $\text{Tm}^{3+}$ -doped fiber lasers. In this wavelength region, the interplay of anomalous group velocity dispersion (GVD) in silica and self-phase modulation (SPM) causes phase matching for degenerate four-wave mixing (DFWM). The resulting parametric gain leads to MI starting from noise.

This parametric gain scales with the intensity and the interaction length in the fiber, which limits the maximum fiber length of the laser. Since a longer fiber was previously shown to potentially enhance pulse energy extraction, an optimal design must find a trade-off. This section provides an analysis of the MI gain to determine the critical fiber length beyond which these nonlinear effects become the dominant limitation.

The MI analysis was performed considering the linearly polarized Q-switched Tm-20-300 fiber laser from sec. 3.1. This setup differed from the unpolarized configuration analyzed in the previous section only by the addition of two thin-film polarizers (TFPs), one inside the cavity and one at the output (see fig. 3.1a). Because the parasitic cavity is not affected by this change, the threshold for parasitic lasing is identical to the unpolarized configuration, resulting in the same maximum initial gain. However, the TFPs cause additional losses in the unblocked cavity, resulting in a higher threshold gain  $G_{\text{th}}$ , and at the output. In the experiment, this led to a reduction of the maximum pulse energy from  $\sim 800\ \mu\text{J}$  to  $\sim 625\ \mu\text{J}$  and the peak power from 18.5 kW to 13.7 kW. To adapt the model to this performance reduction, 10 % additional

losses at the output were applied, and the HR feedback was reduced to  $R_{\text{HR}} = 50\%$ . This large reduction in  $R_{\text{HR}}$  is not only attributed to the intracavity TFP, but also to the stronger spectral broadening by SPM for the linear polarization, resulting in a higher spectral content outside the VBG bandwidth.

To accurately model the parametric gain in the Q-switched fiber oscillator, the measured output spectrum of the polarized Tm-20-300 fiber laser shown in fig. 4.7a was examined. The spectrum, measured at maximum peak power with a 2 nm resolution, exhibited characteristic MI side peaks. These side peaks were more than 33 dB below the central laser peak and contained less than 1 % of the total power. The first order peaks were located at wavelengths of  $\sim 2024$  nm and  $\sim 2064$  nm, corresponding to a spectral shift of  $\sim 20$  nm from the central laser line at 2044 nm. This reveals an important difference from the standard fiber amplifier model for MI described in sec. 2.3.3.

In a fiber amplifier, the peaks of the local parametric gain spectrum result from the local power  $P(z)$ , according to eq. (2.237). The total parametric gain is then found by integrating these local spectra over the fiber length (see eq. (2.236)). Consequently, as illustrated in fig. 2.35, the spectral location of the MI peaks depends on the entire signal power distribution along the fiber.

In a fiber oscillator, the local power in the cavity also increases from the HR towards the output end, as the small power fraction reflected from the OC is amplified to the much higher output power level after one round trip. However, the measured locations of the spectral side peaks do not align with a gain spectrum determined by locally varying gain peaks. Instead, they coincide with a gain spectrum whose peak locations are governed only by the maximum intracavity peak power  $P_{\text{peak}}/\eta_{\text{R}}$ . This key finding was consistently observed in the output spectra of other oscillator setups as well (eg. fig. 3.7b and fig. 3.15a).

To explain this difference between oscillators and amplifiers it is instructive to consider the parametric gain as a result of DFWM. The mode coupling between the degenerate pump waves and the side bands can then be described analogously to eq. (2.124) with a local gain coefficient  $g_{\text{MI}}(z)$  that results from a nonlinear coupling constant  $\kappa(z)$  and a phase mismatch  $\Delta k$ . Thus, eq. (2.236) for the total gain coefficient along the fiber can be rewritten into the form

$$g_{\text{MI}} = \frac{2}{L} \text{Im} \left\{ \int_0^L \sqrt{\left(\frac{\Delta k}{2}\right)^2 - \kappa^2(z)} dz \right\}. \quad (4.6)$$

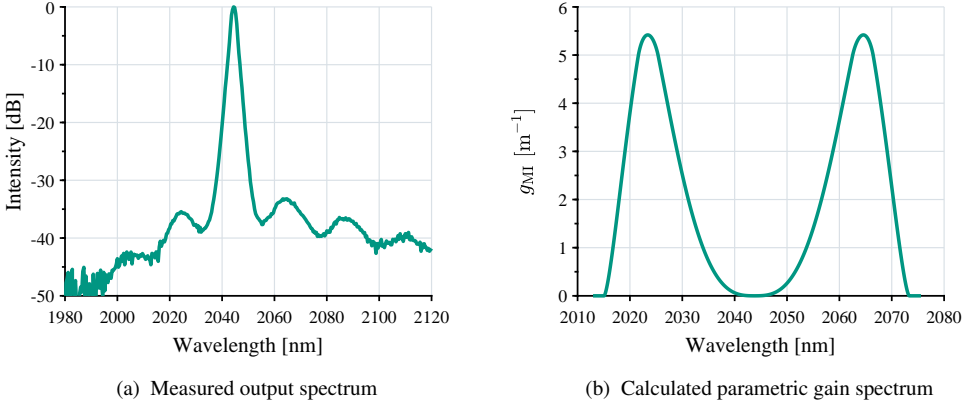


Figure 4.7: Measured output spectrum and calculated parametric gain spectrum for modulation instability in the linearly polarized Tm-20-300 fiber laser at maximum peak power.

For both amplifiers and oscillators, the coupling constant is local and power-dependent:  $\kappa(z) = \gamma P_s(z)$ . The difference between the architectures lies in the phase matching: while the relative phase mismatch in an amplifier evolves continuously as a result of material dispersion and self-phase modulation depending on the local power, the field in an oscillator must reproduce its phase after each round trip to be a stable resonator mode. This global constraint fixes the phase relationship in an oscillator. As experimentally observed (see fig. 3.10b), this results in an equivalently broadened spectrum along the entire laser cavity, implying the nonlinear phase contribution by SPM is effectively constant and governed by the maximum peak power  $P_{s,\max}$ .

This leads to a  $z$ -independent phase mismatch for the oscillator, determined by material dispersion ( $\Delta k_{\text{MD}} \approx \beta_2 \Omega^2$ ) and the maximum peak power:

$$\Delta k_{\text{osc}} \approx \beta_2 \Omega^2 + 2\gamma P_{s,\max} . \quad (4.7)$$

When this oscillator-specific  $\Delta k_{\text{osc}}$  is used in the gain integral (eq. (4.6)), the calculated parametric gain spectrum illustrated in fig. 4.7b coincides well with the measured output spectrum in fig. 4.7a.

To calculate the parametric gain with eq. (4.6), the signal power distribution  $P_s(z)$  along the fiber was estimated using some simplifications. Because the VBG filters out the spectral

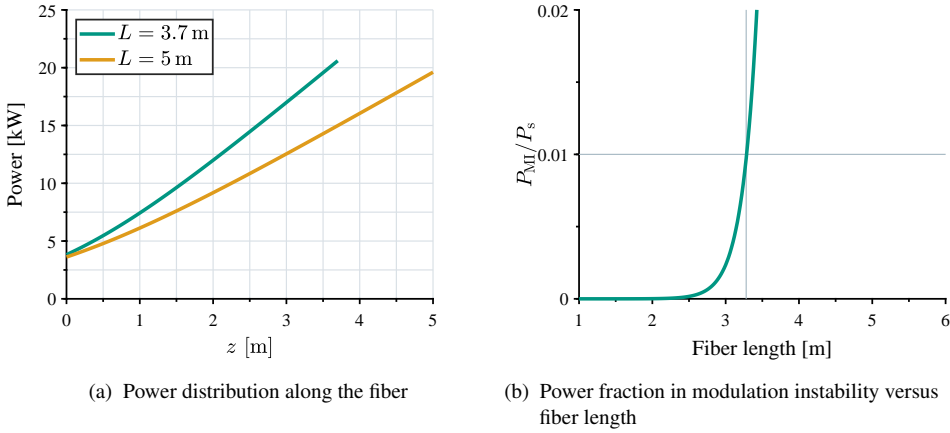


Figure 4.8: Determination of the critical fiber length at which significant modulation instability occurs.

sidebands at the HR end, only a single pass through the fiber was considered to contribute to the MI output. For this single pass, the propagating laser signal was modeled effectively as for a saturated amplifier. Using the determined initial gain, final gain, and saturation energy, an equivalent input pulse energy was calculated from eq. (2.269) that would produce the measured output.

The forward propagation of this input pulse was then numerically solved. Under the assumption of an evenly distributed gain  $g_i = \ln G_i/L$ , the fiber was divided into length segments  $\Delta z$  with an initial small-signal gain of  $G_i(z) = \exp(g_i \Delta z)$ . The Frantz-Nodvik equation (2.270) was then applied sequentially, to calculate the energy distribution  $E(z)$  along the fiber. Finally, to get the local peak power, the pulse was assumed to maintain a Gaussian shape with the measured FWHM pulse duration  $t_p$ , giving  $P_s(z) = 0.94 \cdot E(z)/t_p$ .

Figure 4.8a shows the resulting power distributions for the fiber lengths of 3.7 m and 5 m. For each fiber length, these peak power distributions were used to calculate the parametric gain coefficients from eq. (4.6) using the oscillator-specific phase mismatch  $\Delta k_{osc}$  (eq. (4.7)).

Using this parametric gain, the MI power fraction  $P_{MI}/P_s$  was calculated considering the amplification of noise under the undepleted pump approximation (see sec. 2.3.3). The critical length was defined as the fiber length for which the ratio  $P_{MI}/P_s$  became greater than 1 %,

indicated by the gray line in fig. 4.8. For the linearly polarized Tm-20-300 fiber laser, this analysis yielded a critical length of  $\sim 3.3$  m.

The results show good agreement with the experimental observations. In the experiment a slightly longer length of 3.7 m was found to produce a sideband power content of  $\sim 1\%$ . Therefore, the model provides a good estimate for assessing the optimal fiber length. This analysis, supported by the experimental data, reveals that the 3.7 m Tm-20-300 fiber laser was already operated very close to the optimal conditions. Further pulse energy scaling in this fiber is ultimately limited by nonlinear effects.

## 4.3 Conclusion

This section has established a quantitative framework for analyzing and optimizing nanosecond-pulsed  $\text{Tm}^{3+}$ -doped fiber lasers, moving from the experimental observations of the previous chapter to a predictive model. This analysis confirms that parasitic lasing is the primary gain-limiting mechanism that governs the maximum extractable pulse energy. Other potential gain limitations, such as ASE or pump bleaching, were proven to be much less restrictive and therefore were not relevant under the considered conditions. The model has successfully quantified the critical role of reabsorption in maximizing the energy storage by shifting the parasitic gain peak, as well as the potential for stretching the gain limit at high pump powers via dynamic gain overshoot. Furthermore, this work identified a difference in modulation instability between amplifiers and oscillators, leading to a new proposed parametric gain expression that accounts for the global phase-matching conditions in a resonator. This framework provides the first quantitative tool to evaluate the critical design trade-offs between maximizing gain and mitigating nonlinearities for the development of high-pulse-energy  $\text{Tm}^{3+}$ -doped fiber lasers.

A central advantage of the presented modeling approach lies in its efficiency. By distilling the complex physics into a set of fundamental, rapidly-solvable relationships, it provides a powerful tool for comprehensive parameter optimizations. This enables the rapid evaluation of various fiber and laser designs, without relying on a computationally-intensive full numerical simulation. The model might also serve as a practical starting point for more comprehensive simulations. However, while the already performed experiments showed good agreement with

the modeled behavior, the validity of the performance predictions and of the proposed MI gain theory requires further, dedicated experimental verification.

From this analysis, concrete design strategies for future laser designs can be concluded. To overcome the primary gain limit, the gain for parasitic lasing must be actively suppressed. In the laser design, parasitic feedback can be mitigated by using a wavelength-selective OC or by adopting a MOPA configuration which removes the OC entirely. Within the fiber, the gain for parasitic lasing can be reduced by exploiting the absorption characteristics of the active dopants. While this effect has been investigated for reabsorption by  $\text{Tm}^{3+}$  ions so far, the idea can also be taken further: the incorporation of co-dopants that absorb in the short-wavelength range where parasitic lasing occurs, but not at the signal wavelength might be beneficial. Such a fiber composition actually already exists:  $\text{Tm}^{3+}:\text{Ho}^{3+}$ -co-doped fibers might represent an ideal candidate for high-pulse energy extraction, as the  $\text{Ho}^{3+}$  ions provide high absorption at the  $\text{Tm}^{3+}$  gain peak and simultaneously contribute to the gain at longer wavelengths. The potential of this material composition has already been demonstrated in CW operation, where an exceptionally stable and efficient operation at long emission wavelengths up to  $2.2\ \mu\text{m}$  was found [166]. The initial results in pulsed operation were also promising, indicating that further investigations on this topic could be valuable [226].

To leverage the gain overshoot for high-power operation, fiber laser designs must be robust against thermal effects, e.g. by employing endcaps and an all-in-fiber MOPA architecture (see sec. 2.3.4). Furthermore, this effect is enhanced for an efficient pump process, demanding a large pump overlap factor  $\Gamma_{\text{pump}}$ , a sufficient fiber length, and a high doping concentration accompanied by an improved CR1 rate. In amplifiers, the ability to predict the maximum initial gain  $G_1$  under various operating conditions can also serve as a basis for optimized input pulse shaping.

Finally, this comprehensive analysis of the Tm-20-300 fiber reveals a fundamental performance limit for conventional LMA fibers. Despite these optimization strategies, the performance in LMA fibers is ultimately restricted by the trade-off between gain and nonlinearity, preventing further peak power scaling from their 20–25  $\mu\text{m}$  fiber cores. To push 2  $\mu\text{m}$  fiber lasers beyond this barrier and achieve multi-mJ pulse energies while covering the spatial, spectral, and temporal requirements for OPO pumping, much larger mode field areas are required. This conclusion provides the direct motivation for the investigation of a  $\text{Tm}^{3+}$ -doped PCF in the following section.

## 5 Investigation of a Large-Mode-Area Photonic Crystal Fiber

The preceding analysis in chapter 4 revealed a fundamental performance ceiling for conventional  $\text{Tm}^{3+}$ -doped large-mode-area (LMA) fibers. Although improved design strategies can find an optimal compromise for spatial, temporal, and spectral laser performance, they cannot overcome the ultimate constraining trade-offs between gain enhancement and nonlinear effects. This finding is consistent with the literature reviewed in table 2.2, which shows that 2  $\mu\text{m}$  nanosecond-pulsed LMA fiber lasers were limited to pulse energies  $\leq 1$  mJ. The core diameters of 20–25  $\mu\text{m}$  lead to low saturation energies and intensity-dependent nonlinear spectral broadening, representing a hard barrier to further pulse energy and peak power scaling from LMA fibers. Therefore, to push into the multi-mJ regime while maintaining spectral purity, a new fiber platform with a significantly larger core is required.

Specialty fibers, such as photonic crystal fibers (PCFs) introduced in sec. 2.3.2, offer a solution by enabling larger core areas while maintaining single-mode operation. However, scaling the fiber core in a single- or few-moded fiber comes with a fundamental constraint: the required low numerical aperture (NA) results in weak light guidance, making the fiber highly sensitive to micro- and macro-bending losses. Consequently, large pitch fiber (LPF) rods exhibit large core diameters of  $\sim 80 \mu\text{m}$ , but are not bendable and are therefore practically restricted to short lengths of  $\sim 1$  m, thus partially losing some of the general advantages of fiber lasers. While reported nanosecond-pulsed  $\text{Tm}^{3+}$ -doped LPF systems have delivered multi-mJ pulse energies, their short fiber lengths led to poor efficiencies, preventing average power scaling and restricted their operation to short emission wavelengths  $< 2 \mu\text{m}$  (see table 2.2). These wavelengths are unsuitable for pumping  $\text{ZnGeP}_2$  (ZGP) optical parametric oscillators (OPOs), due to high background absorption in the crystal (see fig. 2.46).

Flexible PCFs represent a promising trade-off: they still have large core diameters of  $\sim 50\ \mu\text{m}$ , but they can be coiled, which enables the use of longer fibers to potentially achieve higher gain and efficiency at longer wavelengths. However, despite this potential, previous work on nanosecond-pulsed  $50\ \mu\text{m}$   $\text{Tm}^{3+}$ -doped PCFs did not achieve higher pulse energies than with LMA fiber systems (see tab. 2.2). Furthermore, these attempts also suffered from low efficiencies and were restricted to short wavelengths  $< 2\ \mu\text{m}$ .

This chapter presents a detailed investigation of  $\text{Tm}^{3+}$ -doped flexible PCFs that unlocks the potential of this promising fiber type. By applying the quantitative model from chapter 4 to a Q-switched  $\text{Tm}^{3+}$ -doped PCF oscillator, the specific challenges of these fibers are identified and addressed. This approach leads to the demonstration of 1.9 mJ pulses at a long emission wavelength of 2050 nm, which more than doubles the previous state of the art in pulse energy from a  $\text{Tm}^{3+}$ -doped flexible PCF. Moreover, this represents the first demonstration of operating such a fiber at an emission wavelength as long as 2050 nm. Parts of the findings and results presented in this chapter have been published in a journal article and in four conference contributions [223, 227–230].

The chapter begins with presenting the  $\text{Tm}^{3+}$ -doped PCF and the adapted Q-switched oscillator setup in sec. 5.1. Section 5.2 details the experimental results and analysis. First, a short 3 m PCF is characterized to identify its critical properties. This analysis leads to the conclusion that a longer 7 m fiber is optimal for high-energy extraction, which is then experimentally verified. Finally, the Q-switched PCF oscillator is power-scaled, demonstrating over 100 W of average output power while maintaining the maximum pulse energy. The chapter is concluded in sec. 5.3, with a summary of the findings, along with a discussion of beneficial laser architectures for fully exploiting the potential of the  $\text{Tm}^{3+}$ -doped PCF.

## 5.1 Experimental Setup

For the experimental investigation of the  $\text{Tm}^{3+}$ -doped PCF, the Q-switched fiber oscillator setup presented in sec. 3.1.1 was slightly adapted to enable operation at higher average power, as shown in fig. 5.1a. The PCF was equipped with endcaps on both fiber ends, allowing higher power handling at the glass-to-air interfaces and improving mechanical stability against thermal misalignment (see sec. 2.3.4). Because the endcapped fiber facet at the output side can no longer

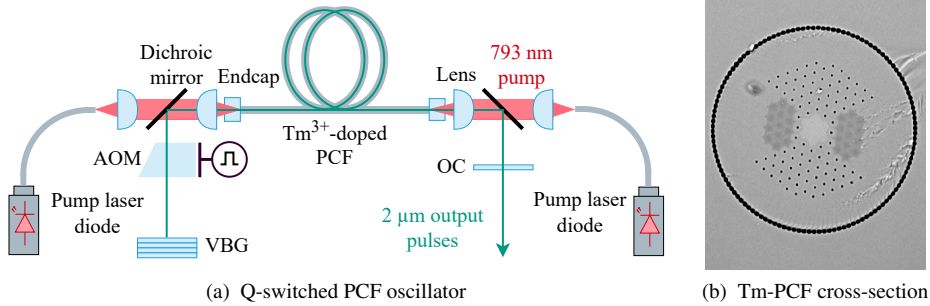


Figure 5.1: Schematic of the experimental setup of the Q-switched PCF and micrograph of the PCF cross-section.

Table 5.1: Geometry parameters of the  $\text{Tm}^{3+}$ -doped PCF.

Designation	PM	$\Lambda_{\text{pitch}}$	$d_{\text{core}}$	$d_{\text{clad}}$	$d_{\text{doped}}$	$w_0$
Tm-PCF	Yes	13 $\mu\text{m}$	50 $\mu\text{m}$	250 $\mu\text{m}$	38 $\mu\text{m}$	19 $\mu\text{m}$

act as the OC, an external mirror with  $\sim 3.5\%$  reflectance was used. At the HR side, the 2050 nm volume Bragg grating (VBG) defined the laser operating wavelength.

The  $\text{Tm}^{3+}$ -doped PCF was coiled with a bending radius of  $\sim 20$  cm and actively water-cooled during the experiments. A micrograph of the PCF cross-section is depicted in fig. 5.1b and important geometry parameters are listed in table 5.1. A regular air hole matrix with a pitch of  $\Lambda_{\text{pitch}} \approx 13 \mu\text{m}$  forms the photonic crystal cladding that provides guiding in the core. The core is defined as the hexagonal region of missing air holes in the center of the photonic crystal cladding. The distance between the opposing air holes in the corners of this hexagon corresponds to a core diameter of 50  $\mu\text{m}$ . In fig. 5.1b, a lighter-colored, star-shaped area is visible within this core region, which is presumably the doped area and has a diameter of  $\sim 38 \mu\text{m}$ . The mode field radius of  $w_0 \approx 19 \mu\text{m}$  given by the manufacturer (NKT Photonics) matches this size. Laterally to the core, two stress rods interrupt the air hole matrix, making the PCF polarization-maintaining (PM), although no polarizers were used in this experiment, resulting in a nearly random polarization of the fiber oscillator. The photonic crystal cladding is surrounded by an air cladding with a diameter of 250  $\mu\text{m}$  that confines the pump light.

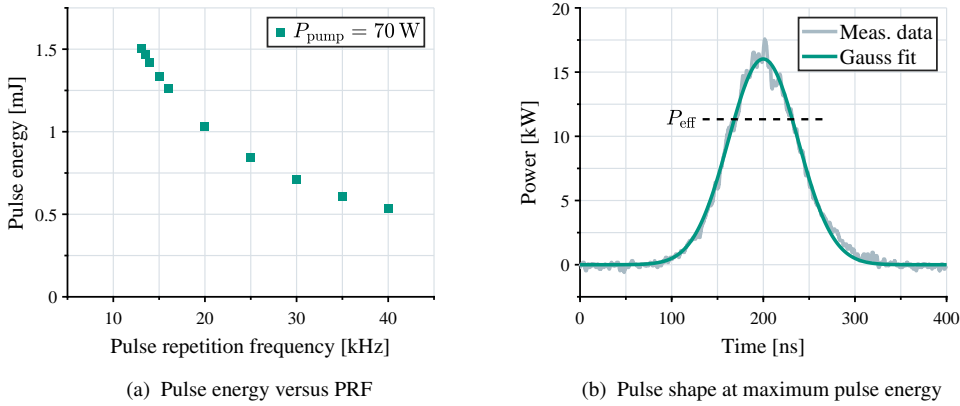


Figure 5.2: Measured pulse characteristics for the 3 m PCF during pulse energy scaling at 2050 nm. A maximum pulse energy of  $\sim 1.5$  mJ was reached at pump power of 70 W and a PRF of 13.1 kHz. The nearly Gaussian pulse shape recorded at the maximum pulse energy has a FWHM pulse duration of  $\sim 88$  ns and a peak power of 16.0 kW.

To experimentally test the conclusions of the previous section, two distinct PCF lengths of 3 m and 7 m were operated in the Q-switched fiber oscillator and investigated for their performance limits. The experimental procedure and measurement instruments used to characterize them were identical to those described in sec. 3.1.

## 5.2 Results and Discussion

### 5.2.1 Initial Experimental Characterization

The investigations on the pulse energy limits in the PCF began with the characterization of the Q-switched 3 m PCF oscillator. At a constant pump power of 70 W, the pulse repetition frequency (PRF) was gradually decreased to scale the pulse energy, as shown in fig. 5.2a. A maximum pulse energy of  $\sim 1.5$  mJ was achieved at a PRF of 13.1 kHz, corresponding to an average output power of 19.7 W. At this point, further pulse energy scaling was limited by the onset of parasitic lasing, which occurred at a wavelength of  $\sim 1927$  nm. The temporal pulse shape recorded at maximum pulse energy (fig. 5.2b) agrees well with a fitted Gaussian profile having an FWHM pulse width of  $\sim 88$  ns and a peak power of  $\sim 16.0$  kW. The effective power was  $\sim 11.3$  kW indicated by the dashed line.

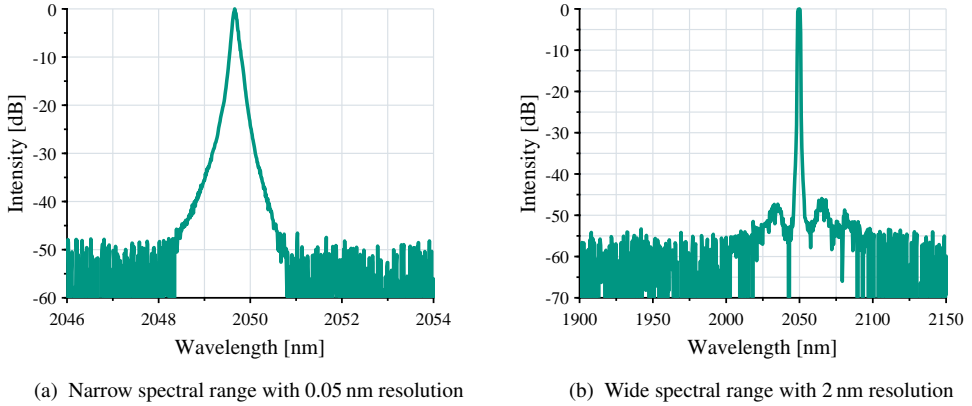


Figure 5.3: Output spectra of the 3 m PCF oscillator measured at maximum pulse energy and peak power. The 10-dB linewidth is  $\sim 250$  pm. The faint MI peaks are shifted by  $\pm 15$  nm from the central laser line and have negligible power content ( $< 0.03\%$ ).

The spectral characteristics at maximum pulse energy and peak power are presented in fig. 5.3. The high-resolution spectrum (fig. 5.3a) demonstrates only weak spectral broadening from self-phase modulation (SPM), with a 3-dB linewidth of  $\sim 100$  pm, a 10-dB linewidth of  $\sim 250$  pm, and a 20-dB linewidth of 510 pm. The wide-range spectrum (fig. 5.3b) confirms excellent spectral purity, showing no detectable amplified spontaneous emission (ASE). Faint modulation instability (MI) side peaks are visible, but they are more than 45 dB below the central peak and contain negligible power. Spectral integration revealed that more than 99.97% of the total output power is contained within a  $\pm 2$  nm band around the central wavelengths of 2049.7 nm. The MI side peaks were shifted by  $\pm 15$  nm from the central laser line.

Finally, the spatial beam quality was characterized. Figure 5.4 shows the measured beam caustic of the focused beam. The measurement was performed at an average output power of 19.7 W and maximum pulse energy of 1.5 mJ. A fit to the data yielded  $M^2$  factors of 1.27 and 1.25 in the transverse  $x$ - and  $y$ -axes, respectively. This excellent, nearly diffraction-limited beam quality is consistent with previous studies on comparable flexible  $\text{Tm}^{3+}$ -doped PCFs [38, 39]. The recorded beam profile is shown in the inset of fig. 5.4.

These baseline results of 1.5 mJ pulse energy and 16 kW peak power with excellent spectral and spatial purity provide the necessary data to calibrate the quantitative model in the next section in order to analyze optimization opportunities.

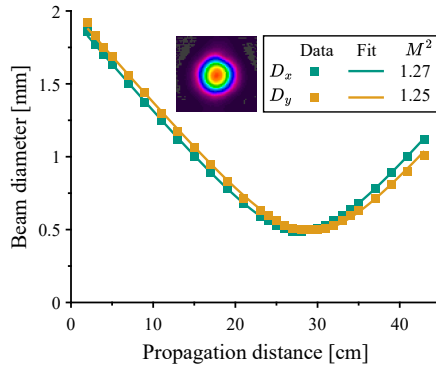


Figure 5.4: Measured beam caustic versus the propagation distance. Fit to the data yields the  $M^2$  factor.

## 5.2.2 Model Calibration and Optimization Strategy

Using the measured pulse characteristics from the Q-switched 3 m PCF, the intrinsic gain characteristics were determined as described in sec. 4.1.1. Table 5.2 lists the input and output parameters of this calculation. For this initial analysis, the resonator parameters and background propagation loss  $\alpha = 0.13$  dB/m were assumed to be identical to those of the Tm-200-300 fiber laser (see tab. 4.1). This calculation yielded a saturation energy of 1.11 mJ, a maximum initial gain of 11.5 dB, and a minimum final gain of 5.2 dB.

These results reveal two important insights about pulse generation in the PCF. First, the maximum initial gain ( $G_{i,\max} \approx 11.5$  dB) achieved in the PCF is significantly lower than that of the LMA fiber laser ( $G_{i,\max} \approx 18.6$  dB). This low initial gain, and correspondingly high final gain, explains the long 88 ns pulses, which is more than double the pulse width of that from the Tm-20-300 laser, despite the shorter length of the PCF (3 m vs. 3.7 m). This implies that the higher pulse energies of the PCF are solely a result of its larger core diameter, manifesting itself in a higher saturation energy.

Second, the saturation energy calculated from the measured pulse dynamic indicates a critical discrepancy: while the doped core area of the PCF is only  $\sim 3.6$  times larger than that of the Tm-20-300 fiber, the model yields a saturation energy that is more than 4.6 times larger. This

Table 5.2: Parameters to model the Q-switched PCF oscillator at an operation wavelength of 2050 nm. The inputs on the left yield the intrinsic gain characteristics on the right.

$E_{\text{pulse}}$	$P_{\text{peak}}$	$R_{\text{OC}}$	$R_{\text{HR}}$	$\alpha$	$L$	$G_{\text{th}}$	$\tau_c$	$E_{\text{sat}}$	$G_{i,\text{max}}$	$G_{i,\text{min}}$
1.5 mJ	16.0 kW	3.5 %	90 %	0.13 dB/m	3 m	6.2 dB	9.3 ns	1.11 mJ	11.5 dB	5.2 dB

significant discrepancy can only be explained by a difference in the spectroscopic cross-sections between the two fibers.

To determine the intrinsic parameters of the PCF ( $\sigma_a$ ,  $\sigma_e$ ,  $N$ , and  $R_{\text{paras}}$ ), the steady-state parasitic threshold gain  $G_{\text{th,paras}}$  must be identified. While the example in sec. 4.1.1 assumed a negligible gain overshoot at low pump power ( $G_{\text{th,paras}} \approx \max G_{i,\text{max}}$ ), this is not valid at the  $P_{\text{pump}} = 70 \text{ W}$  used in this experiment. At this pump power, the effect of dynamic gain overshoot must be taken into account.

Using the overshoot model described in sec. 4.1.2, the predicted enhancement at  $P_{\text{pump}} = 70 \text{ W}$  was calculated to be  $\sim 6.3 \%$  in pulse energy and  $13.9 \%$  in peak power. To find the steady-state gain limit at 2050 nm, the experimentally measured pulse parameters  $E_{\text{pulse}}$  and  $P_{\text{peak}}$  were effectively reduced by these factors. With these corrected values, the gain calculation yielded a steady-state value of  $G(2050 \text{ nm}) \approx 11.2 \text{ dB}$ . This creates a consistent model, as the maximum initial gain  $G_{i,\text{max}}$  increases to the previously determined 11.5 dB when taking into account the gain overshoot at 70 W pump power.

Using this corrected 11.2 dB steady-state limit at 2050 nm, the calibration procedure described in sec. 4.1.1 was performed. This yielded an emission cross section of  $\sigma_e(2050 \text{ nm}) \approx 1.13 \cdot 10^{-25} \text{ m}^2$ , a doping concentration of  $\langle N \rangle \approx 6.6 \cdot 10^{25} \text{ m}^{-3}$ , and a parasitic threshold gain of 28.0 dB corresponding to a parasitic reflectivity of  $-40.6 \text{ dB}$ .

Figure 5.5a shows the full calibrated spectroscopic cross-sections for the PCF, compared against the literature data from [100] for a conventional  $\text{Tm}^{3+}$ -doped aluminosilicate fiber. The calibrated PCF emission cross-section is significantly lower at wavelengths longer than 1950 nm, leading to a high saturation energy but also a low gain at the operating wavelength of 2050 nm. This characteristic can be explained by additional co-dopants, such as fluorine, in the PCF core, which are used to lower the refractive index. Indeed, an energy-dispersive X-ray spectroscopy using a scanning electron microscope confirmed the presence of fluorine in the core. This results in a lower phonon energy in the glass and therefore narrower spectroscopic-cross sections, hence in a gain penalty for longer wavelengths.

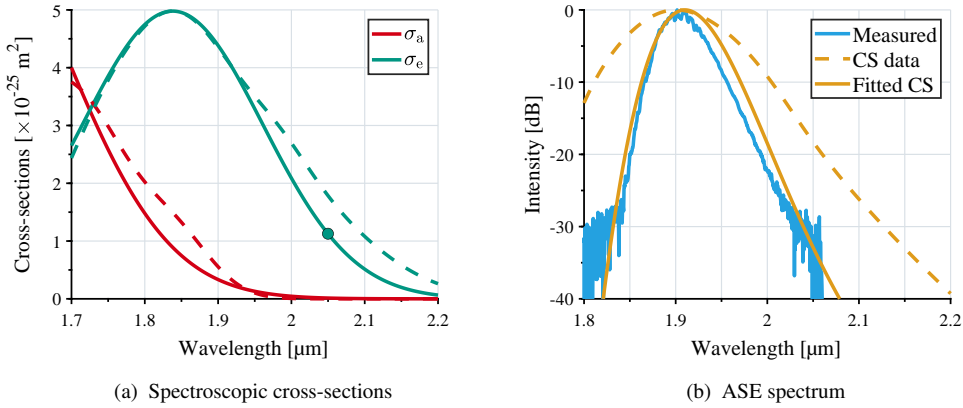


Figure 5.5: Calibrated spectroscopic cross-sections (CS) of the PCF and modeling of the ASE spectrum. In (a), the fitted CS are illustrated by the solid lines and compared with the measured CS data from [100]. In (b), the measured ASE spectrum (blue line) is compared with the calculated ASE spectra using the CS data from [100] (dashed orange line), and using the fitted CS (solid orange line). With the calibrated CS, the ASE spectrum is modeled significantly more accurately.

The validity of the calibrated cross-sections, doping concentration, and parasitic reflectivity was then tested against the measured ASE spectrum, as shown in fig. 5.5b. The ASE spectrum was measured by continuously pumping the endcapped 3 m PCF right below the laser threshold without resonator mirrors. For comparison, two theoretical spectra were calculated: one using the full calibrated model and one using the literature cross-sections from [100]. For the cross-section data from the literature, a doping concentration of  $1.7 \cdot 10^{25} \text{ m}^{-3}$  and a parasitic reflectivity of  $-26.9 \text{ dB}$  were re-calibrated to ensure a fair comparison. As evident from fig. 5.5b, the ASE spectrum calculated with the calibrated cross-sections (solid orange line) shows excellent agreement with the measured data (blue line), while the spectrum calculated from the literature cross-sections (dashed orange line) deviates significantly. This validates the calibrated model and confirms that the cross-sections of the PCF differ substantially from standard  $\text{Tm}^{3+}$ -doped fibers.

With the calibrated model, the pulse energy extraction in the Q-switched PCF were analyzed. Figure 5.6a shows the calculated gain spectrum for the 3 m PCF at the pulse energy limit (including gain overshoot). For this fiber length, the maximum initial gain of 11.5 dB at 2050 nm is significantly below the gain peak at 1927 nm where parasitic lasing occurs. The resulting energy extraction is illustrated in fig. 5.6b. While the high saturation energy allows

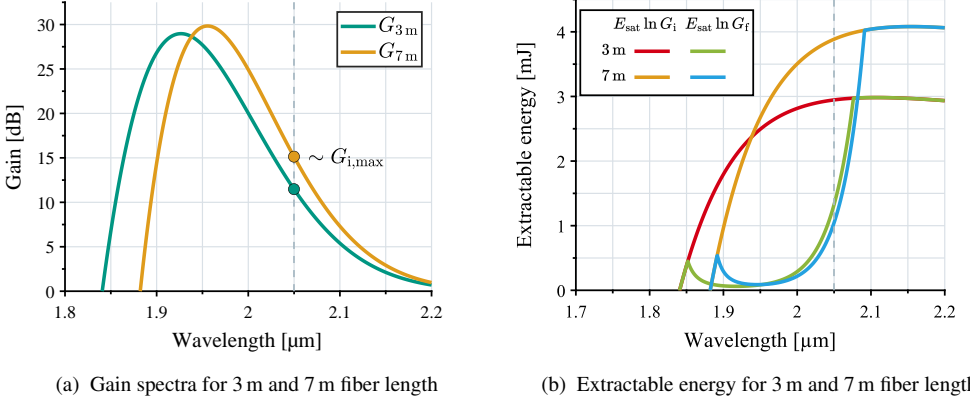


Figure 5.6: Gain spectra and extractable pulse energy of the Q-switched PCF oscillator for 3 m and 7 m fiber length. The low emission cross-section of the PCF at long wavelengths results in a low initial gain at 2050 nm leading to an inefficient energy extraction at this wavelength. Significant improvement is expected for a longer fiber length of 7 m, for which the gain spectrum is red-shifted by reabsorption.

significant energy storage of  $\sim 3$  mJ in the form of population inversion, the low initial gain leads to a slow pulse dynamic and therefore an inefficient energy extraction at the operating wavelength. The extracted energy is illustrated by the gap between the red and the green lines in fig. 5.6b ( $E_{\text{ext}} = E_{\text{sat}}(\ln G_i - \ln G_f)$ ), indicating that a large energy proportion is not extracted but remains in the PCF.

Using a longer fiber length of 7 m should significantly improve the situation, as illustrated by the distinct curves in fig. 5.6. The longer fiber increases reabsorption, which red-shifts the gain spectrum (fig. 5.6a). This results in a higher maximum initial gain  $G_{i,\text{max}}$  at the operation wavelength (orange marker) and thus more efficient energy extraction, as can be seen by the larger gap between the orange and the blue lines in fig. 5.6b.

Figure 5.7 shows the predicted output pulse characteristics of the Q-switched PCF oscillator versus fiber length. The output pulse energy increases with the fiber length, whereby the improvement diminishes with increasing length. The predicted pulse duration exhibits a minimum at  $\sim 2.7$  m, which is a result of two competing effects: the decreasing initial gain for shorter fibers and the increasing cavity length for longer fibers. Therefore, the predicted peak power has an optimum at a fiber length of  $\sim 7$  m.

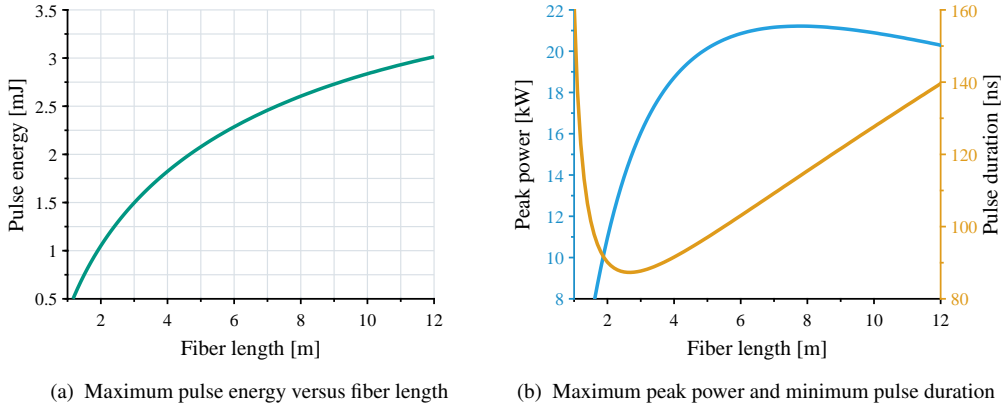


Figure 5.7: Calculated maximum output pulse energy of the PCF and the corresponding maximum peak power and minimum FWHM pulse duration versus the fiber length at an operating wavelength of 2050 nm.

As these predictions are only valid in the absence of significant nonlinear spectral broadening, the impact of nonlinear effects in the PCF was assessed. To calculate the parametric gain for MI in the randomly polarized PCF oscillator, a nonlinear coupling of  $\kappa(z) \approx (5/6) \cdot \gamma P_s(z)$  was used, where the factor  $5/6$  arises from the assumption of circular polarization in an isotropic medium (see sec. 2.3.3). The parametric gain was then calculated using the oscillator-specific phase mismatch (see eq. (4.7)) resulting in the gain spectrum shown in fig. 5.8a. The gain peaks are shifted by around  $\pm 12$  nm from the center at 2050 nm, which is slightly less than the  $\pm 15$  nm shift observed experimentally (see fig. 5.3b). This suggests that the model might slightly underestimate the MI gain, potentially due to an underestimated intracavity peak power  $P_{s,\max}$  or a higher nonlinear parameter  $\gamma$  in the PCF compared to a conventional aluminosilicate fiber.

From this parametric gain, a critical fiber length of 10.9 m was determined as shown in fig. 5.8b. This remarkably long value is a result of the large mode field area in the PCF, but also of the relatively low pulse peak powers caused by the weak emission cross-section at 2050 nm. Based on this analysis, selecting a fiber length of 7 m appears reasonable, even if the parametric gain was slightly underestimated. For this length, the model predicts an excellent trade-off that maximizes pulse energy and peak power on the one hand, while remaining well below the threshold for significant nonlinearities on the other.

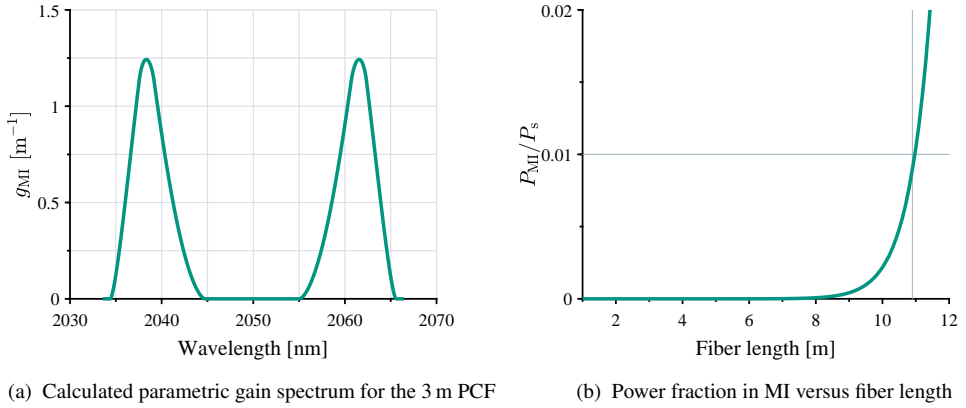


Figure 5.8: Calculated parametric gain spectrum for the Q-switched 3 m PCF at maximum peak power and determination of the critical fiber length.

## 5.2.3 Validation and Refinement

### Experimental Validation of the 7 m PCF

To experimentally validate the predicted pulse energy enhancement, the 7 m PCF was tested in the same Q-switched oscillator configuration. Figure 5.9a shows pulse energy scaling versus the PRF for this PCF length. Due to a lower efficiency of the 7 m PCF, it was pumped with a higher pump power of 75 W to achieve the same output power as for the 3 m PCF. Thus, operating the 7 m PCF at the same PRFs as the 3 m PCF resulted in nearly identical pulse energies in the range of 40–15 kHz. However, with the longer PCF, it was possible to further decrease the PRF before parasitic lasing finally set in. This enabled a maximum pulse energy of  $\sim 1.9$  mJ at a PRF of 9.8 kHz, corresponding to an average output power of 18.5 W. The pulse shape measured at this operating point (fig. 5.9b) exhibits an FWHM pulse duration of 121 ns, a peak power of 14.8 kW, and an effective power of 10.5 kW.

These results confirm the enhancement of pulse energy extraction by utilizing the effect of reabsorption. The 7 m fiber yielded a  $\sim 27\%$  increase in maximum pulse energy compared to the 3 m fiber. In both cases, the maximum pulse energy was limited by the onset of parasitic lasing that clamped the maximum initial gain. Figure 5.10 compares the measured parasitic lasing spectra for both PCF lengths. As expected, the longer fiber led to a shift of

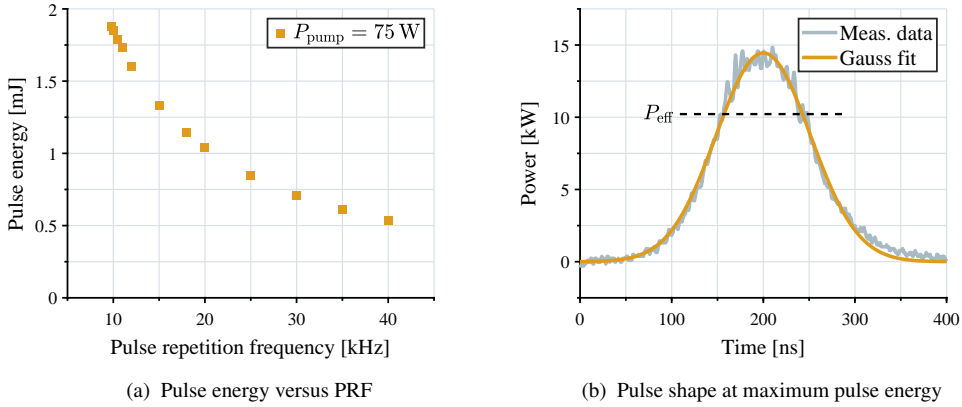


Figure 5.9: Measured pulse characteristics for the 7 m PCF during pulse energy scaling at 2050 nm. A maximum pulse energy of  $\sim 1.9$  mJ was reached at pump power of 75 W and a PRF of 9.8 kHz. The nearly Gaussian pulse shape recorded at the maximum pulse energy has a FWHM pulse duration of  $\sim 121$  ns and a peak power of 14.5 kW.

the parasitic lasing oscillation to longer wavelengths, allowing higher energy storage before the gain was clamped. The parasitic lasing wavelengths of  $\sim 1927$  nm and  $\sim 1950$  nm for the 3 m and 7 m fibers, respectively, coincide well with the peaks of the modeled gain spectra in fig. 5.6a.

However, while the trend was correctly predicted, the quantitative performance fell short of the initial modeling (see fig. 5.7). Both the measured maximum pulse energy (1.9 mJ vs. 2.5 mJ) and peak power (14.8 kW vs. 21.2 kW) were lower than anticipated. This discrepancy suggests that the initial PCF model requires refinement, which will be addressed below.

The measured output spectra at maximum pulse energy and peak power of the 7 m PCF oscillator are shown in fig. 5.11. As expected for the longer interaction length, the high-resolution spectrum (fig. 5.11a) exhibits stronger broadening by SPM compared to the 3 m PCF. However, the linewidth remains remarkably narrow: the 3-dB linewidth is 110 pm, the 10-dB linewidth is 350 pm, and the 20-dB linewidth is 840 pm.

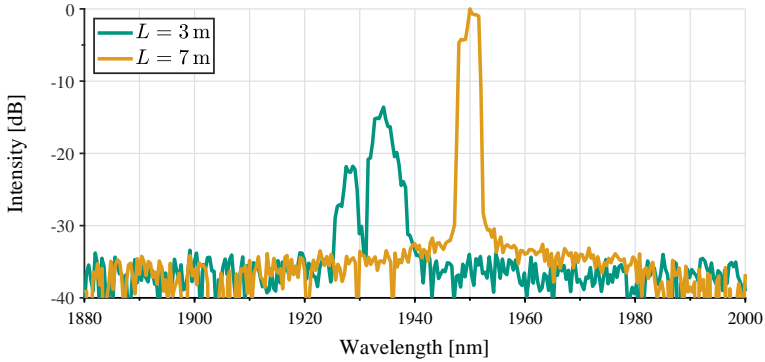


Figure 5.10: Parasitic lasing spectra for the 3 m and the 7 m PCF oscillators measured with a resolution of 2 nm. Stronger reabsorption in the longer fiber red-shifts the parasitic lasing spectrum.

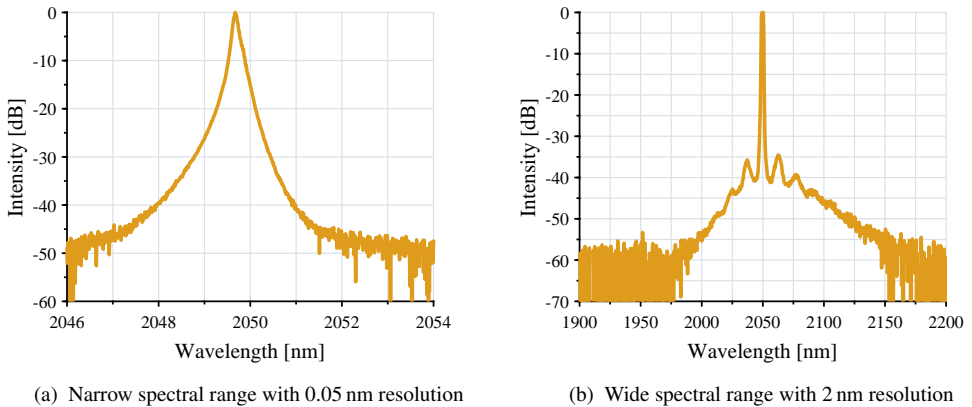


Figure 5.11: Output spectra of the 7 m PCF oscillator measured at maximum pulse energy and peak power. The 10-dB linewidth is  $\sim 350$  pm. The MI peaks are shifted by  $\pm 13$  nm from the central laser line and have negligible power content ( $< 0.4\%$ ).

The wide-range spectrum (fig. 5.11b) shows more pronounced MI peaks than for the 3 m fiber. However, the peaks are still  $\sim 35$  dB below the central peak and have negligible power content. More than 99.6% of the total power resides within a  $\pm 2$  nm band around the  $\sim 2049.7$  nm laser line. The MI peaks are shifted by  $\pm 13$  nm from this central wavelength, which is consistent with the slightly lower peak power compared to the 3 m fiber.

Overall, the 7 m PCF oscillator demonstrates an excellent trade-off between high pulse energy, peak power and a narrow linewidth with negligible nonlinear effects. Although the initial performance prediction was not fully met, these results provide direct experimental evidence for a successful optimization guided by the analysis of reabsorption and MI. A further increase in fiber length would probably not bring a benefit anymore, because nonlinear effects would start to become noticeable while the pulse energy enhancement would diminish.

### **Model Refinement: Impact of Propagation Loss**

The deviation between the initial prediction and the 7 m PCF experiment suggests that the model requires refinement. A likely cause for this discrepancy is the assumption of standard propagation losses. The initial model used  $\alpha \approx 0.13$  dB/m, a value typical for conventional  $\text{Tm}^{3+}$ -doped fibers [224]. However, the guiding mechanism in the photonic crystal cladding is intrinsically leaky and the required low NA that ensures single-mode operation makes the guiding more sensitive to micro- and macro-bending losses. The bending radius of 20 cm used in the experiment is on the lower end of the 20–25 cm range recommended by the manufacturer [231]. Furthermore, the critical bending radius in a PCF is inversely proportional to the wavelength squared (see eq. (2.208)). The long operating wavelength of 2050 nm might therefore suffer from higher propagation losses. For these reasons, it is justified to consider higher propagation losses for modeling the PCF.

Figure 5.12 shows the recalculated modeling results for an adapted higher propagation loss of 0.3 dB/m. This higher loss leads to a stronger performance penalty for longer fiber lengths and therefore to a better—though still not perfect—alignment with the experimental results. For the 7 m PCF length, the adapted model yields a maximum pulse energy of  $\sim 2.2$  mJ, a pulse duration of  $\sim 111$  ns, and a peak power of  $\sim 19.1$  kW. While assuming even higher propagation losses would force a perfect match in the modeled pulse characteristics, it would not be a realistic choice, as the measured efficiency of the 7 m PCF did not drop substantially compared to the shorter fiber. The value of 0.3 dB/m represents a reasonable estimate based on the observed performance.

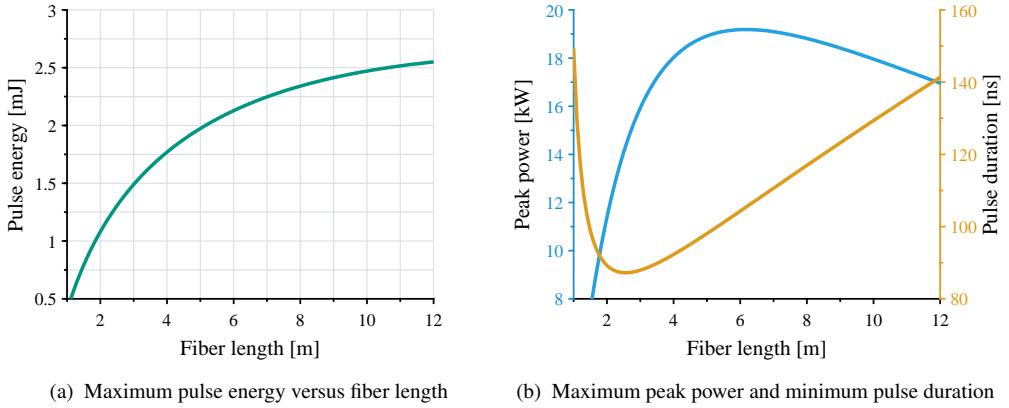


Figure 5.12: Calculated pulse performance versus the fiber length at an operating wavelength of 2050 nm, assuming higher propagation losses of 0.3 dB/m in the PCF.

Adopting the higher propagation loss of 0.3 dB/m results in a change in the calibrated intrinsic PCF properties. The calibration yielded slightly updated values of  $E_{\text{sat}}(2050 \text{ nm}) \approx 1.19 \text{ mJ}$ ,  $\sigma_e(2050 \text{ nm}) \approx 1.06 \cdot 10^{-25} \text{ m}^2$ ,  $R_{\text{paras}} \approx -44.5 \text{ dB}$ , and  $\langle N \rangle \approx 7.5 \cdot 10^{25} \text{ m}^{-3}$ . This new doping concentration corresponds to 1 wt.%, which is more consistent with the 1.1 wt.% reported in other work on this fiber [105], providing support for this adaptation.

To further validate the model refinement, the ASE spectra were re-examined using these updated parameters, as shown in fig. 5.13. The re-calibrated full spectroscopic cross sections are shown in fig. 5.13a, and the re-calculated ASE spectra are compared with the measured spectra for the 3 m and 7 m PCF in fig. 5.13b. Crucially, the ASE spectrum calculated with the refined model coincides even better with the measured 3 m PCF data. Furthermore, the ASE spectrum measured from the 7 m PCF is also modeled with remarkable accuracy. This excellent match for both fiber lengths provides evidence that the assumption of a higher propagation loss improved the modeling accuracy.

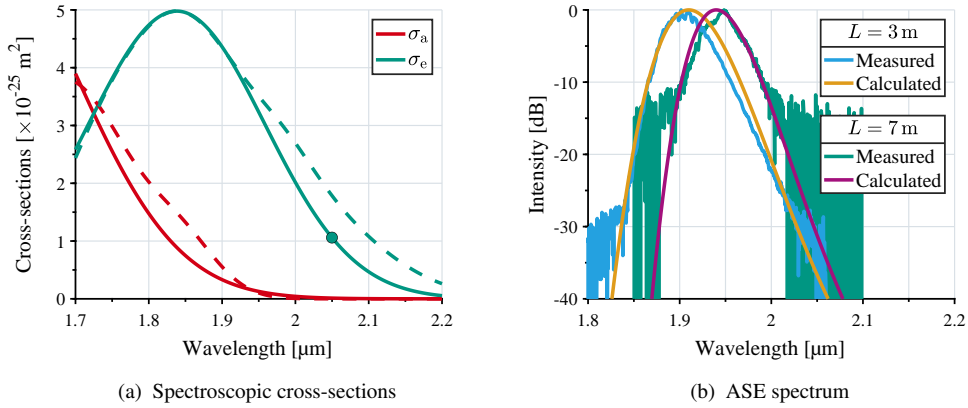


Figure 5.13: Calibrated spectroscopic cross-sections of the PCF and modeling of the ASE spectrum with adapted propagation losses of 0.3 dB/m. With the assumption of higher propagation losses, the emission cross-section at 2050 nm becomes lower compared to fig. 5.1b. The fitted ASE spectra show an even better agreement with the measured spectra than in fig. 5.5b.

## 5.2.4 Power Scaling of the Q-switched Photonic Crystal Fiber Oscillator

Scaling of the average output power was investigated for both fiber lengths. Each configuration was operated at a constant PRF while the pump power was increased until parasitic lasing occurred.

Figure 5.14a shows the results for the 3 m PCF oscillator operated at a PRF of 75 kHz. The fiber laser reached a maximum average output power of 104 W at a launched pump power of 252 W with a slope efficiency of 45.9%. At this power level, the pulse energy was 1.4 mJ, the pulse duration was 102 ns, and the peak power 12.9 kW ( $P_{\text{eff}} \approx 9.1$  kW). The recorded pulse shape is shown in the inset of fig. 5.14a. Further scaling of power and pulse energy by increasing the pump power at this PRF was limited by the onset of parasitic lasing.

The results for power scaling of the 7 m PCF oscillator are shown in fig. 5.14b. At a PRF of 60 kHz, the pump power was increased to 288 W, where an average output of 114 W and a pulse energy of 1.9 mJ were reached, before parasitic lasing limited a further increase. The slope efficiency of 43.5% measured in this experiment was slightly lower compared to 3 m PCF due to higher propagation losses over the longer fiber. The pulse shape recorded at maximum

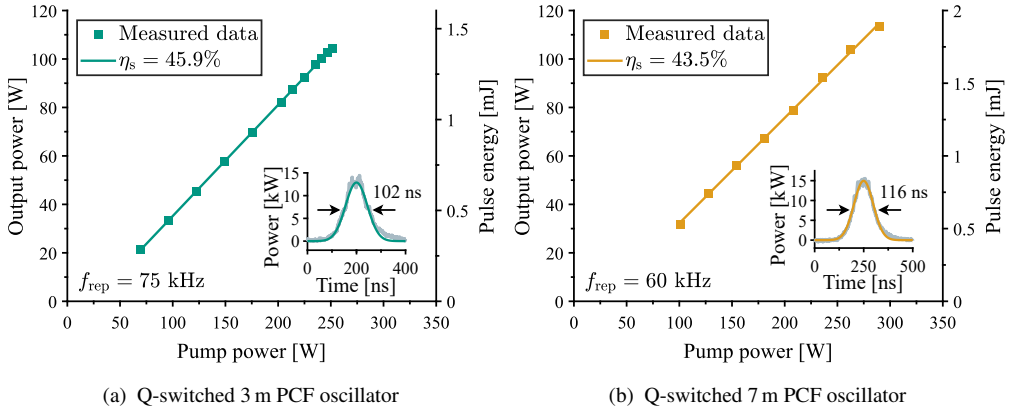


Figure 5.14: Power scaling of the Q-switched PCF oscillator for 3 m and 7 m fiber length. Both configurations delivered average output powers  $> 100$  W. Despite the challenging heat load in the free-space oscillators, the high-power operation achieved comparable pulse energies as at lower average power. This is attributed to the gain overshoot at high pump powers.

average power and pulse energy had an FWHM pulse duration of 116 ns, and a peak power of 15.4 kW (see inset in fig. 5.14b). The effective power was 10.9 kW.

Remarkably, both PCF oscillators largely maintained their maximum pulse energies even when scaled over 100 W of average output power. For the 3 m PCF, the high-power pulse energy limit of 1.4 mJ was only slightly below its 1.5 mJ low-power maximum, and for the 7 m PCF, the maximum pulse energy was the same (1.9 mJ) in both power regimes. Operating a free-space oscillator at such high-power levels is challenging, as it is generally accompanied by detrimental thermal effects: mechanical drift and thermal lensing can cause significant misalignment in the cavity resulting in a degradation of the cavity Q-factor, while precise re-alignment is hardly possible at these power levels. This thermally-induced increase in cavity losses is particularly critical for Q-switched oscillators, as it reduces the efficiency of energy extraction during the high Q-state.

The fact that the generated pulse energies remained high despite these challenges suggests that the high-power regime also comes with a compensating positive effect: the enhanced gain overshoot at high pump powers. Strong evidence for this effect was found especially in the results for the 7 m PCF. At a high pump power of 288 W, the same maximum pulse energy was reached as for operation in the lower power regime, but the measured pulse duration was

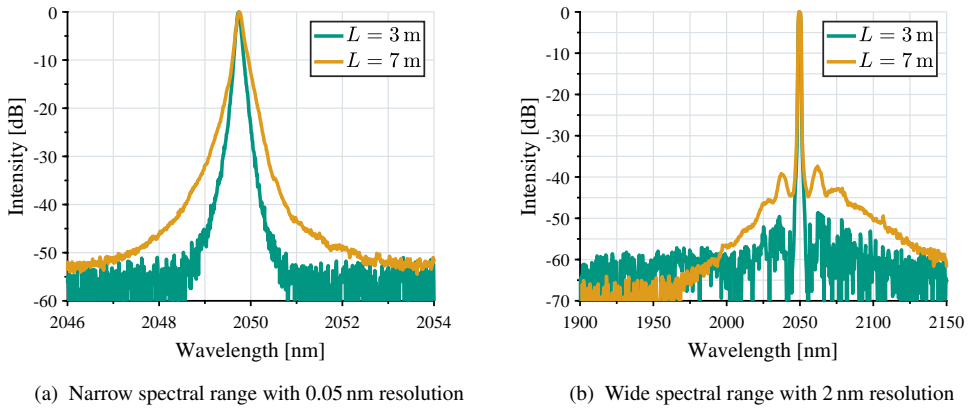


Figure 5.15: Output spectra of the 3 m and 7 m PCF oscillators measured at maximum average output power, pulse energy, and peak power. The spectra in high-power operation are largely identical to the low power operation. The 10-dB linewidths are 220 pm and 340 pm for the 3 m and 7 m PCFs, respectively.

shorter (116 ns vs. 121 ns). This observation implies that a higher initial gain was reached in the high-power regime. The potential enhancement in pulse energy then dissipated into the higher resonator losses due to thermal misalignment.

Finally the output spectra were measured under high-power conditions, as shown in fig. 5.15. The output spectra at maximum average output power and pulse energy are largely identical to those measured in the lower-power regime, because nonlinear spectral broadening depends on peak power, not on average power. The measured 10-dB linewidths were 220 pm for the 3 m PCF and 340 pm for the 7 m PCF. The stronger effect of MI in the longer fiber is again clearly visible in fig. 5.15b, but their power content was still negligible ( $< 0.5\%$ ). Excellent spectral purity was maintained even at average output powers  $> 100$  W.

## 5.3 Conclusion

The investigation of the  $\text{Tm}^{3+}$ -doped PCF successfully identified the specific challenges that hindered its previous application in high-energy pulsed lasers. The primary factor was found to be a significantly lower emission cross-section at the desired long operating wavelengths  $> 2\ \mu\text{m}$  compared to conventional  $\text{Tm}^{3+}$ -doped aluminosilicate fibers. This characteristic is likely due to fluorine co-doping used to lower the refractive index in the PCF core. As a result,

the intrinsically lower gain-per-length at long wavelengths makes the generation of high pulse energies in this spectral range a particular challenge. In addition, the analysis indicated that these PCFs suffer from higher propagation losses than conventional fibers.

This work demonstrated that these intrinsic constraints of the PCF can be overcome through a strategic design that was guided by the analysis method developed in chapter 4. By employing a longer fiber length of 7 m, the effect of reabsorption was successfully leveraged to red-shift the gain spectrum and therefore compensated for the weak emission characteristic at long wavelengths. The resulting increase of the maximum initial gain enhanced the extractable pulse energy at 2050 nm and directly proved the proposed optimization principle.

The optimized Q-switched PCF oscillator sets a new benchmark for pulsed 2  $\mu\text{m}$  fiber lasers. It successfully unifies high pulse energy (1.9 mJ), high average power ( $> 100$  W), nearly diffraction-limited beam quality ( $M^2 \sim 1.3$ ), and excellent spectral purity (10-dB linewidth  $< 350$  pm) at a long emission wavelength of 2050 nm. This performance almost doubles the previous state-of-the-art pulse energy from a fiber laser operating beyond 2  $\mu\text{m}$  with nearly diffraction-limited beam quality.

These results establish the  $\text{Tm}^{3+}$ -doped PCF as a highly promising platform for nonlinear frequency conversion into the mid-IR by pumping a ZGP OPO. The flexible PCF combines two crucial features: a larger fiber core compared to conventional LMA fibers and the use of longer fiber lengths compared to rigid LPF rods by coiling. This unique combination enables pushing the pulse energy limitations in fiber lasers while maintaining spectral purity at long emission wavelengths. However, to achieve a substantial improvement in conversion efficiency for fiber laser-pumped ZGP OPOs, which demands high intensity in all domains (spatial, spectral, and temporal), one critical limitation remains. The intrinsically low gain-per-length of the PCF at the required long emission wavelengths resulted in relatively long pulse durations of  $\sim 116$  ns. Consequently, the effective power of  $\sim 10.9$  kW was not substantially higher than in previous LMA-based systems (see table 2.2). Within the constraints of a Q-switched oscillator, the pulse duration is fundamentally linked to the gain-per-length, hindering further increases in the temporal power density.

To address this final challenge and fully exploit the high-energy storage capacity of the PCF, a different laser architecture is required that decouples the temporal pulse shape from the gain medium. This directs the focus to a master oscillator power amplifier (MOPA) approach, where

the pulse profile can be actively tailored to maximize the temporal power density [181, 182]. The implementation of the  $\text{Tm}^{3+}$ -doped PCF in an actively pulse-shaped amplifier configuration represents the logical conclusion for an optimal OPO pump source. The development of a PCF MOPA is the subject of subsequent work.

# 6 Conclusion and Outlook

## 6.1 Thesis Summary

This thesis investigated the pulse energy limits in  $\text{Tm}^{3+}$ -doped fiber lasers. A detailed analysis of the fundamental limiting mechanisms based on experimental data yielded a general framework for the quantitative modeling of these systems. This not only has refined the understanding of nanosecond-pulsed  $\text{Tm}^{3+}$ -doped fiber lasers, but also identified actionable design strategies to overcome previous performance barriers. Following these strategies, this work culminated in the experimental demonstration of a  $\text{Tm}^{3+}$ -doped photonic crystal fiber (PCF) laser that successfully set a new benchmark for 2  $\mu\text{m}$  nanosecond-pulsed fiber lasers.

The work began with a comprehensive review of the literature. A detailed overview of optical fundamentals, laser physics, and fiber laser design concepts established a solid foundation upon which the approach of this work was developed. From reviewing the publications on nanosecond-pulsed  $\text{Tm}^{3+}$ -doped fiber lasers and fiber-laser-pumped  $\text{ZnGeP}_2$  (ZGP) optical parametric oscillator (OPO), the requirements and limitations for pulse energy scaling and efficient mid-IR generation were synthesized. It was found that the spatial, temporal, and spectral output characteristics are influenced by various parameters in the laser design, each having competing effects on the overall performance. Navigating these parameters requires a quantitative analysis that allows for systematic laser development.

The approach was then focused by the experimental investigation of a Q-switched fiber oscillator and its application to pump a ZGP OPO. This experiment revealed the central conflicts between spatial, temporal, and spectral requirements on the fiber laser pump source for efficient nonlinear conversion. To mitigate an efficiency reduction by spatial walk-off, a large pump spot size is required, while a high intensity well above the OPO threshold must be ensured simultaneously.

This demands a high temporal power density, characterized by a high pulse energy and peak power from the pump laser. However, scaling of the peak power causes nonlinear effects in the fiber laser, resulting in a degradation of its output spectrum, preventing efficient conversion in the OPO. Thus, the central challenge was identified: achieving high pulse energies and peak powers from a fiber laser while maintaining high spectral purity.

The experiments on the Q-switched fiber oscillator also identified the two primary limitations for pulse energy scaling in the  $\text{Tm}^{3+}$ -doped fiber lasers: the limitation of the maximum achievable gain by parasitic lasing, and the intensity-dependent spectral degradation by modulation instability (MI). At the same time, this investigation indicated some mechanisms that can potentially enhance the maximum extractable pulse energy. First, the dynamic gain overshoot above the parasitic lasing threshold results in a higher maximum initial gain at higher pump powers. Second, reabsorption along the fiber can suppress parasitic lasing at short wavelengths, leading to an increase in energy storage capacity before the parasitic lasing threshold is reached. To effectively utilize these effects, an optimal fiber laser design must find a balance between maximizing gain and mitigating severe fiber nonlinearities. This requires a quantitative analysis of how distinct design parameters influence both the achievable laser gain and the detrimental parametric gain for MI.

To enable such a quantitative analysis, a semi-analytical modeling approach was developed that offers a rapid evaluation of the gain characteristics and impact of MI for a wide parameter space. The analysis of the maximum achievable gain focuses on the limitation imposed by parasitic lasing. Other potential gain limitations, such as amplified spontaneous emission or pump bleaching, were found to be much less restrictive and were therefore not relevant under the considered operating conditions.

For the analysis of MI, a novel adaptation of the parametric gain equation in oscillators was proposed. The new expression was based on the empirical observation that the parametric gain peaks in an oscillator do not spectrally coincide with the standard expression for an amplifier. This was attributed to the fixed phase relationship of the mode field in an oscillator, resulting in a global phase-matching condition that is governed by the intra-cavity peak power instead of the locally varying power. The proposed equation for the oscillator-specific parametric gain showed good agreement with measured output spectra, but requires further, dedicated experimental validation in the future.

The developed modeling approach relies on a calibration procedure, in which the investigated  $\text{Tm}^{3+}$ -doped fiber is examined in pulsed operation to determine its gain saturation characteristics. From this, the intrinsic fiber parameters are determined, including doping concentration, spectroscopic cross-sections, and parasitic reflections. Knowing these fiber characteristics allows for predicting the pulse performance by exploring a wide range of design parameters, such as fiber length, pump power, operating wavelength, and laser architecture. Furthermore, calculation of the parametric MI gain allows for evaluating at which peak power and fiber length the spectral degradation by MI becomes critical. Thus, the model provides a powerful tool for selecting fiber and laser design in the development of a nanosecond-pulsed  $\text{Tm}^{3+}$ -doped fiber laser that combines high pulse energy with spectral purity.

The resulting analysis revealed that pulse energy scaling in conventional  $\text{Tm}^{3+}$ -doped large-mode-area (LMA) fibers reached an ultimate limit. Although an optimal design can provide an ideal trade-off between gain enhancement and nonlinear effects, their core diameters of 20–25  $\mu\text{m}$  are ultimately too small to achieve substantial improvements in pulse performance while maintaining spectral purity. Consequently, to generate nanosecond pulses with multi-millijoule pulse energy and narrow linewidth, a fiber with a significantly larger core was required. This motivated the investigation of a large-mode-area  $\text{Tm}^{3+}$ -doped PCF.

The selected  $\text{Tm}^{3+}$ -doped PCF offered a promising combination of crucial features. First, it has a significantly larger core diameter of  $\sim 50 \mu\text{m}$  compared to conventional LMA fibers, enabling higher energy storage and reduced nonlinear effects. Second, in contrast to rigid large pitch fiber (LPF) rods with even larger cores, the investigated PCF is flexible. This allows for using a longer fiber length by coiling, which is critical for achieving high gain at long emission wavelengths. However, despite this potential, previous work on nanosecond-pulsed 50  $\mu\text{m}$  PCFs did not surpass the pulse energies from standard LMA fibers [38, 39].

From the experimental characterization of the  $\text{Tm}^{3+}$ -doped PCF in a Q-switched oscillator configuration, the intrinsic fiber parameters were determined. This identified the primary challenge for pulsed operation of the PCF at long wavelengths. The analysis revealed a weaker emission cross section at long wavelengths compared to standard fibers, resulting in an inherently lower gain in the spectral range beyond 2  $\mu\text{m}$ . Using the developed model, it was found that this intrinsic constraint of the PCF can be effectively compensated for by employing a longer fiber length. A long PCF length of 7 m was predicted to enhance the maximum gain at long wavelengths by leveraging the effect of reabsorption, while the large PCF core still ensures

weak nonlinear spectral broadening. This strategy was successfully validated in the subsequent experiment.

The Q-switched PCF generated Gaussian-shaped 116 ns pulses, with a pulse energy of 1.9 mJ and a peak power of 15.4 kW, while maintaining a narrow 10-dB linewidth of 340 pm at a long emission wavelength of 2050 nm. The pulsed fiber laser was operated at a high average output power of 114 W and delivered close to diffraction-limited beam quality ( $M^2 < 1.3$ ). These results almost doubled the previous state of the art in pulse energy from a nanosecond-pulsed fiber laser with nearly diffraction-limited beam quality at a wavelength longer than 2  $\mu\text{m}$ . By successfully addressing this spectral range, where atmospheric transmission is high and the nonlinear crystal ZGP exhibits low background absorption, this work opens up new opportunities for free-space applications and nonlinear frequency conversion.

## 6.2 General Fiber Laser Design Approach

The analyses presented in this thesis establish a comprehensive framework for understanding, modeling, and optimizing high-energy nanosecond-pulsed  $\text{Tm}^{3+}$ -doped fiber lasers. The developed model provides a powerful tool to guide the design process for the development of pulsed fiber lasers. By applying this framework, the  $\text{Tm}^{3+}$ -doped PCF was identified to be able to overcome the limitations of conventional LMA fibers and thus serves as a highly promising platform for pumping ZGP OPOs.

The methodology developed and validated throughout this work can be synthesized into a general step-by-step procedure for designing nanosecond-pulsed  $\text{Tm}^{3+}$ -doped fiber lasers:

### Step 1: Initial Experimental Characterization

- The selected  $\text{Tm}^{3+}$ -doped fiber is initially characterized in a basic pulsed configuration (e.g. a Q-switched oscillator or pulsed amplifier)
- The pulse energy is scaled until the fundamental limit is reached, typically set by the onset of parasitic lasing.
- The maximum pulse energy and the corresponding temporal pulse profile are measured.

**Step 2: Calibration of Intrinsic Fiber Parameters**

- Using the measured pulse characteristics at the pulse energy limit, the gain saturation characteristics ( $E_{\text{sat}}$ ,  $G_{i,\text{max}}$ ,  $G_{f,\text{min}}$ ) at the operating wavelength are calculated by solving the relevant equations that govern the pulse dynamics, e.g., the Q-switching master equation (eq. (2.261)) for an oscillator or the Frantz-Nodvik equation (eq. (2.269)) for an amplifier.
- These calibrated gain values are used, along with the experimentally observed parasitic lasing wavelength, to determine the intrinsic fiber parameters: the spectroscopic cross-sections  $\sigma_a(\lambda_0)$ ,  $\sigma_e(\lambda_0)$ , the doping concentration  $\langle N \rangle$ , and the parasitic reflectivity  $R_{\text{paras}}$  of the fiber end termination (e.g. angled cleave, splice, or endcap).
- This yields a self-consistent spectral gain model for the specific fiber under investigation, which can be verified by comparing its predicted ASE spectrum against experimental measurements.

**Step 3: Optimization Analysis and Performance Prediction**

- The calibrated model can rapidly simulate the fiber laser pulse performance across a wide parameter space. This includes parameters such as fiber length, pump power, operating wavelength, resonator design (e.g. mirror reflectivities), or input pulse energy.
- This analysis identifies the optimal operating conditions accounting for the trade-off between gain optimization and nonlinear effects. By predicting the maximum achievable pulse performance (pulse energy, peak power, pulse duration) for the investigated fiber, it provides a basis for selecting fiber and laser design.

**Step 4: Experimental Realization and Model Refinement**

- Based on the analysis, an optimized setup can be realized and tested experimentally.
- The model predictions are validated against the measured performance. Discrepancies can provide insights into effects not considered in the analysis (e.g. thermal effects or additional loss mechanisms). If necessary, the model can be refined using this additional experimental data.

Following this strategy, the specific characteristics and challenges of the  $\text{Tm}^{3+}$ -doped PCF were identified and accurately modeled. This led to the experimental demonstration of the highest pulse energies from a nanosecond-pulsed fiber laser operating at wavelengths  $> 2 \mu\text{m}$  with nearly diffraction-limited beam quality.

The model provides a basis for future developments of complex  $\text{Tm}^{3+}$ -based  $2 \mu\text{m}$  fiber laser systems. Although this work primarily focused on the analysis and optimization of Q-switched oscillators, the established framework should be broadly applicable to other fiber laser architectures. The fundamental mechanisms that govern the output characteristics are the same for pulsed amplifiers as for oscillators: the limitation of the maximum initial gain by parasitic lasing and the intensity-limitation by nonlinear effects. The main differences for fiber amplifiers lie in the distinct parasitic cavity defined by reflections at end facets, splice connections, or components from both sides, as well as the different phase matching consideration for MI. Using the proposed calibration procedure, different  $\text{Tm}^{3+}$ -doped fibers can be characterized and evaluated for their suitability and optimal operating conditions. Thus, the design of complex  $\text{Tm}^{3+}$ -doped fiber laser systems can be supported from scratch by the developed model. Such a guided development procedure has not yet been tested, but could provide further validation and possible refinement of the analysis framework, thereby contributing to the general understanding of pulsed fiber lasers in the future.

## 6.3 Implementation of a Photonic Crystal Fiber Amplifier

This work was part of a larger project with the objective of developing a fiber laser pump source for high-power mid-IR generation from a ZGP OPO. As detailed throughout this thesis, an optimal pump laser for efficient nonlinear conversion must satisfy critical requirements. It must simultaneously deliver high spatial intensity (high average output power with nearly ideal beam quality), high temporal power density (high pulse energy combined with high effective power), and high spectral power density (narrow linewidth at a long emission wavelength).

The analysis and optimization of a Q-switched fiber oscillator demonstrated that by employing a large-mode-field-area PCF, the pulse energy constraints in fiber lasers can be overcome. However, while the optimized Q-switched PCF oscillator successfully combined a high pulse energy

of 1.9 mJ with the spatial and spectral requirements, it fell short in terms of temporal power density. The PCF oscillator produced relatively long pulses of  $\sim 116$  ns, resulting in a limited effective power of  $\sim 10.9$  kW, which was shown to be intrinsically linked to the challenging emission characteristics of the  $\text{Tm}^{3+}$ -doped PCF at long wavelengths. This constraint cannot be solved with a Q-switched oscillator architecture, where the pulse dynamic is fundamentally governed by the gain medium. Therefore, a master oscillator power amplifier (MOPA) architecture is required that enables a free choice of the temporal pulse shape.

In parallel to the investigations of this work, an actively pulse-shaping fiber MOPA was developed by Dominik Lorenz. This three-stage all-in-fiber MOPA is capable of delivering arbitrary shaped, linearly polarized pulses with a pulse energy up to  $500 \mu\text{J}$  and an average output power of  $50$  W, ideally suited for pumping a ZGP OPO [232]. To boost these output characteristics even further, the  $\text{Tm}^{3+}$ -doped PCF was implemented as the final power amplifier stage of the actively pulse shaped MOPA. This joint first-author effort combined an advanced fiber laser system with the enhanced pulse energy scaling capabilities of the PCF. The results have been published in a journal article and three conference contributions [179, 233, 234].

The approach of an actively pulse shaped MOPA offers several distinct advantages: First, it allows for freely tailoring the pulse shape to maximize the temporal power density; Second, it separates signal generation from power amplification, simplifying average power scaling and enhancing stability; Third, fiber amplifiers generally possess higher parasitic lasing thresholds compared to oscillators, enabling a higher maximum gain and improved energy extraction; Finally, the architecture is readily implementable into a robust all-in-fiber system, even though the PCF amplifier was initially tested in a free-space configuration.

The PCF amplifier generated close to rectangular-shaped  $2.07$  mJ pulses, with a pulse width of  $49$  ns, and a peak power of  $52$  kW at an average output power of  $207$  W with nearly diffraction-limited beam quality ( $M^2 \sim 1.1$ ). The high effective power of  $42$  kW—an almost fourfold increase compared to the oscillator—combined with excellent spectral purity (10-dB linewidth of  $390$  pm) at a long emission wavelength of  $2048$  nm makes this laser ideally suited for highly-efficient nonlinear frequency conversion.

Finally, the PCF MOPA was applied to pump a mid-IR ZGP OPO to generate high-power coherent radiation in the  $3\text{--}5 \mu\text{m}$  range. This experiment yielded  $25.8$  W of mid-IR average power and  $\sim 1$  mJ mid-IR pulse energy with a record optical-to-optical conversion efficiency of  $68\%$ . To the best of our knowledge, this represents not only the highest output power and

pulse energy reported from a fiber-laser-pumped ZGP OPO but also the highest conversion efficiency for any watt-level ZGP OPO system to date, surpassing even bulk solid-state laser pumped configurations.

This record-breaking performance was enabled by two key improvements to the fiber laser pump source: First, the nearly rectangular pulse shape of the MOPA system provided a higher effective power than with Gaussian pulses and led to a fast mid-IR build-up time in the OPO cavity. Second, a substantial enhancement of maximum pulse energy and effective power was achieved by employing the  $\text{Tm}^{3+}$ -doped PCF, which allowed for a larger pump spot, mitigating the effect of spatial walk-off. By combining these optimization strategies, this collaborative work successfully unified high intensities in the spatial, temporal, and spectral domain within an integrable fiber laser pump source ideally suited for highly efficient nonlinear conversion into the mid-IR.

For these initial results, the PCF MOPA was operated at only 37.6 W of average output power. Since this laser is capable of delivering more than 200 W of pump power, this highlights the immense potential of this approach, paving the way for a future  $> 100$  W mid-IR source pumped by a fiber laser.

## 6.4 Comparison with the State of the Art

### High-Energy Nanosecond-Pulsed $\text{Tm}^{3+}$ -doped fiber lasers

The nanosecond-pulsed  $\text{Tm}^{3+}$ -doped fiber lasers developed in this thesis and in the subsequent collaborative work represent milestones in  $2\ \mu\text{m}$  fiber laser technology. To evaluate the significance of these experimental results, they are compared with the state of the art. In sec. 2.4.3, publications on high-energy nanosecond-pulsed  $\text{Tm}^{3+}$ -doped fiber lasers released prior to the beginning of this work in 2021 were reviewed (see table 2.2). Analogous to that table, table 6.1 lists the relevant publications to date. The rows containing the fiber lasers developed in this thesis and the subsequent collaborative work are highlighted in gray.

The table is organized into three categories based on the fiber type used in the oscillator or final amplifier stage:  $20\text{--}25\ \mu\text{m}$   $\text{Tm}^{3+}$ -doped LMA fibers,  $50\ \mu\text{m}$  flexible  $\text{Tm}^{3+}$ -doped PCFs, and  $80\ \mu\text{m}$  non-flexible LPFs. All listed publications reported nearly diffraction-limited beam quality.

Table 6.1: Overview of high-energy nanosecond-pulsed  $\text{Tm}^{3+}$ -doped fiber lasers with close to diffraction-limited beam quality.

$\lambda_c$	Architecture <sup>1</sup>	Lin. polarization	$\Delta\lambda_{10\text{-dB}}$	$E_{\text{pulse}}$	$P_{\text{eff}}$	$P_{\text{avg}}$	$\eta_s$	Year
20–25 $\mu\text{m}$ $\text{Tm}^{3+}$ -doped LMA fiber								
1950 nm	AF - DS MOPA	Seed lin. polarized	1 nm	1 mJ	9.2 kW	13 W	30 %	2014 [182]
1970 nm	AF - CM MOPA	No	1 nm	750 $\mu\text{J}$	8.5 kW	150 W	37 %	2016 [193]
1977 nm	FS - QS MOPA	Seed PER > 14 dB	4 nm	700 $\mu\text{J}$	3.7 kW	14 W	47 % <sup>2</sup>	2018 [192]
2024 nm	QS Oscil.	PER $\sim$ 16 dB	0.5 nm	575 $\mu\text{J}$	5.9 kW	23 W	33 %	2015 [194]
2043 nm	AF - GS MOPA	No	-	1 mJ	3.2 kW	50 W	44 %	2025 [235]
2044 nm	FS - QS Oscil.	No <sup>2</sup>	$\sim$ 3 nm	810 $\mu\text{J}$	13.1 kW	17 W	35 %	2021 [217]
2048 nm	AF - DS MOPA	PER > 20 dB	380 pm	510 $\mu\text{J}$	10.2 kW	51 W	43 %	2024 [232]
2050 nm	AF - GS MOPA	Seed PER > 16 dB	0.4 nm	1 mJ	6.8 kW	41 W	42 %	2015 [191]
50 $\mu\text{m}$ $\text{Tm}^{3+}$ -doped PCF								
1950 nm	FS - QS Oscil.	PER > 18 dB	-	435 $\mu\text{J}$	6.3 kW	4.4 W	26 %	2012 [38]
1980 nm	FS - QS MOPA	Yes	1.8 nm	840 $\mu\text{J}$	78 kW	3.4 W	7 %	2014 [39]
2048 nm	H - DS MOPA	PER > 23 dB	390 pm	2.1 mJ	42 kW	207 W	45 %	2025 [179]
2050 nm	FS - QS Oscil.	No	340 pm	1.9 mJ	10.9 kW	114 W	44 %	2024 [223]
80 $\mu\text{m}$ $\text{Tm}^{3+}$ -doped rod-type LPF								
1889 nm	FS - QS MOPA	No	$\sim$ 2.5 nm	7 mJ	49 kW	140 W	77 % <sup>2,4</sup>	2024 [236]
1900 nm	FS - QS Oscil.	No	50 nm	2.4 mJ	69 kW	33 W	21 %	2013 [195]
1965 nm	FS - QS MOPA	No	2.6 nm	6.4 mJ	660 kW	6.4 W	9 %	2013 [196]

<sup>1</sup> AF: All-in-fiber, FS: Free-space, H: Hybrid (AF & FS), DS: Diode-seeded, CM: CW-modulated, QS: Q-switched, GS: Gain-switched

<sup>2</sup> with respect to absorbed pump power

<sup>3</sup> maximum pulse energy of 630  $\mu\text{J}$  when linearly polarized

<sup>4</sup> in-band pumped at 1692 nm

In the category of conventional LMA fibers, three notable publications have appeared since 2021. First, the Q-switched LMA fiber oscillator described in sec. 3.1 was published [217]. This laser delivered  $\sim$  41 ns Gaussian-shaped pulses with a high pulse energy of  $\sim$  810  $\mu\text{J}$  and a high effective power of 13.1 kW at a long emission wavelength of 2044 nm. As discussed in chapter 4, this pulse performance was close to the maximum that can be achieved from a 20  $\mu\text{m}$  fiber core when spectral purity is a concern, as further scaling of the pulse energy and peak power would result in significant nonlinear spectral broadening.

Subsequently, the three-stage all-in-fiber MOPA that was later used as the seed for the PCF amplifier was published [232]. Remarkably, although the pulse energy of this system was only 510  $\mu\text{J}$ , it delivered a high effective power of 10.2 kW thanks to its nearly rectangular pulse shape. This highlights the distinct advantage of the active pulse-shaping approach.

The most recent publication based on conventional LMA fibers was in 2025 by Ren et al. [235]. The all-in-fiber MOPA generated high pulse energies of 1 mJ, but with a long FWHM pulse duration of 186 ns. This resulted in a relatively low effective power of 3.2 kW, a trade-off necessary to mitigate severe nonlinear effects in the 25  $\mu\text{m}$  fiber.

Among the specialty fibers with larger core diameters, Lenski et al. demonstrated an approach in 2024 to enhance the average power scalability of 80  $\mu\text{m}$  LPF rods by employing in-band pumping [236]. Previous nanosecond-pulsed LPF systems suffered from low efficiencies due to low absorption over short fiber lengths and weak cross-relaxation rates at high inversion. The in-band pumping approach, realized by four combined Raman amplifiers providing 350 W of pump power at 1692 nm, resulted in a high slope efficiency of 77 % with respect to absorbed pump power. This high internal efficiency reduced thermal load and enabled a high average output power of 140 W. At this power level, the MOPA system generated a high pulse energy of 7 mJ with an effective power of 49 kW. However, because the short length of the LPF rod restricts the gain to short wavelengths, the MOPA operated at 1898 nm, which is not suitable for pumping a ZGP OPO.

To enable high-energy pulses at emission wavelengths longer than 2  $\mu\text{m}$ , this work focused on the employment of a 50  $\mu\text{m}$  flexible PCF. The Q-switched PCF oscillator described in chapter 5 was published in 2024 [223]. Compared to previous publications on 50  $\mu\text{m}$  PCFs, this work more than doubled the maximum pulse energy to 1.9 mJ while simultaneously achieving a long emission wavelength of 2050 nm with high spectral purity. This represented the highest pulse energy from a  $\text{Tm}^{3+}$ -doped fiber laser at wavelengths longer than 2  $\mu\text{m}$  with nearly diffraction-limited beam quality ( $M^2 < 1.3$ ). Furthermore, a significantly higher slope efficiency of 44 % was achieved compared to previous PCF systems, enabling a high average output power of 114 W.

These results were only surpassed by the subsequent collaborative work on the actively pulse-shaped PCF amplifier [179]. The PCF amplifier achieved an even higher maximum pulse energy of  $\sim 2.1$  mJ at a long emission wavelength of 2048 nm with high spectral purity. With a high slope efficiency of 45 %, it delivered the highest average output power of 207 W from a nanosecond-pulsed  $\text{Tm}^{3+}$ -doped fiber laser with nearly diffraction-limited beam quality. In addition, the active pulse-shaping approach enabled a substantial enhancement in effective power to 42 kW, representing an almost four-fold increase at wavelengths  $> 2$   $\mu\text{m}$ . With a high polarization extinction ratio of 23 dB, this is also the only linearly polarized source in the list that generates more than 1 mJ of pulse energy. Thus, the PCF MOPA successfully combined

high average power and excellent beam quality with high pulse energy, high effective power, and a narrow linewidth at a long emission wavelength, making it ideally suited for highly efficient nonlinear frequency conversion.

### **Fiber-Laser-Pumped ZGP OPOs**

The state of the art in high-power, fiber-laser-pumped ZGP OPOs is listed in table 6.2. This table is structured analogously to table 2.3, which was reviewed in sec. 2.5.3 and presented the publications prior to the beginning of this work in 2021. Since 2021, six notable publications have been added to the list, presented in chronological order in table 6.2. The publications resulting from this thesis and the subsequent collaborative work are again highlighted in gray.

First, there was the ZGP OPO pumped by the  $\text{Tm}^{3+}$ -doped LMA fiber oscillator presented in sec. 3.1 [218]. The high effective power of 8.3 kW delivered from the pump laser resulted in a significant improvement in nonlinear conversion efficiency to 39 % compared to previous systems. This initial success emphasized that enhancing the maximum pulse energy from fiber lasers unlocks great potential for efficient mid-IR generation and directly motivated the subsequent investigations on pulse energy scaling detailed in this thesis.

In the same year, Holmen et al. demonstrated the effectiveness of an alternative approach: pumping a ZGP OPO with a diode-seeded, actively pulse-shaped fiber MOPA [237]. The advantageous, nearly rectangular pump pulse shape yielded a further improvement in effective pump power to 10.2 kW. This resulted in the highest conversion efficiency of 59 % from a fiber-laser-pumped ZGP OPO at that time. The final power amplifier was based on a 25  $\mu\text{m}$   $\text{Ho}^{3+}$ -doped LMA fiber that enabled a long emission wavelength of 2108 nm, but also suffered from poor efficiency, limiting average power scalability of the fiber MOPA. The maximum average power of only 5 W from the fiber laser pump source resulted in 3 W of mid-IR power.

A similar MOPA approach was published shortly thereafter by Lorenz et al. in 2022 [238]. The crucial difference was the use of a 25  $\mu\text{m}$   $\text{Tm}^{3+}$ -doped LMA fiber in the final power amplifier stage. Although this led to a shorter emission wavelength of 2048 nm, the MOPA demonstrated improved power scalability. This resulted in a mid-IR output power of 8.1 W with a high conversion efficiency of 44 %. In later work, this MOPA system was further scaled in pulse

Table 6.2: Overview of fiber laser pumped ZGP OPOs.

Architecture*	Pump Laser				Mid-IR Output				
	$E_{\text{pulse}}$	$P_{\text{eff}}$	$\lambda_c$	$d_{\text{pump}}$	$P_{\text{out}}$	$E_{\text{pulse}}$	$\eta_{\text{oo}}$	$M^2$ (S/I)	Year
AF - GS MOPA	96 $\mu\text{J}$	2.1 kW	1995 nm	140 $\mu\text{m}$	0.66 W	22 $\mu\text{J}$	22 %	1.3/2.9	2008 [22]
AF - GS MOPA	127 $\mu\text{J}$	-	2000 nm	170 $\mu\text{m}$	2 W	50 $\mu\text{J}$	15.7 %	-	2008 [215]
AF - GS MOPA	160 $\mu\text{J}$	-	2044 nm	140 $\mu\text{m}$	3 W	50 $\mu\text{J}$	25 %	-/2.1	2012 [201]
FS - QS MOPA	840 $\mu\text{J}$	78 kW	1980 nm	335 $\mu\text{m}$	1.1 W	284 $\mu\text{J}$	28 %	-	2014 [39]
FS - QS Oscil.	500 $\mu\text{J}$	5.1 kW	2024 nm	350 $\mu\text{m}$	6.5 W	163 $\mu\text{J}$	32.5 %	-	2015 [194]
FS - QS Oscil.	340 $\mu\text{J}$	2.5 kW	2090 nm	300 $\mu\text{m}$	8.1 W	81 $\mu\text{J}$	24 %	-	2019 [213]
FS - QS Oscil.	590 $\mu\text{J}$	8.3 kW	2050 nm	300 $\mu\text{m}$	3.9 W	230 $\mu\text{J}$	39 %	1.9/2.1	2021 [218]
AF - DS MOPA	510 $\mu\text{J}$	10.2 kW	2108 nm	350 $\mu\text{m}$	3 W	300 $\mu\text{J}$	59 %	1.7/2.1	2021 [237]
AF - DS MOPA	366 $\mu\text{J}$	7.5 kW	2048 nm	325 $\mu\text{m}$	8.1 W	162 $\mu\text{J}$	44 %	2.2/2.0	2022 [238]
FS - QS Oscil.	627 $\mu\text{J}$	11.6 kW	2100 nm	325 $\mu\text{m}$	12.1 W	271 $\mu\text{J}$	43.3 %	2.2/2.0	2024 [226]
AF - DS MOPA	495 $\mu\text{J}$	10.1 kW	2048 nm	380 $\mu\text{m}$	11.1 W	277 $\mu\text{J}$	56 %	2.2/2.2	2024 [238]
H - DS MOPA	1.5 mJ	30.4 kW	2048 nm	600 $\mu\text{m}$	25.8 W	1.03 mJ	69 %	4.1/4.9	2025

\* AF: All-in-fiber, FS: Free-space, H: Hybrid, GS: Gain-switched, QS: Q-switched, DS: Diode-seeded

energy and average power, resulting in the demonstration of 11.1 W of mid-IR output power with a conversion efficiency of 56 % in 2024 [232].

Another important work was published in 2024 by Forster et al. [226]. A Q-switched fiber oscillator based on an 18  $\mu\text{m}$   $\text{Tm}^{3+}:\text{Ho}^{3+}$ -codoped LMA fiber was used as the pump source. This approach provided a high pump pulse energy of 627  $\mu\text{J}$ , resulting in a high effective power of 11.6 kW at a long emission wavelength of 2100 nm. These favorable pump laser characteristics led to a new record in mid-IR average power of 12.1 W from a fiber-laser-pumped ZGP OPO.

Finally, the two essential approaches of active pulse shaping and pulse energy enhancement in fiber lasers were combined, leading to the shared first-authorship publication of the PCF amplifier in 2025 [179]. The fiber laser provided nearly rectangular pump pulses with a 1.5 mJ pulse energy and an effective power of 30.4 kW. This enabled a substantially larger pump spot diameter of 600  $\mu\text{m}$  compared to previous fiber-laser-pumped ZGP OPOs. The larger pump spot mitigated the detrimental effects of spatial walk-off in the birefringent ZGP crystal while still providing a high peak fluence of  $\sim 1.06 \text{ J cm}^{-2}$  to operate well above the OPO threshold.

The achieved 25.8 W of mid-IR average output power and 1.03 mJ pulse energy represent the highest values reported from a fiber-laser-pumped ZGP OPO to date. Furthermore, the 69 %

conversion efficiency is the highest for any watt-level ZGP OPO, including those pumped by bulk solid-state lasers. The relatively high  $M^2$  values of 4.1 and 4.9 for signal and idler, respectively, were attributed to non-ideal mode coupling in the linear doubly-resonant OPO (DRO) cavity with planar mirrors, but could be improved in the future with an optimized cavity design. These results ultimately highlight the enormous potential of this fiber laser pump source and pave the way for a future  $> 100$  W coherent mid-IR source pumped by a fiber laser.

## 6.5 Outlook

This thesis has investigated and improved pulse energy scaling in  $\text{Tm}^{3+}$ -doped fiber lasers with a special focus on meeting the requirements for pump sources for nonlinear frequency conversion into the mid-IR. While this work achieved significant progress, it also provides a foundation for future investigations.

The developed semi-analytical model provides a comprehensive framework for characterizing  $\text{Tm}^{3+}$ -doped fibers in pulsed operation and can serve as a basis for future fiber laser designs. Some parts of the analysis, however, require further experimental validation, in particular the proposed new expression for modulation instability in oscillators. Dedicated experiments on pulsed fiber oscillators under different operating conditions can either confirm or refine the proposed theory. The current model for estimating the intra-cavity intensity distribution could be further enhanced by incorporating longitudinally-varying gain depending on the pump configuration (e.g. co-pumping, counter-pumping, bi-directional) and reflectivities of the resonator mirrors. Furthermore, the transverse intensity distribution might also have an impact on the phase-matching condition, which has not yet been considered.

The  $\text{Tm}^{3+}$ -doped PCF was shown to be an effective platform for pushing the pulse energy limits compared to conventional  $\text{Tm}^{3+}$ -doped LMA fibers. However, it was tested only in free-space configurations so far. Practical implementation of the PCF in a robust and reliable laser system requires integration into an all-in-fiber architecture. The most critical component for realizing such an all-in-fiber PCF laser is a mode field adapter from a standard LMA to the PCF, ideally combined with a tapered fiber bundle to couple pump light into the PCF air cladding. Such PCF pump and signal combiners have been successfully demonstrated for  $\text{Yb}^{3+}$ -doped PCFs as well as for  $\text{Tm}^{3+}$ -doped PCFs but are not yet commercially available

standard components [239–241]. The further development and improvement of these PCF components is therefore an essential prerequisite for integrated high-power PCF laser systems in the future.

The investigated  $\text{Tm}^{3+}$ -doped PCF itself was found to have challenging emission characteristics at long wavelengths, most likely due to its special doping composition. As discussed in sec. 2.3.2, the core of active PCFs is often co-doped with index-depressing elements such as fluorine to better match the index of the pure silica in the cladding. This compensates for the index-raising effect of the  $\text{Tm}^{3+}$ - and  $\text{Al}^{3+}$ -doping in the core and ensures that the guiding is primarily governed by the PCF microstructures. However, there are also alternative techniques to control the core index that could enable improved performance of  $\text{Tm}^{3+}$ -doped PCFs at long wavelengths. The stack-and-draw fabrication process allows for creating fine-structured core designs by placing doped silica rods alongside pure silica rods [138]. Another potential path for generating higher pulse energies at wavelengths beyond  $2\ \mu\text{m}$  might be the development of a  $\text{Tm}^{3+}:\text{Ho}^{3+}$ -codoped PCF. Advanced fiber design and manufacturing therefore remain key to performance improvements in future  $2\ \mu\text{m}$  fiber laser systems.

The collaborative work subsequent to this thesis has already demonstrated that an actively pulse shaped PCF amplifier is a highly promising pump source for a ZGP OPO to generate high-power mid-IR radiation. Although a record optical-to-optical conversion efficiency of 69 % was achieved, the mid-IR output power was limited to 25.8 W due to the OPO configuration in this initial experiment. The linear OPO design required an optical isolator between the fiber laser and the OPO cavity to protect the pump source from back-reflections. This isolator had a maximum power handling capacity of  $\sim 40\ \text{W}$ , which limited the average power from the PCF amplifier for pumping the ZGP OPO. Employing a ring OPO cavity would eliminate the need for the isolator, as the optical surfaces are tilted to the incident pump beam, allowing this power limit to be overcome in future experiments [242].

Beyond nonlinear conversion in OPOs, other avenues exist to generate high-power mid-IR radiation. A promising alternative is the generation of a mid-IR supercontinuum in soft-glass fibers based on fluoride, tellurite, or chalcogenide that exhibit a wider transparency range than silica glass. Within these mid-IR soft-glass fibers, a  $2\ \mu\text{m}$  pump signal can be strongly spectrally broadened by nonlinear effects to generate a supercontinuum that extends far into the mid-IR. Fluoride fibers are the most mature mid-IR fibers capable of handling power levels of several tens of watts and feasible for direct fusion splicing to silica-based fiber laser systems, thus offering the possibility for high-power all-in-fiber mid-IR sources [243–245]. Mid-IR

supercontinuum sources based on ZBLAN ( $\text{ZrF}_4\text{-BaF}_2\text{-LaF}_3\text{-AlF}_3\text{-NaF}$ ) have demonstrated an output power of 30 W in the spectral range of 1.9–3.4  $\mu\text{m}$  and 20.6 W in the range of 1.9–4.3  $\mu\text{m}$  [246, 247].  $\text{InF}_3$ -based systems have shown even wider spectral coverage, achieving output powers  $> 10$  W within the 1.9–4.9  $\mu\text{m}$  range [248]. Furthermore, recent progress with fluorotellurite fibers has enabled output powers of 50 W in the spectral range from 1.2–3.7  $\mu\text{m}$  and  $\sim 10$  W in the range from 1.8–4.2  $\mu\text{m}$  [249, 250].

To date, these high-power supercontinuum systems have generally relied on pulsed 2  $\mu\text{m}$  fiber laser systems with pulse durations in the picosecond or femtosecond regime [158]. However, the experimental investigations in this thesis have demonstrated that nanosecond-pulsed systems can also provide the required peak powers for supercontinuum generation. Pumping a mid-IR fiber with nanosecond pulses could provide higher pulse energies and improved average power scalability, potentially limited only by the damage threshold of the soft-glasses. Thus, a nanosecond-pulsed supercontinuum source could represent a new pathway for generating high power and pulse energies in the mid-IR.



# References

- [1] T. H. Maiman, “Stimulated optical radiation in ruby,” *nature*, vol. 187, no. 4736, p. 493, 1960.
- [2] J. Schulz, M. Lambert, B. Mayer, and M. Wissert, “Strahlquellen für die EUV-Lithographie: Das Mooresche Gesetz weitertreiben,” *Physik in unserer Zeit*, vol. 56, no. 5, p. 236, 2025. DOI: <https://doi.org/10.1002/piuz.202501732>.
- [3] O. A. Hurricane *et al.*, “Energy principles of scientific breakeven in an inertial fusion experiment,” *Physical Review Letters*, vol. 132, no. 6, p. 065103, 2024.
- [4] L. Dong and M. N. Zervas, “Past, present, and future of fiber lasers and amplifiers,” *Optics Communications*, vol. 577, p. 131419, 2025. DOI: <https://doi.org/10.1016/j.optcom.2024.131419>.
- [5] O. Traxer and E. X. Keller, “Thulium fiber laser: the new player for kidney stone treatment? A comparison with Holmium: YAG laser,” *World journal of urology*, vol. 38, no. 8, p. 1883, 2020.
- [6] P. Kronenberg and O. Traxer, “The laser of the future: Reality and expectations about the new thulium fiber laser—a systematic review,” *Translational andrology and urology*, vol. 8, no. Suppl 4, S398, 2019.
- [7] V. Fomin, M. Abramov, A. Ferin, A. Abramov, D. Mochalov, N. Platonov, and V. Gapontsev, “10 kW single mode fiber laser,” in *5th International Symposium on High-Power Fiber Lasers and Their Applications*, St. Petersburg, 2010.
- [8] K. Scholle, S. Lamrini, P. Koopmann, and P. Fuhrberg, “2  $\mu\text{m}$  laser sources and their possible applications,” in *Frontiers in Guided Wave Optics and Optoelectronics*, B. Pal, Ed., London: IntechOpen, 2010, ch. 21. DOI: 10.5772/39538.

- [9] D. Pal, A. Paul, N. K. Shekhar, S. D. Chowdhury, R. Sen, K. Chatterjee, and A. Pal, "COM stone dusting and soft tissue ablation with Q-switched thulium fiber laser," *IEEE Journal of Selected Topics in Quantum Electronics*, vol. 25, no. 1, p. 1, 2019. DOI: 10.1109/JSTQE.2018.2854538.
- [10] P. Fuhrberg, A. Ahrens, A. Schkutow, and T. Frick, "2.0  $\mu\text{m}$  laser transmission welding: Welding of transparent and opaque polymers with single-mode Tm-doped fiber lasers," *PhotonicsViews*, vol. 17, no. 2, p. 64, 2020.
- [11] I. Mingareev, F. Weirauch, A. Olowinsky, L. Shah, P. Kadwani, and M. Richardson, "Welding of polymers using a 2  $\mu\text{m}$  thulium fiber laser," *Optics Laser Technology*, vol. 44, no. 7, p. 2095, 2012. DOI: <https://doi.org/10.1016/j.optlastec.2012.03.020>.
- [12] K. Li, C. Niu, C. Wu, Y. Yu, and Y. Ma, "Development of a 2  $\mu\text{m}$  solid-state laser for lidar in the past decade," *Sensors*, vol. 23, no. 16, p. 7024, 2023.
- [13] C. Besson, A. Dolfi-Bouteyre, A. Durecu, J. L. Gouet, L. Lombard, and G. Canat, "High peak power fiber laser for long range lidar applications," in *Lasers Congress 2016 (ASSL, LSC, LAC)*, Optica Publishing Group, 2016, LW3B.3. DOI: 10.1364/LSC.2016.LW3B.3.
- [14] UKIRT, *Atmospheric transmission*, <https://about.ifa.hawaii.edu/ukirt/calibration-and-standards/astronomical-utilities/transmission-and-extinction/atmospheric-transmission/>, Accessed: 2025-11-02, 2025.
- [15] L. Dong and B. Samson, *Fiber Lasers: Basics, Technology, and Applications*. CRC press, 2016.
- [16] T. Ehrenreich, R. Leveille, I. Majid, K. Tankala, G. Rines, and P. Moulton, "1-kW, all-glass Tm: fiber laser," in *Proc. SPIE*, vol. 7580, 2010.
- [17] C. Gaida, M. Gebhardt, T. Heuermann, F. Stutzki, C. Jauregui, and J. Limpert, "Ultrafast thulium fiber laser system emitting more than 1 kW of average power," *Opt. Lett.*, vol. 43, no. 23, p. 5853, Dec. 2018. DOI: 10.1364/OL.43.005853.
- [18] B. M. Anderson, J. Solomon, and A. Flores, "1.1 kW, beam-combinable thulium doped all-fiber amplifier," in *Fiber Lasers XVIII: Technology and Systems*, M. N. Zervas, Ed., International Society for Optics and Photonics, vol. 11665, SPIE, 2021, 116650B. DOI: 10.1117/12.2576209.
- [19] B. M. Anderson, A. Taliaferro, and A. Flores, "Mode instability in kW-class thulium doped fiber amplifiers," in *Fiber Lasers XIX: Technology and Systems*, C. Jáuregui-Misas and V. R. Supradeepa, Eds., International Society for Optics and Photonics, vol. 11981, SPIE, 2022, 119810Y. DOI: 10.1117/12.2605409.

- 
- [20] C. Ren, Y. Shen, Y. Zheng, Y. Mao, F. Wang, D. Shen, and H. Zhu, "Widely-tunable all-fiber Tm doped MOPA with > 1 kW of output power," *Opt. Express*, vol. 31, no. 14, p. 22733, Jul. 2023. DOI: 10.1364/OE.494015.
- [21] C. Romano, D. Panitzek, D. Lorenz, P. Forster, M. Eichhorn, and C. Kieleck, "High-power thulium-doped fiber MOPA emitting at 2036 nm," *Journal of Lightwave Technology*, vol. 42, no. 1, p. 394, 2024. DOI: 10.1109/JLT.2023.3310121.
- [22] D. Creeden *et al.*, "Mid-infrared ZnGeP<sub>2</sub> parametric oscillator directly pumped by a pulsed 2  $\mu$ m Tm-doped fiber laser," *Opt. Lett.*, vol. 33, no. 4, p. 315, Feb. 2008. DOI: 10.1364/OL.33.000315.
- [23] I. Galli, S. Bartalini, S. Borri, P. Cancio, D. Mazzotti, P. De Natale, and G. Giusfredi, "Molecular gas sensing below parts per trillion: Radiocarbon-dioxide optical detection," *Phys. Rev. Lett.*, vol. 107, p. 270802, 27 Dec. 2011. DOI: 10.1103/PhysRevLett.107.270802.
- [24] L.-C. Michaud *et al.*, "Towards real-time active imaging of greenhouse gases using tunable mid-infrared all-fiber lasers," *Appl. Opt.*, vol. 62, no. 23, G69, Aug. 2023. DOI: 10.1364/AO.486929.
- [25] C. A. Kendziora, R. Furstenberg, M. Papantonakis, V. Nguyen, J. Byers, and R. A. McGill, "Infrared photothermal imaging spectroscopy for detection of trace explosives on surfaces," *Appl. Opt.*, vol. 54, no. 31, F129, Nov. 2015. DOI: 10.1364/AO.54.00F129.
- [26] M. C. Pierce, S. D. Jackson, M. R. Dickinson, T. A. King, and P. Sloan, "Laser-tissue interaction with a continuous wave 3- $\mu$ m fibre laser: Preliminary studies with soft tissue," *Lasers in Surgery and Medicine: The Official Journal of the American Society for Laser Medicine and Surgery*, vol. 26, no. 5, p. 491, 2000.
- [27] B. Jean and T. Bende, "Mid-IR laser applications in medicine," in *Solid-State Mid-Infrared Laser Sources*, I. T. Sorokina and K. L. Vodopyanov, Eds. Berlin, Heidelberg: Springer Berlin Heidelberg, 2003, p. 530. DOI: 10.1007/3-540-36491-9\_12.
- [28] B. Henderson *et al.*, "Laser spectroscopy for breath analysis: Towards clinical implementation," *Applied Physics B*, vol. 124, no. 8, p. 161, 2018.
- [29] H. Liu, W. Liu, C. Sun, W. Huang, and X. Cui, "A review of non-invasive blood glucose monitoring through breath acetone and body surface," *Sensors and Actuators A: Physical*, vol. 374, p. 115500, 2024. DOI: <https://doi.org/10.1016/j.sna.2024.115500>.
- [30] S. D. Jackson, "Towards high-power mid-infrared emission from a fibre laser," *Nature photonics*, vol. 6, no. 7, p. 423, 2012.
-

- [31] S. Jackson, “Mid-infrared fiber laser research: Tasks completed and the tasks ahead,” *APL Photonics*, vol. 9, no. 7, 2024.
- [32] N. Caron, M. Bernier, D. Faucher, and R. Vallée, “Understanding the fiber tip thermal runaway present in 3 $\mu$ m fluoride glass fiber lasers,” *Opt. Express*, vol. 20, no. 20, p. 22188, Sep. 2012. DOI: 10.1364/OE.20.022188.
- [33] Y. O. Aydin, V. Fortin, R. Vallée, and M. Bernier, “Towards power scaling of 2.8  $\mu$ m fiber lasers,” *Opt. Lett.*, vol. 43, no. 18, p. 4542, Sep. 2018. DOI: 10.1364/OL.43.004542.
- [34] L. J. Mawst and D. Botez, “High-power mid-infrared ( $\lambda \sim 3\text{--}6 \mu\text{m}$ ) quantum cascade lasers,” *IEEE Photonics Journal*, vol. 14, no. 1, p. 1, 2022. DOI: 10.1109/JPHOT.2021.3132261.
- [35] J. R. Meyer, W. W. Bewley, C. L. Canedy, C. S. Kim, M. Kim, C. D. Merritt, and I. Vurgaftman, “The interband cascade laser,” in *Photonics*, MDPI, vol. 7, 2020, p. 75.
- [36] S. Mi, D. Wei, B. Yao, Z. Lei, J. Li, J. Tang, T. Dai, and X. Duan, “Power improvement of a Ho: YAG power amplifier and its application to a 150 W ZGP–OPO,” *Applied Physics B*, vol. 129, no. 11, p. 166, 2023.
- [37] G. Liu *et al.*, “161 W middle infrared ZnGeP<sub>2</sub> MOPA system pumped by 300 W-class Ho:YAG MOPA system,” *Opt. Lett.*, vol. 46, no. 1, p. 82, Jan. 2021. DOI: 10.1364/OL.413755.
- [38] P. Kadwani, N. Modsching, R. A. Sims, L. Leick, J. Broeng, L. Shah, and M. Richardson, “Q-switched thulium-doped photonic crystal fiber laser,” *Opt. Lett.*, vol. 37, no. 10, p. 1664, May 2012. DOI: 10.1364/OL.37.001664.
- [39] M. Gebhardt, C. Gaida, P. Kadwani, A. Sincore, N. Gehlich, C. Jeon, L. Shah, and M. Richardson, “High peak-power mid-infrared ZnGeP<sub>2</sub> optical parametric oscillator pumped by a Tm: fiber master oscillator power amplifier system,” *Opt. Lett.*, vol. 39, no. 5, p. 1212, Mar. 2014. DOI: 10.1364/OL.39.001212.
- [40] B. Saleh and M. Teich, *Fundamentals of Photonics, 2nd Edition*. Hoboken, NJ: Canada Wiley Interscience, Jun. 2007.
- [41] A. E. Siegman, *Lasers* (University science books). Oxford: Oxford University Press, 1986.
- [42] M. Eichhorn, *Laser Physics: From Principles to Practical Work in the Lab* (Graduate Texts in Physics), 1st edition. Cham, Switzerland: Springer International Publishing Switzerland, 2014. DOI: 10.1007/978-3-319-05127-8.

- 
- [43] “Lasers and laser-related equipment – test methods for laser beam widths, divergence angles and beam propagation ratios,” International Organization for Standardization, Geneva, CH, Standard, 2021.
- [44] A. E. Siegman, “Defining, measuring, and optimizing laser beam quality,” in *Laser Resonators and Coherent Optics: Modeling, Technology, and Applications*, A. Bhowmik, Ed., International Society for Optics and Photonics, vol. 1868, SPIE, 1993, p. 2. DOI: 10.1117/12.150601.
- [45] C. Koos, “Nonlinear optics,” Lecture Notes, Summer Term 2018, Apr. 2018.
- [46] G. Meltz, W. W. Morey, and W. H. Glenn, “Formation of bragg gratings in optical fibers by a transverse holographic method,” *Opt. Lett.*, vol. 14, no. 15, p. 823, Aug. 1989. DOI: 10.1364/OL.14.000823.
- [47] Y. Kondo, K. Nouchi, T. Mitsuyu, M. Watanabe, P. G. Kazansky, and K. Hirao, “Fabrication of long-period fiber gratings by focused irradiation of infrared femtosecond laser pulses,” *Opt. Lett.*, vol. 24, no. 10, p. 646, May 1999. DOI: 10.1364/OL.24.000646.
- [48] T. Erdogan, “Fiber grating spectra,” *Journal of Lightwave Technology*, vol. 15, no. 8, p. 1277, 1997. DOI: 10.1109/50.618322.
- [49] I. V. Ciapurin, L. B. Glebov, and V. I. Smirnov, “Modeling of phase volume diffractive gratings, part 1: Transmitting sinusoidal uniform gratings,” *Optical Engineering*, vol. 45, no. 1, p. 015802, 2006.
- [50] I. H. Malitson, “Interspecimen comparison of the refractive index of fused silica,” *J. Opt. Soc. Am.*, vol. 55, no. 10, p. 1205, Oct. 1965. DOI: 10.1364/JOSA.55.001205.
- [51] G. P. Agrawal, *Nonlinear Fiber Optics*, 5th ed. Academic Press, 2012.
- [52] U. Keller, *Ultrafast Lasers: A Comprehensive Introduction to Fundamental Principles with Practical Applications*. Cham: Springer, 2021. DOI: 10.1007/978-3-030-82532-4.
- [53] P. M. Becker, A. A. Olsson, and J. R. Simpson, *Erbium-Doped Fiber Amplifiers: Fundamentals and Technology*. San Diego, CA: Academic Press, 1997.
- [54] Thorlabs, *Optics*, [https://www.thorlabs.com/newgrouppage9.cfm?objectgroup\\_id=949#4668](https://www.thorlabs.com/newgrouppage9.cfm?objectgroup_id=949#4668), Accessed: 2025-05-13, 2025.
- [55] Heraeus Covantics, *Optical applications*, <https://www.heraeus-covantics.com/tools-and-services/tools/transmission-calculator/optical-applications>, Accessed: 2025-05-13, 2025.
-

- [56] M. G. Mayer, "Rare-earth and transuranic elements," *Phys. Rev.*, vol. 60, p. 184, 3 Aug. 1941. DOI: 10.1103/PhysRev.60.184.
- [57] J. V. Vleck, "The puzzle of rare-earth spectra in solids.," *Journal of physical chemistry*, vol. 41, no. 1, p. 67, 1937.
- [58] B. R. Judd, "Optical absorption intensities of rare-earth ions," *Phys. Rev.*, vol. 127, p. 750, 3 Aug. 1962. DOI: 10.1103/PhysRev.127.750.
- [59] G. S. Ofelt, "Intensities of crystal spectra of rare-earth ions," *Journal of Chemical Physics*, vol. 37, no. 3, p. 511, 1962. DOI: 10.1063/1.1701366.
- [60] C. B. Layne and M. J. Weber, "Multiphonon relaxation of rare-earth ions in beryllium-fluoride glass," *Phys. Rev. B*, vol. 16, p. 3259, 7 Oct. 1977. DOI: 10.1103/PhysRevB.16.3259.
- [61] S. Payne, L. Chase, L. Smith, W. Kway, and W. Krupke, "Infrared cross-section measurements for crystals doped with  $\text{Er}^{3+}$ ,  $\text{Tm}^{3+}$ , and  $\text{Ho}^{3+}$ ," *IEEE Journal of Quantum Electronics*, vol. 28, no. 11, p. 2619, 1992. DOI: 10.1109/3.161321.
- [62] D. E. McCumber, "Theory of phonon-terminated optical masers," *Phys. Rev.*, vol. 134, A299, 2A Apr. 1964. DOI: 10.1103/PhysRev.134.A299.
- [63] S. Todoroki, K. Hirao, and N. Soga, "Origin of inhomogeneous linewidth of  $\text{Eu}^{3+}$  fluorescence in several oxide glasses," *Journal of Applied Physics*, vol. 72, no. 12, p. 5853, Dec. 1992. DOI: 10.1063/1.351890.
- [64] R. W. Boyd, *Nonlinear Optics*, 3rd. Amsterdam, Boston: Academic Press, 2008.
- [65] D. A. Kleinman, "Nonlinear dielectric polarization in optical media," *Phys. Rev.*, vol. 126, p. 1977, 6 Jun. 1962. DOI: 10.1103/PhysRev.126.1977.
- [66] J. E. Midwinter and J. Warner, "The effects of phase matching method and of uniaxial crystal symmetry on the polar distribution of second-order non-linear optical polarization," *British Journal of Applied Physics*, vol. 16, no. 8, p. 1135, Aug. 1965. DOI: 10.1088/0508-3443/16/8/312.
- [67] R. Hellwarth, "Third-order optical susceptibilities of liquids and solids," *Progress in Quantum Electronics*, vol. 5, p. 1, 1977. DOI: [https://doi.org/10.1016/0079-6727\(79\)90002-8](https://doi.org/10.1016/0079-6727(79)90002-8).
- [68] e. P. Franken, A. E. Hill, C. Peters, and G. Weinreich, "Generation of optical harmonics," *Physical review letters*, vol. 7, no. 4, p. 118, 1961.

- 
- [69] J. F. Nye, *Physical properties of crystals: their representation by tensors and matrices*. Oxford university press, 1985.
- [70] R. G. Smith, "Effects of momentum mismatch on parametric gain," *Journal of Applied Physics*, vol. 41, no. 10, p. 4121, Sep. 1970. DOI: 10.1063/1.1658422.
- [71] M. Hobden and J. Warner, "The temperature dependence of the refractive indices of pure lithium niobate," *Physics Letters*, vol. 22, no. 3, p. 243, 1966. DOI: [https://doi.org/10.1016/0031-9163\(66\)90591-9](https://doi.org/10.1016/0031-9163(66)90591-9).
- [72] D. E. Zelmon, E. A. Hanning, and P. G. Schunemann, "Refractive-index measurements and sellmeier coefficients for zinc germanium phosphide from 2 to 9  $\mu\text{m}$  with implications for phase matching in optical frequency-conversion devices," *Journal of the Optical Society of America B*, vol. 18, no. 9, p. 1307, 2001.
- [73] R. H. Stolen and C. Lin, "Self-phase-modulation in silica optical fibers," *Phys. Rev. A*, vol. 17, p. 1448, 4 Apr. 1978. DOI: 10.1103/PhysRevA.17.1448.
- [74] T. R. Ensley and N. K. Bambha, "Ultrafast nonlinear refraction measurements of infrared transmitting materials in the mid-wave infrared," *Opt. Express*, vol. 27, no. 26, p. 37940, Dec. 2019. DOI: 10.1364/OE.380702.
- [75] M. T. de Araujo, H. R. da Cruz, and A. S. Gouveia-Neto, "Self-phase modulation of incoherent pulses in single-mode optical fibers," *J. Opt. Soc. Am. B*, vol. 8, no. 10, p. 2094, Oct. 1991. DOI: 10.1364/JOSAB.8.002094.
- [76] P. D. Maker, R. W. Terhune, and C. M. Savage, "Intensity-dependent changes in the refractive index of liquids," *Phys. Rev. Lett.*, vol. 12, p. 507, 18 May 1964. DOI: 10.1103/PhysRevLett.12.507.
- [77] P. L. Kelley, "Self-focusing of optical beams," *Phys. Rev. Lett.*, vol. 15, p. 1005, 26 Dec. 1965. DOI: 10.1103/PhysRevLett.15.1005.
- [78] W. Kaiser and C. Garrett, "Two-photon excitation in  $\text{CaF}_2: \text{Eu}^{2+}$ ," *Physical review letters*, vol. 7, no. 6, p. 229, 1961.
- [79] N. Uchida and Y. Ohmachi, "Elastic and photoelastic properties of  $\text{TeO}_2$  single crystal," *Journal of Applied Physics*, vol. 40, no. 12, p. 4692, Nov. 1969. DOI: 10.1063/1.1657275.
- [80] H. Kogelnik and T. Li, "Laser beams and resonators," *Appl. Opt.*, vol. 5, no. 10, p. 1550, Oct. 1966. DOI: 10.1364/AO.5.001550.
- [81] W. W. Rigrod, "Saturation effects in high-gain lasers," *Journal of Applied Physics*, vol. 36, no. 8, p. 2487, Aug. 1965. DOI: 10.1063/1.1714517.
-

- [82] A. L. Schawlow and C. H. Townes, "Infrared and optical masers," *Phys. Rev.*, vol. 112, p. 1940, 6 Dec. 1958. DOI: 10.1103/PhysRev.112.1940.
- [83] R. Paschotta, *Linewidth*, RP Photonics Encyclopedia, Available online at <https://www.rp-photonics.com/linewidth.html>, 2005. DOI: 10.61835/s4l.
- [84] A. W. Edvardsen and L. G. Holmen, "Kinetics of pair-induced quenching in holmium-doped optical fibers," *Opt. Express*, vol. 32, no. 8, p. 13166, Apr. 2024. DOI: 10.1364/OE.521512.
- [85] S. Jackson, "Cross relaxation and energy transfer upconversion processes relevant to the functioning of 2 m Tm<sup>3+</sup>-doped silica fibre lasers," *Optics Communications*, vol. 230, p. 197, Jan. 2004. DOI: 10.1016/j.optcom.2003.11.045.
- [86] R. L. Sutherland, *Handbook of Nonlinear Optics*, 2nd ed. New York: Marcel Dekker, 2003.
- [87] J. Falk, "Instabilities in the doubly resonant parametric oscillator: A theoretical analysis," *IEEE Journal of Quantum Electronics*, vol. 7, no. 6, p. 230, 1971. DOI: 10.1109/JQE.1971.1076727.
- [88] R. C. Eckardt, C. D. Nabors, W. J. Kozlovsky, and R. L. Byer, "Optical parametric oscillator frequency tuning and control," *J. Opt. Soc. Am. B*, vol. 8, no. 3, p. 646, Mar. 1991. DOI: 10.1364/JOSAB.8.000646.
- [89] A. V. Smith, W. J. Alford, T. D. Raymond, and M. S. Bowers, "Comparison of a numerical model with measured performance of a seeded, nanosecond KTP optical parametric oscillator," *J. Opt. Soc. Am. B*, vol. 12, no. 11, p. 2253, Nov. 1995. DOI: 10.1364/JOSAB.12.002253.
- [90] G. W. Baxter, J. G. Haub, and B. J. Orr, "Backconversion in a pulsed optical parametric oscillator: Evidence from injection-seeded sidebands," *J. Opt. Soc. Am. B*, vol. 14, no. 10, p. 2723, Oct. 1997. DOI: 10.1364/JOSAB.14.002723.
- [91] R. Graham and H. Haken, "The quantum-fluctuations of the optical parametric oscillator. i," *Zeitschrift für Physik A Hadrons and Nuclei*, vol. 210, no. 3, p. 276, 1968. DOI: 10.1007/BF01379946.
- [92] C. D. Nabors, S. T. Yang, T. Day, and R. L. Byer, "Coherence properties of a doubly resonant monolithic optical parametric oscillator," *J. Opt. Soc. Am. B*, vol. 7, no. 5, p. 815, May 1990. DOI: 10.1364/JOSAB.7.000815.

- 
- [93] D. J. Armstrong and A. V. Smith, "Tendency of nanosecond optical parametric oscillators to produce purely phase-modulated light," *Opt. Lett.*, vol. 21, no. 20, p. 1634, Oct. 1996. DOI: 10.1364/OL.21.001634.
- [94] G. Arisholm, G. Rustad, and K. Stenersen, "Importance of pump-beam group velocity for backconversion in optical parametric oscillators," *J. Opt. Soc. Am. B*, vol. 18, no. 12, p. 1882, Dec. 2001. DOI: 10.1364/JOSAB.18.001882.
- [95] A. V. Smith, "Bandwidth and group-velocity effects in nanosecond optical parametric amplifiers and oscillators," *J. Opt. Soc. Am. B*, vol. 22, no. 9, p. 1953, Sep. 2005. DOI: 10.1364/JOSAB.22.001953.
- [96] N. J. Ramírez-Martínez, M. Núñez-Velázquez, A. A. Umnikov, and J. K. Sahu, "Highly efficient thulium-doped high-power laser fibers fabricated by MCVD," *Opt. Express*, vol. 27, no. 1, p. 196, Jan. 2019. DOI: 10.1364/OE.27.000196.
- [97] M. J. Barber, P. C. Shardlow, P. Barua, J. K. Sahu, and W. A. Clarkson, "Nested-ring doping for highly efficient 1907 nm short-wavelength cladding-pumped thulium fiber lasers," *Opt. Lett.*, vol. 45, no. 19, p. 5542, Oct. 2020. DOI: 10.1364/OL.401228.
- [98] A. V. Smith and B. T. Do, "Bulk and surface laser damage of silica by picosecond and nanosecond pulses at 1064 nm," *Appl. Opt.*, vol. 47, no. 26, p. 4812, Sep. 2008. DOI: 10.1364/AO.47.004812.
- [99] N. Platonov, R. Yagodkin, J. D. L. Cruz, C. Arambula, J. Fitts, and V. Sergeev, "7 kW single-mode ytterbium fiber laser with beam quality parameter  $M^2 < 1.1$  and direct diode pumping," in *Fiber Lasers XXII: Technology and Systems*, T. Schreiber and M. Savage-Leuchs, Eds., International Society for Optics and Photonics, vol. 13342, SPIE, 2025, p. 1334202. DOI: 10.1117/12.3043583.
- [100] S. Jackson, "The spectroscopic and energy transfer characteristics of the rare earth ions used for silicate glass fibre lasers operating in the shortwave infrared," *Laser & Photonics Reviews*, vol. 3, no. 5, p. 466, 2009. DOI: <https://doi.org/10.1002/lpor.200810058>.
- [101] A. Sincore, J. D. Bradford, J. Cook, L. Shah, and M. C. Richardson, "High average power thulium-doped silica fiber lasers: Review of systems and concepts," *IEEE Journal of Selected Topics in Quantum Electronics*, vol. 24, no. 3, p. 1, 2018. DOI: 10.1109/JSTQE.2017.2775964.

- [102] B. Faure, W. Blanc, B. Dussardier, and G. Monnom, "Improvement of the  $\text{Tm}^{3+} : ^3\text{H}_4$  level lifetime in silica optical fibers by lowering the local phonon energy," *Journal of Non-Crystalline Solids*, vol. 353, no. 29, p. 2767, 2007. DOI: <https://doi.org/10.1016/j.jnoncrysol.2007.05.025>.
- [103] W. Blanc, T. Sebastian, B. Dussardier, C. Michel, B. Faure, M. Ude, and G. Monnom, "Thulium environment in a silica doped optical fibre," *Journal of Non-Crystalline Solids*, vol. 354, no. 2, p. 435, 2008, Physics of Non-Crystalline Solids 11. DOI: <https://doi.org/10.1016/j.jnoncrysol.2007.06.083>.
- [104] D. Creedon, B. R. Johnson, G. A. Rines, and S. D. Setzler, "High power resonant pumping of tm-doped fiber amplifiers in core- and cladding-pumped configurations," *Opt. Express*, vol. 22, no. 23, p. 29067, Nov. 2014. DOI: 10.1364/OE.22.029067.
- [105] M. Lenski, T. Heuermann, M. Gebhardt, Z. Wang, C. Gaida, C. Jauregui, and J. Limpert, "Inband-pumped, high-power thulium-doped fiber amplifiers for an ultrafast pulsed operation," *Opt. Express*, vol. 30, no. 24, p. 44270, Nov. 2022. DOI: 10.1364/OE.476160.
- [106] B. Jiříčková, M. Grábner, C. Jauregui, J. Aubrecht, O. Schreiber, and P. Peterka, "Temperature-dependent cross section spectra for thulium-doped fiber lasers," *Opt. Lett.*, vol. 48, no. 3, p. 811, Feb. 2023. DOI: 10.1364/OL.479313.
- [107] G. J. Kintz, R. Allen, and L. Esterowitz, "Continuous-wave laser emission at 2.02  $\mu\text{m}$  from diode-pumped  $\text{Tm}^{3+}$ :YAG at room temperature," in *Conference on Lasers and Electro-Optics*, Optica Publishing Group, 1988, FB2.
- [108] P. F. Moulton, G. A. Rines, E. V. Slobodtchikov, K. F. Wall, G. Frith, B. Samson, and A. L. G. Carter, "Tm-doped fiber lasers: Fundamentals and power scaling," *IEEE Journal of Selected Topics in Quantum Electronics*, vol. 15, no. 1, p. 85, 2009. DOI: 10.1109/JSTQE.2008.2010719.
- [109] S. D. Jackson and S. Mossman, "Efficiency dependence on the  $\text{Tm}^{3+}$  and  $\text{Al}^{3+}$  concentrations for  $\text{Tm}^{3+}$ -doped silica double-clad fiber lasers," *Appl. Opt.*, vol. 42, no. 15, p. 2702, May 2003. DOI: 10.1364/AO.42.002702.
- [110] D. Simpson, G. Baxter, S. Collins, W. Gibbs, W. Blanc, B. Dussardier, and G. Monnom, "Energy transfer up-conversion in  $\text{Tm}^{3+}$ -doped silica fiber," *Journal of Non-Crystalline Solids*, vol. 352, no. 2, p. 136, 2006. DOI: <https://doi.org/10.1016/j.jnoncrysol.2005.11.019>.
- [111] D. L. Dexter, "A theory of sensitized luminescence in solids," *The Journal of Chemical Physics*, vol. 21, no. 5, p. 836, May 1953. DOI: 10.1063/1.1699044.

- 
- [112] G. Turri, V. Sudesh, M. Richardson, M. Bass, A. Toncelli, and M. Tonelli, "Temperature-dependent spectroscopic properties of  $\text{Tm}^{3+}$  in germanate, silica, and phosphate glasses: A comparative study," *Journal of Applied Physics*, vol. 103, no. 9, p. 093104, May 2008. DOI: 10.1063/1.2912952.
- [113] S. D. Jackson and T. A. King, "Theoretical modeling of Tm-doped silica fiber lasers," *J. Lightwave Technol.*, vol. 17, no. 5, p. 948, May 1999.
- [114] B. Walsh and N. Barnes, "Comparison of Tm: ZBLAN and Tm: Silica fiber lasers; spectroscopy and tunable pulsed laser operation around  $1.9 \mu\text{m}$ ," *Applied Physics B*, vol. 78, no. 3, p. 325, 2004.
- [115] S. D. Agger and J. H. Povlsen, "Emission and absorption cross section of thulium doped silica fibers," *Opt. Express*, vol. 14, no. 1, p. 50, Jan. 2006. DOI: 10.1364/OPEX.14.000050.
- [116] J. Li, Z. Sun, H. Luo, Z. Yan, K. Zhou, Y. Liu, and L. Zhang, "Wide wavelength selectable all-fiber thulium doped fiber laser between 1925 nm and 2200 nm," *Opt. Express*, vol. 22, no. 5, p. 5387, Mar. 2014. DOI: 10.1364/OE.22.005387.
- [117] E. Snitzer, H. Po, F. Hakimi, R. Tumminelli, and B. C. McCollum, "Double clad, offset core Nd fiber laser," in *Optical Fiber Sensors*, Optica Publishing Group, 1988, PD5. DOI: 10.1364/OFS.1988.PD5.
- [118] S. Bedö, W. Lüthy, and H. Weber, "The effective absorption coefficient in double-clad fibres," *Optics Communications*, vol. 99, no. 5, p. 331, 1993. DOI: [https://doi.org/10.1016/0030-4018\(93\)90338-6](https://doi.org/10.1016/0030-4018(93)90338-6).
- [119] A. Liu and K. Ueda, "The absorption characteristics of circular, offset, and rectangular double-clad fibers," *Optics Communications*, vol. 132, no. 5, p. 511, 1996. DOI: [https://doi.org/10.1016/0030-4018\(96\)00368-9](https://doi.org/10.1016/0030-4018(96)00368-9).
- [120] H. Zellmer, A. Tünnermann, H. Welling, and V. Reichel, "Double-clad fiber laser with 30 W output power," in *Optical Amplifiers and Their Applications*, Optica Publishing Group, 1997, FAW18. DOI: 10.1364/OAA.1997.FAW18.
- [121] E. Snitzer, "Cylindrical dielectric waveguide modes," *J. Opt. Soc. Am.*, vol. 51, no. 5, p. 491, May 1961. DOI: 10.1364/JOSA.51.000491.
- [122] D. Gloge, "Weakly guiding fibers," *Appl. Opt.*, vol. 10, no. 10, p. 2252, Oct. 1971. DOI: 10.1364/AO.10.002252.
-

- [123] A. Snyder, "Asymptotic expressions for eigenfunctions and eigenvalues of a dielectric or optical waveguide," *IEEE Transactions on Microwave Theory and Techniques*, vol. 17, no. 12, p. 1130, 1969. DOI: 10.1109/TMTT.1969.1127112.
- [124] D. Marcuse, "Loss analysis of single-mode fiber splices," *Bell system technical journal*, vol. 56, no. 5, p. 703, 1977.
- [125] D. Marcuse, "Gaussian approximation of the fundamental modes of graded-index fibers," *J. Opt. Soc. Am.*, vol. 68, no. 1, p. 103, Jan. 1978. DOI: 10.1364/JOSA.68.000103.
- [126] I. Kaminow, "Polarization in optical fibers," *IEEE Journal of Quantum Electronics*, vol. 17, no. 1, p. 15, 1981. DOI: 10.1109/JQE.1981.1070626.
- [127] V. Ramaswamy, W. G. French, and R. D. Standley, "Polarization characteristics of noncircular core single-mode fibers," *Appl. Opt.*, vol. 17, no. 18, p. 3014, Sep. 1978. DOI: 10.1364/AO.17.003014.
- [128] J. Noda, K. Okamoto, and Y. Sasaki, "Polarization-maintaining fibers and their applications," *Journal of Lightwave Technology*, vol. 4, no. 8, p. 1071, 1986. DOI: 10.1109/JLT.1986.1074847.
- [129] D. Taverner, D. J. Richardson, L. Dong, J. E. Caplen, K. Williams, and R. V. Penty, "158- $\mu$ j pulses from a single-transverse-mode, large-mode-area erbium-doped fiber amplifier," *Opt. Lett.*, vol. 22, no. 6, p. 378, Mar. 1997. DOI: 10.1364/OL.22.000378.
- [130] Coherent, *Laser- und verstärkerfasern – double- und triple-clad*, <https://www.coherent.com/de/components-accessories/specialty-optical-fibers/laser-and-amplifier-fibers>, Accessed: 2025-08-12.
- [131] Exail, *Thulium doped fibers*, <https://www.exail.com/product/thulium-doped-fibers-photonics>, Accessed: 2025-08-12.
- [132] J. P. Koplow, D. A. V. Kliner, and L. Goldberg, "Single-mode operation of a coiled multimode fiber amplifier," *Opt. Lett.*, vol. 25, no. 7, p. 442, Apr. 2000. DOI: 10.1364/OL.25.000442.
- [133] D. Marcuse, "Field deformation and loss caused by curvature of optical fibers," *J. Opt. Soc. Am.*, vol. 66, no. 4, p. 311, Apr. 1976. DOI: 10.1364/JOSA.66.000311.

- 
- [134] K. Tankala *et al.*, “New developments in high power eye-safe LMA fibers,” in *Fiber Lasers III: Technology, Systems, and Applications*, A. J. W. Brown, J. Nilsson, D. J. Harter, and A. Tünnermann, Eds., International Society for Optics and Photonics, vol. 6102, SPIE, 2006, p. 610206. DOI: 10.1117/12.646663.
- [135] T. A. Birks, J. C. Knight, and P. S. J. Russell, “Endlessly single-mode photonic crystal fiber,” *Opt. Lett.*, vol. 22, no. 13, p. 961, Jul. 1997. DOI: 10.1364/OL.22.000961.
- [136] J. C. Knight, T. A. Birks, P. S. J. Russell, and D. M. Atkin, “All-silica single-mode optical fiber with photonic crystal cladding,” *Opt. Lett.*, vol. 21, no. 19, p. 1547, Oct. 1996. DOI: 10.1364/OL.21.001547.
- [137] V. Kozlov, J. Hernandez-Cordero, R. Shubochkin, A. Carter, and T. Morse, “Silica-air double-clad optical fiber,” *IEEE Photonics Technology Letters*, vol. 12, no. 8, p. 1007, 2000. DOI: 10.1109/68.867990.
- [138] W. J. Wadsworth, R. M. Percival, G. Bouwmans, J. C. Knight, and P. S. J. Russell, “High power air-clad photonic crystal fibre laser,” *Opt. Express*, vol. 11, no. 1, p. 48, Jan. 2003. DOI: 10.1364/OE.11.000048.
- [139] W. Wadsworth, R. Percival, G. Bouwmans, J. Knight, T. Birks, T. Hedley, and P. Russell, “Very high numerical aperture fibers,” *IEEE Photonics Technology Letters*, vol. 16, no. 3, p. 843, 2004. DOI: 10.1109/LPT.2004.823689.
- [140] J. Limpert, T. Schreiber, A. Liem, S. Nolte, H. Zellmer, T. Peschel, V. Guyenot, and A. Tünnermann, “Thermo-optical properties of air-clad photonic crystal fiber lasers in high power operation,” *Opt. Express*, vol. 11, no. 22, p. 2982, Nov. 2003. DOI: 10.1364/OE.11.002982.
- [141] N. A. Mortensen, J. R. Folkenberg, M. D. Nielsen, and K. P. Hansen, “Modal cutoff and the V parameter in photonic crystal fibers,” *Optics letters*, vol. 28, no. 20, p. 1879, 2003.
- [142] M. D. Nielsen, N. A. Mortensen, J. R. Folkenberg, and A. Bjarklev, “Mode-field radius of photonic crystal fibers expressed by the V parameter,” *Optics Letters*, vol. 28, no. 23, p. 2309, 2003.
- [143] A. Tünnermann, T. Schreiber, F. Röser, A. Liem, S. Höfer, H. Zellmer, S. Nolte, and J. Limpert, “The renaissance and bright future of fibre lasers,” *Journal of Physics B: Atomic, Molecular and Optical Physics*, vol. 38, no. 9, S681, Apr. 2005. DOI: 10.1088/0953-4075/38/9/016.
-

- [144] P. Russell, "Photonic crystal fibers," *Science*, vol. 299, no. 5605, p. 358, 2003. DOI: 10.1126/science.1079280.
- [145] N. A. Mortensen and J. R. Folkenberg, "Low-loss criterion and effective area considerations for photonic crystal fibres," *Journal of Optics A: Pure and Applied Optics*, vol. 5, no. 3, p. 163, Mar. 2003. DOI: 10.1088/1464-4258/5/3/303.
- [146] J. Limpert *et al.*, "High-power rod-type photonic crystal fiber laser," *Opt. Express*, vol. 13, no. 4, p. 1055, Feb. 2005. DOI: 10.1364/OPEX.13.001055.
- [147] C. D. Brooks and F. Di Teodoro, "Multimegawatt peak-power, single-transverse-mode operation of a 100 m core diameter, Yb-doped rodlike photonic crystal fiber amplifier," *Applied Physics Letters*, vol. 89, no. 11, p. 111119, Sep. 2006. DOI: 10.1063/1.2348742.
- [148] F. Stutzki, F. Jansen, A. Liem, C. Jauregui, J. Limpert, and A. Tünnermann, "26 mJ, 130 W Q-switched fiber-laser system with near-diffraction-limited beam quality," *Opt. Lett.*, vol. 37, no. 6, p. 1073, Mar. 2012. DOI: 10.1364/OL.37.001073.
- [149] G. P. Agrawal, "Optical pulse propagation in doped fiber amplifiers," *Phys. Rev. A*, vol. 44, p. 7493, 11 Dec. 1991. DOI: 10.1103/PhysRevA.44.7493.
- [150] G. Agrawal, "Modulation instability in erbium-doped fiber amplifiers," *IEEE Photonics Technology Letters*, vol. 4, no. 6, p. 562, 1992. DOI: 10.1109/68.141968.
- [151] J. T. Manassah, "Self-phase modulation of incoherent light revisited," *Opt. Lett.*, vol. 16, no. 21, p. 1638, Nov. 1991. DOI: 10.1364/OL.16.001638.
- [152] K. Tai, A. Hasegawa, and A. Tomita, "Observation of modulational instability in optical fibers," *Phys. Rev. Lett.*, vol. 56, p. 135, 2 Jan. 1986. DOI: 10.1103/PhysRevLett.56.135.
- [153] R. Stolen and J. Bjorkholm, "Parametric amplification and frequency conversion in optical fibers," *IEEE Journal of Quantum Electronics*, vol. 18, no. 7, p. 1062, 1982. DOI: 10.1109/JQE.1982.1071660.
- [154] E. Brainis, D. Amans, and S. Massar, "Scalar and vector modulation instabilities induced by vacuum fluctuations in fibers: Numerical study," *Phys. Rev. A*, vol. 71, p. 023808, 2 Feb. 2005. DOI: 10.1103/PhysRevA.71.023808.
- [155] R. H. Stolen, J. E. Bjorkholm, and A. Ashkin, "Phase-matched three-wave mixing in silica fiber optical waveguides," *Applied Physics Letters*, vol. 24, no. 7, p. 308, Apr. 1974. DOI: 10.1063/1.1655195.
- [156] R. H. Stolen, M. A. Bösch, and C. Lin, "Phase matching in birefringent fibers," *Opt. Lett.*, vol. 6, no. 5, p. 213, May 1981. DOI: 10.1364/OL.6.000213.

- 
- [157] R. Jain and K. Stenersen, "Phase-matched four-photon mixing processes in birefringent fibers," *Applied Physics B*, vol. 35, no. 2, p. 49, 1984.
- [158] J. Swiderski, "Recent development of mid-infrared supercontinuum generation in fluoroindate glass fibers," *Applied Sciences*, vol. 12, no. 10, p. 4927, 2022.
- [159] R. G. Smith, "Optical power handling capacity of low loss optical fibers as determined by stimulated raman and brillouin scattering," *Appl. Opt.*, vol. 11, no. 11, p. 2489, Nov. 1972. DOI: 10.1364/AO.11.002489.
- [160] P. J. Thomas, N. L. Rowell, H. M. van Driel, and G. I. Stegeman, "Normal acoustic modes and brillouin scattering in single-mode optical fibers," *Phys. Rev. B*, vol. 19, p. 4986, 10 May 1979. DOI: 10.1103/PhysRevB.19.4986.
- [161] A. Yeniay, J.-M. Delavaux, and J. Toulouse, "Spontaneous and stimulated brillouin scattering gain spectra in optical fibers," *J. Lightwave Technol.*, vol. 20, no. 8, p. 1425, Aug. 2002.
- [162] R. Shuker and R. W. Gammon, "Raman-scattering selection-rule breaking and the density of states in amorphous materials," *Phys. Rev. Lett.*, vol. 25, p. 222, 4 Jul. 1970. DOI: 10.1103/PhysRevLett.25.222.
- [163] R. H. Stolen and E. P. Ippen, "Raman gain in glass optical waveguides," *Applied Physics Letters*, vol. 22, no. 6, p. 276, Mar. 1973. DOI: 10.1063/1.1654637.
- [164] D. Hollenbeck and C. D. Cantrell, "Multiple-vibrational-mode model for fiber-optic raman gain spectrum and response function," *J. Opt. Soc. Am. B*, vol. 19, no. 12, p. 2886, Dec. 2002. DOI: 10.1364/JOSAB.19.002886.
- [165] F. M. Mitschke and L. F. Mollenauer, "Discovery of the soliton self-frequency shift," *Opt. Lett.*, vol. 11, no. 10, p. 659, Oct. 1986. DOI: 10.1364/OL.11.000659.
- [166] P. Forster, C. Romano, J. Schneider, M. Eichhorn, and C. Kieleck, "High-power continuous-wave  $\text{Tm}^{3+}:\text{Ho}^{3+}$ -codoped fiber laser operation from 2.1  $\mu\text{m}$  to 2.2  $\mu\text{m}$ ," *Opt. Lett.*, vol. 47, no. 10, p. 2542, May 2022. DOI: 10.1364/OL.458921.
- [167] F. Sanson *et al.*, "680 W thulium-doped all-fiber single-oscillator laser emitting at 2036 nm in continuous-wave operation," *Opt. Continuum*, vol. 4, no. 7, p. 1426, Jul. 2025. DOI: 10.1364/OPTCON.566656.
-

- [168] P. Peterka, P. Honzátko, M. Becker, F. Todorov, M. Písařík, O. Podrazký, and I. Kašík, “Monolithic Tm-doped fiber laser at 1951 nm with deep-UV femtosecond-induced FBG pair,” *IEEE Photonics Technology Letters*, vol. 25, no. 16, p. 1623, 2013. DOI: 10.1109/LPT.2013.2272880.
- [169] M. Rochette, L. R. Chen, K. Sun, and J. Hernandez-Cordero, “Multiwavelength and tunable self-pulsating fiber cavity based on regenerative SPM spectral broadening and filtering,” *IEEE Photonics Technology Letters*, vol. 20, no. 17, p. 1497, 2008. DOI: 10.1109/LPT.2008.928531.
- [170] A. Wetter, M. Faucher, and B. Sévigny, “High power cladding light strippers,” in *Fiber Lasers V: Technology, Systems, and Applications*, J. Broeng and C. Headley, Eds., International Society for Optics and Photonics, vol. 6873, SPIE, 2008, p. 687327. DOI: 10.1117/12.763003.
- [171] K. Boyd *et al.*, “CO<sub>2</sub> laser-fabricated cladding light strippers for high-power fiber lasers and amplifiers,” *Appl. Opt.*, vol. 55, no. 11, p. 2915, Apr. 2016. DOI: 10.1364/AO.55.002915.
- [172] L. Sun, S. Jiang, J. D. Zuegel, and J. R. Marciante, “All-fiber optical isolator based on faraday rotation in highly terbium-doped fiber,” *Opt. Lett.*, vol. 35, no. 5, p. 706, Mar. 2010. DOI: 10.1364/OL.35.000706.
- [173] R. Paschotta, *Faraday circulators*, RP Photonics Encyclopedia, 2023. DOI: 10.61835/u6q" title="This link will reload the current page..
- [174] D. J. DiGiovanni and A. J. Stentz, *Tapered fiber bundles for coupling light into and out of cladding-pumped fiber devices*, US Patent 5,864,644, Jan. 1999.
- [175] P. Koška, Y. Baravets, P. Peterka, J. Bohata, and M. Písařík, “Mode-field adapter for tapered-fiber-bundle signal and pump combiners,” *Appl. Opt.*, vol. 54, no. 4, p. 751, Feb. 2015. DOI: 10.1364/AO.54.000751.
- [176] G. P. Valentin and S. Igor, *Coupling arrangement between a multi-mode light source and an optical fiber through an intermediate optical fiber length*, US Patent 5,999,673, Dec. 1999.
- [177] T. Theeg, H. Sayinc, J. Neumann, L. Overmeyer, and D. Kracht, “Pump and signal combiner for bi-directional pumping of all-fiber lasers and amplifiers,” *Opt. Express*, vol. 20, no. 27, p. 28125, Dec. 2012. DOI: 10.1364/OE.20.028125.

- 
- [178] C. Renaud, H. Offerhaus, J. Alvarez-Chavez, C. Nilsson, W. Clarkson, P. Turner, D. Richardson, and A. Grudinin, "Characteristics of Q-switched cladding-pumped ytterbium-doped fiber lasers with different high-energy fiber designs," *IEEE Journal of Quantum Electronics*, vol. 37, no. 2, p. 199, 2001. DOI: 10.1109/3.903069.
- [179] D. Lorenz, J. Schneider, C. Romano, D. Panitzek, J. Lautenschläger, M. Eichhorn, and C. Kieleck, "Actively pulse-shaped linearly polarized 200 W photonic crystal fiber MOPA at 2048 nm with 2 mJ pulse energy," *Opt. Lett.*, vol. 50, no. 14, p. 4490, Jul. 2025. DOI: 10.1364/OL.562668.
- [180] L. M. Frantz and J. S. Nodvik, "Theory of pulse propagation in a laser amplifier," *Journal of Applied Physics*, vol. 34, no. 8, p. 2346, Aug. 1963. DOI: 10.1063/1.1702744.
- [181] A. Malinowski, K. T. Vu, K. K. Chen, J. Nilsson, Y. Jeong, S. Alam, D. Lin, and D. J. Richardson, "High power pulsed fiber MOPA system incorporating electro-optic modulator based adaptive pulse shaping," *Opt. Express*, vol. 17, no. 23, p. 20927, Nov. 2009. DOI: 10.1364/OE.17.020927.
- [182] Z. Li *et al.*, "High-energy diode-seeded nanosecond 2  $\mu\text{m}$  fiber MOPA systems incorporating active pulse shaping," *Opt. Lett.*, vol. 39, no. 6, p. 1569, Mar. 2014. DOI: 10.1364/OL.39.001569.
- [183] C. D. Brooks and F. D. Teodoro, "1-mJ energy, 1-MW peak-power, 10-W average-power, spectrally narrow, diffraction-limited pulses from a photonic-crystal fiber amplifier," *Opt. Express*, vol. 13, no. 22, p. 8999, Oct. 2005. DOI: 10.1364/OPEX.13.008999.
- [184] J. Alvarez-Chavez, A. Grudinin, J. Nilsson, P. Turner, and W. Clarkson, "Mode selection in high power cladding pumped fibre lasers with tapered section," in *Technical Digest. Summaries of papers presented at the Conference on Lasers and Electro-Optics. Postconference Edition. CLEO '99. Conference on Lasers and Electro-Optics (IEEE Cat. No.99CH37013)*, 1999, p. 247. DOI: 10.1109/CLEO.1999.834141.
- [185] J. Nilsson, R. Paschotta, J. E. Caplen, and D. C. Hanna, "Yb<sup>3+</sup>-ring-doped fiber for high-energy pulse amplification," *Opt. Lett.*, vol. 22, no. 14, p. 1092, Jul. 1997. DOI: 10.1364/OL.22.001092.
- [186] Y. Wang and H. Po, "Dynamic characteristics of double-clad fiber amplifiers for high-power pulse amplification," *Journal of Lightwave Technology*, vol. 21, no. 10, p. 2262, 2003. DOI: 10.1109/JLT.2003.818166.
-

- [187] Y. Sintov, O. Katz, Y. Glick, S. Acco, Y. Nafcha, A. Englander, and R. Lavi, "Extractable energy from ytterbium-doped high-energy pulsed fiber amplifiers and lasers," *J. Opt. Soc. Am. B*, vol. 23, no. 2, p. 218, Feb. 2006. DOI: 10.1364/JOSAB.23.000218.
- [188] J. A. Alvarez-Chavez, H. L. Offerhaus, J. Nilsson, P. W. Turner, W. A. Clarkson, and D. J. Richardson, "High-energy, high-power ytterbium-doped Q-switched fiber laser," *Opt. Lett.*, vol. 25, no. 1, p. 37, Jan. 2000. DOI: 10.1364/OL.25.000037.
- [189] G. Canat, J.-C. Mollier, J.-P. Bouzinac, G. M. Williams, B. Cole, L. Goldberg, Y. Jaouën, and G. Kulcsar, "Dynamics of high-power erbium–ytterbium fiber amplifiers," *J. Opt. Soc. Am. B*, vol. 22, no. 11, p. 2308, Nov. 2005. DOI: 10.1364/JOSAB.22.002308.
- [190] L. Dong, "Nonlinear propagation in optical fibers with gain saturation and gain dispersion," *Journal of Lightwave Technology*, vol. 38, no. 24, p. 6897, 2020. DOI: 10.1109/JLT.2020.3019972.
- [191] L. Li, B. Zhang, K. Yin, L. Yang, and J. Hou, "1 mJ nanosecond all-fiber thulium-doped fiber laser at 2.05  $\mu\text{m}$ ," *Opt. Express*, vol. 23, no. 14, p. 18098, Jul. 2015. DOI: 10.1364/OE.23.018098.
- [192] A. Abdulfattah, A. Sincore, J. Bradford, N. Bodnar, J. Cook, L. Shah, and M. Richardson, "700  $\mu\text{J}$ , 100 ns, 20 kHz pulses from a 1.5 m Thulium-doped fiber amplifier," in *Laser Technology for Defense and Security XIV*, M. Dubinskiy and T. C. Newell, Eds., International Society for Optics and Photonics, vol. 10637, SPIE, 2018, p. 106370I. DOI: 10.1117/12.2305160.
- [193] X. Wang, X. Jin, P. Zhou, X. Wang, H. Xiao, and Z. Liu, "All-fiber high-average power nanosecond-pulsed master-oscillator power amplifier at 2  $\mu\text{m}$  with mJ-level pulse energy," *Appl. Opt.*, vol. 55, no. 8, p. 1941, Mar. 2016. DOI: 10.1364/AO.55.001941.
- [194] C. Kieleck, A. Berrou, B. Donelan, B. Cadier, T. Robin, and M. Eichhorn, "6.5 W ZnGeP<sub>2</sub> OPO directly pumped by a Q-switched Tm<sup>3+</sup>-doped single-oscillator fiber laser," *Opt. Lett.*, vol. 40, no. 6, p. 1101, Mar. 2015. DOI: 10.1364/OL.40.001101.
- [195] F. Stutzki, F. Jansen, C. Jauregui, J. Limpert, and A. Tünnermann, "2.4 mJ, 33 W Q-switched Tm-doped fiber laser with near diffraction-limited beam quality," *Opt. Lett.*, vol. 38, no. 2, p. 97, Jan. 2013. DOI: 10.1364/OL.38.000097.
- [196] C. Gaida, M. Gebhardt, P. Kadwani, L. Leick, J. Broeng, L. Shah, and M. Richardson, "Amplification of nanosecond pulses to megawatt peak power levels in Tm<sup>3+</sup>-doped photonic crystal fiber rod," *Opt. Lett.*, vol. 38, no. 5, p. 691, Mar. 2013. DOI: 10.1364/OL.38.000691.

- 
- [197] E. Lippert, S. Nicolas, G. Arisholm, K. Stenersen, and G. Rustad, "Midinfrared laser source with high power and beam quality," *Appl. Opt.*, vol. 45, no. 16, p. 3839, Jun. 2006. DOI: 10.1364/AO.45.003839.
- [198] L. Wang, T. Xing, S. Hu, X. Wu, H. Wu, J. Wang, and H. Jiang, "Mid-infrared ZGP-OPO with a high optical-to-optical conversion efficiency of 75.7%," *Opt. Express*, vol. 25, no. 4, p. 3373, Feb. 2017. DOI: 10.1364/OE.25.003373.
- [199] P. G. Schunemann, K. T. Zawilski, L. A. Pomeranz, D. J. Creeden, and P. A. Budni, "Advances in nonlinear optical crystals for mid-infrared coherent sources," *J. Opt. Soc. Am. B*, vol. 33, no. 11, p. D36, Nov. 2016. DOI: 10.1364/JOSAB.33.000D36.
- [200] S. Mi, J. Tang, D. Wei, B. Yao, J. Li, K. Yang, T. Dai, and X. Duan, "Thermal-birefringence-induced depolarization in a 450 W Ho:YAG MOPA system," *Opt. Express*, vol. 30, no. 12, p. 21501, Jun. 2022. DOI: 10.1364/OE.462617.
- [201] N. Simakov, A. Davidson, A. Hemming, S. Bennetts, M. Hughes, N. Carmody, P. Davies, and J. Haub, "Mid-infrared generation in ZnGeP<sub>2</sub> pumped by a monolithic, power scalable 2- $\mu$ m source," in *Fiber Lasers IX: Technology, Systems, and Applications*, E. C. Honea and S. T. Hendow, Eds., International Society for Optics and Photonics, vol. 8237, SPIE, 2012, 82373K. DOI: 10.1117/12.909766.
- [202] G. D. Boyd, E. Buehler, and F. G. Storz, "Linear and nonlinear optical properties of ZnGeP<sub>2</sub> and CdSe," *Applied Physics Letters*, vol. 18, no. 7, p. 301, Apr. 1971. DOI: 10.1063/1.1653673.
- [203] S. Lin, Y. Tanaka, S. Takeuchi, and T. Suzuki, "Improved dispersion equation for MgO:LiNbO<sub>3</sub> crystal in the infrared spectral range derived from sum and difference frequency mixing," *IEEE Journal of Quantum Electronics*, vol. 32, no. 1, p. 124, 1996. DOI: 10.1109/3.481928.
- [204] G. Hansson, H. Karlsson, S. Wang, and F. Laurell, "Transmission measurements in KTP and isomorphic compounds," *Appl. Opt.*, vol. 39, no. 27, p. 5058, Sep. 2000. DOI: 10.1364/AO.39.005058.
- [205] K. W. Aniolek, T. J. Kulp, B. A. Richman, S. E. Bisson, P. E. Powers, and R. L. Schmitt, "Trace gas detection in the mid-IR with a compact PPLN-based cavity ring-down spectrometer," in *Application of Tunable Diode and Other Infrared Sources for Atmospheric Studies and Industrial Processing Monitoring II*, A. Fried, Ed., International Society for Optics and Photonics, vol. 3758, SPIE, 1999, p. 62. DOI: 10.1117/12.366469.

- [206] S. D. Setzler *et al.*, “Characterization of defect-related optical absorption in ZnGeP<sub>2</sub>,” *Journal of Applied Physics*, vol. 86, no. 12, p. 6677, Dec. 1999. DOI: 10.1063/1.371743.
- [207] P. G. Schunemann, K. T. Zawilski, T. Lobay, B. Porth, and M. D. Thomas, “Laser damage threshold study of ZGP, CSP, GaAs, and GaP,” in *Nonlinear Frequency Generation and Conversion: Materials and Devices XXII*, P. G. Schunemann, Ed., International Society for Optics and Photonics, vol. PC12405, SPIE, 2023, PC124050G. DOI: 10.1117/12.2655108.
- [208] C. Kieleck, M. Eichhorn, A. Hirth, D. Faye, and E. Lallier, “High-efficiency 20–50 kHz mid-infrared orientation-patterned gaas optical parametric oscillator pumped by a 2  $\mu\text{m}$  holmium laser,” *Opt. Lett.*, vol. 34, no. 3, p. 262, Feb. 2009. DOI: 10.1364/OL.34.000262.
- [209] V. Petrov, F. Noack, I. Tunchev, P. Schunemann, and K. Zawilski, “The nonlinear coefficient  $d_{36}$  of CdSiP<sub>2</sub>,” in *Nonlinear Frequency Generation and Conversion: Materials, Devices, and Applications VIII*, P. E. Powers, Ed., International Society for Optics and Photonics, vol. 7197, SPIE, 2009, p. 71970M. DOI: 10.1117/12.809586.
- [210] K. T. Zawilski, P. Schunemann, S. Horton, L. Pomeranz, L. Goldberg, B. Cole, J. Slagle, and K. Averett, “Comparison of ZGP and CSP for generation of high average power mid IR light,” in *Nonlinear Frequency Generation and Conversion: Materials and Devices XXI*, P. G. Schunemann and V. Petrov, Eds., International Society for Optics and Photonics, vol. PC11985, SPIE, 2022, PC1198502. DOI: 10.1117/12.2609222.
- [211] S. Brosnan and R. Byer, “Optical parametric oscillator threshold and linewidth studies,” *IEEE Journal of Quantum Electronics*, vol. 15, no. 6, p. 415, 1979. DOI: 10.1109/JQE.1979.1070027.
- [212] P. Phua, B. Xu, T. Chong, and Y. Fong, “Oscillation threshold of pulsed doubly resonating optical parametric oscillator operating near degeneracy,” *Optics Communications*, vol. 139, no. 4, p. 320, 1997. DOI: [https://doi.org/10.1016/S0030-4018\(97\)00131-4](https://doi.org/10.1016/S0030-4018(97)00131-4).
- [213] N. Dalloz, T. Robin, B. Cadier, C. Kieleck, M. Eichhorn, and A. Hildenbrand-Dhollande, “High power Q-switched Tm<sup>3+</sup>, Ho<sup>3+</sup>-codoped 2  $\mu\text{m}$  fiber laser and application for direct OPO pumping,” in *Fiber Lasers XVI: Technology and Systems*, A. L. Carter and L. Dong, Eds., International Society for Optics and Photonics, vol. 10897, SPIE, 2019, 108970J. DOI: 10.1117/12.2507844.

- 
- [214] A. Hemming, J. Richards, A. Davidson, N. Carmody, S. Bennetts, N. Simakov, and J. Haub, “99 W mid-IR operation of a ZGP OPO at 25% duty cycle,” *Opt. Express*, vol. 21, no. 8, p. 10062, Apr. 2013. DOI: 10.1364/OE.21.010062.
- [215] D. Creeden *et al.*, “Thulium fiber laser-pumped mid-IR OPO,” in *Laser Source Technology for Defense and Security IV*, M. Dubinskii and G. L. Wood, Eds., International Society for Optics and Photonics, vol. 6952, SPIE, 2008, 69520S. DOI: 10.1117/12.775196.
- [216] C. Kieleck, M. Eichhorn, D. Faye, E. Lallier, and S. D. Jackson, “Polarization effects and fiber-laser-pumping of a 2- $\mu\text{m}$ -pumped OP-GaAs OPO,” in *Nonlinear Frequency Generation and Conversion: Materials, Devices, and Applications IX*, P. E. Powers, Ed., International Society for Optics and Photonics, vol. 7582, SPIE, 2010, p. 758212. DOI: 10.1117/12.846917.
- [217] J. Schneider, P. Forster, C. Romano, M. Eichhorn, and C. Kieleck, “Investigation of the pulse energy limits of actively Q-switched polarization-maintaining  $\text{Tm}^{3+}$ -doped fiber lasers,” *OSA Continuum*, vol. 4, no. 5, p. 1577, May 2021. DOI: 10.1364/OSAC.423812.
- [218] J. Schneider, P. Forster, C. Romano, M. Eichhorn, and C. Kieleck, “High pulse energy  $\text{ZnGeP}_2$  OPO directly pumped by a Q-switched  $\text{Tm}^{3+}$ -doped single-oscillator fiber laser,” *Opt. Lett.*, vol. 46, no. 9, p. 2139, May 2021. DOI: 10.1364/OL.422702.
- [219] J. Schneider, P. Forster, M. Eichhorn, and C. Kieleck, “High-pulse-energy actively Q-switched polarization-maintaining  $\text{Tm}^{3+}$ -doped silica fiber laser,” in *OSA High-brightness Sources and Light-driven Interactions Congress 2020 (EUVXRAY, HILAS, MICS)*, Optica Publishing Group, 2020, MF2C.3. DOI: 10.1364/MICS.2020.MF2C.3.
- [220] J. Schneider, P. Forster, C. Romano, M. Eichhorn, and C. Kieleck, “Advances in 2  $\mu\text{m}$  polarization-maintaining thulium-doped Q-switched fiber lasers for frequency conversion into the mid-IR,” in *Nonlinear Frequency Generation and Conversion: Materials and Devices XX*, P. G. Schunemann and K. L. Schepler, Eds., International Society for Optics and Photonics, vol. 11670, SPIE, 2021, 116700B. DOI: 10.1117/12.2577118.
- [221] J. Schneider, P. Forster, C. Romano, M. Eichhorn, and C. Kieleck, “High-power Q-switched  $\text{Tm}^{3+}$ -doped fiber laser for nonlinear frequency conversion into the mid-IR,” in *Nonlinear Frequency Generation and Conversion: Materials and Devices XXII*, P. G. Schunemann, Ed., International Society for Optics and Photonics, vol. 12405, SPIE, 2023.
-

- [222] M. Eichhorn and S. D. Jackson, “High-pulse-energy actively Q-switched  $\text{Tm}^{3+}$ -doped silica 2  $\mu\text{m}$  fiber laser pumped at 792 nm,” *Opt. Lett.*, vol. 32, no. 19, p. 2780, Oct. 2007. DOI: 10.1364/OL.32.002780.
- [223] J. Schneider *et al.*, “High-energy nanosecond pulse extraction from a  $\text{Tm}^{3+}$ -doped photonic crystal fiber laser emitting at 2050 nm with narrow linewidth,” *Opt. Express*, vol. 32, no. 18, p. 32309, Aug. 2024. DOI: 10.1364/OE.531146.
- [224] M. P. Buckthorpe, R. Švejkar, and W. A. Clarkson, “Determining the relative impact of quantum efficiency and core propagation loss on efficient power scaling of thulium-doped silica fibre lasers,” in *Solid State Lasers XXXIII: Technology and Devices*, W. A. Clarkson and R. K. Shori, Eds., International Society for Optics and Photonics, vol. 12864, SPIE, 2024, 128640W. DOI: 10.1117/12.3002641.
- [225] B. Jiříčková, O. Schreiber, P. Varak, M. Grábner, J. Aubrecht, and P. Peterka, “Temperature-dependence of cross-relaxation coefficient of the thulium-doped silica fibers,” in *Specialty Optical Fibres*, K. Kalli, A. Mendez, and P. Peterka, Eds., International Society for Optics and Photonics, vol. 12573, SPIE, 2023, 125730H. DOI: 10.1117/12.2666642.
- [226] P. Forster, J. Lautenschläger, D. Lorenz, J. Schneider, D. Panitzek, C. Romano, M. Eichhorn, and C. Kieleck, “12.2 W ZGP OPO pumped by a Q-Switched  $\text{Tm}^{3+}:\text{Ho}^{3+}$ -codoped fiber laser,” in *Nonlinear Frequency Generation and Conversion: Materials and Devices XXIII*, P. G. Schunemann, Ed., International Society for Optics and Photonics, vol. 12869, SPIE, 2024, p. 1286905. DOI: 10.1117/12.3002253.
- [227] J. Schneider *et al.*, “High-pulse-energy actively Q-switched  $\text{Tm}^{3+}$ -doped photonic crystal fiber laser operating at 2050 nm with narrow linewidth,” in *Laser Congress 2023 (ASSL, LAC)*, Optica Publishing Group, 2023, AW4A.3. DOI: 10.1364/ASSL.2023.AW4A.3.
- [228] J. Schneider *et al.*, “High-pulse-energy actively Q-switched  $\text{Tm}^{3+}$ -doped photonic crystal fiber laser operating at 2050 nm with narrow linewidth,” in *Fiber Lasers XXI: Technology and Systems*, C. Jollivet, Ed., International Society for Optics and Photonics, vol. 12865, SPIE, 2024, p. 1286517. DOI: 10.1117/12.3002397.
- [229] J. Schneider *et al.*, “High-pulse-energy  $\text{Tm}^{3+}$ -doped photonic crystal fiber laser for nonlinear frequency conversion into the mid-IR,” in *High-Power Lasers and Technologies for Optical Countermeasures II*, International Society for Optics and Photonics, vol. PC13201, SPIE, 2024, PC1320106. DOI: 10.1117/12.3031761.

- [230] J. Schneider, D. Lorenz, J. Lautenschläger, C. Romano, M. Eichhorn, and C. Kieleck, "Optimization of nanosecond pulse energy extraction from  $\text{Tm}^{3+}$ -doped photonic crystal fibers," in *Laser Congress 2024 (ASSL, LAC, LS&C)*, Optica Publishing Group, 2024, AM3A.1. DOI: 10.1364/ASSL.2024.AM3A.1.
- [231] NKT Photonics, *Ytterbium doped double clad fibers*, <https://www.nktphotonics.com/products/optical-fibers-and-modules/ytterbium-doped-double-clad-fibers/>, Accessed: 2025-10-25.
- [232] D. Lorenz, C. Romano, D. Panitzek, P. Forster, J. Schneider, J. Lautenschläger, M. Eichhorn, and C. Kieleck, "High repetition rate pulsed all-in-fiber thulium doped fiber MOPA for OPO pumping," in *Nonlinear Frequency Generation and Conversion: Materials and Devices XXIII*, P. G. Schunemann, Ed., International Society for Optics and Photonics, vol. PC12869, SPIE, 2024, PC1286909. DOI: 10.1117/12.3003070.
- [233] J. Schneider, D. Lorenz, C. Romano, D. Panitzek, J. Lautenschläger, M. Eichhorn, and C. Kieleck, "High-Power Actively-Pulse-Shaped 2 mJ Nanosecond-Pulsed  $\text{Tm}^{3+}$ -Doped Photonic Crystal Fiber Amplifier Emitting At 2048 nm," in *2025 Conference on Lasers and Electro-Optics Europe European Quantum Electronics Conference (CLEO/Europe-EQEC)*, 2025, p. 1. DOI: 10.1109/CLEO/Europe-EQEC65582.2025.11111105.
- [234] D. Lorenz, J. Schneider, C. Romano, D. Panitzek, J. Lautenschläger, M. Eitner, M. Eichhorn, and C. Kieleck, "Actively pulse-shaped 2 mJ, 200 W fiber MOPA at 2048 nm for mid-IR generation in OPOs," in *High-Power Lasers and Technologies for Optical Countermeasures III*, M. Eichhorn and G. D. Lewis, Eds., International Society for Optics and Photonics, vol. 13675, SPIE, 2025, p. 1367506. DOI: 10.1117/12.3075755.
- [235] J. Ren, Y. Qi, Z. He, T. Yu, and X. Ye, "Investigation of suppressing ASE in all-fiber TDFA by modulating MI from seed and realization of a 2043 nm, 45 dB, 1 mJ amplifier with single-stage structure," *Optical Fiber Technology*, vol. 90, p. 104103, 2025. DOI: <https://doi.org/10.1016/j.yofte.2024.104103>.
- [236] M. Lenski, T. Heuermann, Z. Wang, C. Aleshire, C. Gaida, C. Jáuregui, and J. Limpert, "In-band pumped, Q-switched thulium-doped fiber laser system delivering 140 W and 7 mJ pulse energy," *Opt. Lett.*, vol. 49, no. 14, p. 4042, Jul. 2024. DOI: 10.1364/OL.528330.
- [237] L. G. Holmen and H. Fonnum, "Holmium-doped fiber amplifier for pumping a  $\text{ZnGeP}_2$  optical parametric oscillator," *Opt. Express*, vol. 29, no. 6, p. 8477, Mar. 2021. DOI: 10.1364/OE.419939.

- [238] D. Lorenz, C. Romano, D. Panitzek, P. Forster, J. Schneider, H. Bükler, M. Eichhorn, and C. Kieleck, “Nanosecond pulsed narrow-linewidth all-fiber source for ZGP-OPO pumping,” *Opt. Continuum*, vol. 2, no. 3, p. 660, Mar. 2023. DOI: 10.1364/OPTCON.486081.
- [239] B. G. Ward, D. L. S. Jr., and J. D. Tafoya, “A monolithic pump signal multiplexer for air-clad photonic crystal fiber amplifiers,” in *Fiber Lasers VII: Technology, Systems, and Applications*, K. Tankala, Ed., International Society for Optics and Photonics, vol. 7580, SPIE, 2010, p. 75801C. DOI: 10.1117/12.845769.
- [240] D. L. S. Jr., J. D. Tafoya, D. S. Schulz, B. G. Ward, and C. G. Carlson, “Advanced components for multi-kW fiber lasers,” in *Fiber Lasers IX: Technology, Systems, and Applications*, E. C. Honea and S. T. Hendow, Eds., International Society for Optics and Photonics, vol. 8237, SPIE, 2012, 82370P. DOI: 10.1117/12.909337.
- [241] A. Sincore, J. Tafoya, D. S. Jr., L. Leick, L. Shah, and M. Richardson, “Photonic crystal fiber pump combiner for high-peak power all-fiber thulium lasers,” in *Fiber Lasers XI: Technology, Systems, and Applications*, S. Ramachandran, Ed., International Society for Optics and Photonics, vol. 8961, SPIE, 2014, p. 896133. DOI: 10.1117/12.2041327.
- [242] E. Lippert, H. Fonnum, G. Arisholm, and K. Stenersen, “A 22-watt mid-infrared optical parametric oscillator with V-shaped 3-mirror ring resonator,” *Opt. Express*, vol. 18, no. 25, p. 26475, Dec. 2010. DOI: 10.1364/OE.18.026475.
- [243] G. Newburgh and M. Dubinskii, “Power and efficiency scaling of Er: ZBLAN fiber laser,” *Laser Physics Letters*, vol. 18, no. 9, p. 095102, 2021.
- [244] H. Okamoto, K. Kasuga, and Y. Kubota, “Efficient 521 nm all-fiber laser: Splicing Pr<sup>3+</sup>-doped ZBLAN fiber to end-coated silica fiber,” *Opt. Lett.*, vol. 36, no. 8, p. 1470, Apr. 2011. DOI: 10.1364/OL.36.001470.
- [245] L. Yang, B. Yan, R. Zhao, D. Wu, T. Xu, P. Yang, Q. Nie, and S. Dai, “Ultra-low fusion splicing loss between silica and ZBLAN fiber for all-fiber structured high-power mid-infrared supercontinuum generation,” *Infrared Physics Technology*, vol. 113, p. 103576, 2021. DOI: <https://doi.org/10.1016/j.infrared.2020.103576>.
- [246] L. Yang, Y. Li, B. Zhang, T. Wu, Y. Zhao, and J. Hou, “30-W supercontinuum generation based on ZBLAN fiber in an all-fiber configuration,” *Photon. Res.*, vol. 7, no. 9, p. 1061, Sep. 2019. DOI: 10.1364/PRJ.7.001061.

- [247] L. Yang, B. Zhang, X. He, K. Deng, S. Liu, and J. Hou, "20.6 W mid-infrared supercontinuum generation in ZBLAN fiber with spectrum of 1.9–4.3  $\mu\text{m}$ ," *Journal of Lightwave Technology*, vol. 38, no. 18, p. 5122, 2020. DOI: 10.1109/JLT.2020.2999730.
- [248] L. Yang, B. Zhang, X. He, K. Deng, S. Liu, and J. Hou, "High-power mid-infrared supercontinuum generation in a fluoroindate fiber with over 2 W power beyond 3.8  $\mu\text{m}$ ," *Opt. Express*, vol. 28, no. 10, p. 14973, May 2020. DOI: 10.1364/OE.393132.
- [249] Y. Jiao *et al.*, "Over 50 W all-fiber mid-infrared supercontinuum laser," *Opt. Express*, vol. 31, no. 19, p. 31082, Sep. 2023. DOI: 10.1364/OE.498183.
- [250] L. Yang *et al.*, "High-power ultraflat broadband supercontinuum generation in fluorotellurite fiber pumped by a dual-wavelength femtosecond laser," *Opt. Lett.*, vol. 50, no. 2, p. 618, Jan. 2025. DOI: 10.1364/OL.546477.



# Publications and Conference Contributions

## Peer-Reviewed Publications (First Author)

- J. Schneider, P. Forster, C. Romano, M. Eichhorn, and C. Kieleck, "Investigation of the pulse energy limits of actively Q-switched polarization-maintaining  $\text{Tm}^{3+}$ -doped fiber lasers," *OSA Continuum*, vol. 4, no. 5, p. 1577, May 2021. DOI: 10.1364/OSAC.423812.
- J. Schneider, P. Forster, C. Romano, M. Eichhorn, and C. Kieleck, "High pulse energy  $\text{ZnGeP}_2$  OPO directly pumped by a Q-switched  $\text{Tm}^{3+}$ -doped single-oscillator fiber laser," *Opt. Lett.*, vol. 46, no. 9, p. 2139, May 2021. DOI: 10.1364/OL.422702.
- J. Schneider *et al.*, "High-energy nanosecond pulse extraction from a  $\text{Tm}^{3+}$ -doped photonic crystal fiber laser emitting at 2050 nm with narrow linewidth," *Opt. Express*, vol. 32, no. 18, p. 32309, Aug. 2024. DOI: 10.1364/OE.531146.

## Peer-Reviewed Publication (Shared First Author)

- D. Lorenz, J. Schneider, C. Romano, D. Panitzek, J. Lautenschläger, M. Eichhorn, and C. Kieleck, "Actively pulse-shaped linearly polarized 200 W photonic crystal fiber MOPA at 2048 nm with 2 mJ pulse energy," *Opt. Lett.*, vol. 50, no. 14, p. 4490, Jul. 2025. DOI: 10.1364/OL.562668.

## Peer-Reviewed Publications (Co-Author)

- P. Forster, C. Romano, J. Schneider, M. Eichhorn, and C. Kieleck, “High-power continuous-wave  $\text{Tm}^{3+}:\text{Ho}^{3+}$ -codoped fiber laser operation from 2.1  $\mu\text{m}$  to 2.2  $\mu\text{m}$ ,” *Opt. Lett.*, vol. 47, no. 10, p. 2542, May 2022. DOI: 10.1364/OL.458921.
- D. Lorenz, C. Romano, D. Panitzek, P. Forster, J. Schneider, H. Bükler, M. Eichhorn, and C. Kieleck, “Nanosecond pulsed narrow-linewidth all-fiber source for ZGP-OPO pumping,” *Opt. Continuum*, vol. 2, no. 3, p. 660, Mar. 2023. DOI: 10.1364/OPTCON.486081.
- M. Rupp, D. Lorenz, K. Goth, J. Deutsch, J. Schneider, C. Romano, M. Eichhorn, and C. Kieleck, “Actively pulse shaped hybrid rare-earth-doped silica fiber/ $\text{Ho}^{3+}$ :YAG MOPA system at 2048 nm,” *Opt. Express*, vol. 33, no. 10, p. 20467, May 2025. DOI: 10.1364/OE.559360.

## Conference Contributions

- J. Schneider, P. Forster, M. Eichhorn, and C. Kieleck, “High-pulse-energy actively Q-switched polarization-maintaining  $\text{Tm}^{3+}$ -doped silica fiber laser,” in *OSA High-brightness Sources and Light-driven Interactions Congress 2020 (EUVXRAY, HILAS, MICS)*, Optica Publishing Group, 2020, MF2C.3. DOI: 10.1364/MICS.2020.MF2C.3.
- J. Schneider, P. Forster, C. Romano, M. Eichhorn, and C. Kieleck, “Advances in 2  $\mu\text{m}$  polarization-maintaining thulium-doped Q-switched fiber lasers for frequency conversion into the mid-IR,” in *Nonlinear Frequency Generation and Conversion: Materials and Devices XX*, P. G. Schunemann and K. L. Schepler, Eds., International Society for Optics and Photonics, vol. 11670, SPIE, 2021, 116700B. DOI: 10.1117/12.2577118.
- J. Schneider, P. Forster, C. Romano, M. Eichhorn, and C. Kieleck, “High-power Q-switched  $\text{Tm}^{3+}$ -doped fiber laser for nonlinear frequency conversion into the mid-IR,” in *Nonlinear Frequency Generation and Conversion: Materials and Devices XXII*, P. G. Schunemann, Ed., International Society for Optics and Photonics, vol. 12405, SPIE, 2023.
- J. Schneider *et al.*, “High-pulse-energy actively Q-switched  $\text{Tm}^{3+}$ -doped photonic crystal fiber laser operating at 2050 nm with narrow linewidth,” in *Laser Congress 2023 (ASSL, LAC)*, Optica Publishing Group, 2023, AW4A.3. DOI: 10.1364/ASSL.2023.AW4A.3.

- J. Schneider *et al.*, “High-pulse-energy actively Q-switched  $\text{Tm}^{3+}$ -doped photonic crystal fiber laser operating at 2050 nm with narrow linewidth,” in *Fiber Lasers XXI: Technology and Systems*, C. Jollivet, Ed., International Society for Optics and Photonics, vol. 12865, SPIE, 2024, p. 1286517. DOI: 10.1117/12.3002397.
- J. Schneider *et al.*, “High-pulse-energy  $\text{Tm}^{3+}$ -doped photonic crystal fiber laser for nonlinear frequency conversion into the mid-IR,” in *High-Power Lasers and Technologies for Optical Countermeasures II*, International Society for Optics and Photonics, vol. PC13201, SPIE, 2024, PC1320106. DOI: 10.1117/12.3031761.
- J. Schneider, D. Lorenz, J. Lautenschläger, C. Romano, M. Eichhorn, and C. Kieleck, “Optimization of nanosecond pulse energy extraction from  $\text{Tm}^{3+}$ -doped photonic crystal fibers,” in *Laser Congress 2024 (ASSL, LAC, LS&C)*, Optica Publishing Group, 2024, AM3A.1. DOI: 10.1364/ASSL.2024.AM3A.1.
- J. Schneider, D. Lorenz, C. Romano, D. Panitzek, J. Lautenschläger, M. Eichhorn, and C. Kieleck, “High-Power Actively-Pulse-Shaped 2 mJ Nanosecond-Pulsed  $\text{Tm}^{3+}$ -Doped Photonic Crystal Fiber Amplifier Emitting At 2048 nm,” in *2025 Conference on Lasers and Electro-Optics Europe European Quantum Electronics Conference (CLEO/Europe-EQEC)*, 2025, p. 1. DOI: 10.1109/CLEO/Europe-EQEC65582.2025.11111105.
- J. Schneider, P. Forster, D. Panitzek, D. Lorenz, C. Romano, M. Eichhorn, and C. Kieleck, “Pulse energy enhancement by means of fiber bragg gratings in actively Q-switched  $\text{Tm}^{3+}$ -doped fiber lasers operating at 2050 nm and 2090 nm,” in *EPJ Web of Conferences*, EDP Sciences, vol. 267, 2022, p. 02004.



# List of Acronyms

<b>EUV</b>	extreme ultraviolet
<b>SNR</b>	signal-to-noise ratio
<b>CW</b>	continuous-wave
<b>mid-IR</b>	mid-infrared
<b>OPO</b>	optical parametric oscillator
<b>YAG</b>	$\text{Y}_3\text{Al}_5\text{O}_{12}$
<b>ASE</b>	amplified spontaneous emission
<b>LMA</b>	large-mode-area
<b>PCF</b>	photonic crystal fiber
<b>LPF</b>	large pitch fiber
<b>FWHM</b>	full width at half maximum
<b>ZGP</b>	$\text{ZnGeP}_2$
<b>TEM</b>	transverse electromagnetic
<b>SVEA</b>	slowly varying envelope approximation
<b>HR</b>	high reflective
<b>AR</b>	anti-reflective
<b>UV</b>	ultraviolet
<b>GVD</b>	group velocity dispersion
<b>ZDW</b>	zero dispersion wavelength
<b>SHG</b>	second-harmonic generation

<b>OR</b>	optical rectification
<b>SFG</b>	sum-frequency generation
<b>DFG</b>	difference-frequency generation
<b>ODE</b>	ordinary differential equation
<b>SPM</b>	self-phase modulation
<b>XPM</b>	cross-phase modulation
<b>DFWM</b>	degenerate four-wave mixing
<b>FWM</b>	four-wave mixing
<b>AOM</b>	acousto-optical modulator
<b>SBS</b>	stimulated Brillouin scattering
<b>SRS</b>	stimulated Raman scattering
<b>OC</b>	output coupler
<b>HR</b>	high reflector
<b>FSR</b>	free spectral range
<b>SRO</b>	singly-resonant oscillator
<b>DRO</b>	doubly-resonant oscillator
<b>GVM</b>	group velocity mismatch
<b>PM</b>	polarization-maintaining
<b>CR</b>	cross-relaxation
<b>EM</b>	energy migration
<b>ETU</b>	energy transfer upconversion
<b>ESA</b>	excited-state absorption
<b>FBG</b>	fiber Bragg grating
<b>VBG</b>	volume Bragg grating
<b>NA</b>	numerical aperture
<b>HCF</b>	hollow-core fiber
<b>FSM</b>	fundamental space-filling mode

<b>MI</b>	modulation instability
<b>NLSE</b>	nonlinear Schrödinger equation
<b>NLS</b>	nonlinear Schrödinger
<b>MOPA</b>	master oscillator power amplifier
<b>OPA</b>	optical parametric amplifier
<b>CLS</b>	cladding light stripper
<b>EOM</b>	electro-optical modulator
<b>PER</b>	polarization extinction ratio
<b>OP-GaAs</b>	orientation-patterned GaAs
<b>CSP</b>	Cadmium Silicon Phosphide
<b>TFP</b>	thin-film polarizer
<b>PRF</b>	pulse repetition frequency
<b>PEM</b>	photoelectromagnetic
<b>OSA</b>	optical spectrum analyzer



# Danksagung

Zum Abschluss möchte ich all jenen danken, die mich während den vergangenen Jahren meiner Promotionszeit und der Fertigstellung dieser Arbeit begleitet und unterstützt haben. Die hier zusammengestellte Forschungsarbeit ist das Ergebnis erfolgreicher Zusammenarbeit am Karlsruher Institut für Technologie (KIT) und dem Fraunhofer IOSB. Sie wäre ohne den wertvollen fachlichen sowie persönlichen Beitrag von Betreuern, Kollegen, Freunden und Familie nicht möglich gewesen.

Mein Dank geht zunächst an meinen Doktorvater Prof. Dr. Marc Eichhorn für die Betreuung meiner Arbeit und den fachlichen Austausch. Außerdem möchte ich Dr. Christelle Kieleck danken, die die Abteilung Lasertechnologie am Fraunhofer IOSB leitet. Ihr beide habt am KIT und IOSB einzigartige Bedingungen für erfolgreiche Forschung geschaffen, die mir die entscheidenden Möglichkeiten und Freiheiten zur Gestaltung meines Promotionsthemas eröffnet haben.

Außerdem möchte ich Dr. Patrick Forster und Dr. Clément Romano danken, die mich in die Arbeit im Laserlabor einführten und mir auch später stets mit Rat und Tat zur Seite standen. Ihr seid in Eurer jeweils eigenen Art wahre Vorbilder für mich.

Großen Dank geht an meinen Büronachbar Dominik Lorenz für die zahlreichen spannenden Diskussionen und die gute Zusammenarbeit am PCF-Verstärker. Danke für Deine Freundschaft in den vergangenen Jahren.

Weiterhin geht mein Dank an alle Kollegen am KIT und IOSB. Jan Lautenschläger, Dr. Marius Rupp, Dr. Stefan Püschel und insbesondere Dr. Katharina Goth möchte ich für Ihre große Hilfe beim Korrekturlesen meiner Doktorarbeit danken. Außerdem danke ich Hugo Lassiette und Marie Pagès für die wertvolle Arbeit im Rahmen ihrer Studentenpraktika. Besonderer Dank

geht auch an Artur Schander für den Entwurf und die Fertigung essentieller optomechanischer Bauteile in der IOSB Werkstatt und Nicolas Wannenmacher für die Bereitstellung der IT-Infrastruktur. Ich danke allen Kollegen für Eure ständige Unterstützung und die wunderbare Arbeitsatmosphäre.

Zu guter Letzt möchte ich meine tiefe Dankbarkeit für meine Familie und Freunde zum Ausdruck bringen. Diese richtet sich insbesondere an meine Eltern Brigitte und Stefan, sowie an meinen Bruder Johannes. Was Ihr mir mitgegeben habt ist nicht in Worte zu fassen. Ich danke Euch für Eure bedingungslose Unterstützung für meinen Bildungsweg. Ich möchte außerdem meinem guten Freund Nicolas Lang und meinem Patenkind Elsa danken. Euch allen, auch denen die hier nicht namentlich genannt sind, danke ich für Euren Rückhalt und hoffe in Zukunft wieder mehr für Euch da zu sein.





INSTITUTE OF CONTROL SYSTEMS

LASERS AND OPTRONICS: MATERIALS,  
TECHNOLOGIES AND APPLICATIONS

06

This series contains scientific reports on laser technology and optronics performed at or in cooperation with the IRS. The topics range from laser-related materials like crystals and glasses and their elaboration over laser physics and technologies up to laser and optronic applications.

Thulium-doped fiber lasers are a compact and reliable technology for generating high-power  $2\ \mu\text{m}$  laser radiation but their pulsed operation is constrained by intensity-dependent nonlinear effects and gain limitations. This work addresses the challenge of pulse energy scaling in nanosecond-pulsed thulium-doped fiber lasers. Supported by experimental investigations, a general framework for their quantitative modeling is developed to analyze fundamental design trade-offs. From this analysis, strategies to overcome performance barriers were identified and experimentally validated, culminating in the demonstration of a thulium-doped photonic crystal fiber laser that sets a new benchmark for  $2\ \mu\text{m}$  laser technology. Furthermore, the fiber laser enables highly efficient nonlinear conversion by pumping a  $\text{ZnGeP}_2$  optical parametric oscillator, paving the way for future  $>100\ \text{W}$  mid-infrared sources.